ВІСНИК
КИЇВСЬКОГО НАЦІОНАЛЬНОГО УНІВЕРСИТЕТУ ІМЕНІ ТАРАСА ШЕВЧЕНКА

ISSN 1728-2306

РАДІОФІЗИКА ТА ЕЛЕКТРОНІКА 1(23)/2015

Засновано 1999 року

УДК 517

Публікуються результати експериментальних та теоретичних досліджень у галузях фізичної електроніки, фізики плазми, фізики поверхні твердого тіла, емісійної електроніки, кріогенної та мікроелектроніки, нанофізики та наноелектроніки, високотемпературної надпровідності, квантової радіофізики, функціональної електроніки, твердотільної електроніки, мобільного зв'язку, медичної радіофізики, методів отримання діагностичної інформації та її комп'ютерної обробки.

Для науковців, викладачів вищої школи, студентів.

Experimental and theoretical contributions are published in the following fields: physical electronics, plasma physics, solid-state surface physics, emission electronics, cryogenic electronics, microelectronics, nanophysics and nanoelectronics, high-temperature supercondactive electronics, solid-state electronics, functional electronics, microwave electronics, quantum electronics, mobile communication, medical radiophysics, methods of receipt and computer processing of diagnosis information

Designed for researches, university teachers, students.

РЕДАКЦІЙНА КОЛЕГІЯ	**І. О. Анісімов, д-р фіз.-мат. наук, проф. (відп. ред.); Г. А. Мелков, д-р фіз.-мат. наук, проф. (заст. відп. ред.); В. А. Львов, д-р фіз.-мат. наук, проф. (наук. ред.); Т. В. Родіонова, канд. фіз.-мат. наук, ст. наук. співроб. (відп. секр.); Ю. В. Бойко, канд. фіз.-мат. наук, доц.; А. М. Веклич, д-р фіз.-мат. наук, проф.; В. І. Висоцький, д-р фіз.-мат. наук, проф.; В. І. Григорук, д-р фіз.-мат. наук, проф., І. В. Зависляк, д-р фіз.-мат. наук, проф.; Б. О. Іванов, д-р фіз.-мат. наук, проф.; В. І. Кисленко, канд. фіз.-мат. наук, доц.; В. Ф. Коваленко, д-р фіз.-мат. наук, проф.; І. П. Коваль, канд. фіз.-мат. наук, доц.; М. В. Кононов, канд. фіз.-мат. наук, доц.; В. Г. Литовченко, д-р фіз.-мат. наук, проф.; Є. В. Мартиш, д-р фіз.-мат. наук, проф.; С. Д. Погорілий, д-р техн. наук, проф.; С. М. Савенков, д-р фіз.-мат. наук, доц.; В. А. Скришевський, д-р фіз.-мат. наук, проф.; В. Я. Черняк, д-р фіз.-мат. наук, проф.; M. Bartlova (Milada Bartlová), Ph. D., (Brno University of Technology, Czech Republic); N. Kukhtarev (Nickolai Kukhtarev), Research Professor, (Alabama A&M University, USA)**
Адреса редколегії	**03127, м. Київ-127, просп. акад. Глушкова, 4 Г, факультет радіофізики, електроніки та комп'ютерних систем. ☎ (38044) 526 05 60**
Затверджено	**Вченою радою радіофізичного факультету 13.10.14 (протокол № 3)**
Атестовано	**Вищою атестаційною комісією України. Постанова Президії ВАК України № 1-05/1 від 10.02.2010 р.**
Зареєстровано	**Міністерством юстиції України. Свідоцтво про державну реєстрацію КВ № 15797-4269Р від 02.10.2009 р.**
Засновник та видавець	**Київський національний університет імені Тараса Шевченка, ВПЦ "Київський університет" Свідоцтво внесено до Державного реєстру ДК № 1103 від 31.10.02**
Адреса видавця	**01601, Київ-601, б-р Т.Шевченка, 14, кімн. 43 ☎ (38044) 239 31 72, 239 32 22; факс 239 31 28**

© Київський національний університет імені Тараса Шевченка, ВПЦ "Київський університет", 2015

ЗМІСТ

ЗМІСТ

СОДЕРЖАНИЕ

СОДЕРЖАНИЕ

CONTENTS

CONTENTS

UDC 577.359: 576.32/.36:616-092.18:576.385

V. Bilonozhko, stud.,
Department of Electrophysics, Faculty of Radio Physics, Electronics and Computer Systems,
Taras Shevchenko National University of Kyiv
K. Gurzhiy, post. grad. stud., E. Lukyanetz, Dr.Sci, Prof.
Bogomoletz Institute of Physiology, NAS of Ukraine

INVESTIGATION OF THE DEATH OF HIPPOCAMPAL NEURONS UNDER THE INFLUENCE OF HYPOXIA BY USING A LASER SCANNING CONFOCAL MICROSCOPY

Investigation of the death of hippocampal neurons under the influence of hypoxia by using a laser scanning confocal microscopy was fulfilled. Using double staining of the cells with fluorescent dyes propidium iodide and Hoechst 33258 it was revealed that 15-minutes gas hypoxia caused the death of 5% neurons and neuronal apoptosis observed in 40%.

Key words: *rat, confocal microscope, necrosis, apoptosis, fluorescent dyes.*

Introduction. Brain hypoxia is a serious neurological disease associated with lack of oxygen in the brain due to various reasons. Prolonged hypoxia induces neuronal cell death via apoptosis, resulting in a hypoxic brain injury. While programmed cell death, apoptosis, occurs as a necessary and natural event for multicellular organisms, necrosis is a form of unplanned cell death as a result of pathological or chemical trauma. There are numerous molecular and morphological differences between these two forms of the cell death, whose decision is based on the type and dose of the stress [1].

The aim of our experiments was to study the death of hippocampal neurons of a rat under the influence of the hypoxia with using of laser scanning confocal microscope. Cultures of rat hippocampal neurons were selected as the object of study in this work because the brain is one of the first organs to fail in hypoxia, due to its high intrinsic rate of oxygen consumption. Hippocampus plays an important role in the consolidation of information from short-term memory to long-term memory and learning.

Fluorescence microscopy is based on the study of microscopic objects which able to luminescence. Fluorescence microscopy allows analyzing the distribution and dynamics of functional molecules in single intact living cells. The method of image formation in a confocal microscope is achieved by scanning one or more focused beams of light from a laser across the specimen, Fig.1. The images produced by scanning the specimen in this way are called optical sections. Confocal microscopy offers several advantages over conventional widefield optical microscopy, including the ability to control depth of field, elimination or reduction of background information away from the focal plane (that leads to image degradation), and the capability to collect serial optical sections from thick specimens (greater than 2 micrometers). The basic key to the confocal approach is the use of spatial filtering techniques to eliminate out-of-focus light or glare in specimens whose thickness exceeds the immediate plane of focus.

Coherent light emitted by the laser system (excitation source) passes through a pinhole aperture that is situated in a conjugate plane (confocal) with a scanning point on the specimen and a second pinhole aperture positioned in front of the detector (a photomultiplier tube). As the laser is reflected by a dichromatic mirror and scanned across the specimen in a defined focal plane, secondary fluorescence emitted from points on the specimen (in the same focal plane) pass back through the dichromatic mirror and are focused as a confocal point at the detector pinhole aperture, Fig.1.

The significant amount of fluorescence emission that occurs at points above and below the objective focal plane is not confocal with the pinhole and forms extended Airy disks in the aperture plane. Because only a small fraction of the out-of-focus fluorescence emission is delivered through the pinhole aperture, most of this extraneous light is not detected by the photomultiplier and does not contribute to the resulting image. The dichromatic mirror, barrier filter, and excitation filter perform similar functions to identical components in a widefield epi-fluorescence microscope. Refocusing the objective in a confocal microscope shifts the excitation and emission points on a specimen to a new plane that becomes confocal with the pinhole apertures of the light source and detector.

Visualization of a cell with fluorescent compounds provides a wide variety of information for the analysis of cell functions. Various activities and structures of a cell can be targeted for staining with fluorescent compounds.

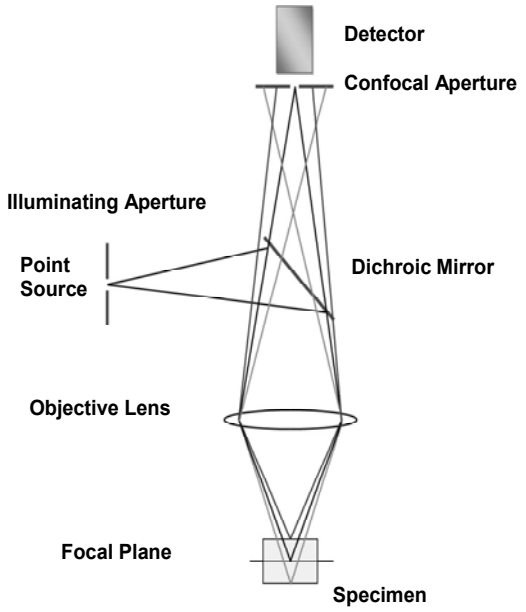

Fig. 1. Principle of confocal microscopy

Methods. In our experiments, the hippocampal cell cultures were prepared from hippocampal neurons of newborn Wistar rats. All experiments with animal were performed in strict compliance with all applicable international and local regulations for the proper use of animals in researches. Neurons were cultivated for 12–13 days in the culture.

We used double staining for neuronal death detection. Double stain apoptosis detection method (Hoechst 33258/ Propidium iodide) employs two dyes assaying normal, apoptotic, and dead cells. This method provides a rapid and convenient assay for apoptosis based upon fluorescent detection for the compacted state of the chromatin in apoptotic cells. These dyes bound to DNA. Hoechst 33258, a kind of blue-fluorescence dye (excitation/ emission maxima ~350/461 nm (Fig. 2), when bound to DNA), stains the condensed chromatin in apoptotic cells

© Bilonozhko V., Gurzhiy K., Lukyanetz E., 2015

more brightly than the chromatin in normal cells. Propidium iodide (PI), a red-fluorescence dye (excitation/emission maxima ~535/617 nm, when bound to DNA), is only permeate to dead cells. The simultaneous use of these dyes makes it possible to distinguish normal, apoptotic, and dead cell populations by fluorescence microscopy. Hoechst stains are part of a family of blue fluorescent dyes used to stain DNA. This dyes bind to minor-grooves of DNA (multiple affinity types) with fluorescence enhancement. The Hoechst 33258 dye has been used widely for staining the nuclei of living cells because they are high membrane permeability. We have used this dye because of its non-toxicity, ability to be excited by most common light sources (i.e. argon/ion laser), and suitability for multicolor imaging (large Stocke's shift). This dye fluoresces strongly when bound to DNA, but are not visible under transmitted light.

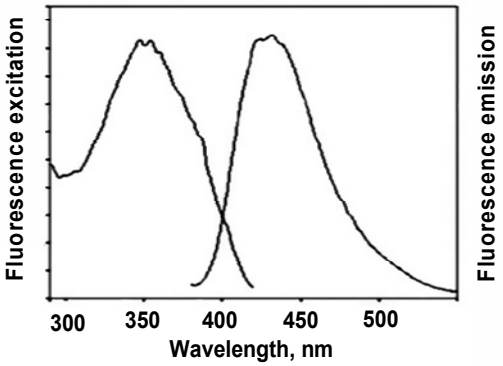

Fig. 2. Absorption and emission spectra of Hoechst 33258 bound to DNA

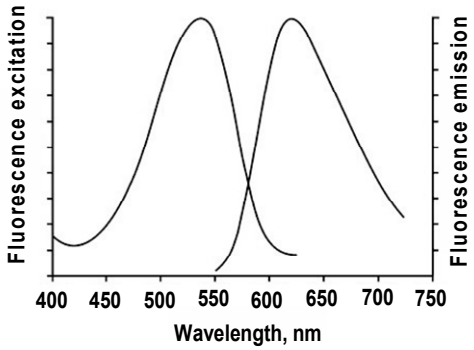

Fig. 3. Absorption and emission spectra of Propidium Iodide

To load the neurons with fluorescent dyes, the cells were kept in the solution with the addition 5 μg/ml of a fluorescent dye propidium iodide for 15min than it was washed and kept in the solution with the addition 1 μg/ml of a fluorescent dye Hoechst 33258 for 20 min. After staining cells were fixed by the Aqua PolyMount solution.

For simulation the hypoxic state we used application of the solution with low oxygen content. For lowering values of pO_2 this solution for 15 minutes was subjected to processing with nitrogen. Bubbles of nitrogen were passed through the solution that create hypoxic conditions. We used the polarographic method for a partial oxygen pressure measuring within the cell washing solution.

Investigation of the survival of hippocampal neurons was based on fluorescent detection by using confocal microscope OLYMPUS FV1000. The dye Propidium Iodide was alternately excited by He-Ne laser at wavelength 545nm with emission detected from 595nm to 660nm; the dye Hoechst 33258 was excited by Argon laser at wavelength 350nm with emission from 420nm to 510nm. The emission was detected by photomultiplier tube (PMT) and then was transferred to a computer. Processing of the data obtained were performed using ImageJ software (National institute of health, USA).

Experimental results and discussion. Our experiments were aimed to determine the rat hippocampal neuron death in culture, which was treated with hypoxic solution. Figure 4 shows phase contrast image of cultured hippocampal neurons obtained with confocal microscope. To do hypoxic conditions, the cells were incubated with nitrogen saturated solution (30–40% hypoxia), and then were used for the double staining procedure with two dyes that bind to DNA: Hoechst 33258 and propidium iodide. Hoechst 33258 after binding to the DNA of living cells shows the blue spots in the cell images (Fig. 4 A). In turn, propidium iodide – a red fluorescent dye which is permeable only for dead cells (Fig. 4, B). Simultaneous staining by these dyes allows to distinguish between living and dead (necrotic) neurons by using a confocal laser scanning microscopy.

Based on our resulting images the population of neurons was separated into three groups: live cells showed only a low level of fluorescence; apoptotic cells showed a higher level of blue fluorescence, and dead cells showed low-blue and red fluorescence. The reddish-stained cells are those which lost the intactness of their cell membrane Propidium Iodide gets into the cell and stain the nuclei in red (necrosis).

According to resulting data the number of the necrotic cells was 5%, number of apoptotic cells was 40% after creating hypoxic state.

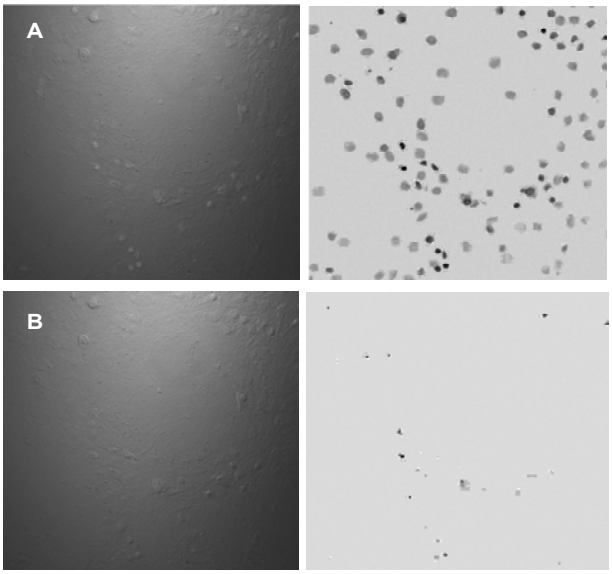

Fig. 4. The confocal microscopic image of the hippocampal neurons stained by Hoechst 33258 (A) and PI (B). Phase contrast image (left), fluorescent (right)

Conclusions. Investigation of the death of hippocampal neurons under the influence of hypoxia by using a laser scanning confocal microscopy was fulfilled. According to our experiments after creating the hypoxic conditions the number of the necrotic cells was 5%, and number of apoptotic cells was 40% to compare the control where the quantity of living cells were 94%. These data indicate a high sensitivity of hippocampal neurons to hypoxic conditions.

REFERENCE

1. *Lukyanetz E. A.* Action of hypoxia on different types of calcium channels in hippocampal neurons / E. A. Lukyanetz, V. M. Shkryl, O. V. Kravchuk, P. G. Kostyuk // Biochimica et Biophysica Acta – Biomembranes. – 2003. – 1618. – P. 33–38.

2. *Lukyanetz E. A.* Effect of hypoxia on calcium channels depends on extracellular calcium in CA1 hippocampal neurons / E. A. Lukyanetz, V. M. Shkryl, O. V. Kravchuk., P. G. Kostyuk // Brain Res. – 2003. – 980. – P. 128–134.

3. *Rieger A. M.* Modified Annexin V/Propidium Iodide Apoptosis Assay For Accurate Assessment of Cell Death / A. M. Rieger, K. L. Nelson, J. D. Konowalchuk, D. R. Barreda // Journal of Visualized Experiments. – 2011.

4. *Shkryl V. M.* Dual action of cytosolic calcium on calcium channel activity during hypoxia in hippocampal neurones / V. M. Shkryl, P. G. Kostyuk, E. A. Lukyanetz // Neuroreport. – 2001. – 12. – P. 4035–4039.

5. *Shkryl V. M.* High-threshold calcium channel activity in rat hippocampal neurones during hypoxia / V. M. Shkryl, L. M. Nikolaenko, P. G. Kostyuk, E. A. Lukyanetz // Brain Res. – 1999. – 833. – P. 319–328.

Submitted on 02.06.15

В. Білоножко, студ.,
каф. електрофізики, факультет радіофізики, електроніки та комп'ютерних систем,
Київський національний університет імені Тараса Шевченка
К. Гуржій, асп., О. Лук'янець д-р біолог. наук, проф.
Інститут фізіології ім. О. О. Богомольця НАН України

ДОСЛІДЖЕННЯ СМЕРТІ НЕЙРОНІВ ГІПОКАМПУ ПІД ВПЛИВОМ ГІПОКСІЇ ЗА ДОПОМОГОЮ ЛАЗЕРНОЇ СКАНУЮЧОЇ КОНФОКАЛЬНОЇ МІКРОСКОПІЇ

Проведено дослідження смерті нейронів гіпокампу під впливом гіпоксії за допомогою лазерної скануючої конфокальної мікроскопії. Використовуючи подвійне фарбування клітин флуоресцентними барвниками пропідіум йодид та Hoechst 33258 встановлено, що 15-хвилинна газова гіпоксія викликає загибель 5% нейронів і у 40% нейронів спостерігається апоптоз.

Ключові слова: *щур, конфокальний мікроскоп, некроз, апоптоз, флуоресцентні барвники.*

В. Билоножко, студ.,
каф. электрофизики, факультет радиофизики, электроники и компьютерных систем,
Киевский национальный университет имени Тараса Шевченка
К. Гуржий, асп., Е. Лукьянец д-р биолог. наук, проф.
Институт физиологии им. А. А. Богомольца НАН Украины

ИССЛЕДОВАНИЕ СМЕРТИ НЕЙРОНОВ ГИППОКАМПА ПОД ВЛИЯНИЕМ ГИПОКСИИ С ПОМОЩЬЮ ЛАЗЕРНОЙ СКАНИРУЮЩЕЙ КОНФОКАЛЬНОЙ МИКРОСКОПИИ

Проведено исследование смерти нейронов гиппокампа под влиянием гипоксии с помощью лазерной сканирующей конфокальной микроскопии. Используя двойное окрашивание клеток флуоресцентными красителями пропидиум йодид и Hoechst 33258 установлено, что 15-минутная газовая гипоксия вызывает гибель 5% нейронов и у 40% нейронов наблюдается апоптоз.

Ключевые слова: *крыса, конфокальный микроскоп, некроз, апоптоз, флуоресцентные красители*

UDC 621.372

A. Bychok, Asp., Yu. Hayday, PhD
Department of Quantum Radiophysics
Faculty of Radiophysics, Electronics and Computer Systems,
National Taras Shevchenko University of Kyiv
O. Zorenko, PhD
State Enterprise Institute "Orion"

THE RESEARCH OF THE IMPEDANCE CHARACTERISTICS OF THE IMPATT DIODES IN AVALANCHE BREAKDOWN MODE FOR USE THEM AS A SOLID SOURCE OF NOISE IN SUBMILLIMETER RANGE

This article presents the results of the calculation and measurement of impedance characteristics of single-drift silicon impact ionization avalanche transit-time (IMPATT) diodes. Using the method of the CV characteristics the width of the depletion region, the avalanche breakdown voltage and doping profile of diodes were defined. With the help of the theoretical calculation method the impedance of diodes was calculated. Data is presented for further analysis and selection of diode impedance matching modes with the impedance of the transmission line in a microwave chamber. IMPATT diode operates in avalanche mode, and is used as a solid-state source of noise in submillimeter range.

Key words: *submillimeter range, IMPATT diode, the coefficients of impact ionization, C-V characteristics, the profile diode doping, full impedance, a solid state source of noise.*

Introduction. In connection with the intensive development of the submillimeter range and the creation of highly sensitive receiver's application area of which extends from the communication and radar stations to radio astronomy, solid noise sources that intended to calibrate and measure noise parameters of such receivers are highly demanded.

It is convenient to use an IMPATT diode as an active element of a solid-state source of noise, the supply voltage of which is several times lower than in vacuum devices. Thus, it is necessary to conduct a study of impedance characteristics for further analysis and selection of diode impedance matching modes with the impedance of the transmission line in a microwave chamber.

For determination of the impedance and current-voltage characteristics of diodes data from two methods was used: theoretical and experimental. The experimental method determines the diameter of the chip, the avalanche breakdown voltage and the dopant concentration using the CV diode characteristics; the theoretical method determines the total impedance of a diode and the diode matching method with the transmission line in a microwave – chamber.

For experimental studies, IMPATT diode with beam leads samples with a breakdown voltage U_{b1}=8 V and U_{b2}=22 V volts were taken. The structure of the diodes is single-span p+-n-n+, with an asymmetric sharp p-n–transition and linear profile doping in n–area. Using empirical formulas from [1], we find the dopant concentration in the n–field for two diodes – $N_{b1}=1.53\times10^{17}$ cm^{-3} and $N_{b2}=3.75\times10^{16}$ cm^{-3} respectively. Knowing the concentration, we can

© Bychok A., Hayday Yu., Zorenko O., 2015

calculate the width of the diode depletion region [5]. The width of the depletion region W for two diodes with concentrations given above N_{b1} and N_{b2}, is 0.06 μm and 0.11 μm respectively.

Also, using the empirical formula of [5], we find that the maximum intensity of the electric field E_m in both diodes – 6.1×10^5 V/cm and 5×10^5 V/cm respectively.

The measuring of the diameter of the mesa structures of the diodes is made. They are d_1=79.6 μm and d_2=52.7 μm for the two diodes, respectively.

The most important parameter of the p-n–transition, the calculation of which is needed during the development and research of devices with avalanche breakdown is the avalanche breakdown voltage. The calculations of avalanche breakdown voltage are the solution of the inverse task of determining the concentration of impurities in the lightly doped region.

Avalanche breakdown condition is the fulfillment of one of the two equations given in [5] when ionization integral equal to one.

Using the empirical formulas (1) and (2) from [2] that describe the dependence of impact ionization coefficients on the value of the electric field and temperature, we can find the coefficients of impact ionization of electrons and holes, as well as the breakdown voltage of two IMPATT diodes from the avalanche breakdown condition.

$$\alpha(E,T)=25\left(1+10^{-3}T\right)\exp\left[-141{,}43\frac{1+6.25\cdot10^{-4}T}{E}\right], \quad (1)$$

$$\beta(E,T)=140\left(1+10^{-3}T\right)\exp\left[-205.57\frac{1+6.25\cdot10^{-4}T}{E}\right] \quad (2)$$

Then we have α_{n1}=1.214, U_{b1}=8.02 V and α_{n2}=2.287, U_{b2}=21.99 V, respectively for two diodes.

For both considered diodes dependencies of the coefficients of impact ionization and electric field distribution in the n–area on the pitch over the length of the base of the diode (the length of the bases for the two diodes L_{n1}=260 nm and L_{n2}=880 nm divided by 100 parts) Fig. 1.

The electric field does not penetrate in highly doping p^+–area.

Using the results of measurements CV characteristics we can calculate the width of the depletion region for both diodes [5]. Then W will be 0.08 μm and 0.17 μm, respectively. These values are somewhat more than theoretically calculated, due to the closeness of empirical formulas used, as well as the fact that initially we considered dopant concentration constant within the limits diode base.

Also, we can calculate the concentration of impurities $N_x(i)$ in the base point i and the distance from the point with concentration N_x to p-n–transition using the finite difference method

$$N_x(i)=\frac{\left(\frac{C_{1+i}+C_{2+i}}{2}\right)^3}{e\varepsilon\varepsilon_0A^2}\times\left(\frac{C_{1+i}\;\;C_{2+i}}{U_{2+i}\;\;U_{1+i}}\right)^{-1} \quad (3),$$

$$x(i)=\frac{\varepsilon\varepsilon_0A}{\frac{(C_{1+i}+C_{2+i})}{2}} \quad (4),$$

where C_{1+i} and C_{2+i} are the capacitance values of two adjacent points, U_{2+i} and U_{1+l} are the voltages in two adjacent points, i=n-2 – the number of points, e – the electron charge, ε – the dielectric constant of silicon, ε_0 – the electric constant, $A=(\pi d^2)/4$ – square p-n–transition.

Then, from the formulas (3) and (4) we can plot of dependence of the concentration of impurities in the point from the distance to the p-n–transition, i.e. to get the profile diode doping (Fig. 2).

We can see that the doping profile is complex and differs from the flat. The choice of the creation of such base doping profile of diodes was based on data from [6], order to localize and reduce the multiplication region.

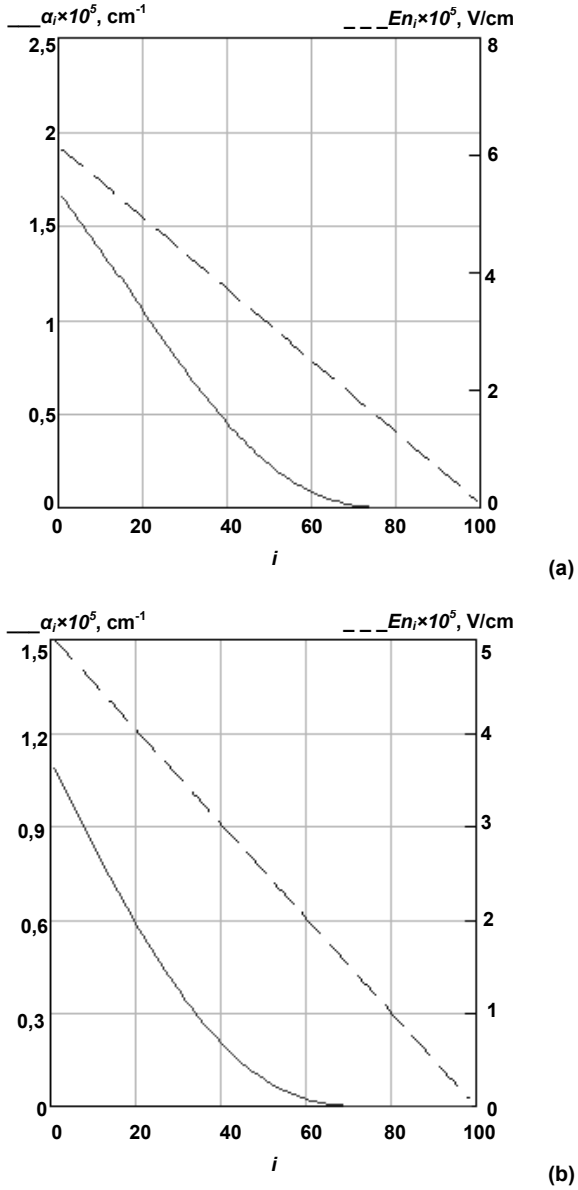

Fig. 1. The dependence of the coefficient of impact ionization (lower curves) and the values of the electric fields on the selected step in n–areas for (a) diodes with $N_{b1}=1.53\times10^{17}$ cm^{-3} and (b) diodes with $N_{b2}=3.75\times10^{16}$ cm^{-3}

At low frequencies, the resistance of the IMPATT diode Z_d is determined by the parasitic resistance of the passive region R_s, which is connected with contacts, external connections, and so on. as well as the resistance R_{sc}, which is connected with the space charge of the carriers. It has to be said that the diode is created using membrane technology and the thickness of the silicon in mesa-structure is 10 μm.

Then, using the method with [4] for the first diode R_s=0.02 ohm, R_{sc}=0.285 ohm and Z_d=0.305 ohm, and for the second one – R_s=0.046 ohm, R_{sc}=7.5 ohm and Z_d=7.55 ohm.

In the high frequency range (operating frequency F=300 GHz), the total impedance of the IMPATT diode is described as shown in [3]. Resonance frequency of the avalanche can be found by the parity

$$\omega_a = \sqrt{\frac{2\alpha_0' v_s J_0}{\varepsilon\varepsilon_0}} \quad (5),$$

where α_0' – the derivative by the field of impact ionization coefficient, v_s – drift velocity of the saturation of the carriers for silicon, $J_0=I_0/A$ – density of DC, I_0 – DC value for the supply [1]. In our case I_0=100 mA.

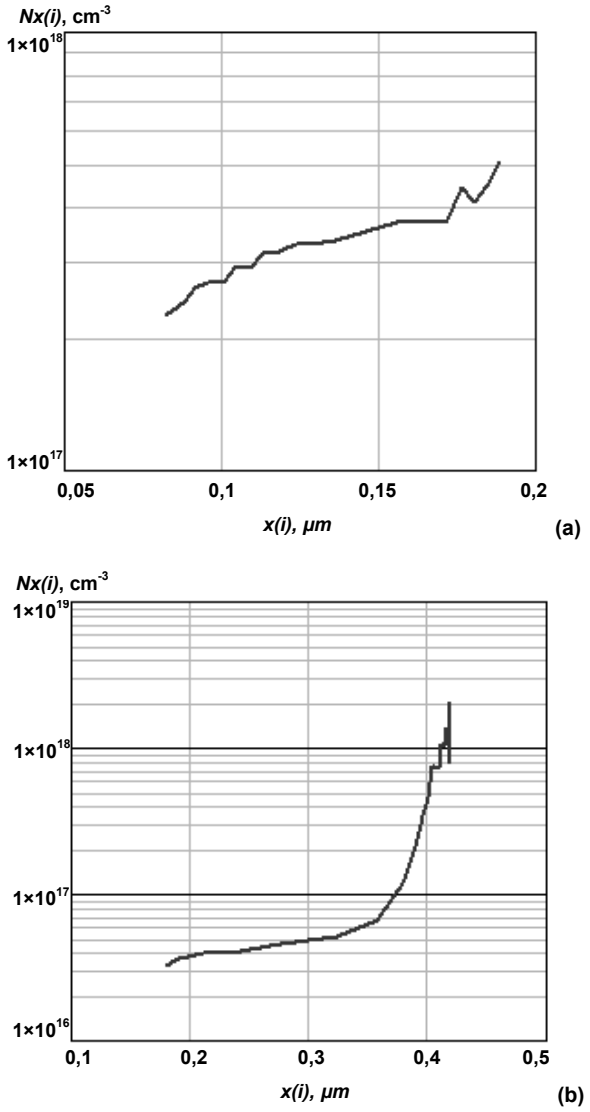

Fig. 2. The graph of the concentration of impurities on the distance to the – transition for diodes with (a) U_{b1}=8 V and (b) U_{b2}=22 V

Then, using the formula (5) and empirical formulas of [1], it was possible to calculate the frequency of the avalanche resonance F_a for both IMPATT diodes. It was 97.6 GHz and 119.5 GHz, respectively. Then we can build a dependence of the real and imaginary parts of the impedance on the diode frequency (Fig. 3).

The impedance of IMPATT diodes on operating frequency F=300 GHz are equal to Z=(0.014–0.273i) ohm and Z=(0.035–2.13i), respectively.

We see that at frequencies other than the avalanche for the investigated diodes the real part of the total impedance is greater than zero, which indicates the absence of the auto-generation and the possibility of obtaining an even noise, also at the frequencies above 200 GHz.

Low-voltage diodes are better suited for use in noise generator, as they have a high doping level, and thus the high electric field breakdown. Then the quantity of carriers that create a fractional noise – current fluctuations will be greater than in the high-voltage diodes. Accordingly, the spectral power density of the noise such diodes above. Also, the length of the crystal for low-voltage diodes smaller, which leads to a reduction in the negative resistance region [4].

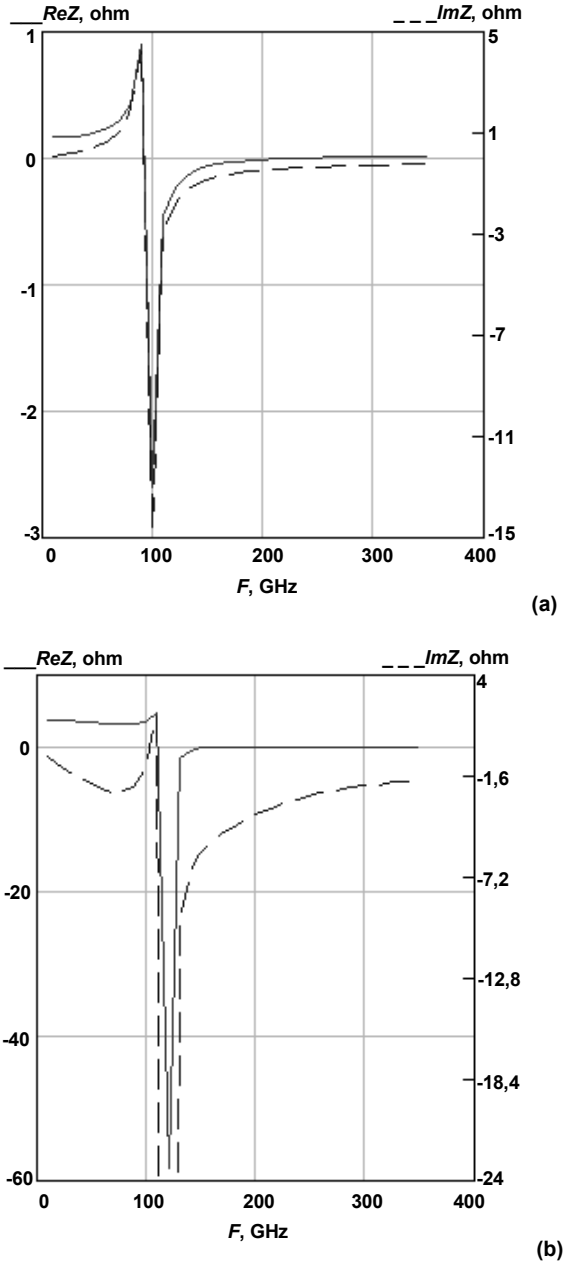

Fig. 3. The dependence of the real and imaginary parts of the impedance of the diode on the frequency for (a) diodes with $N_{b1}=1.53\times10^{17}$ cm^{-3} and (b) diodes with $N_{b2}=3.75\times10^{16}$ cm^{-3}

Conclusion. As a result of this work, profiles of doping diodes were experimentally obtained. The use of CV characteristics allows to accurately determining the parameters of the diode in the pre-breakdown state. The obtained values of resistance of the diode are low, and, based on that, special diode impedance to the transmission line in the microwave-camera matching circuit must be used. A hybrid-integrated version represents a possible option [1].

On the basis of the data obtained conclusions on the possibility of using solid-state diodes as sources of noise submillimeter range were made.

REFERENCE

1. *Fusco V.* Microwave circuits. Analysis and Computer-aided Design / V. Fusco // Trans. From English. Ed. – M.: "Radio and Communications", 1990. – 288 p.
2. *Grant W. N.* Electron and hole ionization rates in epitaxial silicon at high electric fields / W. N. Grant // Bell Laboratories, New Jersey, 1972, P. 1189–1202.
3. *Howes M.* Semiconductors in microwave circuits / M. Howes, D. Morgan // Trans. From English. Ed. – M.: "World", 1979. – 444 p.
4. *Muruynenko Yu. V.* The broadband noise generators on the IMPATT diode in hybrid-integrated performance / Yu. V. Muruynenko, Berezyuk F. B., Gutsul A. V., Zorenko A. V., Wang Lei // Machinery and microwave devices, №2. 2009. P. 41–43.
5. *Sze S. M..* Physics of Semiconductor Devices / S. M. Sze, K. Kwok // 3rd Edition, John Wiley & Sons, Inc. 2007. – 510 p.
6. *Tager A. S.* IMPATT diodes and their application in microwave technology / A. S. Tager, V. M. Vald-Perlov // M.: "Soviet radio", 1968. – 480 p.

Submitted on 15.10.15

Бичок А., асп., Гайдай Ю., канд. фіз.-мат. наук
каф. квантової радіофізики, факультет радіофізики, електроніки та комп'ютерних систем
Київський національний університет імені Тараса Шевченка
Зоренко О., канд. техн. наук,
Державне підприємство науково-дослідний інститут "Оріон"

ДОСЛІДЖЕННЯ ІМПЕДАНСНИХ ХАРАКТЕРИСТИК ЛПД В РЕЖИМІ ЛАВИННОГО ПРОБОЮ ДЛЯ ВИКОРИСТАННЯ ЙОГО В ТВЕРДОТІЛЬНОМУ ДЖЕРЕЛІ ШУМУ СУБМІЛІМЕТРОВОГО ДІАПАЗОНУ

У даній статті викладені результати розрахунку і вимірювань імпедансних характеристик однодрейфових кремнієвих лавинно-прольотних діодів (ЛПД). Методом вольтфарадних характеристик визначені: ширина збідненої області, напруга лавинного пробою і профіль легування діодів. За допомогою теоретичного методу проведений розрахунок повного опору діодів. Дані наводяться для подальшого аналізу і вибору режимів узгодження імпедансу діодів з опором лінії передачі в НВЧ камері. ЛПД працює в режимі лавинного пробою і використовується в якості твердотільного джерела шуму субміліметрового діапазону.

Ключові слова: *субміліметровий діапазон, ЛПД (лавинно-пролітний діод), коефіцієнти ударної іонізації, вольтфарадна (C-V) характеристика, профіль легування діоду, повний імпеданс, твердотільне джерело шуму.*

Бычок А., асп., Гайдай Ю., канд. физ.-мат. наук,
каф. квантовой радиофизики, факультет радиофизики, электроники и компьютерных систем
Киевский национальный университет имени Тараса Шевченко
Зоренко А., канд. техн. наук,
Государственное предприятие научно-исследовательский институт "Орион"

ИССЛЕДОВАНИЕ ИМПЕДАНСНЫХ ХАРАКТЕРИСТИК ЛПД В РЕЖИМЕ ЛАВИННОГО ПРОБОЯ ДЛЯ ИСПОЛЬЗОВАНИЯ ЕГО В ТВЕРДОТЕЛЬНОМ ИСТОЧНИКЕ ШУМА СУБМИЛЛИМЕТРОВОГО ДИАПАЗОНА

В данной статье изложены результаты расчета и измерений импедансных характеристик однодрейфовых кремниевых лавинно – пролетных диодов (ЛПД). Методом вольтфарадных характеристик определены: ширина обедненной области, напряжение лавинного пробоя и профиль легирования диодов. С помощью теоретического метода произведен рассчет полного сопротивления диодов. Данные приводятся для последующего анализа и выбора режимов согласования импеданса диодов с сопротивлением линии передачи в СВЧ–камере. ЛПД работает в режиме лавинного пробоя и используется в качестве твердотельного источника шума субмиллиметрового диапазона.

Ключевые слова: *субмиллиметровый диапазон, ЛПД (лавинно-пролетный диод), коэффициенты ударной ионизации, вольтфарадная (C-V) характеристика, профиль легирования диода, полный импеданс, твердотельный источник шума.*

UDC 004.021,004.67

M. Vasylets, stud., A. Udachyna, stud., V. Gryaznova, Ph.D.
Faculty of Radiophysics, Electronics and Computer systems
Taras Shevchenko National University of Kyiv
e-mail: vasylets.m.a@gmail.com

ANALISYS OF UNIVERSITY STUDENTS GRADING AIMED TO ECTS GRADING SCALE IMPLEMENTATION

Different patterns of students grading were detected for lecturers of Kyiv National Taras Shevchenko University by cluster analysis methods. Clustering was performed according to k-means algorithm with Euclidean distance as the metrics. Also, the problems of conversion of scores on criterion-based grading scales to ECTS grades are reviewed. Various ways of calculating the ECTS grades are investigated, and practical algorithm of calculation is proposed.

Key words: *students grading, clustering, k-means algorithm, ECTS grade, methods of calculating ECTS grades.*

Introduction. Significant part of integration of Ukrainian universities into European education system is implementation of a new Diploma Supplement of European model, which uses the ECTS grading scale [1]. Nowadays in educational institutions of the world there coexist several different assessment systems of student progress: evaluation on a 100-point scale, on different national scales and on ECTS scale, which are not always successfully combined, because of the fact that while grading student progress on a 100-point scale or on a national scale, lecturers do not always follow the normal distribution which is necessary for ECTS scale, and different lecturers have different criteria and methods of knowledge evaluation. One of the ways of solving such problems is to use methods of processing and analyzing data.

Experimental. To select the categories of lecturers by their grading patterns, we assort them into appropriate clusters using Data Mining methods. In our investigation, lecturers of Kyiv National Taras Shevchenko University were considered as objects for clustering (sample elements) on the base of the students scores, rated by given lecturer. Properties of these objects are percent of scores on a 100-point scale within the ranges: 60–64, 65–69, and so on till 95–100, critical ranges: 73–74, 88–89 and also precisely scores of 60, 75 and 90, averaged for every lecturer by all the subjects, taught by him/her during the entire period of teaching at Kyiv National Taras Shevchenko University. Such a choice was conditioned by relation of national 5-point scale with 100-point scale as follows: 90–100 points on a 100-points scale corresponds to score 5 on the national scale, 75–89 points corresponds to score 4, and 60–74 points corresponds to score 3 (Table 1).

***Table* 1**

Correspondence between 5- and 100-point scale

Grade in 5-point scale	Grade in 100-point scale
3	60–74
4	75–89
5	90–100

© Vasylets M., Udachyna A., Gryaznova V., 2015

For dividing the lecturers into categories *k*-means algorithm [2] was used. *K*-means algorithm allows to distribute the objects under consideration into categories (clusters), estimating the similarity of properties that characterize these objects. The algorithm consists of the following steps:

1. Definition of random initial cluster centers;
2. Determination of the cluster, to which the object belongs, for every element of the sample;
3. Updating cluster centers, based on sample units included in the cluster.

The algorithm terminates when the cluster centers are unchanged.

As a space metric, in the process of calculations Euclidean distance was used. Euclidean distance of the object to a cluster center is calculated by the formula:

$$\rho = \sqrt{\sum_{i=1}^{n} | x_j - c_j |^2} , \quad (1)$$

where is the *j*-th-property of the corresponding cluster center *c*, is the *j*-th-property of the sample element *x*, $j = \overline{1,n}$, and *n* is the number of the properties of a sample element.

The sample element is considered belonging to the cluster with the nearest center. After distributing all of the sample elements to the clusters, all the cluster centers are updated so that centroids of the corresponding clusters became the new cluster centers.

There is a problem of the optimal number of clusters into which the sample divides. Optimum partitioning into clusters was determined by estimating the mean square error of clustering, defined as

$$e^2 = \sum_{j=1}^{k} \sum_{i=1}^{nj} | x_i^j - c_j |^2 , \quad (2)$$

where is the *j*-property of corresponding cluster center *c*, x_i^j is the value of the *i*-th object in *j*-th cluster, n_j – number of objects in *j*-th cluster, *k* – number of clusters.

Obviously, the value of mean square error of clustering decreases while number of clusters increases due to the fact that increasing number of clusters leads to reduction of their size, and therefore reduction of the distance from the object to appropriate cluster center. But while the number of clusters continues to increase, decrease of mean square error of clustering becomes less intense and the clusters become more similar to each other that cause the emergence of excess clusters. The moment when increasing the number of clusters still has significant influence for reducing the mean square error can be determined using so called elbow method [3].

Fig.1 shows the dependence of mean square error, normalized to the range [0, 1] by feature scaling, on the number of clusters for the data of RECS faculty. Number of clusters, at which the curve "breaks" shows optimal breakdown. As shown in the graph, curve has 2 breaks, corresponding to 4 and 6 clusters. This behavior is typical for our investigation and is caused by the choice of properties of the objects (coordinates) used for clustering. As it was mentioned above, the first 8 coordinates describe the overall distribution of ratings in even ranges, and the last 5 coordinates clarify details of distribution: the use of threshold percentage (60, 75, 90) and transitional (73–74, 88–89) points, so, as it can be seen later from Fig.5 (RECS faculty clusters) break for 4 clusters correlates to the optimal number of clusters considering the uniform distribution for only 60–100 grades rating (first 8 coordinates) and 6 clusters allow to consider features of patterns more precisely using the whole scale of coordinates.

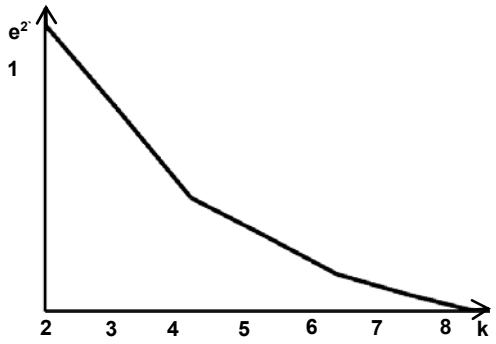

Fig. 1. Elbow method illustration

Clustering was carried out separately for different faculties of Kyiv National Taras Shevchenko University and for the university as a whole. Results of the clustering demonstrate that lecturers from the faculties of sciences and lecturers from the faculties of arts possess different patterns in grading of students progress. In particular, the distribution of scores in faculties of arts patterns dominates with the scores above 90 points on a 100-point scale, whereas the patterns of scores distribution in faculties of sciences are more diverse.

To show points in an *n*-dimensional space we use parallel coordinates [4], so, a point in *n*-dimensional space is represented as a polyline with vertices on the parallel axes; the position of the vertex on the *i*-th axis corresponds to the value of *i*-th coordinate of the point.

At faculties of arts there dominates the distribution of scores patterns with the scores above 90 points on a 100-point scale.

Fig. 2 shows the distribution of scores patterns at historical faculty.

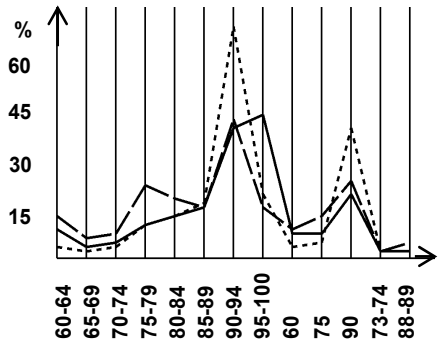

Fig. 2. Historical faculty clusters

Fig. 3 shows the distribution of scores patterns at institute of journalism.

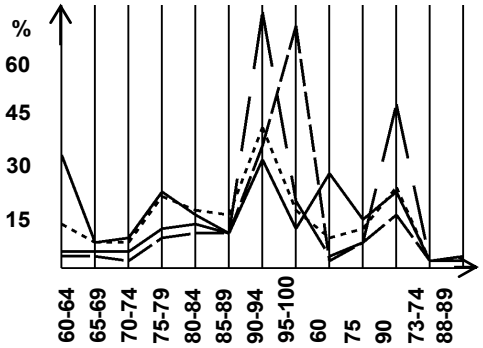

Fig. 3. Institute of journalism clusters

Fig. 4 shows the distribution of scores patterns at faculty of psychology.

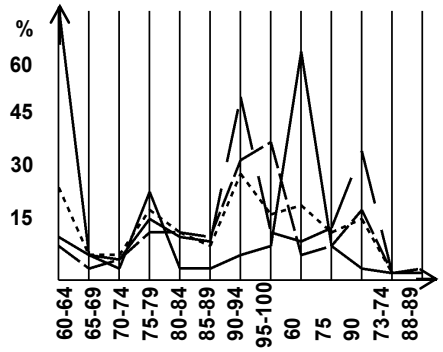

Fig. 4. Faculty of psychology clusters

At faculties of sciences the distributions of scores patterns are more diverse:

- with domination of scores above 90 points on a 100-point scale (cluster A);
- with domination of scores 60–74 points on a 100-point scale (cluster B);
- with domination of scores above 75–89 points on a 100-point scale (cluster C);
- with almost equal scores 60–74, 75–89, 90–100 (cluster D).

Fig. 5 shows the distribution of scores patterns at RECS faculty.

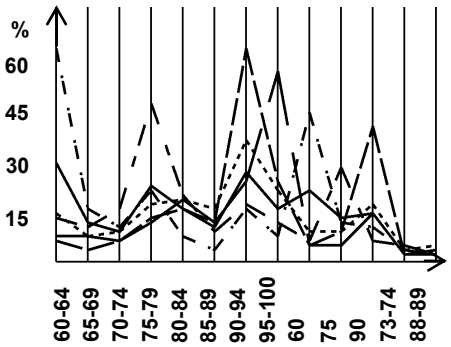

Fig. 5. RECS faculty clusters

Fig. 6 shows the distribution of scores patterns at cybernetics faculty.

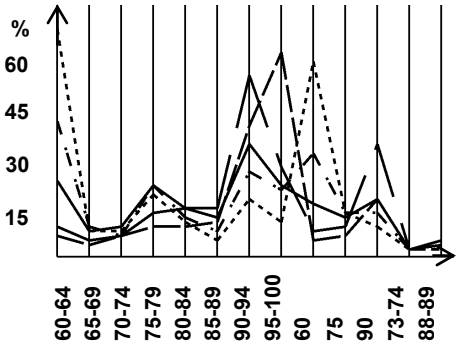

Fig. 6. Cybernetics faculty clusters

Fig. 7 shows the distribution of scores patterns at mechanics and mathematics faculty.

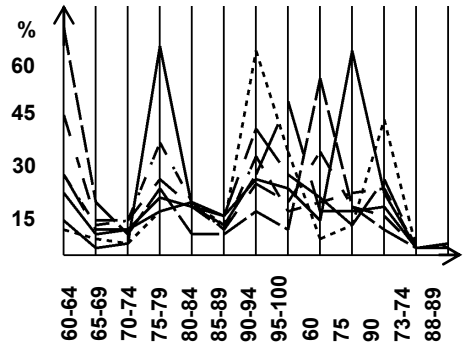

Fig. 7. Mechanics and Mathematics faculty clusters

Substantial result achieved in above-mentioned clustering process is that distributions of scores in patterns corresponding to the clusters can differ in many ways from the normal distribution, underlying the grading scale ECTS. Taking into account existence of such different distributions, we can conclude that usage of the same algorithm for transferring grades on a 100-point or national scales to ECTS grades can be unsuitable.

Besides the fact that there are different categories of lecturers, and, therefore, the process of conversion the scores on national grading scale into ECTS grades becomes not so obvious, there also exist more problems related with the fact that sometimes allocating the necessary percentile groups of students is very difficult [5]. One of the problems arises when the group is small (for example, 15 students), because in this case allocating the necessary percentile groups is often impossible at all. The main decision of the small group problem is to use distribution of grades for a few years, that is more likely resulting in a balanced outcome. Another problem arises, when is not possible to form the necessary percentile groups, as grade is basically subjective. It can be assumed from empirical considerations that the grade on a 100-point scale is determined with precision ± 5%. In order to consider this fact in our investigation, inaccuracy of size of percentile groups (±5%) is allowed: grades “A” and “E”, instead of 10%, can vary from 5% to 15%, grades “B” and “D”, instead of 25%, – from 20% to 30%, grade “C”, instead of 30%, – from 25% to 35%.

Due to the fact that inaccuracy of the size of percentile groups is allowed, in this paper we compared three main methods of calculating the ECTS grades, which resulted in the formation of various distributions, namely (all percentile groups are calculated with a tolerance of ±5%):

- “A-E” – the method in which ECTS grades calculated from “A” to “E”, namely, at first there are determined approximately 10% of the best students of the group (grade "A"), then – about 25% of students who receive "B", about 30 % of students who receive "C", about 25% of students who receive “D” and about 10% of the worst students (grade "E");
- “E-A” – the method in which ECTS grades calculated from “E” to “A”, namely, at first there are determined approximately 10% of the worst students of the group (grade "E"), then – about 25% of students who receive “D”, about 30% of students who receive "C", about 25% of students who receive "B" and about 10% of the best students (grade "A");
- “A-E-C” – the method in which ECTS grades calculated from edges to the middle (to “C”), namely, at first there are determined approximately 10% best and worst students of the group (grades "A" and "E", appropriately), then – about 25% of students who receive "B" and “D”, and at least about 30% of students who receive "C".

Each percentile group is calculated as follows. At first, distribution of grades is formed on the base of relation of each grade of 100-point scale to the percentage of students of group who received it. Depending on the grade, from which the calculation begins (from grade “A” or “E”), distribution proceeds accordingly (to grade “A” – descending 100-point grade, to grade “E” – ascending 100-point grade). Then the necessary percentile group is formed from the first grade in the distribution by gradually adding the percentage of students who received the next grade of the distribution until the percentile group will be greater or equal to the necessary percentage. The next step is to compare received group with the same group without percentage of the latter grade in the distribution. At this step, the group that has a smaller difference with the sample percentage is chosen. Moreover, it is important to check that the received difference of selected group would not exceed 5%. If the difference is more than 5%, then percentages of current and next ECTS grade are combined and percentile group for the formed grade has to be calculated. However, in this case there is a problem which ECTS grade should be chosen for the selected in such a way group of students. There are three different ways: always to choose lower amongst the two grades (for example, to choose “B” amongst the grades “A” and “B”), always to choose higher amongst the two grades (for example, to choose “A” among the grades “A” and “B”), to choose that grade amongst the two, which is closer to the ”C“ (for example, to choose “B” amongst the grades of “A” and “B”, and “D” amongst the grades “D” and “E”).

Methods were used both on normal distribution of ratings in the group, and distribution with the statistics for two years (methods for this distribution with the word in the title – Statistic).

As cost function that has to be optimized during the research, thus determining the best method of calculation, we propose to use the grade variance.

As at faculties of sciences the distributions of scores patterns are more diverse, for the obtained 4 clusters (with domination of scores above 90 points on a 100-point scale; with domination of scores 60–74 points on a 100-point scale; with domination of scores above 75–89 points on a 100-point scale; with almost equal scores 60–74, 75–89, 90–100) were calculated ECTS grades by six different ways (Table 2).

***Table* 2**

Results for different types of distributions (the smallest cost function values are selected)

Method	Claster A – Credit for the course "Digital Signal Processing" (23 students)	Claster B – exam for the course "Molecular Physics" (93 students)	Claster C – exam for the course "Electricity and Magnetism" (99 students)	Claster D – exam for the course "Object-Oriented Programming" (87 students)
A-E	13796.80	5192.67	676.15	1799.85
A-E-C	20568.11	5240.16	676.15	1854.40
E-A	7485.46	4769.15	672.69	7487.96
A-E Statistic	7189.71	5522.55	5699.53	12567.90
A-E-C Statistic	7189.71	5585.42	5753.99	12567.90
E-A Statistic	7189.71	10455.81	5696.67	12511.06

From the results seen for the cluster A of distribution does not matter which method to use (A-E, A-E-C or E-A). For the clusters B and C is the best method for E-A, and in the case of the cluster D – A-E. Thus, for most cases, the best method to use E-A, however, for even distribution method should be used A-E.

To determine the limit of the number of students groups for which statistics has to be used, we have calculated ECTS grades using different methods for several cases. It can be obviously seen from the results that for small groups (less than about 25 students) calculations that use statistical data for two past years is better, otherwise usage of statistics is impractical because it requires additional resources and results is not improved significantly.

In order to determine, what grade should be chosen in case when it is impossible to select necessary ECTS grade percentile group, we calculated the average value of each percentile group for ECTS grades for the faculties and the university as a whole by different methods.

As cost function at this stage we propose to use the sum of squares of the differences of the received averages and sample values of percentile groups of all the ECTS grades. In that way, the smaller is cost function value, the closer to the sample are percentile groups.

Results for historical, physical, law, philosophical, the RECS faculties and for the university as a whole are given in Table 3. Methods, designated by “Worse”, are those, in which amongst the two grades always the lower has been chosen, designated by “Better” – those, in which amongst the two grades always the higher has been chosen, and methods designated by “Middle” are those, in which the grade closer to the ”C“ has been chosen amongst the two.

***Table* 3**

Results by faculties (the smallest cost function values are selected)

Method	Faculty of History	Faculty of Physics	Faculty of Law	Faculty of Philosophy	RECS Faculty	University
A-E Better	36.87	75.72	43.81	50.00	31.99	47.60
A-E Middle	87.80	41.53	77.24	35.06	24.69	46.79
A-E Worse	67.90	37.78	83.63	50.51	91.98	59.24
A-E-C Better	291.39	194.56	163.79	214.21	120.48	167.76
A-E-C Middle	254.75	199.81	129.39	160.08	120.84	133.72
A-E-C Worse	282.95	241.73	144.81	194.80	166.00	167.12
E-A Better	212.31	135.85	105.34	133.16	77.65	101.32
E-A Middle	229.41	155.16	131.59	107.83	58.34	91.32
E-A Worse	34.67	25.83	23.84	19.38	31.75	22.58

The results show that mainly the best method of calculating ECTS grades is the method named “E-A Worse”.

Conclusions. Although ECTS is convenient, it has its drawbacks. Data Mining enables to analyze deep enough the different situations that may arise while transferring the grades from the national to the European scale, and find an algorithm that solves possible problems. It can be concluded that mainly expedient is to use a method of calculation, from ECTS grade «E» toward the ECTS grade «A», and if it turns out that grade is controversial, then the lower grade of the two has to be chosen. Also, when the number of students in the group less than 25, use distribution with statistics for two years is more likely resulting in a balanced outcome.

REFERENCE

1. *European Commission*. ECTS Users' Guide. // Luxembourg: Office for Official Publications of the European Communities, 2009. – 60 pp.
2. *Hartigan J. A*. Algorithm AS 136: A K-Means Clustering Algorithm / J. A. Hartigan, M. A. Wong // Journal of the Royal Statistical Society. Series C (Applied Statistics). – 1979. – Vol. 28, №1. – P. 100–108.
3. *Hastie T*. Estimating the number of clusters in a data set via the gap statistic / T. Hastie, R.Tibshirani, G.Walthe // Journal of the Royal Statistical Society: Series B (Statistical Methodology). – 2001. – Vol. 63. – Issue 2. – P. 411–423.
4. *Wegman E. J*. Hyperdimensional Data Analysis Using Parallel Coordinates / E. J. Wegman // Journal of the American Statistical Association. – 1990. – Vol. 85. – Issue 411. – P. 664–675.
5. *Lieponienė J*. The Grades Transfer from One Grading Scale to Other Algorithmization / J. Lieponienė, R. Kulvietienė // Informatics in Education. – 2011, Vol. 10, №2. – P. 233–244.

Submitted on 18.06.15

Василець М., студ., Удачина А., студ., Грязнова В., доц., канд. фіз.-мат. наук
Факультет радіофізики, електроніки та комп'ютерних систем
Київський національний університет імені Тараса Шевченка

АНАЛІЗ ОЦІНЮВАННЯ СТУДЕНТІВ УНІВЕРСИТЕТУ З МЕТОЮ ВПРОВАДЖЕННЯ СИСТЕМИ ОЦІНЮВАННЯ ECTS

Класифікація викладачів Київського національного університету імені Тараса Шевченка за характером оцінювання успішності студентів методами кластерного аналізу. Кластеризація була проведена за допомогою алгоритму k-середніх з Евклідовою відстанню у якості метрики. Розгляд проблеми переведення балів зі 100-бальної шкали оцінювання до шкали ECTS. Дослідження різних способів розрахунку ECTS.

Ключові слова: *оцінювання студентів, кластеризація, алгоритм к-середніх, шкала ECTS, методи розрахунку оцінки ECTS.*

Василець М., студ., Удачина А., студ., Грязнова В., доц., канд. физ.-мат. наук
Факультет радиофизики, электроники и компьютерных систем
Киевский национальный университет имени Тараса Шевченка

АНАЛИЗ ОЦЕНИВАНИЯ СТУДЕНТОВ УНИВЕРСИТЕТА С ЦЕЛЬЮ ВНЕДРЕНИЯ СИСТЕМЫ ОЦЕНИВАНИЯ ECTS

Классификация преподавателей Киевского национального университета имени Тараса Шевченко по характеру оценивания успеваемости студентов методами кластерного анализа. Кластеризация была проведена с помощью алгоритма k-средних с Эвклидовым расстоянием в качестве метрики. Рассмотрение проблемы перевода баллов из 100-бальной шкалы оценивания в шкалу ECTS. Исследование различных способов расчета ECTS.

Ключевые слова: *оценивание студентов, кластеризация, метод к-средних, шкала ECTS, методы расчета оценки ECTS.*

UDC 537.86/.87

A. Vladymyrskyi, stud., V. Malyshev, As. Prof.,
A. Goriachko, Ph.D., V. Moiseienko, lead. engineer ,
Taras Shevchenko National University of Kiev
A. Matviyenko, lead. engineer, A. Tovstolytkin, Doct. Of Sci., Prof.
Institute of Magnetism of the NAS of Ukraine and MES of Ukraine

EFFECT OF IRREGULAR ARRAYS OF METALLIC NANOSTRUCTURES ON TRANSMISSION CHARACTERISTICS OF MICROWAVE FILTERS

We report the results of experimental studies of physical properties of irregular arrays of metallic nanostructures and their impact on the transmission characteristics of microwave filters based on YIG. Investigations were conducted on the YIG films with the use of electromagnetic waves in 6 centimeter wavelengths range. The effect of partial metallization of the films on the amplitude-frequency characteristics (AFC) and the response capacity of the films formed with nanostructures was studied. The peculiar features of the effect of the partial metallization on the width of ferromagnetic resonance line and shape of the AFC curve has been clarified, which is an important task for the construction of microwave filters on magnetostatic waves (MSW). The results of investigations were verified and additionally analyzed using atomic force microscopy (AFM).

Key words: *Spin waves, yttrium-iron garnet, magnetic nanostructures, dipole-exchange spin waves, wave front reversal, microwave filter.*

Introduction. Study and application of ferromagnets and ferrites in ultra-high frequency range (UHF) occupy a leading position in solid state physics. Ferrite and ferromagnets have several significant advantages over traditional UHF materials. This is wide frequency waveband, the ability to easy control the dispersion characteristics, and others. The main and indisputable advantage of ferrites is strongly expressed nonlinearity. Some nonlinear effects occur even when input UHF signal is of several microWatts. Creating a unique ferrite – yttrium-iron garnet (YIG) – was a great breakthrough in science of UHF materials. YIG grown by epitaxy has a record low value of attenuation in the centimeter range of wavelengths. A number of nonlinear devices, such as UHF signals power constraints, noise suppressers, regenerative amplifiers, active and passive delay lines and others, were developed on the basis of ferrites.

The ability to create specific periodic structures (magnetic dots) based on thin magnetic films appeared with the development of nanolithography technology [1, 2, 4, 6]. The unique magnetic properties of submicron planar magnetic objects and their two-dimensional arrays, attracted the attention of many researchers due to the possibility of using the potential of such structures in magnetic memory devices. In these structures, a specific inhomogeneous distribution of magnetization, the so-called magnetization vortex, may be realized. Although this phenomenon was predicted by Hubert in 1998, the current interest arose because the vortex can be the ground state in nanostructured magnetic

© Vladymyrskyi A., Malyshev V., Goriachko A., Moiseienko V., Matviyenko A., Tovstolytkin A., 2015

particles. Spin waves can propagate in cylindrical nanostructures. However, the nature of these waves depends on the geometrical dimensions of nanoparticles - thickness L and radius R. Even in thin disks ($L/R \le 0.1$) the finiteness of the radius of nanodot should be taken into account. This leads to the fact that:

- waves with longitudinal wave vector appear that form radial standing spin waves;
- demagnetization factor and internal magnetic field become functions of the radial coordinate.

As a results, the resonances are almost equidistant, unlike quadratic Kittel's dispersion law.

Electronic beam epitaxy is quite expensive method to fabricate nanodots. For this reason, we proposed an alternative method which includes growth and investigation of irregular (non-periodic) arrays of magnetic nanoparticles. The structures of such kind can be fabricated on a surface of yttrium-iron garnet film grown on a substrate from the gadolinium-gallium garnet (GGG) by magnetron sputtering with the use of a VUP-5M installation. In the experiments, nonmagnetic Cu was used as the material of irregular metallic arrays.

This work is devoted to the experimental investigation of physical properties of irregular arrays of metallic nanostructures and their impact on the transmission characteristics of microwave filters based on YIG.

To form Cu island films, a magnetron vacuum evaporation installation VUP-5M was used. At the first stage, two witnesses – the first on the dielectric substrate, and the second on quartz substrate with preliminary deposited Pt layer (100 Angstroms) – were loaded to VUP-5M. The distance between Cu target and substrate was 45 mm.

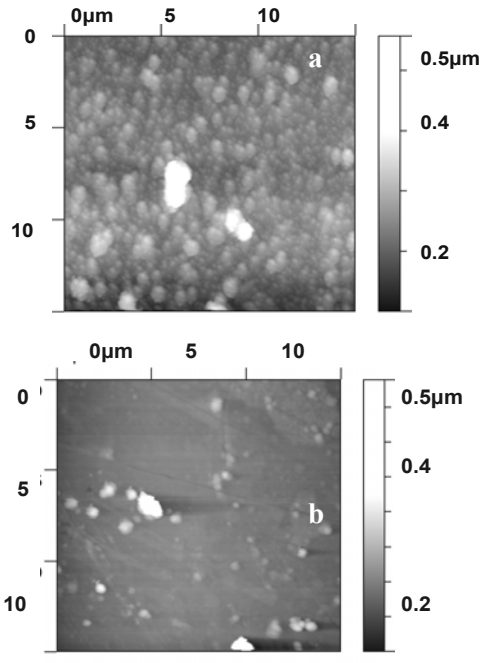

Fig. 1. AFM image of the Cu / YIG film surface before and after sputtering: (a) clean YIG surface, (b) metallized surface

Working modes during sputtering were: U_{plasma} = 350 V, I_{plasma} = 250 mA, the pressure of Ar in the vacuum cell – $5 \cdot 10^{-2}$ Torr. Sputtering time – 60 s. The thickness of the films obtained, measured with the use of interference microscope MII-4, was 300 Angstrom, which made it possible to determine the the rate of sputtering: 5 Angstroms/s.

It is known that coalescence of Cu nucleation centers, their growth and formation of continuous film occur at a nominal film's thickness of about 15 Angstroms [3]. Thus, a sputtering time required for the formation of Cu islands on the surface of YIG film was determined to be 3 seconds.

Fig. 1 shows typical AFM image of the film's surface before and after sputtering.

The topology of pure YIG surface for the film with thickness of 14.6 microns is shown in Fig. 1 (a). It is characterized by a large number of granules (grains) with a height of about 500 nm and an average size of 1 mkm^2. Fig. 1 (b) shows that greater part of cavities is filled with Cu atoms and the surface of the YIG film become smoother. As a result of the Cu deposition, the number of grains was reduced by about 1000 times, and the height of max grain was equal to 390 nm with an average grain size of 0.04 mkm^2.

The next step of Cu / YIG nanostructures investigation was to study the impact of sputtered Cu nanoislands on amplitude-frequency characteristics (AFC) of films for such geometries as bulk volume (BVMSW) and surface (SMSW) magnetostatic waves.

To do this, a set of YIG films with thicknesses of 5 to 64 microns was analyzed for comparison a frequency response for films with and without deposited nanostructures (as this was done in Ref. [5]). Research was carried out on the panoramic VSWR meter and YA2R-67 attenuator with oscillatory frequency generator calibrated for research on transmission. AFC response was recorded with an oscilloscope Tektronix TDS 3032B. Samples were placed between the poles of a permanent magnet with an external magnetic field magnitude of 930 Oe, so that the excitation conditions fulfilled BVMSW and SMSW.

The results of experimental investigations of AFC response for both BVMSW and SMSW field geometries are shown in Fig. 2 (a) and Fig. 2 (b), respectively. Investigations were conducted on the YIG films with thicknesses of 14.6; 15.97, 16.7 and 64 micron with the use of electromagnetic waves in 6 centimeter wavelengths range. Such film's thicknesses were selected for sputtering.

It should be noted that to make easier the curves comparison, all curves were normalization to their max value. Thus, the comparison of experimental AFC response graphs before and after sputtering makes it possible to conclude that the nanostructured arrays of Cu were actually formed on the surface of a YIG thin film and this led to appearing of additional peaks and increase of the bandwidth of AFC response for these types of waves.

Also Fig. 2 (b) shows that in SMSW geometry, this effect was much more pronounced than in BVMSW one. AFC has undergone significant modification: it attained a form inversion, much deeper cuts on the curve (many resonances) and expanding bandwidth for SMSW. Bandwidth of 5–7 dB was observed for Cu / YIG films, which is better than for similar films without nanostructures. This can be explained by the fact that the metallization has a much greater impact on the distribution of MSW on the surface of the sample than on its volume.

It has been verified as cutting presenting on the AFC response associated with the passage of MSW on the film. For comparative used rectangular microwave pulse, which was applied to the data structure and thus changed the magnetic field around the range is developed for the existence of this wave of microwave frequency waves. A comparison was observed that pure YIG film passed the maximum amplitude of the signal was observed only once for the entire range of the magnetic field, and for films with nanostructures such highs were 3–4.

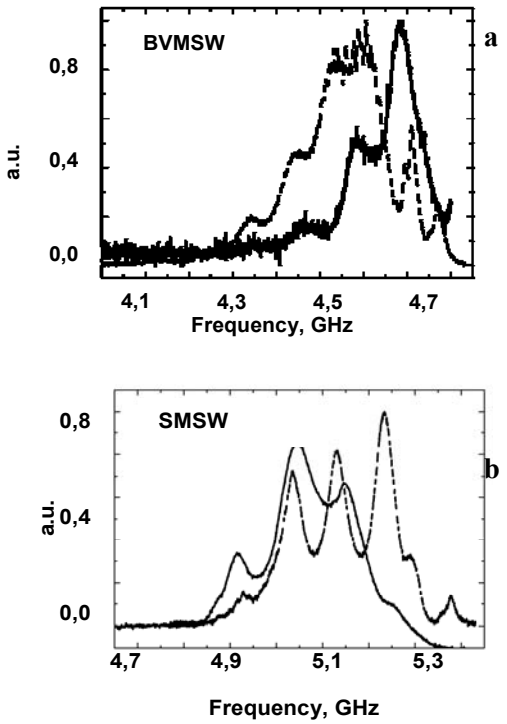

Fig. 2. AFC of Cu / YIG films before (solid line) and after (dashed curve) copper deposition. Data in (a) obtained for BVMSW geometry, and (b) for SMSW geometry

These experimental studies have been confirmed in all samples with nanostructures. And the signal completely disappeared and again appeared. These results also confirm that the Cu changed the conditions of microwave signals MSW passage in waveguide based in thin YIG. These properties of nanostructures can be used for construction of microwave filters based on MSW.

The last step was to determine the influence of nano-island metallization on MSW dissipation in thin films of YIG. To do this, the approach described in Ref. [8] was used. The approach is based on the determination of FMR line width resulted from the analysis of spatial coefficient of MSW attenuation. This coefficient was calculated by means of linearization of dependence of WFR signal's power on the time from the input of an electromagnetic pumping to the parametric system with open dielectric resonator (ODR) and YIG film. The linearization was conducted for large values of the time from the input of an electromagnetic pumping, which corresponded to wavefront reversal (WFR) for dipole-exchange spin waves (DESW).

Measurements were carried out on an experimental section described in [7]. It consists of a YIG film mounted in an ODR and placed on two, formed by photolithographic method, input and output microstrip antennas, a width of 25 μm with lead lines. The distance between the antennas was 6 mm. The test sample of the ferromagnetic film of 1.5 mm in width was cut from a single-crystal YIG film (5.1 μm in thickness) with low magnetic losses ($\Delta H = 0.3\,Oe$). The film was grown on a GGG substrate by liquid phase epitaxy. Saturation magnetization of the film is 1750 Gauss. The film was magnetized to saturation by a bias magnetic field H_0 = 930 Oersteds, which was applied in the film plane in the direction of wave propagation. Measuring section is located at the output flange of 3 cm waveguide of pumping channel by which the pumping signal was brought into the system. As the pumping source was used pulsed magnetron M857. Maximum impulse power of the pumping signal at the output flange of the pumping channel was 7 Watts.

In the process of measurements, the following processes occur in the film: microwave generator and additional high-speed modulators generate microwave signal pulse which is applied to the input microstrip antenna converter. The latter excites BVMSW or SMSW in the film, which propagates along the film. As a result of two magnon scattering on film inhomogeneities, a slow DESW appears, whose wavelength is much longer than BVMSW/SMSW.

If after some specific time (longer than time phasing, but less than relaxation time), an external electromagnetic radiation with double frequency ($f_p = 2f_s$) acts on DESW through the open dielectric resonator, this will result in the pumping of the parametric interaction with DOSH, there appear inverse DESW.

They move to the same irregularities and can form, due to the reverse process, BVMSW/SMSW that comes back and, as a result, an antenna input signal appears which is a delayed spin-wave echoes. After two stages of amplification, these signals are fed to the semiconductor detector, where their envelope was registered with an oscilloscope Tektronix TDS 3032B. WFR signal and the amplified signal are suitable for research, but because it is more convenient to use only one input antenna, all subsequent measurements we performed for the WFR signal.

The carrier frequency signal and pumping respectively have the following values: $f_s = 4705$ MHz, $f_p = 9410$ MHz. Power of input signals was $P_s = -75$ dBm, pumping $P_p = -7.5$ dBm. The duration of the input signals was $\tau_p =$ 50 ns, duration of the pumping $\tau_p =$ 80 ns.

The results of experimental studies, depending on signal power BWF time filing electromagnetic pump, ar shown in Fig. 3.

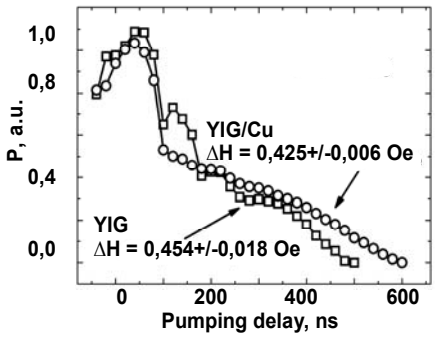

Fig. 3. Experimental BWF signal power depending on the time of the filing of the electromagnetic pumping pure YIG film and metallized by nanoislands of 300 angstroms in size. The film thickness is 14.6 microns

Thus, using the method described above, it was determined that the FMR line-widths for pure YIG film and metallized by the copper islands of 300 angstroms in size are equal to 0.454 Oe and 0.425 Oe, respectively. Partial metallization of such kind results in 5–7 dB improvement of transmission characteristics of YIG films, as described previously, by means of modifying the shape of the curve response. It should be noted that these results are a significant confirmation of the advantages of this technology for the manufacture of nanostructures, which is cheaper than e-beam epitaxy.

The sputtering of Cu nanoislands on YIG films was carried out in the Institute of Magnetism of the NAS of Ukraine and MES of Ukraine.

REFERENCE

1. *Kalinikos B. A.* Theory of dipole-exchange spin wave spectrum for ferromagnetic films with mixed exchange boundary conditions / B. A. Kalinikos, A. N. Slavin. – J. Phys. C: Solid State Phys.– 1986.– 19.– P. 70–72.
2. *Mayssel L.* Technology of thin films. Directory. / L. Mayssel., R. Hlenh. – Moscow, Soviet radio, 1977. – Vol.2. – 768–770 p. (in Russian).
3. *Metlov K. L.* Quasiuniform magnetization state in soft ferromagnetic nanocylinders / K. Metlov, K. Guslienko. – Phys. Rev. B.– 2004.– 70.– P. 67–68.
4. *Moiseienko V. A.* Pro zbudjenya magnitostatychnyh chvyl' microsmujkovymy antenamy. – Visnyk Kyivskogo Nacionalnogo Universytetu im. T. Shevchenka. Seria : fizyko-matematychni nauky – 2012, – № 2. – P. 279–282. (in Ukrainian).
5. *Vasyuchka V. I.* Non-resonant wave front reversal of spin waves used for microwave signal processing / V. I. Vasyuchka, G. A. Melkov, A. N. Slavin. – J. Phys. D: Appl. Phys. – 2010 – V.43 – P.32–35.
6. *Zavislyak I. V.* Physical fundamentals of functional micro-electronics. / I. V. Zavislyak, A. I. Tychynskyy – Kiev: CMD PA, – 1989. – 105–106 p. (in Russian).

Submitted on 15.06.15

Владимирський А., студ., Малишев В., асист., Горячко А., канд. фіз.-мат. наук, Мойсеєнко В., пров. інж.
кафедра нанофізики та наноелектроніки, Київський національний університет ім. Тараса Шевченка,
Матвієнко О., пров. інж., Товстолиткін О., проф.
Інститут магнетизму НАН України та МОН України

ДОСЛІДЖЕННЯ ФІЗИЧНИХ ВЛАСТИВОСТЕЙ НЕРЕГУЛЯРНИХ МАСИВІВ МАГНІТНИХ НАНОСТРУКТУР

Наведено результати експериментальних досліджень фізичних властивостей нерегулярних масивів магнітних наноструктур та їх впливу на передаточні характеристики мікрохвильових фільтрів на базі плівок ЗІГ. Дослідження проводилися на плівках ЗІГ в шестисантиметровому діапазоні довжин хвиль. Досліджено вплив часткової металізації на форму кривої АЧХ та пропускну здатність плівок утвореної наноструктури. Визначено, яким чином часткова металізація впливає на ширину лінії ФМР та форму кривої АЧХ, що є важливою задачею для побудови НВЧ фільтрів на магнітостатичних хвилях. Результати досліджень перевірялись та аналізувались за допомогою атомної силової мікроскопії.

Ключові слова: *спінові хвилі, залізо-ітрієвий гранат, магнітні наноструктури, дипольно-обмінні спінові хвилі, обернення хвильового фронту, НВЧ фільтр.*

Владимирский А., студ., Малышев В., асисст., Горячко А., канд. физ.-мат. наук, Мойсеенко В., вед. инж.
кафедра нанофизики та наноелектроники Киевский национальный университет им. Тараса Шевченко
Матвиенко А., вед. инж., Товстолиткин А., проф.
Институт магнетизма НАН Украины и МОН Украины

ИССЛЕДОВАНИЕ ФИЗИЧЕСКИХ СВОЙСТВ НЕРЕГУЛЯРНЫХ МАССИВОВ МАГНИТНЫХ НАНОСТРУКТУР

Приведены результаты экспериментальных исследований физических свойств нерегулярных массивов магнитных наноструктур и их влияния на передаточные характеристики микроволновых фильтров на базе пленок ЖИГ. Исследования проводились на пленках ЖИГ в шестисантиметровом диапазоне длин волн. Исследовано влияние частичной металлизации на форму кривой АЧХ и пропускную способность пленок образованной наноструктуры. Определено, каким образом частичная металлизация влияет на ширину линии ФМР и форму кривой АЧХ, что является важной задачей для построения СВЧ фильтров на магнитостатических волнах. Результаты исследований проверялись и анализировались с помощью атомной силовой микроскопии.

Ключевые слова: *спиновые волны, железо-иттриевый гранат, магнитные наноструктуры, дипольно-обменные спиновые волны, обращение волнового фронта, СВЧ фильтр.*

UDC 535.56

A. Gnatenko, Postgraduate, Yu. Machekhin, Doctor of Science, K. Vasko, Stud.,
Department of Physical Foundations of Electronic Engineering, Faculty of Electronic Engineering,
Kharkov National University of Radioelectricity

PROVIDING CONTROL OF THE POLARIZATION INSIDE THE RESONATOR FIBER RING LASER

This paper presents the implementation of the mode-locked fiber laser ring by nonlinear rotation polarization (NPR). This method is implemented using liquid crystal (LC) cells, which control the polarization of laser light by applying them an alternating signal. It was also conducted experiments of interaction of laser radiation (wavelength 1550 nm) from the LC cell. It was built and research diagrams the stability of the polarization in the fiber ring laser.

Key words: *fiber laser, liquid crystal cells, femtosecond pulses, control voltage, wave plates, mode locking.*

Introduction. At present there is a lot of fiber lasers that operate in the mode-locking. These lasers are used in metrology, spectroscopy, THz generation, micro processing, microscopy and other. Mode locking can be passive and active. The advantage of passive mode locking consists in availability of optical components. Fiber ring laser with passive mode locking can reach the shortest pulse durations – tens femtoseconds. Usually, passive mode locking of fiber lasers is achieved by nonlinear polarization rotation. Therefore, the main task for the creation of such lasers is to improve and implement a new approach to the establishment of mode locking.

Mode locking of laser. Generation of dissipative solitons and comprehensive study of the physics of the process of their formation, preceded the advent of lasers, preceded the appearance of lasers that operate in the mode-locked and generate ultrashort pulses. In a simple laser longitudinal modes propagate independently of one another in the cavity. It looks like a set of independent lasers that operate at different frequencies. The individual phases of the light waves in each mode are not fixed and may change randomly, is the result of factors such as thermal vibrations of the laser design, mechanical vibration and others. The lasers are supported by only a few oscillating modes, the interference between the modes can cause the effect of beating on their outputs. This leads to random fluctuations of intensity. The lasers, which propagates thousands of modes, these interference effects are generally averaged out to a constant intensity. This mode of operation is called a continuous wave. The electric field of pulsed radiation in which the laser modes are not synchronized, can be written as:

$$E(t) = \sum_{m=1}^{N} A_m \cos(\omega_0 + m\Delta\omega t + \varphi_m) \qquad (1)$$

where φ_m - phase of the laser mode, $\Delta\omega = 2\pi c / 2$ - the distance between modes (for ring resonator) , $\Delta\omega = \pi c / 2$ - the distance between modes (for linear resonator). If $\varphi_1 = \varphi_2 = \varphi_N = 0$ and $A_1 = A_2 = A_N = E_0$, the formula that describes the electric field in the mode-locking is written as follows:

© Gnatenko A., Machekhin Yu., Vasko K., 2015

$$E(t) = \frac{E_0 \sin(N\Delta\omega t)}{2} \cos ec(\frac{\Delta\omega t}{2}) \cos(\omega_0 t) \qquad (2)$$

If each mode will oscillate with a fixed ratio between its phase and the phases of the other modes, the output of the cavity formed by a short pulse of high intensity. Modes laser will periodically interfere with each other, creating a burst of intensity, fig. 1. This type of laser will be called laser mode-locked.

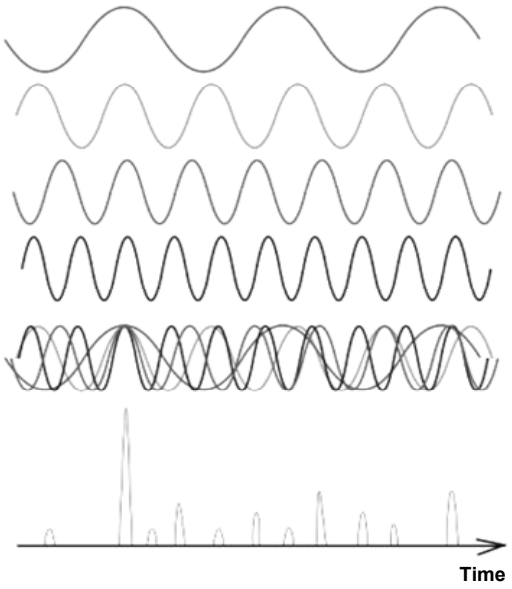

Fig. 1. Interference of longitudinal modes of the laser resonator

Pulse period T will be equal to the period bypass: for a ring resonator $T = Ln/c$, for linear resonator $T = 2Ln/c$, where L - cavity length, n - refractive index of the optical medium, c - speed of light. This time corresponds to the frequency interval between any two adjacent modes $\Delta\nu = 1/T$. The duration of each light pulses is determined by the amount of modes that oscillate with identical phase (but in reality do not always laser modes are synchronized in phase). If N of modes is synchronized with a frequency interval $\Delta\nu$, the total width of synchronized modes corresponds $\Delta\nu N$ and this value is the greater, the shorter the duration of the laser pulse. In practice, the actual pulse width is determined by the shape of each pulse, which in turn is determined by the exact ratio of the amplitude and phase of each longitudinal mode. Limiting the duration of the pulse τ is related to the spectral width ν of the generated radiation (3):

$$\nu\tau \geq k, \qquad (3)$$

where k - correction coefficient associated with the pulse shape, for example a Gaussian pulse, $k = 0.441$, and for the pulse-shaped square hyperbolic secant $k = 0.315$.

This section has been described mode locking lasers.

Erbium fiber ring femtosecond laser. Figure 2 depicts diagram of a typical erbium-doped fiber femtosecond laser that operates in the mode-locked by the method of nonlinear polarization rotation.

Nonlinear rotation of the polarization is carried out by rotating the set of wave plates in space.. There are several schemes of erbium-doped fiber femtosecond laser using a different set of plates. Scheme shown in fig. 2 has a big disadvantage - it is the instability of work. Any movement of the fiber, temperature change or switch button pump can lead to loss of mode locking and loss of generation. As a result, in practice, quarter− and half−wave plates inside the cavity need to be adjusted from time to time, either manually or automatically (e.g., using motorized holders). This is a significant drawback of NPR mode locking, since it requires continuous maintenance (manual plates adjustment) or increases overall laser cost (automatic plates adjustment). Passive mode locking using saturable absorber also require proper adjustment of the polarization inside the cavity to obtain mode−locking [2, 4]. Although, some configurations based on polarization maintaining (PM) fibres were demonstrated [3], high cost of PM optical elements is their significant drawback. However, the output characteristics of these lasers is worse than that of lasers with nonlinear polarization rotation. Therefore, we suggest using the method of nonlinear polarization rotation mode locking without the wave plates. Instead, we propose to apply the liquid crystal cells that are controlled by an electric signal.

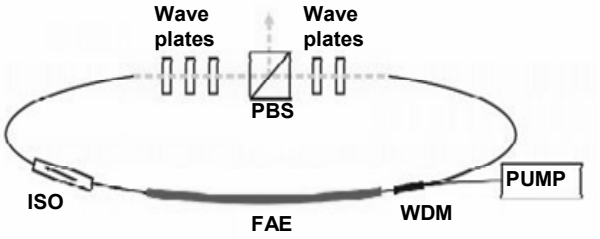

Fig. 2. Scheme of a typical erbium-doped fiber ring femtosecond laser: PBS – polarizing beam splitter; EDF – erbium-doped fiber; WDM – device for input radiation into the resonator; ISO – optical isolator; PUMP – diode pumping at 980 nm

Application of liquid crystal cells in the scheme with nonlinear rotation polarization. Scheme with the liquid crystal cell shown in figure 3.

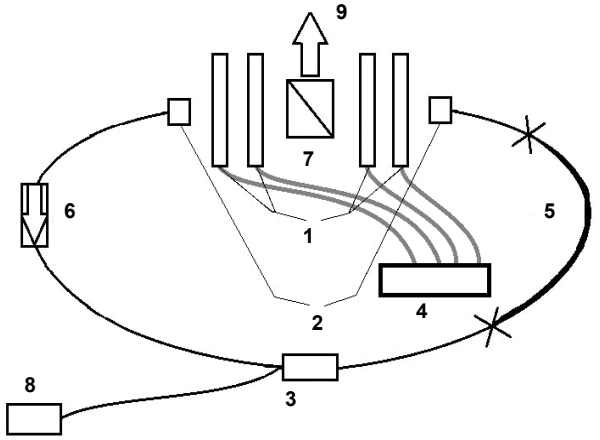

Fig. 3. Scheme fiber laser with LC cells: 1 – LC cells; 2 – collimators; 3 – device for input radiation into the resonator; 4 – control system for LC cells; 5 – one meter of erbium doped fiber.; 6 – optical isolator; 7 – polarizing beam splitter; 8 – diode pumping at 980 nm; 9 – radioation with a wavelength of 1550 nm.

In contrast to the wave plates LC cell are immune to many types of interference. Therefore, using a liquid crystal cells does not require constant adjustment of synchronization modes as is the case with wave plates. Liquid crystal cells operate in the wavelength range 1530–

1560 nm and a manipulated variable signal with a frequency of 1 kHz. The amplitude of the signal is adjusted in the range from 0 to 10 V. When we provide the electric field on the LC cell, it is deformed. That is, it changed at the angle of inclination of the internal elements. Figure 4 shows the variation in the intensity of the transmitted light through the LC cell. That is an effect of polarization rotation. Study transmittance LC cells was performed using the stand shown in Figure 5. By means of this experiment, we verified the proper operation of the cell, i.e. they can rotate the polarization. In our scheme, we use the four LC cells to fine tune the mode locking.

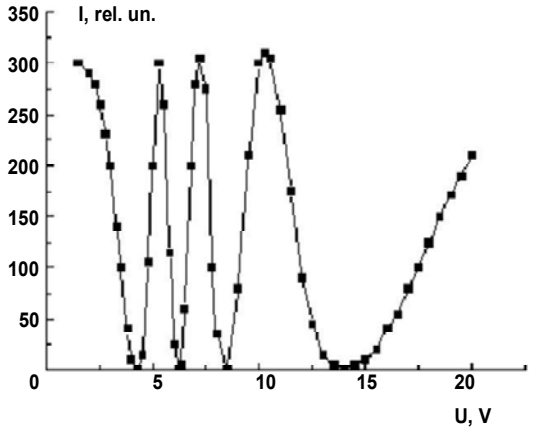

Fig. 4. The light transmittance of the LC cell depending on the applied AC voltage

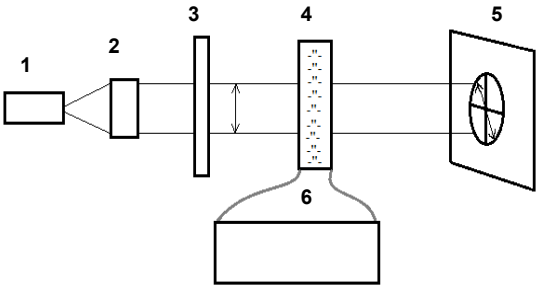

Fig. 5. The stand for investigation of the influence of the LC cell to laser radiation : 1 – source of radiation at a wavelength of 1550 nm; 2 – collimator; 3 – polarizing plate; 4 – LC cell; 5 – recording unit; 6 – control block for LC cell

Diagrams stability. However, studies conducted in the previous section insufficiently. In this section, we present stability diagrams [1] of polarization for the schema of the laser with nonlinear polarization rotation. Figures 6–9 show the area of stability depending on the angles of rotation of polarization at each of the controllers, where α1, α2, α3, α4 – the angles of rotation of the polarization in the first, second, third and fourth polarization controllers. But also in these graphs, you can see the local maximums, this is the best area of stability. They are achieved in a very small range of angles of rotation of the polarization. It is easy to notice that when applying the wave plates, setting mode locking the laser will be carried out with great difficulty and great expense of time.

Therefore, we propose to replace a number of wave plates in the LC cells by which to manage the polarization by an applied electric field to them. The voltage can be changed to several decimal places, provides the best stability polarization for mode locking.

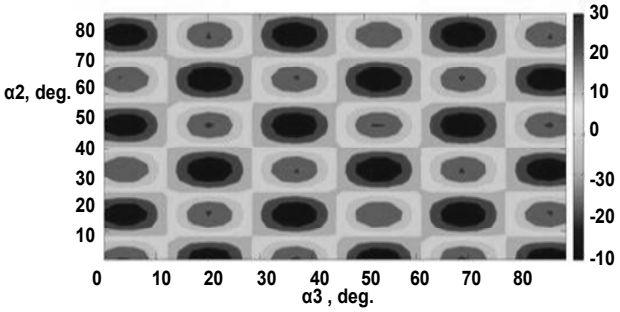

Fig. 6. Diagram stability when α1 = α4 = 0 deg

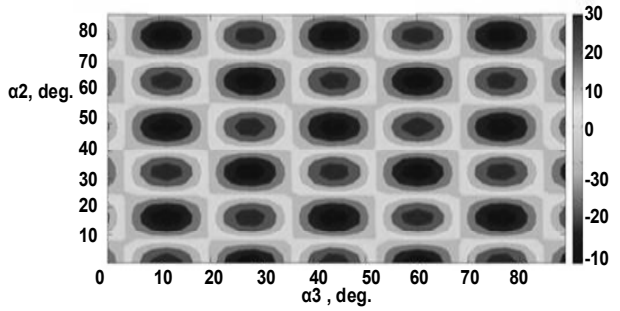

Fig. 7. Diagram stability when α1 =30 deg, α4 = 0 deg

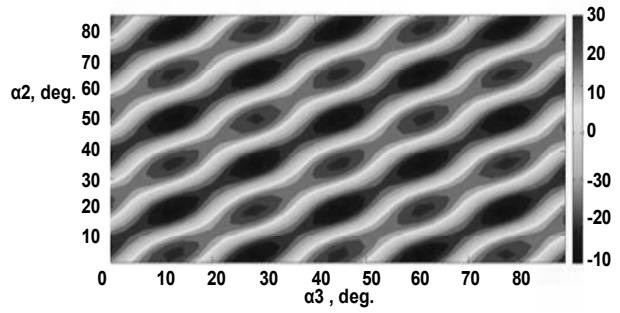

Fig. 8. Diagram stability when α1 = 0 deg,α4 = 45 deg

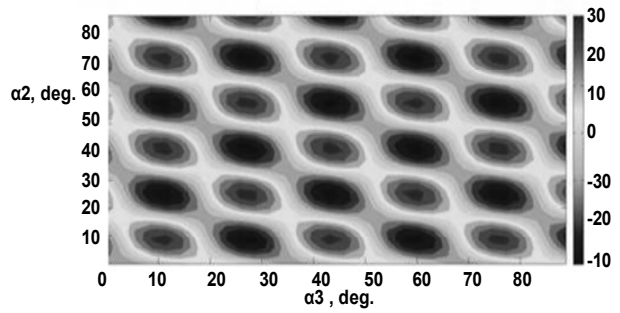

Fig. 9. Diagram stability when α1 = 45 deg,α4 = 45 deg

Conclusions. In this paper we were investigated the LC cell to control the polarization of the laser emission. These results serve to create an annular femtosecond fiber laser with passive mode locking, which is adjusted by applying an electrical signal of the LC cell. It is assumed that such a laser is easy to set up and stable work, regardless of external influences, such as micro-vibration, temperature drift diode pumping or simply pressing the power of the laser. Also, we calculated and analyzed the stability diagram of the polarization. Due to effect of the nonlinear rotation polarization can be achieved to mode lock in a ring fiber laser with a pulse duration of femtosecond order.

Another important point is that the use of LC cells are cheaper than the use of high-precision motorized rotating systems. It is also a great advantage our design before others, that are used in various fields of science and technology, in particular optical information technology, that operate in the telecommunications C-band.

REFERENCE

1. Gnatenko A. S. . Generation mode stability of a fiber ring laser / A.S. Gnatenko, Yu.P. Machekhin // Telecommunications and Radio Engineering. – 2015 – Vol.74, №7. – P. 641–647

2. Kurtner F. X. Mode−locking with slow and fast saturable absorbers−what's the difference? / F. X. Kurtner, J. A. der Au, and U. Keller. // IEEE Selected Topics in Quantum Electronics. – 1998. – Vol.4, №2. – P. 159–168.

3. Nishizawa N. All−polarization−maintaining Er−doped ultrashort−pulse fibre laser using carbon nanotube saturable absorber / N. Nishizawa, Y. Seno, K. Sumimura, Y. Sakakibara, E. Itoga, H. Kataura, and K. Itoh // Opt. Express. – 2008 – Vol. 16, №13. – P. 9429–9435.

4. Sotor J. Er−doped fibre laser mode−locked by mechanically exfoliated graphene saturable absorber / J. Sotor, G. Sobon, and K. M. Abramski. // Opt. Electron. Rev. – 2012. – Vol.20, №4. – P. 362–366.

Submitted on 12.11.15

Гнатенко А., асп., Мачехін Ю., д-р техн. наук, Васько К., студ.,
каф. фізичних основ електронної техніки, факультет електронної техніки,
Харківський національний університет радіоелектроніки

ЗАБЕЗПЕЧЕННЯ КОНТРОЛЮ ПОЛЯРИЗАЦІЇ ВСЕРЕДИНІ РЕЗОНАТОРА ВОЛОКОННОГО КІЛЬЦЕВОГО ЛАЗЕРА

У цій статті представлена реалізація синхронізації мод кільцевого волоконного лазера методом нелінійного обертання поляризації. Цей метод реалізований за допомогою рідкокристалічних (РК) комірок, які управляють поляризацією лазерного випромінювання шляхом подачі на них змінного сигналу. Також був проведений експеремент по взаємодії лазерного випромінювання (довжиною хвилі 1550 нм) з РК коміркою. Були побудовані та досліджені діаграми стабільність поляризації в волоконному кільцевому лазері.

Ключові слова: *волоконний лазер, рідкокристалічні комірки, фемтосекундні імпульси, керування напругою, хвильові пластини, синхронізація мод.*

Гнатенко А., асп., Мачехин Ю., д-р техн. наук, Васько К., студ.,
каф. физических основ электронной техники, факультет электронной техники,
Харьковский национальный университет радиоэлектроники

ОБЕСПЕЧЕНИЕ КОНТРОЛЯ ПОЛЯРИЗАЦИИ ВНУТРИ РЕЗОНАТОРА ВОЛОКОННОГО КОЛЬЦЕВОГО ЛАЗЕРА

В этой статье представлена реализация синхронизации мод кольцевого волоконного лазера методом нелинейного вращения поляризации. Этот метод реализован с помощью жидкокристаллических (ЖК) ячеек, которые управляют поляризацией лазерного излучения путем подачи на них переменного сигнала. Также был проведен эксперимент по взаимодействии лазерного излучения (длиной волны 1550нм) с ЖК ячейкой. Были построены и исследования диаграммы стабильность поляризации в волоконном кольцевом лазере.

Ключевые слова: *волоконный лазер, жидкокристаллические ячейки, фемтосекундные импульсы, управление напряжением, волновые пластины, синхронизация мод.*

UDC 57.042:57.024:615.21:612.821.5

V. Gorbachenko, stud., I. Chereda, stud.,
Department of Medical Radiophysics,
Faculty of Radio Physics, Electronics and Computer Systems,
Taras Shevchenko National University of Kyiv
J. Kruchenko, Ph.D., E. A. Lukyanetz, Dr.Sci, Prof.
O. O. Bogomoletz Institute of Physiology, NAS of Ukraine

MEASUREMENTS OF THE TIME PARAMETERS OF CONDITIONED FOOD REFLEX IN RATS UNDER MEMANTINE TREATMENT WITH USING OF AUTOMATIC REGISTRATION SYSTEM

Temporal features of motor phenomena of rats in the performance of food operant conditioned reflex obtaining food from feeders to response on a short beep were studied. Using device and software developed by us to register individual components of sensorimotor motor reaction the latent period, motor response time obtaining food, the amount needed for this and other attempts timing were analyzed. These indicators characterize the speed of information processing in the central nervous system and the overall level of excitability and motivation of animals. Temporal characteristics of individual units of sensorimotor responses are informative indicators of the functional state of the central nervous system, able to ensure the effectiveness of its monitoring and correction. The aim of our studies was to determine the effect of the drug memantine on these parameters, which is used in the treatment of Alzheimer's disease. We found that memantine increased the performance of old rats and slowed down their motor responses.

Key words: *cognitive abilities, food reflex, rat, photoelectric registration, memantine.*

Introduction. Alzheimer's disease (AD) is caused by progressive loss of cognitive abilities and is characterized by the formation of senile plaques of beta-amyloid and neurofibrillary glomeruli in neurons of the brain. AD is a neurological disease that is the most common cause of dementia, it is more than 65% of dementia in the elderly. Alzheimer's disease affects about 4% of people aged 65 to 74 years and more than 30% – over the age of 85 years. Therefore, it is important to study the mechanisms of AD and to develop new effective drugs to treat the disease. With this aim in biomedical research simulation diseases in animals is used, particularly in the study of neurodegenerative diseases to study of changes in the functioning of the central nervous system (CNS) on laboratory animals [1].

The most widely used marker of functional state of the CNS is to assess the characteristics of sensory-motor response (SMR). In most cases, establishment of dynamics or other differences in SMR accomplished through analysis of changes in reaction time (*RT*). To explain most of the neurophysiologic processes that lead to *RT*, often the term "latent period" (*LP*) is used − the time between the start of the stimulus and the occurrence of motor response. Value of *LP* is due to the implementation of physical-chemical process in the receptor, the passage of nerve impulses along pathways, analytical and synthetic activity in brain structures and operation of muscles. The dependence of speed and accuracy of performance of SMR on stability of attention, anxiety, age, pathological factors was found. In this regard, these are widely used as an objective and

© Gorbachenko V., Chereda I., Kruchenko J., Lukyanetz E., 2015

reliable enough indicators of the functional state of the CNS in healthy people in clinical studies and in animal experiments in modeling various neurodegenerative diseases. In our experiments, we used earlier developed experimental system of registration of food reflex in rats in order to evaluate changes in temporal parameters of the conditioned reflex in rats exposed to drug memantine, used in the treatment of Alzheimer's disease. Memantine slows down the progression of neurodegenerative processes and causes neuromodulatory effect.

Method of determination of conditioned reflex by using infrared sensors. We used the device and software developed by us [2], to register individual components of sensorimotor reaction. The principle of the registrations based on the operation of sensory infrared sensors. Briefly about the principle of their operation: a pair of sensors (Fig.1. (3)) is mounted on the wall near the food window (Fig.1 (2)) so the edge of plate with food cells and holes (Fig.1 (1)) passes between a pair of sensors (Fig.1. (3)) during rotation plate (Fig.1 (1)). This sensor (Fig.1 (3)) determines the position of each cell in coincidence with the axis of the cell hole between this pair of sensor and microcontroller counts how many steps motor is to move the plate from the starting position to each hole of the next cell. After loading the cells with food (food balls) pair of sensor (Fig.1 (3)) detects the presence of food in the cell by the presence or absence of cell hole which is closed in the presence of food. In the absence, feed motor returns the next cell in the "open" position relative to the food window after submitting audio signal. The other pair of sensors (Fig.1 (4)) is on the wall with a window so that the axis between a pair of sensors crosses food window and responds on probationer to crossing window. Thus, the sensor registers an attempt of probationer to get food from the cell.

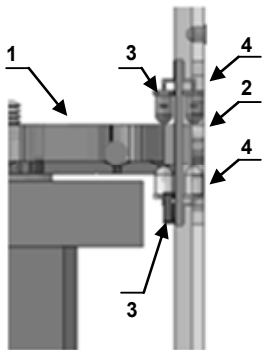

Fig. 1. Infrared sensors for registration of conditioned food reflex. 1 – turntable plate with cells, 2 – window for food delivery, 3 – a pair of sensors for detecting the presence of food in the cell, 4 – a pair of sensors for detecting the presence of limb in the cell

Experimental results and discussion. Our experiments were conducted on rats Wistar aged 12 months. Temporal features of motor phenomena of rats in the performance of food operant conditioned reflex obtaining food from feeders to response on a short beep were studied. In our experiments we used the protocol illustrated on Fig. 2. This is standard protocol for estimation food conditioned reflex, which was proposed earlier [3].

The next parameters were analyzed: latent period − the time before the first attempt of food withdrawal after the stimulus supply (*tl*); a motor response of obtaining food – the total time between the reactions of obtaining of food (TRr_n); time between successive attempts (IRI_n); the number of required attempts for this (*RN*); interstimulus period − number of approaches to the position between the signals (*ISP*); limb stays in the food cell before supplying the food (*rt*); total time of obtaining the food from the food cell (*RT*); and the time of the limb staying in the food cell during the obtaining of food (RD_n).

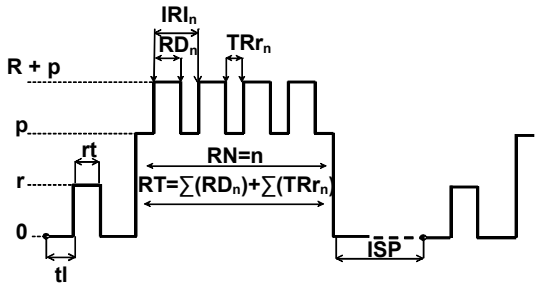

Fig. 2. Protocol of experiment for photoelectric registration of conditioned food reflex

These indicators characterize the speed of information processing in the central nervous system and the overall level of excitability and motivation animals. Temporal characteristics of individual units of sensorimotor responses are informative indicators of the functional state of the central nervous system; they able to ensure the effectiveness of its monitoring and correction. In our experiments, we studied the effect on these parameters the drug memantine (4 mg/kg), used in the treatment of Alzheimer's disease and that is an antagonist of NMDA receptors.

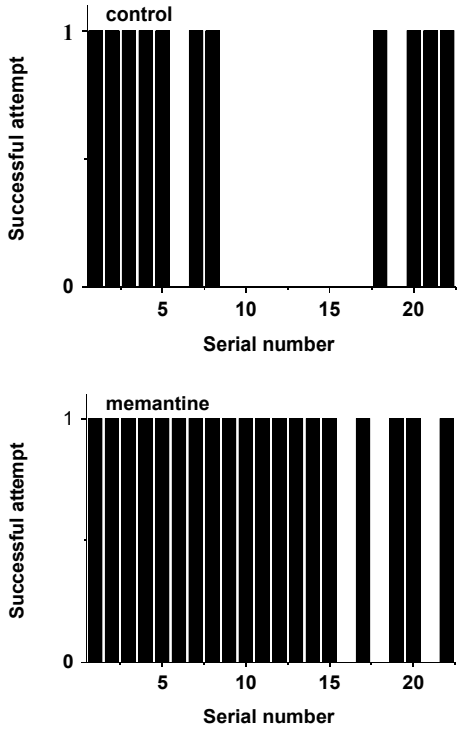

Fig. 3. An example of registration of successfulness of conditional food reflex (rat obtaining of feed after sound) measured in control conditions (left) and after effects of the drug memantine (right)

Experiments were conducted as follows, the beep and following food were supplied to old rats (aged 12 months), which produced a conditioned reflex. These successive presentations (signal-food) were 20÷25. If the rat

responded to the sound stimulus and pick up the food (a conditioned reflex worked), an attempt was considered successful. Fig. 3 shows the result of this experiment in one of the rats. As can be seen, under the control conditions, the rat reacted not all of the repeated successive stimulus presentations.

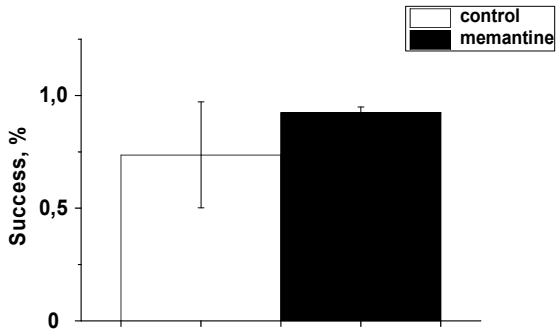

Fig. 4. The mean data of registration of successfulness of conditional food reflex (rat obtaining of feed after sound) measured in control conditions (white) and in rats which consumed memantine (black)

The success of attempts was 50% of all presentations, while in the case of the drug memantine, the success greatly increased, and accounted of 86%. It should be noted, that this index was slightly different in different rats and the effect of the drug was more effective in those rats, which in control conditions showed lower performance. Fig.4 demonstrates the mean data of successful operation of the conditioned food reflex in rats for control and memantine conditions.

As it can be seen, after treatment with memantine, the rats were more successful in getting food. Although a difference is quite enough (~18%), but it is not statistically significant. The latter is because in the control group the individuals with varying degrees of success were observed. Among them were more or less successful rats. At the same time, after the effect of memantine, less successful rat became more successful (Figure 3).

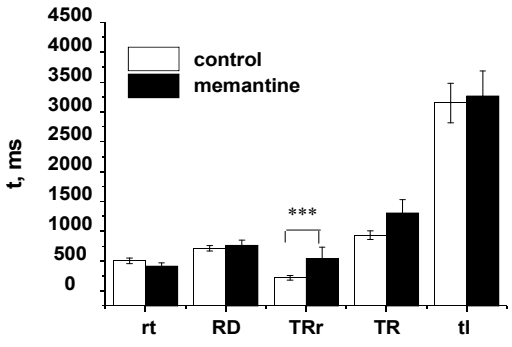

Fig. 5. The average values of temporal characteristics of rat food reflex recorded in the control and under the application of drug memantine

During these experiments, we also recorded the temporal characteristics of the conditioned reflex of rat, Fig. 5. We was found that under the influence of memantine the main characteristics remained without significant changes, except for two parameters – *RT* (total time obtaining food from the cell of feeder) and *TRr* (total reaction time between obtaining food). That is, the drug memantine influenced the response speed of the motor reaction of rat – it slowed down. Whereas, the other parameters such as *rt*, *RD*, *tl* were slightly influenced by memantine, Fig. 5.

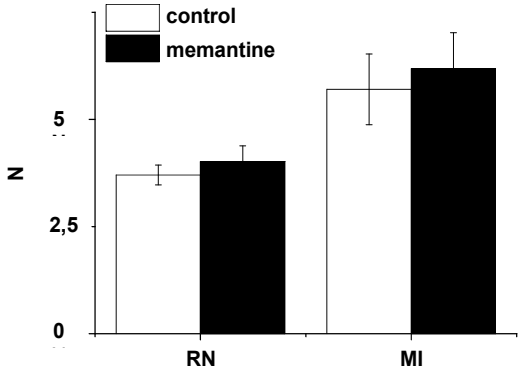

Fig. 6. The average values of quantitative characteristics of rat food reflex recorded in the control and under the application of drug memantine

We also measured the average values of quantitative characteristics of rat food reflex recorded in the control and under treatment of rats with drug memantine. These data are presented on Fig. 6. As it can be seen, in this case the mean quantitative parameters were not significantly different.

It is known, that AD accompanied psychopathic disorders (emotional disorders, anxiety, restlessness, depression, disorientation, apathy (indifference) to the environment, problems with movement, loss of capacity for independent thinking and movement), the use of experimental situations that cause these conditions, can be one of methods of finding the effective means of its correction. Experimentally proved that the nature of motor activity of rats placed in an unfamiliar environment, reflect their psycho-emotional status [3] and can be used to assess the effectiveness of effects of different pharmacological agents for certain forms of its detection.

In our previous studies, we found that memantine [4] weakened of fear and anxiety in old rats that promoted rapid adaptation of animals to new environment. In presented data we demonstrate that memantine also affect the temporal characteristics of conditioned reflex of old rats and increase its performance.

Conclusions. Thus, we have found that a drug that is used for the treatment of AD, increases the performance of old rats and slows down their motor responses.

REFERENCE

1. *Bures J.,* Techniques and basic experiments for the study of brain and behavior / J. Bures, O. Bureshova, D. P. Houston – Moscow: Vysshaya Shkola, 1991. – P. 216–220. (in Russian).

2. Gorbachenko V. A. Development and testing of the experimental system for registration of food reflex in rats / V. A. Gorbachenko, I. S. Chereda, S. V. Vrublevsky, Zh. A. Kruchenko, E. A. Lukyanetz// Bulletin of National Taras Shevchenko University of Kyiv. Series: Radio Physics and Electronics", 2015. T. 1, №21. – P. 31–33.

3. *Kostyuk P. G.* Calcium ions in brain function - from physiology to pathology / P. G. Kostyuk, E. P. Kostyuk, E. A. Lukyanetz –- Kyiv: Naukova Dumka, 2005. – P. 99–152. (in Ukrainian).

4. *Kruchenko Zh. A.* Effect of memantine on motor behavioral phenomena in rats of different ages / Zh. A. Kruchenko, V. A. Gorbachenko, I. S. Chereda, E. A. Lukyanetz // Neurophysiology. – 2014. Vol. 45, No. 5, – P. 448–451.

Submitted on 10.12.15

Горбаченко В., студ., Череда І., студ.,
каф. медичної радіофізики, радіофізичний факультет,
Київський національний університет імені Тараса Шевченка
Крученко Ж., канд. біол. наук, Лук'янець О., д-р біол. наук, проф.
***Інститут фізіології ім. О. О. Богомольця НАН України**

ВИМІРЮВАННЯ ЧАСОВИХ ПАРАМЕТРІВ УМОВНОГО ХАРЧОВОГО РЕФЛЕКСУ ЩУРІВ ПРИ ЗАСТОСУВАННІ МЕМАНТИНУ З ВИКОРИСТАННЯМ АВТОМАТИЧНОЇ СИСТЕМИ РЕЄСТРАЦІЇ

Вивчались особливості часових показників рухових феноменів щурів при виконанні харчового оперантного умовного рефлексу діставання їжі з годівниці у відповідь на дію короткого звукового сигналу. За допомогою розробленого нами пристрою та програмного забезпечення реєстрації окремих компонентів сенсомоторної рухової реакції аналізували латентний період, час моторної реакції діставання їжі, кількість необхідних для цього спроб та інші часові параметри. Ці показники характеризують як швидкість переробки інформації в ЦНС, так і рівень загальної збудливості і мотивації тварини. Часові характеристики окремих ланок сенсомоторної реакції є інформативними показниками функціонального стану ЦНС, здатними забезпечити ефективність його контролю і корекції. Метою наших досліджень було визначення впливу препарату мемантину, який застосовується при лікуванні хвороби Альцгеймера, на вказані параметри. Ми встановили, що мемантин збільшував успішність старих щурів і уповільнював їх рухові реакції.

***Ключові слова:** когнітивні здібності, харчовий рефлекс, щур, фотоелектрична реєстрація, мемантін.*

Горбаченко В., студ., Череда И., студ.,
каф. медицинской радиофизики, радиофизический факультет,
Киевский национальный университет имени Тараса Шевченка
Крученко Ж., канд. биол. наук, Лукьянец Е., д-р биол. наук, проф.
***Институт физиологии им. А. А. Богомольца НАН Украины**

ИЗМЕРЕНИЯ ВРЕМЕННЫХ ПАРАМЕТРОВ УСЛОВНОГО ПИЩЕВОГО РЕФЛЕКСА КРЫС ПРИ ПРИМЕНЕНИИ МЕМАНТИНА С ИСПОЛЬЗОВАНИЕМ АВТОМАТИЧЕСКОЙ СИСТЕМЫ РЕГИСТРАЦИИ

Изучались особенности временных показателей двигательных феноменов крыс при выполнении пищевого оперантного условного рефлекса доставания пищи из кормушки в ответ на действие короткого звукового сигнала. С помощью разработанного нами прибора и программного обеспечения регистрации отдельных компонентов сенсомоторной двигательной реакции анализировали латентный период, время моторной реакции получения пищи, количество необходимых для этого проб и другие временные параметры. Эти показатели характеризуют как скорость переработки информации в ЦНС, так и уровень общей возбудимости и мотивации животного. Временные характеристики отдельных звеньев сенсомоторной реакции являются информативными показателями функционального состояния ЦНС, способными обеспечить эффективность его контроля и коррекции. Целью наших исследований было определение влияния препарата мемантина, который применяется при лечении болезни Альцгеймера, на указанные параметры. Мы установили, что мемантин увеличивал успешность старых крыс и замедлял их двигательные реакции.

***Ключевые слова:** крыса, когнитивные способности, пищевой рефлекс, фотоэлектрическая регистрация, мемантин*

UDC 537.311.33, 621.315.592

V. Grygoruk, PhD, R. Kuzmych, stud., O. Oberemok, PhD., S. Pavlyuk, PhD
Faculty of Radiophusics Electronics and Computer Science
Taras Shevchenko National University of Kyiv

ABNORMAL UNSTEADY HEAT CONDUCTION SEMICONDUCTOR DIODE STRUCTURES

The work is devoted to the calculation of thermal conductivity, heat flow and the coefficient of thermal straightening silicon diode structures. Theoretical dependences of thermal conductivity of silicon and the type of temperature based on the temperature dependences of the thermal conductivity of all components of the members. Calculation of the thermal conductivity of the silicon semiconductor diode conducted in the temperature range 300–1000 K. The heat flow patterns calculated in both directions. Estimation of the coefficient of thermal straightening held as the ratio of the flow in one direction to flow backwards. Theoretical evaluations were conducted using computer software calculations. The results may be useful in the design of high power semiconductor devices and to control heat flow in electronic circuits.

***Key words:** semiconductor devices, semiconductor junctions, silicon, thermal rectifier*

Introduction. In recent years, semiconductor crystals began to be used as fuel elements. At the end of 80 years of the last century proposed and put into production way of collecting power diodes, diode when through crystal with a flattened him served conclusions passed a current pulse of power required for its heating to the melting point of the solder on the findings. Thus the conclusions to soldered of [1].

In 2000 he published work, which described the use of a semiconductor crystal micro-soldering-iron fuel elements [2]. In those same years published several works where KSDI structure was used as fuel elements for spraying specific substances. Through it was passed as a powerful impetus to the current structure and heating to high temperatures [3]. In all these cases the important rule was compliance with the conditions of his uniform heating. If it is heated up evenly, then it appeared large mechanical stresses, leading to the split of the crystal, that is, to his destruction.

The study of these effects is useful for the study and design of high-power semiconductor devices such as transistors, diodes, integrated circuits, which released more energy. For example, diodes, who commute large currents, transistors, in which semiconductor crystal attached to a special radiator which removes heat. In such cases, it is important to know how the heat, and the speed with which the crystal is cooled.

Experimental study of heat conduction diodes are described in [4–8], but theoretical calculations were not performed. Thus, the aim of the work was experimental and theoretical study of thermal conductivity and thermal diffusivity of semiconductor diode structures that are very relevant to the present.

Experimental part. Studied silicon crystals used in the production of industrial diodes KD 105, KD 209. They are made of silicon CE-mark 40 with a resistivity base ρ = 40 Om·sm, donor concentration procedure 10^{14}sm^{-3}. On one end of the crystal boron diffusion was created p^+ region with a resistivity ρ = 0,1 Om·sm, the concentration of acceptors order 10^{17}sm^{-3} and a thickness of 0.01 cm and the other end of phosphorus diffusion region received contact to n^+ p area. The crystals have a cylindrical shape with a diameter of 0.18 cm, 0.03 cm thick.

The main element of the experimental setup is pulsed electric heater, which conducted the studied heating module. It consists of a diode structure located between

© Grygoruk V., Kuzmych R., Oberemok O., Pavlyuk S., 2015

two thermo-compensator are made in a gilded kovar discs welded them to the conclusions of two thermocouples.

Investigated module before the experiment were pre-heated to provide "grabbing" all three elements (diode structure between two thermo-compensator) a solid block next division which is impossible without destroying the crystal silicon. Thus, the thermal contact resistance between the ends of the p^- and n-regions diode structure and attached them thermo-compensator were reliably recorded before the measurements. In this regard, under these conditions, there were no factors that could affect the change in the transition thermal resistance revolution in the investigated module on the surface of the heating element to change the orientation of the p-n junction to the source of heat.

Heating time diode structure change within 2–10 seconds. The temperature of the heating thermo-compensator recorded using an oscilloscope amplifier with memory. Measurements were carried out at different temperatures diode crystal orientation in relation to the heater by turning investigated alternate module on the surface of the heater.

Fig. 1 shows the change in temperature difference ΔT between the upper and lower thermocouples during heating. Curve 1 – heat flow directed from p- to n-region. Curve 2 – heat flow directed from n – to p-region. As seen in Figure 1, the passage of heat flow from n- to p-region temperature difference between the upper and lower thermocouples decreases. Consequently, the heat flow more in the direction of n- to p-region rather than vice versa.

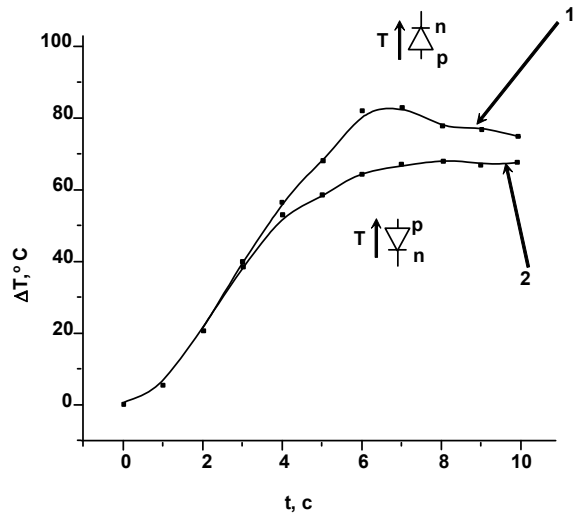

Fig. 1. Changes in temperature difference ΔT between the upper and lower thermocouples

Calculated part. Calculation of thermal conductivity, heat flow and thermal coefficient of silicon rectifier diode structures.

The calculation of the theoretical dependence of thermal conductivity on temperature held by the formula for the total thermal conductivity:

$$\frac{\chi}{\sigma T} = \frac{\chi_l}{\sigma T} + \frac{2k^2}{e^2} + (4 + \frac{\Delta E}{kT})^2 \frac{k^2 np \mu_e \mu_h}{e^2 (n\mu_e + p\mu_h)^2}. \quad (2.1)$$

Since the second term on the right hand side of (2.4.1), which is responsible for the contribution of free carriers in full conductivity is generally small, it is not considered in the calculation. Therefore, the thermal conductivity was reduced to the formula:

$$\frac{\chi}{\sigma T} = \frac{\chi_l}{\sigma T} + (4 + \frac{\Delta E}{kT})^2 \frac{k^2 np \mu_e \mu_h}{e^2 (n\mu_e + p\mu_h)^2}. \quad (2.2)$$

Theoretical calculation of the temperature dependence of the thermal conductivity was performed taking into account the temperature dependences of the thermal conductivity of all components of the members. Mainly it was necessary to show what contribution does the third term on the right hand side of (2.1) (mixed conductivity) in complete thermal conductivity at high temperatures.

Almost measure the heat flow in the diode structure impossible. However, this value can be calculated indirectly. It would be handy to have a formula for the heat flux at given temperatures at both ends of the sample. The calculated in [15], depending not be used to verify them experimentally (temperature at the ends of the device taken in an arbitrary scale – T_1 = 1,0 and T_2 = 0,2), since they are obtained by computer simulation. Therefore, in order to be able to estimate the heat flux, need a simple ratio. To this end, proposed the following method.

So, for use of the analytical solution approach. We approximate the function of heat in the considered temperature range of linear dependence. In this case, the equation should be solved with the boundary conditions have the form:

$$\begin{cases} \frac{d}{dx}\left(\chi(T(x))\frac{dT(x)}{dx}\right) = 0 \\ T(0) = T_1 \\ T(L) = T_2 \\ \chi_1(T(L/2))\frac{dT(L/2)}{dx} = \chi_2(T(L/2))\frac{dT(L/2)}{dx} \\ \chi_1(T) = a_1 T + b_1 \\ \chi_2(T) = a_2 T + b_2 \end{cases}. \quad (2.3)$$

Solution of system (2.3) has the form:

$$a\frac{T^2}{2} + bT = C1x + C2 \Rightarrow T(x) = \frac{-b \pm \sqrt{b^2 + 2aC2 + aC1x}}{a}. \quad (2.4)$$

Using the boundary conditions and the condition of stitching, easy to obtain analytical view of the temperature *T(x)* distribution throughout the structure. Then under heat flow counting formula:

$$J = -\chi_1(T(L/3))\frac{dT(L/3)}{dx}. \quad (2.5)$$

Typical dependence of the lattice thermal conductivity on temperature for silicon is shown in Figure 2.

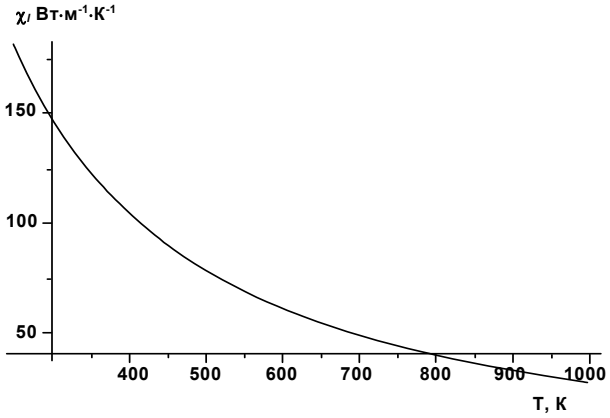

Fig. 2. Dependence of lattice thermal conductivity on temperature

As can be seen from Figure 2, the lattice thermal conductivity of silicon decreases with increasing temperature. And at very high temperatures it decreases significantly.

Figure 3 shows the theoretical dependence of thermal conductivity on temperature mixed silicon and p type.

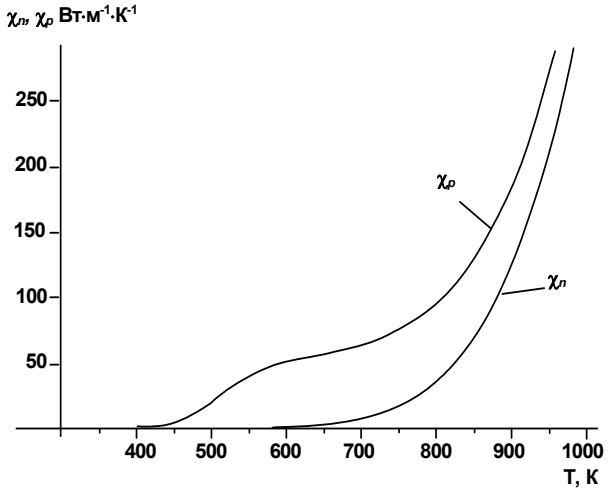

Fig. 3. Theoretical dependence of thermal conductivity on temperature mixed silicon and p-type

As seen in Figure 3, mixed conductivity at low temperatures is rather small size, but since the value of 500 K silicon p-type and 750 K for silicon-type conductivity increases dramatically. With further increase in temperature it increases several times.

Figure 4 depicts the theoretical dependence of thermal conductivity ratio mixed to full temperature for p-type silicon. As can be seen from the figure, the contribution to the total thermal conductivity of the mixed conductivity is very significant at high temperatures. The graph shows that at temperatures of the order of 900 K the thermal conductivity of the mixed contribution to the total is about 80%. This gives reason to believe that under these conditions the mixed conductivity makes the most significant contribution to the total thermal conductivity among all the other components of its members.

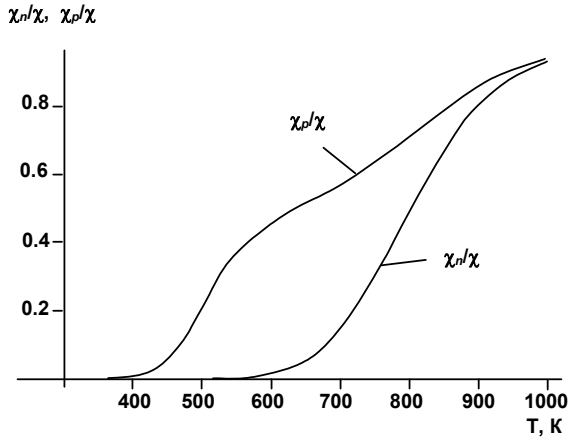

Fig. 4. Dependence of thermal conductivity ratio mixed to full temperature for silicon and p-type

Fig. 5 show the heat flux along the diode structure in both directions as a function of the temperature difference.

The right side of the graph (positive) shows the heat flow from the region n to the region p. The left side of the graph (negative) – on the contrary. As seen in Figure 5, the qualitative progress dependence is similar in both directions, but heat flows differ in absolute values. From the figure shows that the heat flow on the right of the chart are larger than the flow in the left. Thus, the flow of the field in the region n p is greater than vice versa.

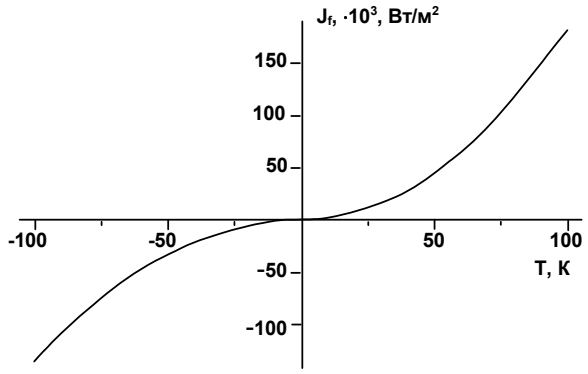

Fig. 5. The dependence of the heat flux diode structure in both directions as a function of the temperature difference

In Figure 6 presents the dependence of the thermal straightening structure, the ratio of heat flow in one direction (flow from region to region n p) to flow in reverse (flow from the field in the region p n) as a function of the temperature difference.

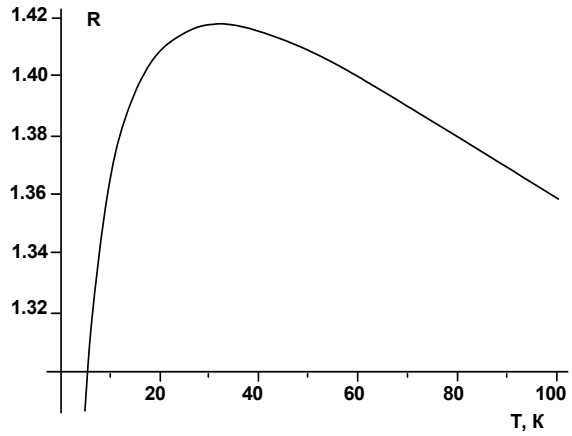

Fig. 6. Dependence of thermal straightening structure as a function of the temperature difference

From Figure 6 shows the effect of straightening indeed present, and this gives reason to believe that the working structure works as a thermal rectifier. Also from the figure shows that at 30 K temperature difference observed maximum straightening, and the coefficient is approximately 1.42.

Conclusions. During the performance calculated theoretical dependence of thermal conductivity silicon diode temperature.

Theoretical calculations of the contribution of different mechanisms of thermal conductivity and thermal conductivity to the total shown that the contribution to the total mixed thermal conductivity at high temperatures is around 80%.

Calculated and graphs heat flux diode structure in both directions and it is shown that they differ in absolute values. Stream from region to region n p is greater than vice versa.

The coefficient of thermal straightening structure has a maximum close to 1.42 for the temperature difference of 30 K.

REFERENCE

1. *Dobrovolskyy V.* The dependence of the thermal conductivity of the crystal diode orientation p – n junction / Volodymyr Dobrovolskyy, Larysa

Ischuk, Serhii Pavlyuk, Viktor Kyslitsyn // Bulletin of Kiev University. Series Phys. – Mat. Science. – 2006. – № 2. P. 123–132.

2. *Kushnirenko V.* Investigation of silicon diffusion resistors Volodymyr Kushnirenko, Grygorii Ninidze, Leonid Konovalenko, Serhii Pavlyuk // Technology and design of electronic equipment. – 2005. – № 5 (59). – P. 23–26.

3. *Pavlyuk S.* Using silicon as a semiconductor elements mikropayalnikov / Serhii Pavlyuk, Grygorii Kutlin, Viktor Kislitsyn, Anatolii Rossoshinsky // Automatic Welding. – 1999. – No. 2. – P. 41–44.

4. *Pavlyuk S.* Anisotropy of thermal conductivity in diode structures / Serhii Pavlyuk, Larysa Ischuk, Viktor Kyslitsyn // Bulletin of Kiev University. Series Phys. - Mat. Science – 2007. – № 3. P.88–92.

5. *Peyrard M.* The design of a thermal rectifier / M. Peyrard // Europhysics Letters. – 2006. –P. 1–7.

6. *Rossoshinsky A. A* method of assembling semiconductor devices / A. A Rossoshinsky, V. A. Lebiga, V. M. Kislitysn, E. A. Al'perovich // AS No. 355696 USSR. – 1972. – Byul.№ 31. P. 32–34.

Submitted on 30.04.15

Григорук В., д-р фіз.-мат. наук, Кузьмич Р., студ.,
Оберемок О., канд. наук, Павлюк С., канд. фіз.-мат. наук,
факультет радіофізики, електроніки та комп'ютерних систем
Київський національний університет імені Тараса Шевченка

АНОМАЛЬНА НЕСТАЦІОНАРНА ТЕПЛОПРОВІДНІСТЬ НАПІВПРОВІДНИКОВИХ ДІОДНИХ СТРУКТУР

Робота присвячена розрахунку теплопровідності, теплового потоку та коефіцієнта теплового випрямлення кремнієвих діодних структур. Отримано теоретичні залежності теплопровідності кремнію та типу від температури з урахуванням температурних залежностей усіх складових членів теплопровідності. Розрахунок теплопровідності напівпровідникового кремнієвого діода проводився в діапазоні температур 300–1000 К. Тепловий потік структури розраховувався в обох напрямках. Оцінка коефіцієнта теплового випрямлення проводилася як відношення потоку в одному напрямку до потоку в зворотному. Теоретичні оцінки проводились за допомогою комп'ютерних програм розрахунків. Отримані результати можуть бути корисними при проектуванні напівпровідникових приладів великої потужності та для керування тепловими потоками в електронних мікросхемах.

Ключові слова: *діод, температура, модифікація, імпульс струму*

Григорук В., д-р физ.-мат. наук, Кузьмич Р., студ.,
Оберемок Е., канд. наук, Павлюк С., канд. физ.-мат. наук
факультет радиофизики, електроники и компьютерных систем
Киевський национальный университет имени Тараса Шевченко

АНОМАЛЬНАЯ НЕСТАЦИОНАРНАЯ ТЕПЛОПРОВОДИМОСТЬ ПОЛУПРОВОДНИКОВЫХ ДИОДНЫХ СТРУКТУР

Работа присвящена расчету теплопроводимости теплового потока и коэффициента теплового выпрямления кремниевых диодных структур. Получено теоретические зависимости теплопроводимости кремния р и n типа от температуры с учетом температурных зависимостей всех составляющих членов теплопроводимости. Расчет теплопроводимости полупроводникового кремниевого диода проводился в диапазоне температур 300–1000 К. Тепловой поток структуры рассчитывался в обоих направлениях. Оценка коэффициента теплового выпрямления проводился как соотношение потока в одному направлении до потока в обратном. Теоретические оценки проводились при помощи компьютерных программ расчетов. Полученные результаты могут быть полезными при проектировании полупроводниковых приборов большой мощности и для управления тепловыми потоками в электронных микросхемах.

Ключевые слова: *диод, температура, модификация, импульс тока*

UDC 621.396.6.001.63;621.396.001.66

V. Dan'ko, Ph. D., I. Koval, Ph. D., O. Kisil, Head of laboratory, V. Solovyov, adv. eng.
Department of Nanophysics and Nanoelectronics, Faculty of Radio Physics, Electronics and Computer Systems,
Taras Shevchenko National University of Kyiv

DEVELOPMENT OF MEASUREMENT CHANNELS FOR GAS ANALYSIS SYSTEMS ON MODERN RADIO COMPONENTS

A block diagram of the measuring channel of gas analysis system built on integrated circuits (ICs) of Analog Devices. Detailed description of its key elements and their use is justified. An example of connecting the electrochemical sensor for measuring the concentration of Cl_2, CO, H_2S, SO_2, H_2, HCl, NH_3, NO_2, O_3 in the air. We also show examples of connecting sensors of hydrocarbons and relative humidity. Described the basic advantages of the proposed structure, namely the unification of measuring channel with reduced total cost of multichannel measuring system.

Key words: *gas analysis system, electrochemical sensor, catalytic sensor, multichannel measuring system*

Introduction. In recent years, a wide range of integrated circuits (ICs) from Analog Devices appeared on the market of electronic components. It has allowed revision some principles of design of measuring channel for gas detection systems. The proposed ICs have the high performance, represent a wide range of functional properties and have the best quality / price ratio. Furthermore, the use of integrated circuits of one manufacturer facilitates the development of devices and organization of their production.

In this paper we have proposed some variants of design a multichannel gas measuring system built on Analog Devices ICs.

Block diagrams of measuring channel. Fig. 1 show the structure of our proposed measuring channel. It consists of an 8-channel analog multiplexer, an instrumentation amplifier with a bias source, 24-bit sigma-delta analog-to-digital converter (ADC), the voltage reference circuit and electrical isolation of the digital signals.

Set of sensors (1 to 8) is connected to the inputs of an analog multiplexer through appropriate matching units. Multiplexer switches the signals of both positive and negative polarities. This makes it possible to unify the measurement channel. The iCMOS technology analog multiplexer IC ADG1408 is used. It has open channel resistance of 4.7 ohms. A leakage current of channels does not exceed ±0.6 nA. The iCMOS (industrial CMOS) modular manufacturing process combines high voltage CMOS (complementary metal-oxide semiconductor) and bipolar technologies. Unlike analog ICs using conventional CMOS processes, iCMOS components can tolerate to high supply voltages while providing increased performance, dramatically lower power consumption, and reduced package size. The stability and ultralow on resistance of these multiplexers makes them ideal solutions for data acquisition [1].

A signal from multiplexer output comes to input of instrumentation amplifier AD622, which has a high linearity of gain (10 ppm), as well as the relatively low bias current (2 nA). AD622 is a differential signal amplifier system, which also provides excellent linearity and common-mode rejection ratio (CMRR) due to internal precision laser-

© Dan'ko V., Koval I., Kisil O., Solovyov V., 2015

trimmed resistors [2]. A feature of this amplifier is the presence of the bias input, which is important for the implementation of measurement method that we proposed. The gain is set by an external resistor in the range of 1 to 1000. Output signal bias of the instrumentation amplifier is provided by means of voltage reference IC ADR03BR, which generates a bias voltage of +2.5 V with a temperature coefficient of 3 ppm/°C. The ADR03 is compact, low drift voltage reference that provides an extremely stable output voltage from a wide supply voltage range [9]. The output signal of the instrumentation amplifier through a resistive divider is applied to the non-inverting input of the ADC; the inverted input is connected to the output of the bias source.

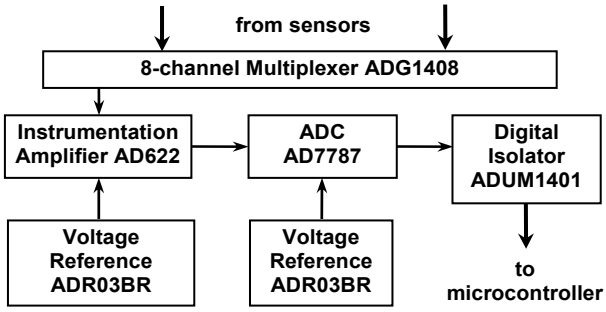

Fig. 1. Block diagram of measuring channel

We have three advantages using this measuring technique:

- small signals precise measurement;
- the ability to measure bipolar signals;
- high input impedance in all dynamic range (from parts of millivolts to 10 Volts)

All described features are reaching using low-cost unipolar ADC IC (AD7787). The AD7787 is a low power, complete analog front end for low frequency measurement applications. It contains a low noise 24-bit sigma-delta ADC with one differential input and one unbalanced input that can be buffered or unbuffered. The device operates from an internal clock. Therefore, the user does not have to supply a clock source to the device. The output data rate from the part is software programmable and can be varied from 9.5 Hz to 120 Hz, with the rms noise equal to 1.1 μV at the lower update rate. The internal clock frequency can be divided by a factor of 2, 4, or 8, which leads to a reduction in the current consumption. The update rate, cut-off frequency, and settling time scales with the clock frequency. The part operates with a single power supply from 2.5 V to 5.25 V [3]. It has three-wire synchronous serial interface SPI for data exchange with microcontroller. Measurement of bipolar signals is achieved by the presence in AD7787 of the bipolar mode in which half of the scale corresponds to zero voltage differential input. As a voltage reference applied to ADC, ADR03BR IC with +2.5 V output voltage is used.

For electric isolation of ADC's digital signals four channel digital isolator IC ADUM1401 is used. It has insulation strength of 1 kV. The ADuM1401 is a quad-channel digital isolator based on Analog Devices, Inc., iCoupler® technology. Combining high speed CMOS and monolithic air core transformer technology, these isolation components provide outstanding performance characteristics superior to alternatives, such as optocoupler devices. By avoiding the use of LEDs and photodiodes, iCoupler devices remove the design difficulties commonly associated with opto-couplers. The typical optocoupler concerns regarding uncertain current transfer ratios, nonlinear transfer functions, and temperature and lifetime effects are eliminated with the simple iCoupler digital interfaces and stable performance characteristics. The need for external drivers and other discrete components is eliminated with these iCoupler products. Furthermore, iCoupler devices consume one-tenth to one-sixth of the power of optocouplers at comparable signal data rates [8].

It should be noted that for the realization of a device constructed according to the block diagram shown in Figure 1, each functional unit is implemented on a single Analog Devices ICs.

One can propose an alternative variant of technical realization of a measuring channel using one of the latest developments of the Analog Devices - IC ADuCM361 [5]. This chip contains almost all functional components needed to build the structure shown in Fig. 1 (See Fig. 2). Only the digital isolator is missing.

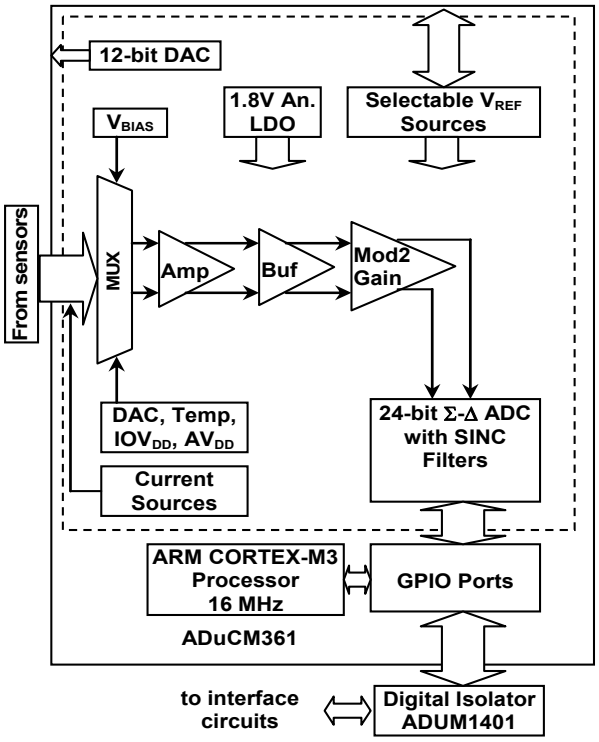

Fig. 2. Block diagram of measuring channel based on ADuCM361 IC

The ADuCM361 is a fully integrated, 4 kSPS, 24-bit data acquisition system incorporating high performance multi-channel sigma-delta (Σ-Δ) analog-to-digital converter (ADC), 32-bit ARM Cortex M3® MCU, and Flash/EE memory on a single chip allowing direct interfacing to external precision sensors in both wired and battery powered applications. The microcontroller core is a low power ARM Cortex-M3, 32-bit RISC machine, offering up to 20 MIPS peak performance, incorporating a flexible 11-channel DMA controller supporting SPI, UART, I2C communication peripherals. 128k Bytes Flash/EE and 8k Bytes SRAM are integrated on-chip.

The analog subsystem consists of ADC, connected to a flexible input multiplexer (MUX). ADC can operate in fully differential and single-ended modes. Other on-chip ADC features include dual programmable excitation current sources, diagnostic current sources, and a bias voltage generator of AVDD_REG/2 (900 mV) to set the common-mode voltage of an input channel.

Multi-channel gas analyzer, built on IC ADuCM361 has good potential for modernization and development.

Primary processing of sensor signals. Let us consider typical scheme of primary processing of sensor signals. Among them can be conditionally outlined three variants of the matching with the measuring channel:

- connection circuit of three-electrode electrochemical primary converter;
- bridge connection circuit for the catalytic sensors;
- bridge connection circuit for thermal resistance converter.

Fig. 3 shows a circuit diagram of the connection of three-electrode electrochemical sensor for measuring channel. Such circuit uses an electrochemical chlorine sensor CL_2 / M20 (Membrapor). By the same method the concentration in the air CO, H_2S, SO_2, H_2, HCl, NH_3, NO_2, O_3 is measured.

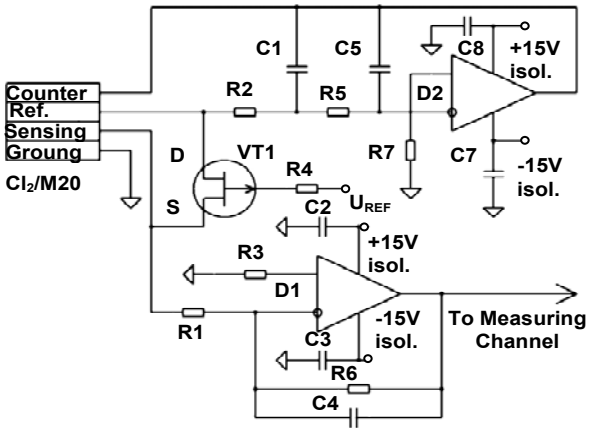

Fig. 3. The electrical circuit connecting the three-electrode electrochemical sensor for measuring channel

The circuit operates as follows. The current proportional to the concentration of chlorine in the air is supplied from the working electrode of the sensor to the input of the current-voltage converter D1 that is built on an operational amplifier OP97. This chip is a low-cost precision operational amplifier with low power consumption. The chip consumes only 600 μA, has an ultralow bias voltage (25 μV) and its temperature drift (0.6 μV/°C). It should also be noted his low input bias current of 250 pA over the entire range of operating temperatures (–40 ... +85 °C) and high CMRR (114 dB) [4]. The resistor R3 is installed to reduce the error due to a difference input currents of amplifier. The capacitor C4 prevents the self-excitation of the operational amplifier D1. The operating mode of the sensor is provided by a potentiostat circuit. This scheme supports the potential of the working electrode close to the potential of analog ground by setting the required level of voltage to the auxiliary electrode. It is implemented on the operational amplifier D2 (OP97). Elements R2, C1, R5, and C5 form a low pass filter which prevents self-oscillation of the operational amplifier D2. FET VT1 provides a connection between the working and reference electrodes in the absence of power. This prolongs the life of the sensor [7].

Figure 4 shows a circuit diagram of the connection of catalytic sensors.

In this example, we will consider the connection of the sensor of hydrocarbons TGS6810 (Figaro).

As a matching device we used specialized operational amplifier D1.2 (AD8279). Feedback resistors which determine the operating mode of the differential amplifier are formed on a single chip with amplifier circuit using a laser trimming method. This allows for extremely high CMRR (80 dB) and high temperature stability and accuracy of the gain (0.02% and 1ppm/°C, respectively) [6].

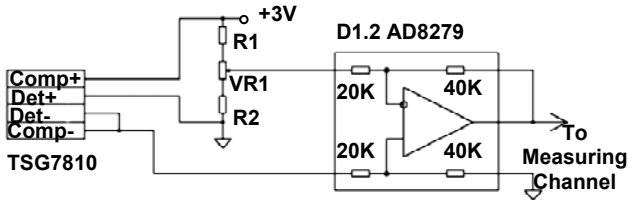

Fig. 4. The electrical circuit connecting the catalytic sensor for measuring channel

Conclusions. Use of Analog Devices ICs has made it possible to standardize the structure of the measuring channel in the gas analysis system. This can significantly reduce the total cost of the development, production and operation of the measuring multi-channel complex.

REFERENCE

1. 4 Ω R_{on}, 4-/8-Channel ±15V/+12V/±5V iCMOS Multiplexers ADG1408/ ADG1409, Analog Devices, Inc., 2006–2009, Rev. B.

2. Low Cost Instrumentation Amplifier AD622, Analog Devices, Inc., 1996–2012, Rev. E.

3. Low Power, 2-Channel 24-Bit Sigma-Delta ADC AD7787, Analog Devices, Inc., 2004, Rev. O.

4. Low Power, High Precision Operational Amplifier OP97, Analog Devices, Inc., 1997–2009, Rev. G.

5. Low Power, Precision Analog Microcontroller with Dual Sigma-Delta ADCs, ARM Cortex-M3. Analog Devices, Inc., 2014, Rev. C.

6. Low Power, Wide Supply Range, Low Cost Difference Amplifiers, G=1/2, 2 AD8278, AD8279, Analog Devices, Inc., 2009–2011, Rev. C

7. Potentiostat Circuit for Electrochemical Cells. US Patent 5,466,356, Nov. 14, 1995.

8. Quad-Channel Digital Isolators ADuM1400 / ADuM1401 / ADuM1402, Analog Devices, Inc., 2003–2012 Rev. H.

9. Ultracompact, Precision 10.0 V/5.0 V/2.5 V/3.0 V Voltage References ADR01 / ADR02 / ADR03 / ADR06, Analog Devices, Inc., 2002–2012, Rev. R.

Submitted on 22.10.15

Данько В., канд. фіз.-мат. наук, Коваль І., канд. фіз.-мат. наук, Кисіль О., зав. НДЛ, Соловйов В., пров. інж.
каф. нанофізики та наноелектроніки, факультет радіофізики, електроніки та комп'ютерних систем
Київський національний університет імені Тараса Шевченка

РЕАЛІЗАЦІЯ ВИМІРЮВАЛЬНОГО КАНАЛУ ДЛЯ СИСТЕМ ГАЗОАНАЛІЗУ НА СУЧАСНІЙ ЕЛЕМЕНТНІЙ БАЗІ

Запропоновано структурну схему вимірювального каналу системи газоаналізу, побудовану на інтегральних схемах (ІС) компанії Analog Devices. Докладно описані її ключові елементи та обґрунтовано їх застосування. Наведено приклад підключення електрохімічних сенсорів для вимірювання концентрації в повітрі Cl_2, CO, H_2S, SO_2, H_2, HCl, NH_3, NO_2, O_3. Показано приклади підключення сенсорів вуглеводнів і відносної вологості повітря. Вказано основні переваги пропонованої структури, а саме: уніфікація вимірювального каналу зі зниженням сумарної вартості багатоканального вимірювального комплексу.

Ключові слова: *система газоаналізу, електрохімічний сенсор, каталітичний сенсор, багатоканальний вимірювальний комплекс.*

Данько В., канд. физ.-мат. наук, Коваль И., канд. физ.-мат. наук, Кисиль А., зав. НИЛ, Соловьев В., вед. инж.
каф. нанофизики и наноелектроники, факультет радиофизики, электроники и компьютерных систем
Киевский национальный университет имени Тараса Шевченко

РЕАЛИЗАЦИЯ ИЗМЕРИТЕЛЬНОГО КАНАЛА ДЛЯ СИСТЕМ ГАЗОАНАЛИЗА НА СОВРЕМЕННОЙ ЭЛЕМЕНТНОЙ БАЗЕ

Предложена структурная схема измерительного канала системы газоанализа, построенная на интегральных схемах (ИС) компании Analog Devices. Подробно описаны ее ключевые элементы и обосновано их применение. Приведен пример подключения электрохимических сенсоров для измерения концентрации в воздухе Cl_2, CO, H_2S, SO_2, H_2, HCl, NH_3, NO_2, O_3. Показаны примеры подключения сенсоров углеводородов и относительной влажности воздуха. Указаны основные преимущества предлагаемой структуры, а именно: унификация измерительного канала со снижением суммарной стоимости многоканального измерительного комплекса.

Ключевые слова: *система газоанализа, электрохимический сенсор, каталитический сенсор, многоканальный измерительный комплекс*

UDC 537.226.4: 537.226.1: 537.226.83: 537.226.86

M. Zelenyuk, PhD stud., A. Susla, eng.,
H. Guyvan, PhD, A. Slivka, Prof, Dr., V. Kedyulich, PhD
Faculty of Physics, Uzhhorod National University, Uzhhorod, Ukraine
e-mail: kaf-optics@uzhnu.edu.ua

UNIAXIAL PRESSURE EFFECT ON PHASE TRANSITION OF CR3+-DOPED TGS CRYSTALS

The results of experimental studies of the uniaxial pressure effect on the dielectric properties of TGS crystals doped with metallic impurities of Cr3+ in the vicinity of the ferroelectric structural phase transition are presented. The phase σ2,T-diagram is constructed and the pressure coefficient of the shift the phase transition temperature of the crystal is determined.

Key words: *ferroelectrics, phase transition, TGS, metallic impurities, uniaxial pressure, dielectric constant.*

Introduction. An important issue in discovering the structural phase transitions in solids is the study of phase diagrams to determine the nature and conditions of polycritical phenomena. Therefore, the studies of the physical properties of crystals with hydrogen bonds in the conditions of uniaxial pressure are relevant. They make it possible to obtain important additional information about the nature of physical processes and phenomena and may serve as a basis for improvement of theoretical models describing the phase transitions of ferroactive crystals. At the same time, as we know, by using the external pressure can be made purposeful control of physical parameters of the crystals to achieve their optimal values.

Among the ferroelectric crystals with hydrogen bonds triglycine sulfate $(NH_2CH_2COOH)_3 \cdot H_2SO_4$ (TGS) investigated the most fully. They are ferroelectrics with second order phase transition of "order-disorder" type. The crystal has monoclinic symmetry and belongs to centrosymmetric class 2/m above the Curie temperature T_C = 322 K. Below T_C the mirror plane disappears and the crystal belongs to the polar point group 2 of the monoclinic system.

In real crystals, the defects and impurities perform a great influence on the ferroelectric properties. Defects can occur during the crystal growth as a result of various external factors. Because of occurrence of elementary defects (point, linear, surface and volumetric) around them occurs a distortion of the crystal lattice, which is associated with the displacement of atoms, ions and molecules from equilibrium states. Radiation defects damages the molecules of glycine and causes the formation of stable free radicals. They are also affecting the physical properties of crystals as shown in [1]. A similar influence is performed by metallic and organic impurities [6].

The aim of this research is to study the uniaxial pressure effect on the dielectric properties of TGS crystals doped with metallic impurities of Cr^{3+} in the vicinity of the structural ferroelectric phase transition. The concentrations of impurities for these crystals are 2%.

Experimental. Controlled and uncontrolled impurities differently distort the crystal lattice by changing the domain structure and physical properties of crystals. By the nature of placement in lattice, metallic impurities related to inculcation type of impurities and organic – to replacement type.

The influence of impurities on the physical properties of crystals depends on their concentration, the sign of the charge and changes of the balance of relation forces in the crystal structure. When doping TGS crystals the chromium ion is inculcated into the lattice and inside a cluster of atoms of nitrogen and oxygen of glycine molecules and oxygen SO_{4-} groups [4].

As a result of incoming of impurities forms an effective electric field of point defects, under the influence of which the domain walls are fixed on them. This leads to a decrease in the agility of the walls and the formation of the natural-unipolar state of crystal.

The dielectric constant of the crystals was determined by the results of experimental measurements of the capacitance of samples and was calculated by using the formula for a plane capacitor. The capacitance of samples was directly measured by using an AC bridge LCR E7-12 at a frequency of 1 MHz with a measuring field of 1.25 V/cm.

Samples were made in the form of a parallelepiped, oriented according to the crystallographic axes. At the edge, which are perpendicular to the polar direction, were applied electrical contacts with silver paste.

The accuracy of registration of the uniaxial pressure is ± 5%.

Uniaxial mechanical stress was created by a spring dynamometer and was transferred on sample through a punch with floating heads (fig. 1).

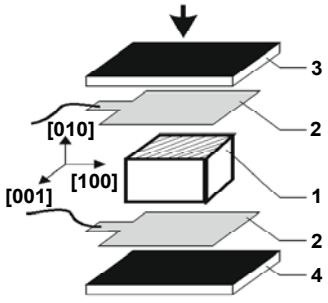

© Zelenyuk M., Susla A., Guyvan H., Slivka A., Kedyulich V., 2015

Fig. 1. Method of the uniaxial compression (1 – sample, 2 – cooper foil contacts, 3 – floating head punch, 4 – cell support)

The samples were placed in a specially constructed thermostat which allowed to gradually adjust the temperature of sample. The temperature was measured by the copper-constantan thermocouple with an accuracy of ± 0.1 K. To improve heat transfer and to prevent contact with air the sample and thermocouple were filled by silicone oil. Uniaxial pressure was applied along the ferroelectric axis *b*, which corresponds to the mechanical stress σ_2 [2].

Fig. 2 shows the temperature dependence of the dielectric constant of TGS+Cr^{3+} crystals under the influence of uniaxial pressure σ_2. It can be seen that the application of uniaxial mechanical stress decreases the maximum value of dielectric constant and the temperature of this maximum.

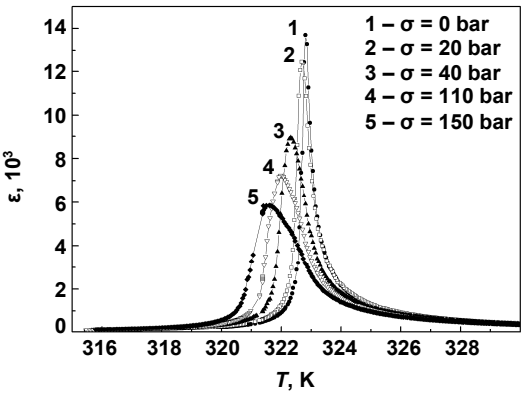

Fig. 2. Temperature dependence of the dielectric constant of TGS+Cr^{3+} crystals for different values of uniaxial pressure

Fig. 3 shows the temperature dependence of the inverse dielectric constant.

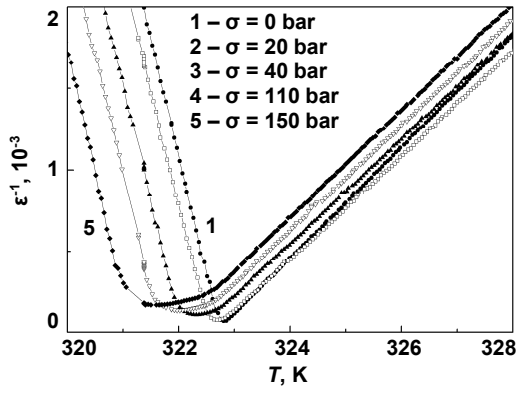

Fig. 3. Temperature dependence of the inverse dielectric constant of TGS+Cr^{3+} crystals for different values of uniaxial pressure

Fig. 4 shows the phase σ_2, *T*-diagrams of TGS+Cr^{3+} crystals.

To construct the phase diagram the extrapolating of the inverse temperature dependence of the dielectric constant to zero in the paraelectric phase was performed [3].

The pressure coefficient of the shift the phase transition temperature of considered crystal has next value: $dT_C/d\sigma_2 = -5.9$ K/kbar. The shift of the phase transition temperature under the influence of uniaxial pressure along the ferroelectric axis of the crystals was more than for TGS+Co^{2+} and TGS+Cu^{2+} crystals. The values of the pressure coefficients of the change the phase transition temperature for TGS+Co^{2+} and TGS+Cu^{2+} crystals are $dT_C/d\sigma_2 = -5.2$ K/kbar and $dT_C/d\sigma_2 = -5.3$ K/kbar, respectively [5, 7].

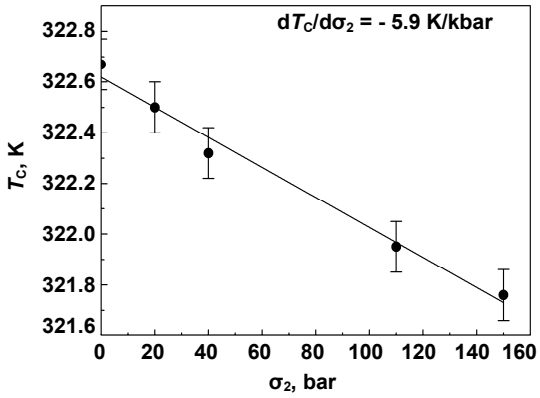

Fig. 4. The phase σ_2,*T*-diagram of TGS+Cr^{3+} crystals

Analysis of our studies of the effect of metallic impurities on the properties of TGS crystals showed that this effect on the dielectric properties increases with increasing of the atomic mass of impurity.

Conclusions.

1. Experimentally proved that for TGS+Cr^{3+} crystals uniaxial pressure σ_2 leads to a decrease in the maximum values of the dielectric constant and decrease the phase transition temperature.

2. It was found that the doping TGS crystals by metallic impurities of Cr^{3+} lead to an increase in the phase transition temperature.

3. The phase σ_2,*T*-diagram is constructed and the pressure coefficient of the shift the phase transition temperature of the TGS+Cr^{3+} crystal is determined. It is $dT_C/d\sigma_2 = -5.9$ K/kbar.

4. It is shown that the influence of metallic impurities on the dielectric properties of TGS crystals increases with increasing of the atomic mass of impurity.

Reference

1. *Hilczer B.* Influence of lattice defects on the properties of ferroelectrics // Mater. Sci. (PRL). 1976. Vol. 2, N. 1–2. P. 3–12.

2. *Kedyulich V. M.* et all. Condensed Matter Physics. – Vol. 3. №4 (24), 2000. P. 851–856.

3. *Kiyoyasu Imai.* Effect of Uniaxial Pressure on the Ferroelectric Phase Transition of Tri-Glycine Sulfate // Journal of the Physical Society of Japan. – Vol. 36. №4, April 1974.

4. *Nishimura K., Hashimoto T.* ESR investigation of TGS doped with Cr3+ ions // J. Phys. Soc. Jap. 1973. Vol. 35, N. 6. P. 1699–1703.

5. *Susla A. I., Zelenyuk M. S., Guyvan H. M.* et all. The influence of mechanical and electric fields on the dielectric properties of Co-doped TGS crystals // British Journal of Education and Science. – London, 2014, № 2 (6). P. 305–308.

6. *Tsedric M. S., Zaborovski G. A.* Critical behavior and internal bias of TGS and isomorphous crystals depending on growth conditions // Krist. und. Techn. 1976. Vol. 11, N. 4. P. 373–381.

7. *Zelenyuk M. S., Susla A. I., Guyvan H. M.* et all. The influence of an external electric field and uniaxial pressure on the dielectric properties of TGS crystals doped with metallic impurities of Cu^{2+} // XIV Intrnational Young Scientists' Conference on Applied Physics. – K.: Taras Shevchenko National University of Kyiv. 2014. P. 89–90.

Submitted on 10.11.14

Зеленюк М. С., асп., Сусла А. І., пров. інж., Гуйван Г. М., канд. фіз.-мат. наук, доц.
Сливка О. Г., д-р фіз.-мат. наук, проф., Кедюлич В. М., канд. фіз.-мат. наук, доц.
фізичний факультет, ДВНЗ "УжНУ", Ужгород, Україна

ВПЛИВ ОДНОВІСНОГО ТИСКУ НА ФАЗОВИЙ ПЕРЕХІД В КРИСТАЛАХ ТГС, ЛЕГОВАНИХ МЕТАЛІЧНИМИ ДОМІШКАМИ Cr^{3+}

Представлено результати експериментальних досліджень впливу одновісного тиску на діелектричні властивості кристалів ТГС, легованих металічними домішками Cr^{3+}, в околі сегнетоелектричного структурного фазового переходу. Побудовано фазову σ_2,T-діаграму і визначено баричний коефіцієнт зсуву температури фазового переходу даного кристалу.

Ключові слова: *сегнетоелектрики, фазовий перехід, ТГС, металічні домішки, одновісний тиск, діелектрична проникність.*

Зеленюк М. С., асп., Сусла А. И., вед. инж., Гуйван А. М., канд. физ.-мат. наук, доц..
Сливка А. Г., д-р физ.-мат. наук, проф., Кедюлич В. М., канд. физ.-мат. наук, доц.
физический факультет, ГВНЗ "УжНУ", Ужгород, Украина

ВЛИЯНИЕ ОДНООСНОГО ДАВЛЕНИЯ НА ФАЗОВЫЙ ПЕРЕХОД В КРИСТАЛЛАХ ТГС, ЛЕГИРОВАННЫХ МЕТАЛЛИЧЕСКИМИ ПРИМЕСЯМИ Cr^{3+}

Представлено результаты экспериментальных исследований влияния одноосного давления на диэлектрические свойства кристаллов ТГС, легированных металлическими примесями Cr^{3+}, в окрестности сегнетоэлектрического структурного фазового перехода. Построено фазовую σ_2,T-диаграмму и определено барический коэффициент сдвига температуры фазового перехода данного кристалла.

Ключевые слова: *сегнетоэлектрики, фазовый переход, ТГС, металлические примеси, одноосное давление, диэлектрическая проницаемость.*

UDC 621.315.592

L. Ishchuk, Ph.D., S. Pavlyuk, Ph.D., O. Zubrikova, Stud.,
Department of Electrophysics,
A. Paltsev, Stud.,
Department of Physical Electronics
Faculty of Radiophysics, Electronics and Computer Systems,
National Taras Shevchenko University of Kyiv

FILM THICKNESS DETERMINATION FROM ITO REFLECTION SPECTRA OF INFRARED RADIATION

Determining the thickness of transparent film deposited on transparent substrate causes difficulties because the common optical methods are unsuitable. In this paper, the film thickness was determined from the plasma wavelength obtained from infrared reflection spectra. Matching results obtained with profilometer method confirms the possibility of both methods of thickness measurement for ITO thin films. Their relationship with the mechanical properties of film deposition system simplifies the definition of film thickness.

Key words: *transparent film, thickness measurement, profilometer, reflection spectrum, plasma wavelength.*

Introduction. Due to its unique combination of properties (high conductivity, light reflection in the near infrared (IR) spectrum and transparency in the visible spectrum), indium tin oxide (ITO) has wide application (see., eg [1,8]).

In the process of device miniaturization also reduces film thickness, resulting in increased current density that flows through the ITO films. This leads to considerable Joule heating of the film. This heating can significantly change the electrical and optical properties of the films [3, 5]. In this regard, for predicting the reliability of the devices containing the ITO film, it is important to know the cross-sectional area of the film, which includes the film thickness. Because of the small size of devices direct measurements of the film thickness are impossible.

The article offers a contactless method for determining of the film thickness by the number of magnetron turns in their deposition, calibrated in thickness by two independent methods – IR reflectance spectra and by profilometer.

Method of determination of the film thickness from reflectance spectra of IR radiation. It is known [1], that ITO films have a high reflectance in the near IR spectrum. At the same time, in the visible spectrum reflectance is practically zero. The wavelength λ_p, when the reflection becomes dominant, known as plasma wavelength. Plasma wavelength depends on the concentration of charge carriers. According to the classical theory [4], it is associated with concentration as

$$\lambda_p = \frac{2\pi c}{e}\sqrt{\frac{\varepsilon_0 \varepsilon m^*}{n}}, \qquad (1)$$

where c is the speed of light in vacuum, e is electron charge, ε_0 is dielectric constant, $\varepsilon = 4$ is permittivity of the ITO material, $m^* = 0,29m_e$ is the effective mass of the electrons in it [1], m_e is electron mass. Defining the plasma wavelength λ_p from reflectance spectrum, we can calculate the concentration of electrons in the film by the formula (1).

The mobility of the charge carriers μ and their concentration n are usually determined from measurements of the Hall effect [6]. If a weak magnetic field condition, μ and n can be determined from a Hall measurement as

$$\mu = \frac{l}{b}\cdot\frac{U_H}{U\cdot B}, \qquad (2)$$

$$n = \frac{1}{ed}\cdot\frac{JB}{U_H}, \qquad (3)$$

where l and b are the length and width of the sample, respectively, U is a voltage drop on it, U_H is Hall electromotive force (emf), J is the current flowing in the film, B is magnetic field. From (2) and (3) is obviously, that knowing planar dimensions, the mobility can be determined directly from the Hall effect measurements (2), and to determine their concentration n we need to know the thickness of the film d.

Thus, defining the carrier concentration independently with the formula (3) the film thickness d can be calculated.

Samples. ITO films were fabricated by magnetron sputtering [7]. The target of In-Sn alloy was sputtered in a mixture of argon and oxygen. The content of tin in the target ranged from 0 to 30%. Pressure of gas mixture was p = 0,57 Pa, and the partial pressure of oxygen p_{O_2} was chosen in a such way that the value p_{O_2}/p was

© Ishchuk L., Pavlyuk S., Zubrikova O., Paltsev A., 2015

0,085 ± 5%, thus ensuring approximation electrical and optical parameters of the films to actually used in engineering applications [2].

Films were deposited on substrates of chemically pure glass with dimensions 2cm×2cm×0,05cm at room temperature, covering the entire surface of substrate.

The thickness of the films in the deposition process was measured relatively. Magnetron was placed in a cylindrical chamber, and the cassettes with substrates were fixed on the inner wall of the chamber. In the process of deposition magnetron turned around a vertical axis several times, passing over each of the substrates. The number N of such turns was calculated. In samples under investigation this number was ranged from 3 to 15. Film uniformity of some samples was examined by probe method [5].

Plasma wavelength definition. IR reflectance spectra were measured by IKS-20 spectrometer. First of all, the spectra calibration was performed, i.e. registration of mirror reflectance spectrum. Mirror is a surface that is in the range of wavelengths used shows the reflectance $R_m \approx 1$. Separately recorded the reflection spectrum of the substrate R_s.

The radiation falls on the film normally to the surface (Fig. 1).

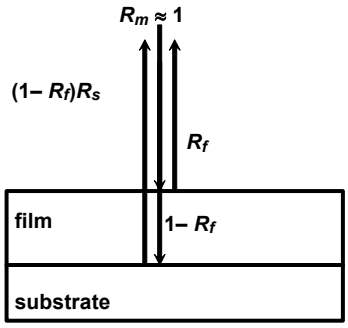

Fig. 1. Schematic drawing of the IR rays passing in the film under investigation

We assume that the intensity of radiation falling on the film surface is 1, the outer surface reflectance of the film is R_f, the substrate reflectance is R_s. Then on the interface between the film and the substrate falls the ray intensity $1-R_f$, will be reflected $(1-R_f)R_s$, and the spectrometer will register the signal intensity $R = R_f + (1-R_f)R_s$, consisting of the signal reflected by film (first term), and the signal reflected on the boundary of the film and the substrate (second term). Then for each wavelength of the spectrum the film itself reflectance will be determined as

$$R_f = \frac{R - R_s}{1 - R_s}. \qquad (4)$$

IR reflection spectrum calculated by such algorithm (4) for the film, containing 91% In + 9% Sn, and was received at the ratio of pressure p_{O_2}/p =0.085, is shown on Fig. 2. Number of turns of the magnetron was N =5.

Then by formula (1) the concentration of charge carriers n in the films was determined, and by formula (3) their thicknesses d were calculated. The film thickness vs the number of magnetron turns dependence received by the proposed method are shown in Fig. 3 with empty circles.

IR radiation reflection spectra obtained for the films of other composition and of other thicknesses qualitatively coincide with illustrated in Fig. 2. Quantitative differences were associated with different concentrations of electrons in them.

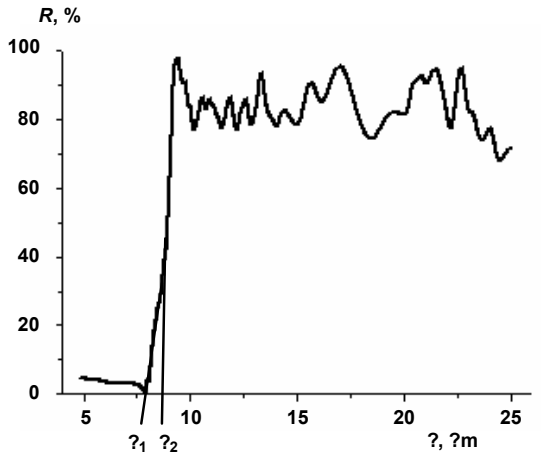

Fig. 2. IR reflection spectrum of the ITO film, and an illustration of the determination of plasma wavelength

Plasma wavelength was determined for reasons that when $\lambda \geq \lambda_p$ the reflection of electromagnetic waves becomes predominant. Since the transition to reflection looks like indistinct step, to determine λ_p on the spectrum we approximated areas with the lowest and highest rates of growth to the wavelength axis, finding λ_1 and λ_2, respectively. Then $\lambda_p = (\lambda_1 + \lambda_2)/2$. For the spectrum shown in Fig. 2 λ_1=7.88 μm, λ_2 =8.46 μm, so λ_p =8.17 μm. Measurement error for this method was (3…5)% for different samples.

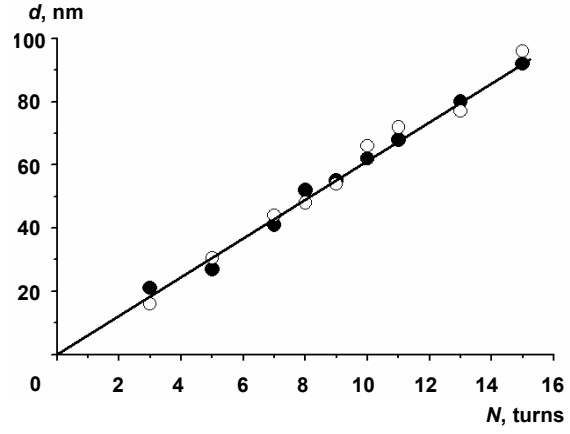

Fig. 3. The film thickness vs the number of magnetron turns dependence received from the spectra of IR radiation reflection (empty circles) and by profilometer (black circles)

To confirm the validity of the proposed method an independent measurements of film thickness were made by profilometer of 296 industrial model. The results are shown in Fig. 3 with black circles. The results obtained with both methods agree well.

Conclusion. The paper presents an alternative non-contact method of the film thickness determining, based on the determination of plasma wavelength from the IR radiation reflectance spectra. A reconciliation of the results obtained by this method with measurements of thickness using profilometer confirms the viability of the proposed

method. Matching the results of two independent methods simplifies determining of the thickness reducing it to counting the number of magnetron turns and using the calibration dependence $d(N)$.

REFERENCE

1. *Dawar A. L.* Review. Semiconducting transparent films: Their properties and aplications. / A. L. Dawar, J. C. Joshi // J.Mat.Sci. – 1984. – V.19, № 1. – P.1–23.
2. *Demchishin A. V.* Electrofizicheskie i opticheskie kharakteristiki prozrachnykh provodyashchikh plenok legirovannogo olovom oksida indiya/ A. V. *Demchishin*, V. N.Dobrovolsky, L. V. Ishchuk et al //Trudy 2 Vsesoyuznoy konferencii "Materialovedenie khalkogenidnykh i kislorodosoderzhashchikh poluprovodnikov". – V.1. – Chernovtsy. – 1986. – P. 205.
3. *Dobrovolsky V. N.* Change of In_2O_3(Sn) film properties with the current of extremely high density / V. N.Dobrovolsky, L. V. Ishchuk, A. G. Gontar, G. K. Ninidze // Physics of Electronic Materials PHYEM'02: international conference, October 1–4, 2002, Kaluga, Russia: abstracts. – Kaluga. – 2002. – P. 58–59.
4. *Fistul V. I.* Silno legirovannye poluprovodniki / V. I. *Fistul*. – Moskwa: Nauka, 1967. – 415 p.
5. *Ishchuk I. V.* The roughness of substrate influence on ITO films conductivity / L. V. Ishchuk, S. O. Kostiuchenko, S. P. Pavlyuk// XV International young scientists' conference on applied physics, june 10–13, 2015, Kyiv, Ukraine: abstracts. – Kyiv. – 2015. – P. 80–81.
6. *Kuchis E. V.* Metody issledovaniya effekta Holla / E. V. *Kuchis*. – Moskwa: Sov.radio, 1974. – 328 p.
7. *Schiller S.* Use of the ring gap plasmatron for high rate sputtering / S. Schiller, U. Heisig, K. Goedicke // Thin Solid Films. – 1977. – V.40, №4. – P. 327–334.
8. *Vaufrey D.* ITO-on-top organic light-emitting devices: a correlated study of opto-electronic and structural characteristics / D. Vaufrey, M. Ben Khalifa, J. Tardy // Semicond. Sci. Technol. – 2003. – V.18, N4. – P. 253–260

Submitted on 01.07.15

Іщук Л., канд. фіз.-мат. наук, Павлюк С., канд. фіз.-мат. наук,
Зубрікова О., студ., каф. електрофізики,
Пальцев А., студ., каф. фізичної електроніки
факультет радіофізики, електроніки та комп'ютерних систем
Київський національний університет імені Тараса Шевченка

ВИЗНАЧЕННЯ ТОВЩИНИ ПЛІВОК ІТО ЗА СПЕКТРАМИ ВІДБИТТЯ ІНФРАЧЕРВОНОГО ВИПРОМІНЕННЯ

Визначення товщини прозорої плівки, нанесеної на прозору підкладку, викликає труднощі, тому що найбільш поширені оптичні методи виявились непридатними. У цій статті товщина плівки була визначена за плазмовою довжиною хвилі, отриманої зі спектрів відбиття інфрачервоного випромінення. Узгодження отриманих результатів із отриманими методом профілометрії підтверджує можливість використання обох методів вимірювання товщини для тонких плівок ІТО. Їхній зв'язок з механічними властивостями системи осадження плівки спрощує визначення її товщини.

Ключові слова: *прозора плівка, вимірювання товщини, профілометр, спектр відбиття, плазмова довжина хвилі.*

Ищук Л., канд. физ.-мат. наук, Павлюк С., канд. физ.-мат. наук,
Зубрикова О., студ., каф. электрофизики,
Пальцев А., студ., каф. физической электроники
факультет радиофизики, электроники и компьютерных систем
Киевский национальный университет имени Тараса Шевченко

ОПРЕДЕЛЕНИЕ ТОЛЩИНЫ ПЛЕНОК ПО СПЕКТРАМ ОТРАЖЕНИЯ ИНФРАКРАСНОГО ИЗЛУЧЕНИЯ

Определение толщины прозрачной пленки, нанесенной на прозрачную подложку, вызывает трудности, так как наиболее распространенные оптические методы оказались непригодными. В этой статье толщина пленки была определена по плазменной длиной волны, полученной из спектров отражения инфракрасного излучения. Согласование полученных результатов с полученными методом профилометрии подтверждает возможность использования обоих методов измерения толщины для тонких пленок ІТО. Их связь с механическими свойствами системы осаждения пленки упрощает определение ее толщины.

Ключевые слова: *прозрачная пленка, измерения толщины, профилометрия спектр отражения, плазменная длина волны*

UDC 535.373, 538.958

A. Karlash, Ph.D.
Department Electrophysics,
Faculty of Radiophysics, Electronics and Computer Systems
Taras Shevchenko National University of Kyiv

LUMINESCENT NANOCOMPOSITES BASED ON NANOSILICON IN SILICA AEROGEL MATRIX

Optical and photoluminescent properties of nc-Si/ar-SiOx nanocomposites have been investigated using FTIR spectroscopy and PL lifetime spectroscopy. Powdered silica aerogel was prepared from sodium silicate water solution using sol-gel technique. Nanocomposites were produced by pressing the mixture of the silica aerogel powder with the nanocrystalline silicon powder into pellets. The intensive photoluminescence was observed with two stipulated peaks at short-wave (at around 400 nm with maxima at 475, 556 and 596 nm due to the aerogel photoemission) and long-wave (at around 630 nm with the maxima at 610, 630 and 660 nm caused by the emission processes in nanosilicon) regions. Variation of the component ratio in composite material allows the modulation of the intensity ratio at maximum and get a different color range when using these materials as phosphors. Storage at ambient conditions caused the PL peak intensity increasing by 6 times at 1 month aging and about 20 times at 2 months aging. Such effects are explained in terms of both surface passivation and carrier confinement in silicon nanocrystals. Process of nc-Si oxidation is accompanied by suppressing of non-radiative recombination channels.

Key words: *powdered silica aerogel, nanosilicon, defect states, FTIR transmission spectroscopy, PL lifetime spectroscopy.*

Introduction. During last decades the porous silicon and silicon nanoparticles have been considered as promising materials for LED construction due to the high luminescence yield in visible region [6]. The first estimation showed that photoluminescence (PL) quantum yield can achieve more than 10% [19] and the electroluminescence with much lower quantum yield was observed too [8]. Now the production of efficient silicon photodetectors is rather technological task than the research subject. However, the nanosilicon have been observed to degrade during aging in ambient atmosphere or under UV illumination due to progressive oxidation of its large internal surface [20]. The passivation of nanosilicon surface is absolutely necessary to prevent the non-radiative recombination channels (*e.g.* trapping by surface states) and the PL degradation due to chemical evolution of nanosilicon surface. Different approaches have been proposed in order to stabilize the nc-Si luminescence: Si ion implantation into SiO_2 substrate [22], LPCVD deposition of non-stoichiometric SiO_x ($1<x<2$) with subsequent thermal annealing precipitation [3], surface modification and covering of PS surface [4]. The creation of nc-Si/SiO_x nanocomposites by different

© Karlash A., 2015

methods [1, 23] allowed obtaining Si nanoparticles embedded into the dielectric envelope preventing the oxidation processes.

Different composite materials have been used like phosphorescent materials, photodetectors, catalysts, lasers and sensors [15, 17, 18]. There has been resent interest in the study of the properties of silica aerogel powders [11] and silica aerogel-nc-Si composites that also demonstrate intense luminescence in the visible region [1, 13]. Silica aerogel (ar-SiO_x) demonstrates a strong visible PL in the blue–green region [2].

In this work we have investigated the evolution of PL spectra of nc-Si/ar-SiO_x nanocomposites with the different nc-Si – ar-SiO_x concentration ratio. Nanocomposites were produced by pressing the mixture of the silica aerogel powder with the nanocrystalline silicon powder into pellets [13, 14]. The considered nanoporous materials are simple and inexpensive in preparation.

Experiment. Powdered silica aerogel ar-SiO_x was prepared from sodium silicate water solution and ethanol-based catalyst [13]. The drying process was carried out in an autoclave at supercritical parameters (T=240°C and $p=8\cdot10^6$ Pa) in the presence of ethanol. These conditions are maintained for a short time with subsequent slow pressure reduction down to athmospheric pressure. As prepared material was then annealed at 450°C at oxygen athmosphere. In our earlier work [1] it was observed using X-ray difraction analyses that porous aerogel ar-SiO_x is the mixture of amorphous and crystal phases that consists of crystobalite and quartz.

Nanocrystalline silicon (nc-Si) powder was produced by electrochemical etching of p-Si plates in $HF:C_2H_5OH:H_2O$ electrolyte at constant current mode of 50 $mAcm^{-2}$ during 2,5 hours. Porous powder was then rinsed in ethanol, dried in air and thoroughly grated. The final product were characterized to be the silicon nanocrystallites surrounded by the porous silicon shell with the mean diameters of (2–3) nm [14]. Their porosity was about 60–70%.

FTIR measurements were carried out using Fourier spectrometer "Perkin-Elmer Spectrum BX" in the range of 400–4000 cm^{-1} with 4 cm^{-1} resolution.

The samples used for PL measurements were prepared by pressing the mixture on nc-Si and ar-SiO_x powders with the different nc-Si – ar-SiO_x concentration ratio into pellets with diameter of about 12 mm and typical thickness of 0,2÷0,3 mm at a pressure of 10 MPa and 18 MPa. Fig. 1 shows the image of nanocomposite surface obtained using AFM.

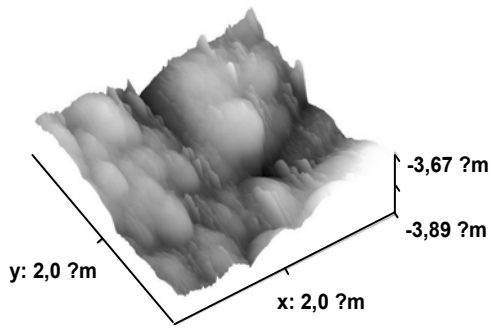

Fig. 1. FM image of nc-Si/ar-SiO_x nanocomposite: the surface morphology

The temporal domain PL spectra were measured at the room temperature using the analogous registration scheme [4]. The samples were excited with nitrogen laser pulses at 337 nm (3.68 eV), repetition rate 100 Hz, pulse duration τ=8 ns and average power 20 mW. The proper band of emission was selected by a monochromator (MS2004, SOLAR TII) and registered by a combination of photomultiplier (HAMAMATSU C6270) and analog-to-digital board (up to 1 GHz sample rate). The signal was processed and analyzed by PC.

FTIR spectroscopy. Fig. 2 shows the FTIR transmittance spectrum of nc-Si/ar-SiO_x(1:50) nanocomposite. The presence of rocking (467 cm^{-1}), bending (796 cm^{-1}) and stretching LO (1160 cm^{-1}) and TO (1076 cm^{-1}) bands of silicon oxide have been revealed [9]. Keeping at ambient conditions even for a short time leads to partial oxidation of silicon nanocrystals, that's why we almost don't observe the presence of Si-H groups in the FTIR spectrum of nc-Si/ar-SiO_x sample. The absorption peak at 600 cm^{-1} corresponds to volume Si-Si bonds in silicon nanocrystallites [9]. The contribution of absorbed water and surface OH groups have also been revealed in the spectral region of 3000–3700 cm^{-1} with the maximum at 3466 cm^{-1} (O-H stretching vibration modes and adsorbed water) as well as at 1687 cm^{-1} (O-H bending vibration modes). Two shoulders at 3600 and 950 cm^{-1} associated with Si-OH vibration modes [9].

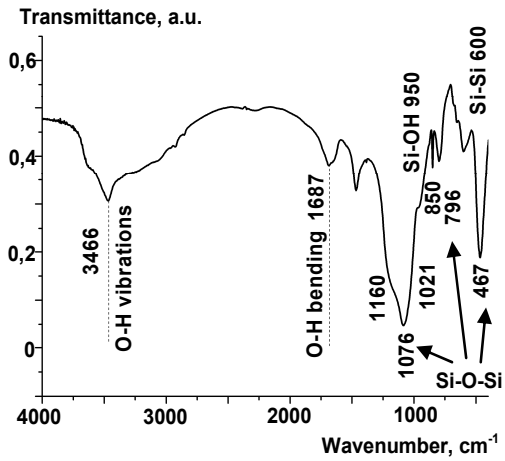

Fig. 2. FTIR transmittance spectrum \ of nc-Si/ar-SiO_x nanocomposite, correlated by KBr spectrum. Characteristic absorbing modes are indicated

As a result, the FTIR transmittance spectra revealed that in the considered aerogel processing from water solution the internal surface of nc-Si/ar-SiO_x nanocomposite is almost fully covered with hydroxyl groups, that play the dominant role in the oxidation processes at a humid atmosphere.

PL spectroscopy. The photoluminescence was studied for the samples with the different ratio of silica aerogel and nc-Si (Fig. 3a). There are two clearly separated luminescent bands: band at around 400 nm with maxima at 475, 556 and 596 nm due to the aerogel photoemission, and band at around 630 nm with the maxima at 610, 630 and 660 nm caused by the emission processes in nanosilicon. The variation of component ratio in composite material allows the modulation of the intensity ratio at maximum and get a different color range when using these materials as phosphors (Fig. 3, b,c).

Maximum PL for porous Si is observed at 650 nm, and is usually attributed by band-to-band recombination in Si nanoparticles of 2–3 nm diameters [7]. The XRD spectrum of nc-Si/arSiO_x composite presented in our early work [14] reveals diffraction peaks of nanocrystalline Si. The average Si crystallite sizes were roughly estimated from these

diffraction peaks and the wide size distribution was revealed in the range <9 nm.

In [14] the fractal model of silicon nanocrystals embedded into silica aerogel matrix was proposed. According to this model, the PL emission band of nanosilicon stipulated by the exciton recombination in silicon crystallite involving surface states formed due to the interaction with the oxide matrix.

The comparing PL of pure components displays that emission yield in porous Si at least one order is stronger than that of silica aerogel. Silica aerogel displays wide PL spectra that can be fitted by Gauss components at 380, 410, 490, 570 and 660 nm. All PL peaks appear well below the band gap of stoichiometric SiO_2 (8.2 eV) [13]. However, the band gap of non-stoichiometric SiO_x is less and spreads up to 1.1 eV when x=0. It means that emission of aerogel is attributed ether to non-stoichiometric structure SiO_x (1<x<2) or to defects or surface states.

The structure of material and defect states are determined by preparation technology (temperature during the process of gel formation, concentration of reagents, pH level, etc.) [2, 10, 12].

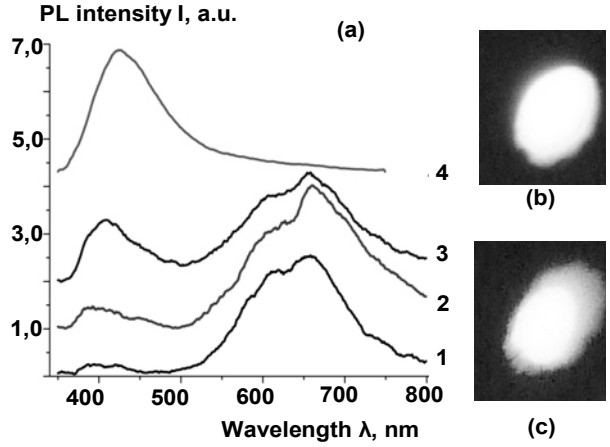

Fig. 3. (a) PL spectra of nc-Si/ar-SiO_x nanocomposites with nc-Si: ar-SiO_x concentration ratio: 1 – 0:1 (pure nc-Si); 2 – 3:2; 3 – 5:1; 4 – 1:0 (pure aerogel). Photos of light emission of the pressed samples: (b) – ar-SiO_x (blue) and (c) – nc-Si/ar-SiO_x (orange) under excitation by pulsed nitrogen laser (λ=337 nm)

Silica aerogels have several types of microstructural defects that can give contribution to the photoemission [2]. If PL excitation energy is 3.68 eV (nitrogen laser), the contribution to the photoemission of stoichiometric SiO_2 phase can produce only defects determined by the interaction within individual SiO_x tetrahedra. These include defects with dangling bonds: 1) non-bounded oxygen hole center (NBOHC), which is described as follows: $\equiv Si - O\bullet$ where the dot means the unpaired electron; 2) peroxide radicals (POR) $\equiv Si - O_2\bullet$ and 3) oxygen-deficient centers (ODC) which include oxygen vacancies and divacancies and two-coordinate silicon (ODC(II)) [21].

Fig.4 shows the evolution of PL spectra for nc-Si/ar-SiO_x composites during storage at ambient conditions for a week. Samples were formed at different pressure (10 MPa and 18 MPa), the relative concentration of nanosilicon in composite was 2% (ncSi:ar-SiO_x = 1:50). Analyzing the obtained data, we can conclude that in both samples the long-wave PL band intensity increases under oxidation at ambient atmosphere. As mentioned above, this peak corresponds to the radiative recombination transitions in silicon nanoclusters. At the same time, the short-wave PL band intensity is significantly reduced in aged samples. It should be noted that these effects are more pronounced for the sample formed at higher pressure.

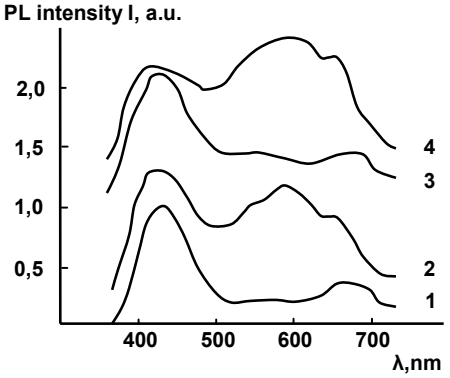

Fig. 4. The evolution of the PL spectra of nc-Si/ar-SiO_x nanocomposites with comcentration ratio 1:50 under oxidation at ambient conditions: sample formed at pressure of 10MPa freshly prepared (1) and after 7 days aging (2); sample formed at pressure of 18MPa freshly prepared (3) and after 7 days aging (4)

The dependence of PL from external factors (external pressure) or from the variation of the nc-Si chemistry (oxidation) is naturally accounted for by surface states changes [5] and size reduction. Indeed, the same effect of nanocomposite spectra evolution is observed during the aging in ambient atmosphere.

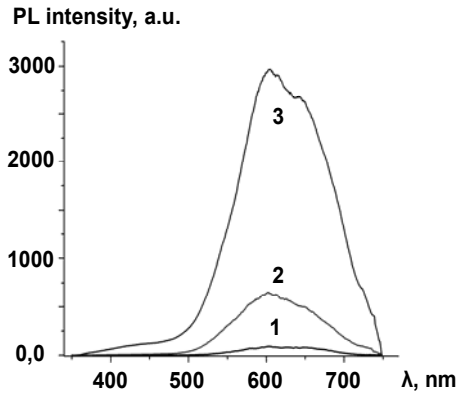

Fig. 5 The evolution of integrated PL spectra under process of aging at ambient conditions for nc-Si/ar-SiO_x sample: 1 – freshly prepared sample and after aging during: 2 – 1 month; 3 – 2 months

Fig. 5 demonstrates the PL spectra of the nc-Si/SiO_x sample pressed under 10 MPa as prepared and aged during 1 and 2 months. The PL peak intensity increases by 6 times at 1 month aging and about 20 times at 2 months aging. Such PL behavior is typical for PS: keeping in ambient air results in emission blue shifting, however, the PL intensity canboth increases and decreases [5, 16]. Such effects are explained in terms of both surface passivation and carrier confinement. Among reasons we can note the subsequent nc-Si oxidation due to both solid-solid interaction with hydroxyl terminated silica aerogel (the last is very clearly detected in FTIR spectra of aerogel [13]) and reactions with atmospheric oxygen and water: $Si+O_2 \rightarrow SiO_2$ or $Si+2H_2O \rightarrow SiO_2+H_2$. Process of nc-Si oxidation is accompanied by suppressing of non-radiative recombination channels.

Conclusions. In this work we have investigated the photoluminescent properties of nc-Si/ar-SiO_x nanocomposites with the different nc-Si – ar-SiO_x concentration ratio. Nanocomposites were produced by pressing the mixture of the silica aerogel powder with the nanocrystalline silicon powder into pellets

The FTIR transmittance spectra revealed that in the considered aerogel processing from water solution the internal surface of nc-Si/ar-SiO_x nanocomposite is almost fully covered with hydroxyl groups, that play the dominant role in the oxidation processes at a humid atmosphere.

The intensive photoluminescence was observed with two stipulated peaks at short-wave (blue) and long-wave (orange) regions. The variation of component ratio in composite material allows the modulation of the intensity ratio at maximum and get a different color range when using these materials as phosphors.

Storage at ambient conditions caused the PL peak intensity increasing by 6 times at 1 month aging and about 20 times at 2 months aging. Such effects are explained in terms of both surface passivation and carrier confinement. Process of nc-Si oxidation is accompanied by suppressing of non-radiative recombination channels.

REFERENCE

1. *Amonkosolpan J.* Porous silicon nanocrystals in a silica aerogel matrix / Amonkosolpan, J.; Wolverson, D.; Goller, B. et al.// 2012, Nanoscale Research Letters. – Vol.7. – 397p.
2. *Ayers M.* Visibly photoluminescent silica aerogels / Ayers, M.; Hunt, A. // 1997, J. Non-Cryst. Solids. – Vol.217. – 229–235 p.
3. *Baron T.* Silicon quantum dot nucleation on Si_3N_4, SiO_2 and SiOxNy substrates for nanoelectronic devices/ Baron T., Martin F., Mur P.// 2000, J. Cryst. Growth. – Vol.209. – 1004–1008 p.
4. *Benilov A.* Influence of pH solution on photoluminescence of porous silicon / Benilov, A., Gavrilchenko, I.; Benilova, I. et al.// 2007, Sens. Act. A.- Vol.137. – 345–349 p..
5. *Bisi O.* Porous silicon: a quantum sponge structure for silicon based optoelectronics/ Bisi O., Ossicini S., Pavesi L.// 2000, Surface Sci.Reports.- Vol. 38. – 1–126 p.
6. *Canham. L. T.* Properties of porous silicon /Ed. by Canham. L. T. 1997. – Malvern: Emis Series 18. – 405 p.
7. *Fauchet P. M.* The Strong Visible Luminescence in Porous Silicon: Quantum Confinement, not Oxide-Related Defects / Fauchet P. M., von Behren J.// 1997, Phys. Stat. Sol. B. - Vol.204(1). – R7–R8 p.
8. *Gelloz B.* Highly Enhanced Efficiency and Stability of Photo- and Electro-luminescence of Nano-crystalline Porous Silicon by High-Pressure Water Vapor Annealing/ Gelloz B., Koshida N.// 2006, Jpn. J. Appl. Phys. Part 1. – Vol.45. – 34–62 p.
9. Handbook of infrared spectroscopy of ultrathin films / Ed. by Tolstoy, V.; Chernyshova, I.; Skryshevsky, V. – N.J.: Willey, 2003.
10. *Hinić I.* Influence of the synthesis conditions on the photoluminescence of silica gels / Hinić, I.; Stanišić, G.; Popović, Z.// 2003, J. of Serb. Chem. Soc. – Vol. 68(12). – 953–959 p.
11. Hong Sung Ki, Yoon Mi Young, Hwang Hae Jin, J. Ceram. Process Res 13(1). – 2012 – 145–148 p.
12. *Inaki, Y.* Active Sites on Mesoporous and Amorphous Silica Materials and Their Photocatalytic Activity: An Investigation by FTIR, ESR, VUV−UV and Photoluminescence Spectroscopies / Inaki, Y.; Yoshida, H.; Yoshida, T. et al.// 2002, J. Phys.Chem. B. – Vol. 106(35). – 9098–9106 p.
13. *Karlash A.* Photoluminescence properties of silica aerogel/porous silicon nanocomposites / Karlash A.; Zakharko Yu.; Skryshevsky V. et al.// 2010, J. Phys. D: Appl. Phys. – Vol.48. – 335–405 p.
14. *Karlash A.* Evolution of visible photoluminescence of Si quantum dots embedded in silicon oxide matrix / Karlash, A.; Skryshevsky, V.; Kuznetsov, G. et al.// 2013, J. of Alloys and Compounds.. – Vol. 577. – 283–287 p.
15. *Koch C. C.* Nanostructured materials: Prosessing Properties and Applications, William Andrew Inc., Norwich, NY,2007.
16. *Maruyama T.* Photoluminescence of porous silicon exposed to ambient air/ Maruyama T., Ohtani S.// 1994, Appl. Phys. Lett. – Vol. 65. – 1346 p.
17. *Moshnikov V.* Hierarchical nanostructured semiconductor porous materials for gas sensors / Moshnikov, V.; Gracheva, I.; Kuznezov, V. et al.// 2010, J. of Non-Cryst. Solids. – Vol.356(37–40). – 2020–2025 p.
18. *Pavezi L.* Optical gain in silicon nanocrystals. / Pavezi, L.; Dal Negro, L.; Mazzoleni, C. et al.// 2000, Nature. – Vol.408. – 440–444 p.
19. *Skryshevsky V. A.* Evaluation of quantum efficiency of porous silicon photoluminescence/ Skryshevsky V. A., Laugier A., Strikha V. I. et al.// 1996, Materials Science and Engineering B. – Vol.40. – 54–57 p.
20. *Skryshevsky V. A.* Photoluminescence of inhomogeneous porous silicon at gas adsorption// 2000, Appl. Surf. Sci. – Vol.157(3). – 145–150 p.
21. *Skuja L.* Optically active oxygen-deficiency-related centers in amorphous silicon dioxide// 1998, J. of Non-Cryst. Solids. – Vol. 239. – 16–48
22. *Tsutomu Shimizu-Iwayama*. Visible photoluminescence from silicon nanocrystals formed in silicon dioxide by ion implantation and thermal processing/ Tsutomu Shimizu-Iwayama, Yoichi Terao, Atsushi Kamiy, et al.// 1996, Thin Solid Films. – Vol. 276.– 104–107 p.
23. *Wang Y. Q.* Getting high-efficiency photoluminescence from Si nanocrystals in SiO_2 matrix/ Wang Y. Q., Kong G. L., Chen W. D. et al.// 2002, Appl. Phys. Lett. – Vol. 81. – 417–441 p.

Submitted on 15.06.2015

Карлаш А. , канд. фіз.-мат. наук
каф. електрофізики, Факультет радіофізики, електроніки та комп'ютерних систем
Київський національний університет імені Тараса Шевченка

ЛЮМІНЕСЦЕНТНІ НАНОКМПОЗИТИ НА ОСНОВІ НАНОКРЕМНІЮ В МАТРИЦІ АЕРОГЕЛЮ КРЕМНЕЗЕМУ

Проведено дослідження оптичних та фотолюмінесцентних властивостей нанокомпозитів nc-Si/ar-SiOx з використанням FTIR спектроскопії пропускання та фотолюмінесцентної спектроскопії. Порошкоподібний аерогель кремнезему було виготовлено на основі водного розчину силікату з використанням технології золь-гель синтезу. Нанокомпозити виготовлено шляхом пресування у вигляді пігулок суміші порошків аерогелю кремнезему та нанокристалічного кремнію. Виявлено інтенсивну фотолюмінесценцію зразків у видимій області спектру з двома основними максимумами: короткохвильовим (біля 400 нм з піками при 475, 556 та 596 нм), обумовленим емісією аерогелю, та довгохвильовим (біля 630 нм з піками при 610, 630 та 660 нм), який виникає внаслідок рекомбінаційних переходів у нанокремнії. Показано, що зміна відносного вмісту компонент в композиті дозволяє модулювати інтенсивність в максимумах фотолюмінесценції, отримуючи при цьому різну кольорову гаму при використанні цих композитів в якості люмінофорів. Витримка композитів nc-Si/ar-SiOx в атмосферних умовах призводить до зростання інтенсивності фотолюмінесценції у 6 разів після витримки протягом 1 місяця та у 20 разів після витримки протягом 2 місяців. Процеси окиснення нанокремнію в композитах nc-Si/ar-SiOx супроводжуються пригніченням каналів безвипромінювальної рекомбінації.

Ключові слова: *порошкоподібний аерогель кремнезему, нанокремній, дефектні стани, FTIR спектроскопія пропускання, фотолюмінесценція.*

Карлаш А., канд. физ.-мат. наук
каф. электрофизики, Факультет радиофизики, электроники и компьютерных систем
Киевський национальный университет имени Тараса Шевченко

ЛЮМИНЕСЦЕНТНЫЕ НАНОКОМПОЗИТЫ НА ОСНОВЕ НАНОКРЕМНИЯ В МАТРИЦЕ АЭРОГЕЛЯ КРЕМНЕЗЕМА

Проведено исследование оптических и фотолюминесцентных свойств нанокомпозитов nc-Si/ar-SiOx с использованием FTIR спектроскопии и фотолюминесцентной спектроскопии. Порошкообразный аэрогель кремнезема изготовлен на основе водного раствора силиката с использованием технологии золь-гель синтеза. Нанокомпозиты изготовлены путем прессования в виде таблеток смеси порошков аэрогеля кремнезема и нанокремния. Обнаружена интенсивная фотолюминесценция образцов в видимой области спектра с выраженными максимумами: коротковолновым (около 400 нм с пиками при 475, 556 и 596 нм), обусловленным эмиссией аэрогеля, и длинноволновым (около 630 нм с пиками при 610, 630 и 660 нм), который возникает вследствие рекомбинационных переходов в нанокремнии. Показано, что изменение относительной концентрации компонент в композитном образце позволяет модулировать интенсивность в максимумах фотолюминесценции при использовании исследуемых образцов в качестве люминофоров. Выдержка композитов nc-Si/ar-SiOx при атмосферных условиях приводит к увеличению интенсивности фотолюминесценции в 6 раз после выдержки в течение 1 месяца и в 20 раз после выдержки в атмосферных условиях в течение 2 месяцев. Процессы окисления нанокремния в композитных образцах сопровождаются пассивацией каналов безизлучательной рекомбинации.

Ключевые слова: *порошкообразный аэрогель кремнезема, нанокремний, дефектные состояния, FTIR спектроскопия пропускания, фотолюминесценция*

UDC 537.622.4

V. Koronovskyy, Ph.D.
Department Electrophysics, Faculty of Radiophysics,
Taras Shevchenko National University of Kyiv

CAUSED BY EXTERNAL ELECTRIC FIELD THE EFFECT OF THE DOMAIN WALLS POSITIONS CHANGES IN EPITAXIAL FERRITE-GARNET FILMS

By method of polarizing microscopy was investigated by us the effect of changes of the domain walls (DWs) positions of epitaxial ferrite garnet films as reaction to combined connection of alternating and static electric fields. In transmitted light was detected a changing of the magneto-optical signal value in local areas of magnetic domain structure with DW in optically scaned film sites. The value of the mentioned effect essentially depended on a magnetic field which has been enclosed in a plane of the investigated sample.

Key words: *domain wall, magneto-electric effect, electric field, magnetic field.*

Introduction. Ferrite-garnets us the object of intense theoretical and experimental investigations are used for a long time [10]. Garnet crystals, as a ferrimagnetic oxide grown on a GGG (non magnetic garnet) substrates are well known to play an important role in technological devices for example in magneto-optical device components for integrated optics, microwave devices. The large unit cell (12.383 A) and the existence of 3 crystallographic sites for magnetic ions give an enormous freedom for substituting. As is well known, garnets are transparent and magneto-optical observation of the magnetic structures of ferrite-garnets is possible. As is generally true for crystalline materials, the basic physical crystal properties (e.g. optical absorption, Faraday rotation) of ferrite-garnets depend to a considerable extent on its defect structure. So, for example, Bi3+ ions are well known to modify strongly the above-quoted magneto-optical crystal properties. Similar influences can be ascribed to Pb2+ impurities, which are always present in ferrite-garnets as part of the usual crystal growth techniques [4]. Particular attention is paid to domain walls of garnets, (in particular of yttrium-iron-garnets (YIG)) as micromagnetic structural elements of these materials.

As it is known, an external magnetic field, applied to a ferrite-garnet crystal induces in it the optical phenomenon – Faraday effect. High Faraday rotation seems to be a property of most garnets, particularly of rare earth iron garnets [4]. But nowadays, except publications about investigations of the magnetic properties of garnets, there are also publications about manifestations of magneto-electric (ME) effect (MEE) in them [12, 2]. The magneto-electric effect consists in induction of polarization by a magnetic field or magnetization by an electric field and expresses the link between magnetic and electric properties in materials [1]:

$$p_i = \alpha_{ij} H_j \; ; \quad m_j = \alpha_{ij} E_i \; ,$$

where α_{ij} – the ME effect tensor components.

The electronic state of the crystal is modified by the externally applied electric field and the modification is detected by the change of the magnetic moment. The starting point for investigations on an actual crystal was marked by Dzyaloshinskii [3] by the prediction of the effect in the antiferromagnetic Cr_2O_3. In crystals of Cr_2O_3 ME effects are allowed by the magnetic symmetry. After this, Astrov [1] reported the experimental observation of MEE. Linear magneto-electric effect has been observed in many magnetic compounds, including yttrium iron garnet. Higher-order effects, the magnetic moment proportional to the square of the electric field were also discovered experimentally.

The first observation of the ME effect in yttrium-iron-garnets (YIG) was reported by O'Dell [9] and was subsequently studied in a number of papers [12, 2]. MEE is not large in the magnitude in YIG but sensitivity of the magneto-optical response of YIGs to an external field is one of the main properties of interest for imaging applications. One of the high-sensitive experimental methods for the ME phenomena investigation deals with the registration of the changes of light polarization plane Faraday rotation (α_{EMO}) under action of an electric field applied to the crystal (optical polarimetry method). The appearance of such changes has been termed the electromagneto-optical (EMO) effect [8]. EMOE can be interesting from the practical point of view as a basis for creation of optical devices with two channel management on electric and magnetic fields.

Of particular interest are the investigations of the behavior of micromagnetic structures of ferrite-garnets in an electric field by optical methods. In our earlier investigations we used EMO method for investigation of MEE in YIG films [6, 7]. Thus, the basic of our conclusions that magnetization value, which mainly defines the light polarization plane rotations, does not change essentially under the electric field action. At the same time we assumed, that the electric field action leads to a small changing of domain-wall positions or theirs width. But we did not spend direct supervisions of the specified displacements of DW.

In this paper, we report the results of some experimental investigations of the influence of alternating and static electric fields (jointly) to the domain structure (DS) of YIG epitaxial films. Special interest represents investigation of reaction of DWs of the YIG films on electric fields.

Experimental. In our experiments, we used the method of optical polarimetry, which allows us to measure the changes of light polarization plane Faraday rotation under action of an electric field applied to the film (EMOE). The measured parametre is the angle of rotation $\alpha_{EMO.}$ Our experimental setup was composed from a high-sensitive laser polarimeter (with the polarizing microscope) described in details in Refs. 6. When a YIG film was viewed in linearly polarized light it was possible to reveal 180^o DWs because of the magneto-optical Faraday effect (in the presence of the analyzer): the DWs appeared as narrow bright areas (boundaries) between the bright and dark domains. At visual observation of domains by means of a polarising microscope, turning the analyzer concerning a polarizer, it is possible to extinguish completely the monochromatic light which is passing through domains of different polarity. When the polarizer and the analyzer are crossed, magnetic domains have identical colour and DW looks like a dark line.

The investigated YIG films with typical labyrinth domain structure were deposited on the $Gd_3Ga_5O_{12}$ substrates with a thickness of about 600 μm. The typical thickness of the films was about 7 μm, the width of domains was about 15 μm at H=0, and the DWs width was about 0.5 μm. The domain's magnetization was normal to the film plane. A low-frequency alternating electric field ($E_{\sim}$) with frequency of 1000 Hz was applied to the sample. The investigated sample was placed between two optically transparent electrodes and one of the electrodes was placed on the

© Koronovskyy V., 2015

YIG film surface and the other one was placed under the substrate. The electrodes were deposited by spraying on the inner surfaces of the two thin glass plates. The static electric field ($E_=$) was applied also. Separately or simultaneously to the sample plugged in the AC and DC voltage. External constant magnetic field was oriented along the plane of the film. A He-Ne laser (λ=0.63 μm) was used. Experiments were carried out at room temperature in geometry when $E_\sim \parallel \mathbf{k}$, $E_= \parallel \mathbf{k}$ and $H \perp \mathbf{k}$, where **k** is a light wave vector. The stripe domains are randomly bent and DW located in different places in the film, indicating that complete isotropy of the properties of this film in its plane.

Results and discussion. Our measurements of EMOE at H=0 ($E_\sim \neq 0$) at local points of laser probing (Ø≈ 3 μm) on separated YIG film sites with DW not showed changes of the angle α_{EMO} value when $E_==0$. Circular diaphragm exposed so that the DW was in the middle of the scanned local area of the film and when the magneto-optical signal (Faraday rotation) is equal to zero. But, with increasing of DC electric field ($E_=$) value and when constant value of AC electric field, we registered changing of EMOE starting from some values of $E_=$-field (see Fig. 1, (a)). Thus, in the absence of external magnetic field, EMOE on film sites with DW can to be shown only when applied DC and AC electric fields simultaneously and α_{EMO} signal value depends essentially from DC field. When we applied magnetic field, oriented in a film plane, display of EMOE was another. So, even at a zero DC field and when $E_\sim \neq 0$, the EMO signal on DW areas was registered (see electric field dependences of EMOE at Fig. 1, (b)). EMOE value was increasing not only with growing of the magnetic field (when $E_\sim \neq 0$) but with growing of the static electric field. It was found from our experiments that the EMO signal essential on value in film area with DW (when H≠0) was registering only under joint action of DC and AC electric fields. Measurements were spent only for straight sections of DW areas.

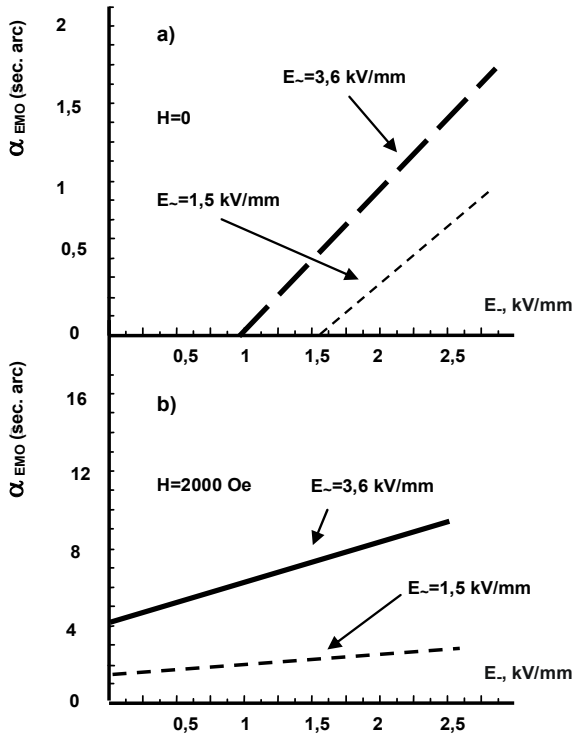

Fig. 1 Electric-field dependences of EMOE for DS-area with DW (for straight section of DW) in region of the laser probe when magnetic field H=0 – (a) and when H=2000 Oe – (b)

In Fig. 2 the dependences of EMOE from positions of scanning diaphragm in the local points of DS with DW in scaning area are presented. Measurements were carried out in longitudinal direction (X direction) of scanning in relation to DWs when H=0 (a) and H=60 Oe (b). In this case to the sample it has been applied the static and alternating electric fields jointly. The scanning index point is chosen arbitrarily for straight sections of DW area. As it is possible to see from presented curves, the EMO signal in some points of optical scanning differs from a signal average level. It is possibly because of the interaction of DWs with microdefects of a film occurs. The reason for sharp EMOE "jumps" on DW is a local fastenings of DW on microdefects of a film with the subsequent separations at change of instant values of a variable E-field.

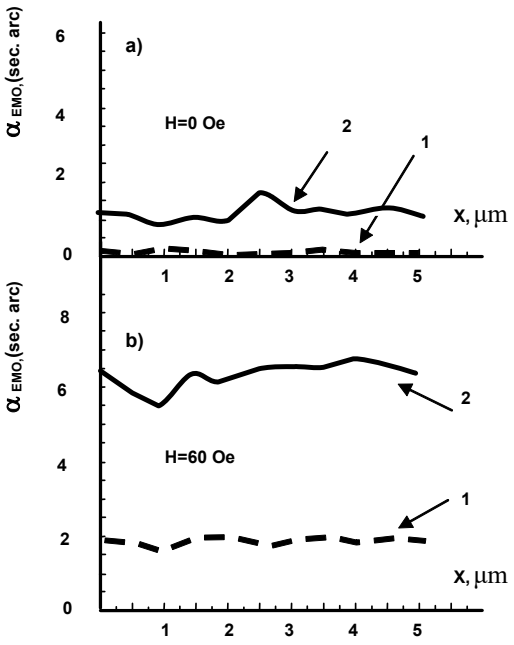

Fig. 2 Dependences of the α_{EMO} from positions of scanning diaphragm in the film region with DW: (a) - H=0; (b) – H=60 Oe. (1 – $E_=$ =1 kV/mm and $E_\sim$ = 3.3 kV/mm; 2 – $E_=$ =2.2 kV/mm and $E_\sim$ = 3.5 kV/mm). Measurements were carried out in longitudinal direction (X direction) in relation to DW for straight section of DW

Explanation of our results, in our opinion, may be as follows. In this case, there are two basic moments which in a complex have led to the received by us results: choice of experimental conditions and the features of object for investigations. Further more detailed about them.

Applied to a film of spatially homogeneous, continuously operating harmonious electric field which is oriented along a normal to the sample, leads to small changes of it magneto-crystallographic anisotropy through direct influence of the E-field on constants of the induced anisotropy. About change of YIG magnetic anisotropy was informed earlier in a number of papers [2, 6]. In our case (magneto-one-axis film), DW represent a three-dimensional objects with non-uniform "vortical" distribution of a magnetisation vector in them ("braided" DW [11]). The structure of such DWs is deformed on a thickness of a film by magneto-static field which is directed perpendicularly to DW surface. This field is created by "magnetic poles" which are located on both surfaces of a film. "Whirlwinds" which for lack of external fields are localised in narrow DWs, are very sensitive to changes of a constant of magnetic anisotropy and react by compression or smearing at its changes. In our experimental conditions, magnetic field oriented in the plane of the sample and when is perpendicular to the DW can change the DW structure [5] and induces the redistribution of the resulting field in the film

plane on a thickness of the sample. It leads to increasing of a magnetic dispersion field at one surface of the film and, accordingly, to easing at another. Specified field is substantially not uniform along the thickness of the film and that creates conditions for a weak deflection of DW. When polarity of a low-frequency electric field changes, because of reduction of an effective operating field, the DW has a bend instability and because of it are possible the harmonious, near the superficial distortions of DW profile.

I.e., probable, we have display of magneto-static instability of the domain which is shown at periodic, very weak, expansion-compression of the domain (one half-cycle of the E-field – expansion, and another – compression). Moreover, parameters of the surface layers of epitaxial garnet films on the free space borders and the substrate differs from each other and the response of the film surfaces to external influences (in particular on the E-field) may be different. Thus, at joint action of the constant H – field oriented in a film plane (i.e. directions of the labyrinth

DWs in a film plane are fixed by this field) and a variable E-field, stability such "created" DWs to small external influenses, in particular, to a constant E-field changes (Fig. 1). It is realised a less "favourable" DW which is less steady against external influenses. A turn or bend of a DW plane are "forbidden" by H-field. The inclination of DW plane is possible only in E – fields and EMO signal reacts to it (see Fig. 1).

Conclusions. Thus, our results of electromagneto-opticall investigations of the ME interaction influense on transformation of the YIG DWs as a inhomogeneous micromagnetic structures showed the following. Small in value but sufficient for registration by magneto-optical methods the influense of the E-field on distribution of the magnetization in these structures is observed only in certain experimental conditions, when a complex influence by constant and variable E-fields (applied perpendicular to the film plane) and a constant H-field (applied in the plane of the sample). On a small near-surface displacement of the DW profile reacts EMO signal by change of the value. In absence of an external H-field, applied in the plane of the film, the ME effect on DW is very small in value. The received results testify in favour of the assumption, that the main cause of ME manifestations in ferrite-garnets is the change of magnetic anisotropy in E-field.

REFERENCE

1. *Astrov D. N.* The magnetoelectric effect in antiferromagnetics // Sov. Phys.-JETP. – 1960. – 11. – P. 708–709.

2. *Aubert G.* A Novel Approach of the magnetoelectric effects in ferrimagnets // JMMM. – 1983. – Vol. 31–34. – P. 767–768.

3. *Dzyaloshinskii I. E.* On the magneto-electrical effects in antiferromagnets // Sov. Phys. – JETP. – 1959. – 10. – P. 33–35.

4. *Hansen P., Klages C., Schuldt J. and Witter K.* Magnetic and Magneto-Optical properties of Bismuth-substituted lutetium iron garnet films // Phys. Rev. B. – 1985. - Vol. 31. – 9. – P. 5858–5862.

5. *Hubert A.* Theorie der domänenwände in geordneten medien // Springer-Verlag. – 1974. – P. 377.

6. *Koronovskyy V. E., Ryabchenko S. M., and Kovalenko V. F.* Electromagneto-optical effects on local areas of a ferrite-garnet film // Phys. Rev. B. – 2005. – 71. – P. 172402–172406.

7. *Koronovskyy V. E., Gorchinski N. D.* The electromagnito-optical effect in local areas of single magnetic domains in epitaxial films of yttrium iron garnet // Functional Materials. – 2011. – Vol.18, №1. – P. 37–41.

8. *Krichevtsov B. B., Pisarev R. V., Selitskij A. G.* The electromagneto-optical effect in yttrium iron garnets $Y_3Fe_5O_{12}$ // JETP Lett. – 1985. – 41. – P. 317–319.

9. *O'Dell T. H.* The electrodynamics of magnetoelectric media. – Philos. Mag., 1967.

10. *Paoletti A.* Magnetic garnet films // Special Issue on Magnetic Garnet Films. – 1984. – 114. – P. 240.

11. *Schlomann E.* // J. Appl. Phys. – 1973. – 44. – P.1837.

12. *Velleaud G., Sangare B., Mercier M., and Aubert G.* Magnetoelectric properties of Yttrium Iron Garnet // Solid State Commun. – 1984. – Vol. 52. – P. 71–74.

Submitted on 15.04.15

Короновський В., канд. фіз.-мат. наук,
каф. Електрофізики, факультет радіофізики, електроніки та комп'ютерних систем
Київський національний університет імені Тараса Шевченка

ІНДУКОВАНИЙ ЗОВНІШНІМ ЕЛЕКТРИЧНИМ ПОЛЕМ ЕФЕКТ ЗМІНИ ПОЛОЖЕНЬ ДОМЕННИХ МЕЖ В ЕПІТАКСІЙНИХ ПЛІВКАХ ФЕРРИТ-ГРАНАТІВ

Методом поляризаційної мікроскопії нами досліджувався ефект зміни положення доменних меж (ДМ) в епітаксійних плівках ферит-гранатів, як реакція на комбінований вплив змінного і постійного електричних полів. У прохідному світлі було зареєстровано зміни магнітооптичного сигналу на локальних ділянках магнітної доменної структури з ДМ на ділянці оптичного сканування. Величина вказаного ефекту суттєво залежала від магнітного поля, підключеного в площині досліджуваного зразка.

Ключові слова: *доменна межа, магнітоелектричний ефект, електричне поле, магнітне поле.*

Короновский В., канд. физ.-мат. наук,
каф. электрофизики, факультет радиофизики, электроники и компьютерных систем
Киевский национальный университет имени Тараса Шевченко

ИНДУЦИРОВАННЫЙ ВНЕШНИМ ЭЛЕКТРИЧЕСКИМ ПОЛЕМ ЭФФЕКТ ИЗМЕНЕНИЯ ПОЛОЖЕНИЙ ДОМЕННЫХ ГРАНИЦ В ЭПИТАКСИАЛЬНЫХ ПЛЕНКАХ ФЕРРИТ-ГРАНАТОВ

Методом поляризационной микроскопии нами исследовался эффект изменения положения доменных границ (ДГ) в эпитаксиальных пленках феррит-гранатов, как реакция на комбинированное влияние переменного и постоянного электрических полей. В проходящем световом луче были зарегистрированы изменения магнитооптического сигнала на локальных участках магнитной доменной структуры с ДГ в области оптического сканирования. Величина указанного эффекта существенно зависела от магнитного поля, подключенного в плоскости исследуемого образца.

Ключевые слова: *доменная граница, магнитоэлектрический эффект, электрическое поле, магнитное поле.*

UDC 538.911

P. Kulyk, stud., B. Pavlenko, stud., Department of Electrophysics
S. Kulyk, Ph.D., P. Strunets, stud., Department of Nanophysics and Nanoelectronics,
A. Goriachko, Ph.D., Department of Physical Electronics,
Faculty of Radiophysics, Electronics and Computer Systems,
National Taras Shevchenko University of Kyiv,
V. Melnyk, Dr.Sc., V. E. Lashkaryov's Institute of Semiconductor Physics NAS of Ukraine

SURFACE PROPERTIES OF GE(111) AND SI(111) AFTER BI ION IMPLANTATION

A single monolayer of Bi atoms was implanted into Ge(111) and Si(111) samples. Morphology, electronic properties and thermal stability of these surfaces after special chemical and thermal treatments were analyzed by means of atomic-force microscopy and Auger electron spectroscopy. The near surface layers of such samples were found in the disordered state, being able to dissolve additional amount of bismuth deposited on the surface from an external source.

Key words: *Si, Bi, Ge, implantation, atomic force microscopy, diffusion.*

Introduction. The surfaces of Si(111) and Ge(111) are major substrates for the creation of modern micro- and nano-electronic devices. Therefore, analysis of their structure and elemental composition is important for modern technology of integrated electronics. At the same time, ion implantation is the primary method for introducing dopants to create integrated electronic devices. The aim of the study was the structure, morphology and chemical composition of Si(111) and Ge(111) with implanted and adsorbed layers of bismuth. Bi was present at the "shallow junction" depth.

Experimental part. Special composition of Si(111) and Ge(111) were found for researching characteristics of diffusion Bi and on theirs surfaces were grown silicon dioxide and germanium dioxide with thickness of 10 nm. The ion implantation of Bi was made with oxide layer with energy of 50 keV and total dose of about $1x10^{15}$ sm^{-2}. After ion implantation of Bi a depth concentration of distribution is non homogeneous with a maximum on a some depth of structure. A typical model of Bi dopant distribution in the depth of structure is shown in a Fig. 1

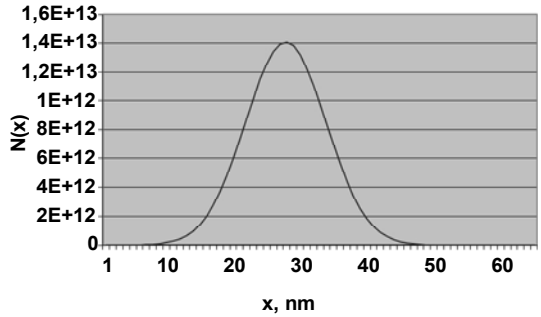

Fig. 1. A typical model of Bi dopant distribution in the depth of Bi or Si structure (atoms per 1 sm^3). A surface coordinate x=0 nm before the processing in HF solution, and x=10 nm after the processing with HF

Parameters of oxidation and ionization were selected so that visible concentration of the Bi begins from the depths which confirm non oxide layers of the structure (beginning from the depth of 10 nm). Such types of structures were subjected of the chemical processing in 5% solution of hydrofluoric acid. This acid dissolves the oxide of Ge or Si fast. It was used in the following work for getting impurity implantation level which began from geometric surface of the semiconductor. Structures of Si(111) or Ge(111) without oxide were washed in distilled water and were moved immediately into a vacuum chamber of experimental equipment after interaction with acid. Downloading was done though the gateway system with it's own backing vacuum pump and sputter-ion pump without disturbing the vacuum in the main chamber where the next in-situ processing of Substrate and it's researching.

Results and discussion. The Substrates were warmed with different temperature during 5 minutes after the researching of diffusion of the impurity. After that determined the chemical composition of the surface with the help of Auger spectroscopy. The main idea of this approach is the ability to capture direct measurement appearing of the Bi at the surface in the case of his thermally activated of segregation from the implanted layer. Identification of the Augers lines were made by spectrum of secondary electrons which were registered with the help of four-net analyzer in dE/dN mode with exposure of Substrate of primary electrons with energy of 3 keV. Including that typical surface elementary sensibility Auger spectroscopy is situated on the 1% monolayer level and also that integral dose of implantation under the curve on Fig. 1 consists of 1 monolayer, they may say that surface concentration with x=10 nm is much less than the border of sensibility. So, growing the number of Bi on the surface of this Substrate to the level which would have done identification of elements possible can happen the result of thermally activated of segregation from depth to the surface or the result of adsorption of atoms Bi from vacuum (spraying from the external source).

On the Fig. 2 there is an Auger spectrum of Substrate Si(111) after the warming to the temperature T=160°C during 5 minutes. On this spectrum LVV lines of Si are fixed, which confirms to Auger crossing in non oxide (92 eV) and oxide (80 eV) atoms of Si. Oxide component can be explained by the Substrate's of Si short staying at the atmosphere.

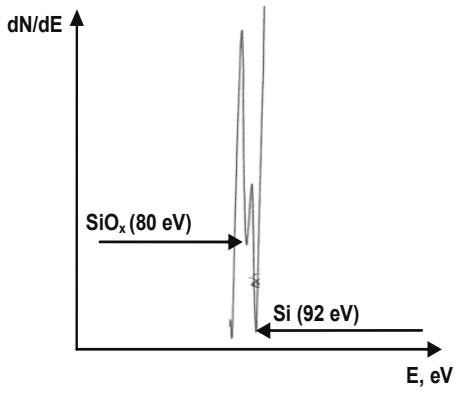

Fig. 2. Auger spectrum of Substrate after the warming with the temperature T=160°C during 5 minutes. There are components of clean (Si) and oxide (SiO_2) Si

Let's note that on the Fig. 2 lines which can be present like Auger crossing in atoms of Bi are not

© Kulyk P., Pavlenko B., Kulyk S., Strunets P., Goriachko A., Melnyk V., 2015

showed. It means that the result of warming with temperature T=160°C during 5 minutes implanted Bi hasn't segregate onto the surface.

There is a hypothesis that segregation of the impurity onto the surface can be deffusion process with unknown energy of activation was decided to do a set of measuring of elementary composition of the surface after the warming with different Substrate. Results of this measuring are on Fig. 3

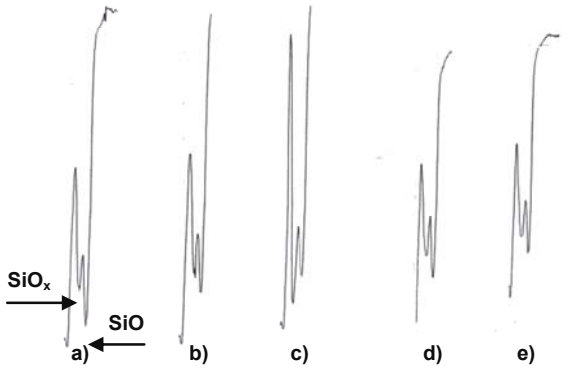

Fig. 3. Auger spectra after the warming of the Substrates during 5 minutes with temperature a) T=150°C; b) T=170°C; c) T=290°C; d) T=379°C; e) T=420°C

On the Fig. 3 there are final spectra for a set of temperature from 150°C to 420°C. It is important that all of them are almost identical to the spectrum on Fig. 2, so it leads us to the same conclusion that segregation is absent onto the surface from implanted layer. In this case the conclusion is write for warming temperature to 420°C. The next growing of the temperature with these conditions was inappropriate because of approaching to the temperature of desorption Bi (~500°C) from the surface of Si. Even if segregation took place Bi would not accumulate on the surface because of evaporation to the vacuum. In return for defining the physical causes of which make getting visible number of Bi on surface of Substrate impossible was decided to provide it on the surface with the help of external source and tracking behaviour such adsorbed layer with increased temperature.

Deposition on the surface of implanted Substrate of Si(111) was made by the way of evaporation from the melt in high vacuum. Technically it provide by warming of drop which was desisted by forces of surface tension in the loop of tungsten wire, which an electrical current was passed through. Control of the number of sprayed Bi was be made with the help of quartz microscales. The temperature of the Substrate during the spraying was 300 K.

On the Fig. 4 there is Auger spectrum of the Substrate after the causing 2 monolayers of Bi. It's comparing to the Fig. 2 shows availability of extra Auger line which was identified as Bi($N_{6,7}O_{4,5}O_{4,5}$ 100 eV). Auger lines of the Si are weakened, but not to zero intensity, as 2 monolayers extra adsorbate are not enough for the full screening Auger electrons which are emitted from the Substrate of Si. After this the Substrate was warmed during 5 minutes with the temperature T=110°C. Auger spectrum after that warming on the Fig. 5. Comparing of spectra on Fig. 4 and Fig. 5 shows reducing the relation of intensity Auger lines Bi and Si from 7.8 to 6.3 as the result of warming. It can be interpret as the result of diffusion from the surface into the depth, or surface diffusion Bi with making three-dimensional islands and cleaning part of the surface of Substrate from adsorbate. Both of these leads to the growing of intensity of Auger signal from Substrate and reducing of Auger signal from adsorbate. The monitoring of Ager spectrum's surface for the set of temperature of warming was made for finding that out, results of which are shown on the Fig. 6

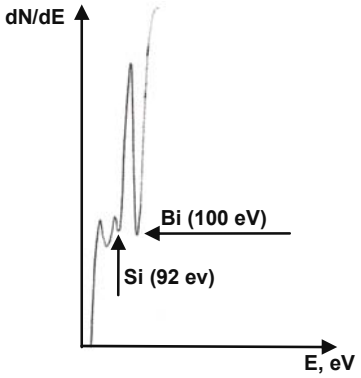

Fig. 4. Auger spectrum of the surface after the spraying films of Bi with the thickness 2 monolayers. Relation of the intensity Bi/Si is 7.8

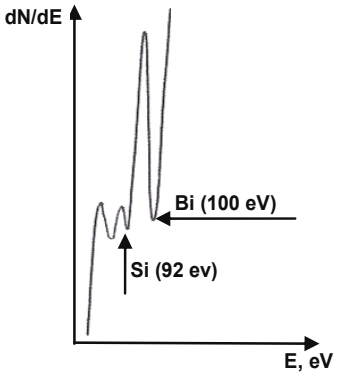

Fig. 5. Auger spectrum after warming with the temperature T=110°C. Relation of the intensity Bi/Si is 6.3

On the Fig. 6 there are spectra of the surface after spraying 2 monolayers of Bi and the next warming with the different temperature from 150°C to 290°C. General trend is that with growing the temperature of warming Auger signal reducing from atoms of Bi and growing from atoms of Si.

Relations of these signals as a function of temperature shows on the Fig. 7. From the Fig. 6. and Fig. 7. they can see that the Bi completely disappears from the surface. It is important that it happens with the temperatures much lower than known temperature of desorption from the surface of Si (~500°C). So, one can make a conclusion that diffusion of Bi from the surface to the sample happens during the warming.

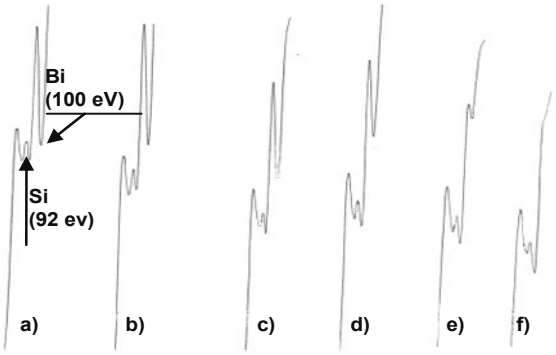

Fig. 6. Auger spectra after the warming of the Substrates during 5 minutes with temperature a) T=150°C; b) T=170°C; c) T=185°C; d) T=230°C; e) T=279°C; f) T=290°C

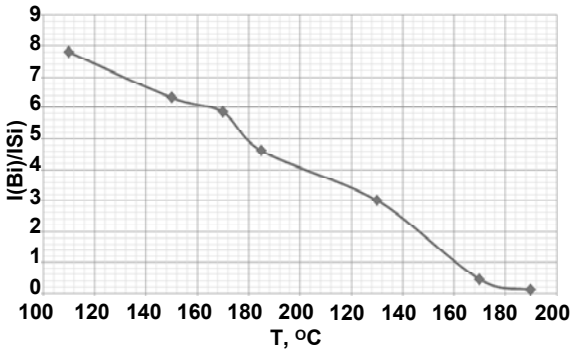

Fig. 7. Graph of relation of the intensity peak-to-peak of Auger lines Bi(NOO)/Si(LVV) from the temperature of sample before the measuring

This result is unexpectable including that insolubility is practically complete in the solid phase of Si. It should be noticed that the sample was under influence of ion implantation and it ruins crystal structure of surface layers. It can completely change solubility of another substances in this Substrate. Obviously that exactly it is tracked by us on the Fig. 5 – Fig. 7. After the implantation the crystal grate of the Substrate has many defects because of which diffusion of Bi from the surface to the deeper layers of the sample becomes possible. After this hypothesis one can found an explanation about absence of segregation implanted Bi onto the surface of Si as a result of warming like on the Fig. 2 – Fig. 3. Including that the layer which the implanted impurity concentrates in, at the same time has the highest concentration of defects, they obviously are a good place for dislocation of atoms of Bi, which keeps them from segregation to the surface. The temperature dependence of the concentration of Bi on the surface of implanted Si allows us to find the activation energy of diffusion of Bi in the perpendicular direction to the sample of the surface. We assume that the number of acts of diffusion per unit time

$$v = v_0 \exp(\frac{-E_d}{kT}), \quad (1)$$

here: v_0 potential factor, E_d energy of activation of diffusion. We write a relative change in thickness q Bi film on the surface during heating t_{21} as:

$$\frac{q_1 - q_2}{q_1} = v_0 t_{21}, \quad \frac{q_1 - q_2}{q_1} = v_0 t_{21}, \quad (2)$$

and q_1 is the nominal film thickness (proportional to the intensity of the Auger peak) before heating, q_2 – after heating. Substituting here the expression for v, one can easily obtain a formula for the diffusion activation energy:

$$E_d = -kT \ln\left[\frac{q_1 - q_2}{v_0 t_{21} q_1}\right], \quad E_d = -kT \ln\left[\frac{q_1 - q_2}{v_0 t_{21} q_1}\right], \quad (3)$$

where $v_0=10^{13}c^{-1}$. Using this expression, based on Fig. 5 – Fig. 7 the following formula of activation energy was received: $E_d=1.5\pm0.2$ *eV*. Comparing the value of previously installed energy desorption of Bi from the surface of Si *2.8±0.1 eV*, one can understand the reason for the disappearance of Auger signal from Bi deposited on the surface from an external source and its complete absence during trying to fix the thermally activated segregation from the bulk to the surface.

Semiconductor's surface condition after ion implantation of Bi through a protective layer of oxide, the chemical dissolution of the latter, and heating the sample in a high vacuum is illustrated by the images of the surface of Ge(111) obtained by atomic force microscopy (AFM) in air environment (Fig. 8 – Fig. 9). Preparation and chemical processing of samples of Ge(111) for loading into the vacuum chamber were identical to the above written Si(111). The temperature of heating in high vacuum was T=150°C, duration – 5 minutes.

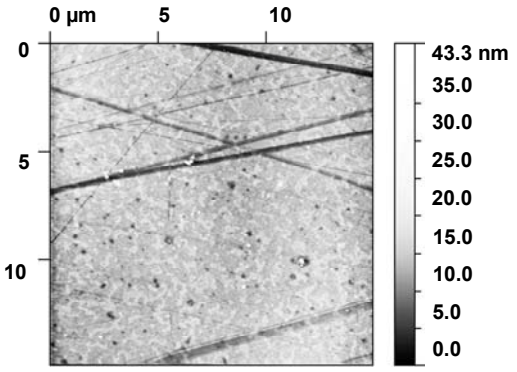

Fig. 8. AFM image of the surface of the Ge(111) after growing GeO_2 wit thickness of 10 nm, implantation (ion energy of 50 keV) 1 ML Bi solving oxide solution of HF, and heating in high vacuum for 5 minutes at 150°C. Figure's size of 15 microns x 15 microns, full gray scale corresponds to the altitude difference of 43 nm

Fig. 8 presents the resulting image of surface measuring 15 mm x 15 mm. A large number of straight-line trenches to a depth of ~20 nm and a length immediately attracts attention which go beyond the field of view. Areas which are separate trenches are not connected to each other. Width of tranches ranges from tens to hundreds nanometers. Including that the source material for preparation samples were high-quality germanium wafers with atomically smooth surface Ge(111), one can assume that observed in Fig. 8 relief develops due to accumulation of mechanical stresses in the crystal lattice of the semiconductor as a result of implantation.

During the heating one can see a partial "healing" lattice defects caused by the implantation process, accompanied by a corresponding expansion of mass transfer and surface topography features linear trench type. On the Fig. 9 AFM is presented much smaller surface areas of Ge(111), which there is no deep trenches on. But even in this case the surface's roughness reaches nearly 30 nm, and its structure is quite disordered. So, the surface's structure is also an indicator of disordering of the surface's layer of the sample, which means availability of many places for energetically favorable arrangement of Bi's atoms. In a result of proximity of physicochemical properties of Si and Ge, one can provide that surfaces of Si(111) were used for the above measurement, had at least qualitatively similar to "loosened" structure.

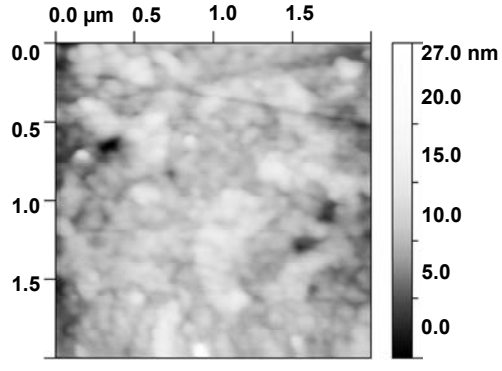

Fig. 9. AFM image of reduced area (2 mm x 2 mm) of the Ge's surface sample (111), which straight deep trench are not presented on

The result of the loosened structure of the surface layer is that Bi which is situated there does not segregate onto the surface at moderate temperatures of warming that were used in our experiments. Moreover, because of loosening the sample, much more energetically favorable locations for dislocation impurities appear in it. As a result, even more (the already implanted) amount of Bi deposited on the surface from the external layer are absorbed by the loosened layer at moderate heat activation. Thus, studies of surfaces Si(111) and Ge(111) of Bi's dopant's deep occurrence by the Auger spectroscopy's method and atomic-powered microscopy demonstrate the resistance of dopant relatively to the impurity segregation layer on the surface at temperatures up to 400°C. Physical reason for is loosening the surface's layer in the process of ion implantation of dopant.

Conclusions. Investigations of shallow doped Si(111) and Ge(111), revealed the lack of thermally activated segregation of the Bi implant on the surface, which is a positive factor of stability for advanced applications of p-n junctions with a new type of electronic doping.

REFERENCE

1. Bulavenko S. Yu. Coadsorption of hydrogen and bismuth on the Si(111)7×7surface / S. Yu. Bulavenko, M. I. Fedorchenko, P. V. Melnik, M. G. Nakhodkin // Surface Science. – 2000. – Vol. 454–456. – P. 213–217. – ISSN:1051–9998.

2. Goriachko A. Initial stages of Bi/Ge(111) Interface Formation: A detailed STM study / A. Goriachko, A. Shchyrba, S. Kulyk, P. V. Melnik, M. G. Nakhodkin // Surface Science. – 2011. – Vol. 605. – P. 1771–1777. – ISSN:1051–9998.

3. Nagao T. Nanofilm Allotrope and Phase Transformation of Ultrathin Bi Film on Si(111)-7x7 / T. Nagao, J. T. Sadowski, M. Saito, S. Yaginuma, Y. Fujikawa, T. Kogure, T. Ohno, Y. Hasegawa, S. Hasegawa, T. Sakurai // Physical Review Letters. – 2004. – Vol. 93. – P. 105501. – ISSN: 0018–9464.

4. Oh Y. Mapping subsurface structure through atomically thin bismuth films on Si(111)-(7x7) with scanning tunneling microscope / Y. Oh, J. Seo, H. Suh, J. S. Seo, S.-J. Kahng, Y. Kuk // Surface Science. – 2008. – Vol. 602. – P. 3352–3357. – ISSN: 0031–9007.

5. Olesinski R. W. The Bi-Si (Bismuth-Silicon) System R. W. Olesinski and G. J. Abbaschian // Bulletin of Alloy Phase Diagrams. – 1985. – Vol. 6. – P. 359–360. – ISSN: 1098–0121.

6. Sadowski J. T. Stability of the quasicubic phase in the initial stage of the growth of bismuth films on Si(111)-7x7 / J. T. Sadowski, T. Nagao, S. Yaginuma, Y. Fujikawa, and T. Sakurai, A. Oreshkin, M. Saito, T. Ohno // Journal of Applied Physics. – 2006. – Vol. 99. – P. 014904. – ISSN: 0003-6951.

7. Shchyrba A. Bismuth growth on Ge(111): Evolution of morphological changes from nanocrystals to films / A. Shchyrba, A. Goriachko, P. Melnik, M. Nakhodkin // Ukrainian Journal of Physics. – 2014. – Vol. 59. – P. 805-818. – ISSN: 2166–2754

Submitted on 11.12.15

Кулик П., студ., Павленко Б., студ., каф. електрофізики,
Кулик С., канд. фіз.-мат. наук, Струнець П., студ.,
Гарячко А., канд. фіз.-мат. наук, каф. фізичної електроніки
каф. нанофізики та наноелектроніки,
факультет радіофізики, електроніки та комп'ютерних систем,
Київський національний університет імені Тараса Шевченка,
Мельник В., д-р фіз.-мат. наук,
Інститут фізики напівпровідників імені В. Є. Лашкарьова НАН України

ВЛАСТИВОСТІ ПОВЕРХОНЬ Ge(111) ТА Si(111) ПІСЛЯ ІОННОЇ ІМПЛАНТАЦІЇ Bi

Моношар атомів Bi був імплантований в зразки Ge(111) та Si(111). Морфологія, електричні властивості та термічна стійкість цих поверхонь після спеціальних хімічної та термічної обробок були проаналізовані методами атомної силової мікроскопії та Оже-спектроскопії. Було показано, що приповерхневі шари цих зразків є неупорядкованими та здатні розчиняти додаткову кількість вісмуту, що нанесена на поверхню за допомогою зовнішнього джерела.

Ключові слова: *Si, Bi, Ge, імплантація, атомно-силова мікроскопія, дифузія.*

Кулик П., студ., Павленко Б., студ., каф. электрофизики,
Кулик С., канд. физ.-мат. наук, Струнец П., студ.,
Гарячко А., канд. физ.-мат. наук, каф. физической электроники,
каф. нанофизики и наноэлектроники,
факультет радиофизики, электроники и компьютерных систем
Киевский национальный университет имени Тараса Шевченко,
Мельник В., д-р. физ.-мат. наук,
Институт физики полупроводников имени В. Є. Лошкарёва НАН Украины

СВОЙСТВА ПОВЕРХНОСТЕЙ Ge(111) И Si(111) ПОСЛЕ ИОННОЙ ИМПЛАНТАЦИИ Bi

Монослой атомов Bi был имплантирован в образцы Ge(111) и Si(111). Морфология, электрические свойства и термическая стойкость этих поверхностей после специальных химической и термической обработок были проанализированы методами атомной силовой микроскопии и Оже-спектроскопии. Было показано, что приповерхностные слои этих образцов являются неупорядоченными и способны растворять дополнительное количество висмута, который был нанесен на поверхность с помощью внешнего источника.

Ключевые слова: *Si, Bi, Ge, имплантация, атомно-силовая микроскопия, диффузия.*

UDC 004.043

D. Kutovyi, stud., M. Vernydub, stud.
D. Gryaznov, assist., Y. Boyko, Ph. D.
Faculty of Radio Physics, Electronics and Computer systems,
Taras Shevchenko National University of Kyiv,
e-mail: mvernydub@gmail.com

RECONSTRUCTION OF DATABASE SCHEMA FROM WSDL

The mechanism of data structure reconstruction while synchronizing information systems by meta descriptions of the transmitted data is proposed. Formalization of data conversion was performed by means of relational algebra.

Key words: *Relational algebra, WSDL, databases, systems synchronizing.*

Introduction. During synchronizing complex information systems often appear problem when one of the systems made changes in the structure of data that must be replicated in other systems [1]. This problem can be solved when the developers of both systems agree on those changes. However, when the interaction between developers

© Kutovyi D., Vernydub M., Gryaznov D., Boyko Y., 2015

complicated, there is a problem to reconstruct changes on the receiver side by incomplete information. In particular, this problem occurs when synchronizing systems of various levels of complexity and inaccessibility of complete information on the data structure of a larger system.

In this paper were solving the problem of constructing a relational database structure based on information about access methods provided by the WSDL (Web Services Description Language).

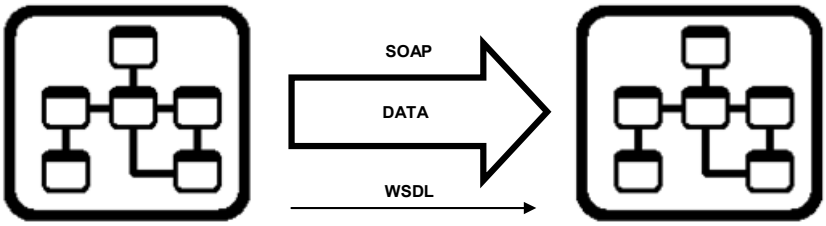

Fig. 1. System structure

Experimental. The overall structure of information exchange between systems can be seen in Figure 1. Data are transferred between them with SOAP (Simple Object Access Protocol), and transmit information about the structure of messages using WSDL (Web Services Description Language). Example of WSDL structure can be seen below:

```
<s:element name="PersonsGet">
<s:complexType>
<s:sequence>
<s:element minOccurs="0" maxOccurs="1" name="SessionGUID" type="s:string"/>
<s:element minOccurs="1" maxOccurs="1" name="Id_Language" type="s:int"/>
<s:element minOccurs="0" maxOccurs="1" name="UIds" type="s:string"/>
</s:sequence>
</s:complexType>
</s:element>
```

Clearly, restoring identical structure with such limited information impossible. However, great practical importance have the construction of normalized data structure as close to the source as possible [2]. To solve this problem proposed automation algorithm, which you can see in Fig. 2. In this algorithm for data conversion process control system used 5 tables: methods table, fields table, parameters table, relations table and attributes table. Information to first three tables automatically synthesized from WSDL structure [3]. The system administrator via a special interface records data to other two tables. During data conversion before updating in their local database, calculating of hash function on these fields and checking of data available hash in the database take place. The data updates only if the hashes do not match, it can reduce the number of update requests to the databaase. If any errors occur during data conversion administrator receives notifications about it in the interface.

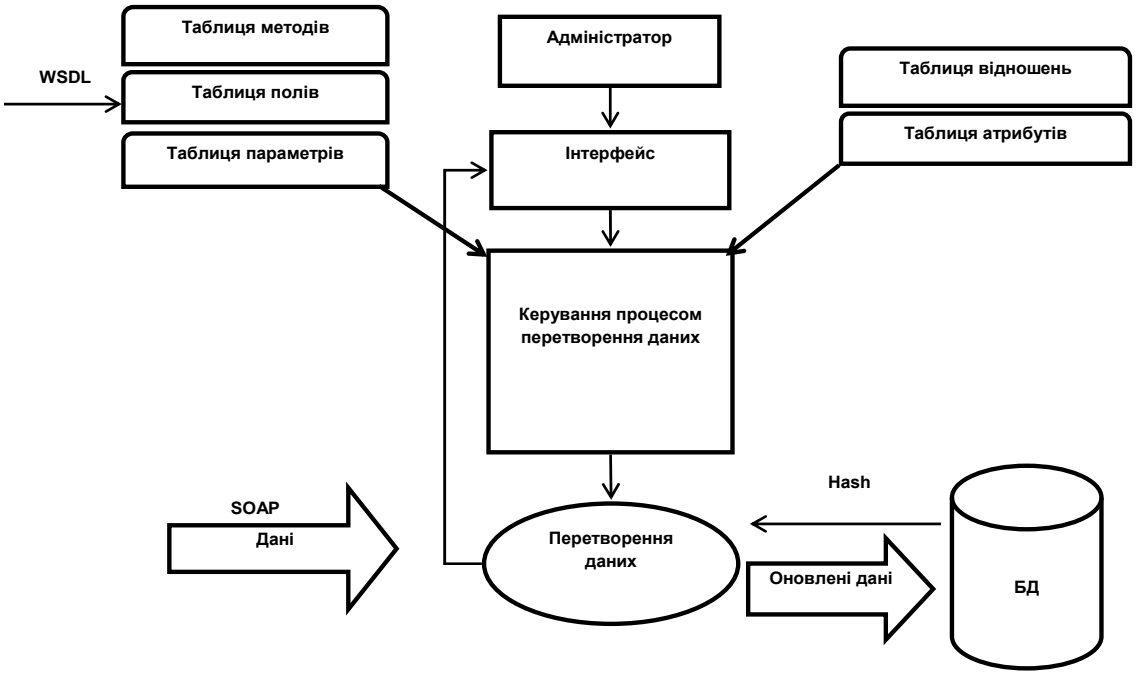

Fig. 2. General scheme of the algorithm

Consider these four types of transformations and give appropriate relational algebra formulas for each of them. For the record, use the following relations and notations their attributes:

S $\{S.A_{id}, S.A_1 \ldots S.A_n\}$ – related data received from SOAP. In this relation A_{id} attribute matches the primary key, attributes $A_1 \ldots A_n$ matches other essential data.

T $\{T.B_{id}, T.B_1 \ldots T.B_m\}$ – main relationship in the local relational structure where data is entered. In this relation B_{id} attribute matches the primary key, attributes $B_1 \ldots B_m$ matches other necessary data.

T_2 $\{T_2.C_{id}, T_2.C_1 \ldots T_2.C_h\}$ – second conversion relation involved in local relational structure. In this relation C_{id} attribute related to the primary key, attributes $C_1 \ldots C_h$ matches other necessary data.

1) Direct data conversion. In this type of transformation, SOAP data directly reflected the appropriate relation (T) in a local relational structure without external keys. The formula is as follows:

$$\rho_{\{S.A_{id},S.A_1 \ldots S.A_m\}/\{T.B_{id},T.B_1 \ldots T.B_m\}} \text{ (P)}$$
$$P = \pi_{\{S.A_{id},S.A_1 \ldots S.A_m\}} \text{ (S)}$$

2) Convert involving foreign keys. This type is used when necessary to insert into relation T primary key of another relation T_2 as a foreign key.

Enter the attributes refer to output formula. Let SOAP attribute data on the value of which will be search in relation T_2, as $S.A_a$. According attribute T_2 in relation to which the search will $T_2.C_a$. Attribute the main relation in which T is necessary to substitute primary key relation T_2 denote $T.B_a$. The formula is as follows:

$$\rho_{\{S.A_{id},\{S.A_1 \ldots S.A_{m+1} \setminus S.A_a\},T_2.C_{id}\}/\{T.B_{id},T.B_1 \ldots T.B_m,T.B_a\}} \text{ (P)}$$
$$P = \pi_{\{S.A_{id},\{S.A_1 \ldots S.A_{m+1} \setminus S.A_a\},T_2.C_{id}\}} \text{ (R)}$$
$$R = \sigma_{S.A_a = T_2.C_a} (S \times T_2)$$

3) Conversion from entering the two dependent relationships with one to many relations. This type finds application in situations where the data should be divided into two dependent relationships T and T_2 in the case when the ratio T must contain a foreign key that refers to the relation of T_2.

Introduce notation for attributes SOAP, we have to preset ratio T_2. $S.A_{aid}$ – contains the primary key for the relation T_2, $S.A_{a1} – S.A_{ah}$ – contains other data to be preset in relation T_2. The result is two different formulas correspond conversion relations for T and T_2.

$$\rho_{\{S.A_{aid},S.A_{a1} \ldots S.A_{ah}\}/\{T_2.C_{id},T_2.C_1 \ldots T_2.C_h\}} \text{ (P)}$$
$$P = \pi_{\{S.A_{aid},S.A_{a1} \ldots S.A_{ah}\}} \text{ (S)}$$

$$\rho_{\{S.A_{id},\{S.A_1 \ldots S.A_{m+h}\} \setminus \{S.A_{a1} \ldots S.A_{ah}\}\}/\{T.B_{id},T.B_1 \ldots T.B_m\}} \text{ (P1)}$$
$$P1 = \pi_{\{S.A_{id},\{S.A_1 \ldots S.A_{m+h}\} \setminus \{S.A_{a1} \ldots S.A_{ah}\}\}} \text{ (S)}$$

4) Conversion with insert to two dependent relations with one to many relations. This type finds application in situations when the data should be divided into two dependent relationships T and T_2 in the case when the relation T_2 must include a foreign key relationship to T.

We use designation SOAP attributes are the same as in the previous conversion. The result is two different formulas correspond conversion relations for T and T_2.

$$\rho_{\{S.A_{aid},S.A_{a1} \ldots S.A_{ah-1},S.A_{id}\}/\{T_2.C_{id},T_2.C_1 \ldots T_2.C_h\}} \text{ (P)}$$
$$P = \pi_{\{S.A_{aid},S.A_{a1} \ldots S.A_{ah-1},S.A_{id}\}} \text{ (S)}$$

$$\rho_{\{S.A_{id},\{S.A_1 \ldots S.A_{m+h+1}\}\{S.A_{aid},S.A_{a1} \ldots S.A_{ah}\}\}/\{T.B_{id},T.B_1 \ldots T.B_m\}} \text{ (P1)}$$
$$P1 = \pi_{\{S.A_{id},\{S.A_1 \ldots S.A_{m+h+1}\}\{S.A_{aid},S.A_{a1} \ldots S.A_{ah}\}\}} \text{ (S)}$$

Conclusions. The proposed system was implemented for the information system of the university during the entrance campaign to synchronize with government education database and proved its efficiency and productivity. Full database synchronization took about 30 minutes. By automating the process of reproduction of data structure with minimal cost in time realized the correct of handling 578 methods data access.

REFERENCE

1. *Wa S.,* International Conference on Mechatronics, Electronic, Industrial and Control Engineering,/ S. Wa // Shenyang, China, – 2015. – P. 1024–1027.

2. *Wignore T.,* Entity-Relationship Approach — ER '94 Business Modelling and Re-Engineering Lecture / T. Wignore, M. Loffredo, M. Gregori, M. Cima // Notes in Computer Science. – 1994. – Vol. 881. – P. 387–402.

3. *White V.,* Evolution and Process / V. White, T. Reichherzer, J. Coffey, N. Wilde // Journal of Software. – 2013. – Vol. 25. – P. 97–109.

Submitted on 19.06.15

Кутовий Д., студ., Вернидуб М., студ.
Грязнов Д., асист., Бойко Ю., канд. фіз.-мат. наук
факультет радіофізики, електроніки та комп'ютерних систем,
Київський національний університет імені Тараса Шевченка

ВІДНОВЛЕННЯ СТРУКТУРИ ДАНИХ ПРИ СИНХРОНІЗАЦІЇ КОМП'ЮТЕРНИХ СИСТЕМ

Запропоновано механізм відтворення структури даних при синхронізації інформаційних систем по метаописам даних, що передаються. Для цього було виконано формалізацію перетворень даних за допомогою реляційної алгебри.

Ключові слова: *реляційна алгебра, WSDL, бази даних, синхронізація систем.*

Кутовой Д., студ., Вернидуб М., студ.
Грязнов Д., ассист., Бойко Ю., канд. физ.-мат. наук
факультет радиофизики, электроники и компьютерных систем
Киевский национальный университет имени Тараса Шевченко

ВОССТАНОВЛЕНИЕ СТРУКТУРЫ ДАННЫХ ПРИ СИНХРОНИЗАЦИИ КОМПЬЮТЕРНЫХ СИСТЕМ

Предложено механизм воссоздания структуры данных при синхронизации информационных систем по метаописаниям данных, которые передаются. Для этого было выполнено формализацию превращения данных с помощью реляционной алгебры.

Ключевые слова: *реляционная алгебра, WSDL базы данных, синхронизация систем.*

UDC 537.877; 537.867; 537.876.45; 621.372.823

O. Maksimenko, junior researcher,
S. Khizhnyak, senior researcher,
National Science Center "Kharkov Institute of Physics and Technology",
G. Zaginaylov, Doctor of Science in Physics and Mathematics, prof.,
National Science Center "Kharkov Institute of Physics and Technology",
V. N. Karazin Kharkov National University

EFFICIENT METHOD FOR ANALYSIS OF MODE CONVERSION AND OHMIC LOSSES IN TERAHERTZ GYROTRONS

Nowadays gyrotrons have a great potential as efficient sources of terahertz (THz) radiation. However, they still suffer significantly from excessive ohmic load of cavity walls and spurious radiation appearing inside the gyrotron cavity. A numerically efficient method to consider these effects is suggested. It allows us to reduce a boundary value problem for a longitudinally inhomogeneous (irregular) open waveguide with impedance walls (which models a gyrotron cavity) to a set of ordinary differential equations (SODE) without any simplifying assumptions. Effects of ohmic losses and mode conversion on resonant frequencies and quality factors of THz gyrotron cavity are investigated in details. It is shown that amplitudes of spurious modes can be comparable with the operational one at the output section of the THz gyrotron cavity. Also a rapid convergence of the obtained results with respect to the number of modes considered is demonstrated. Specific calculations were performed for the cavity of THz gyrotron developed in Fukui University, Japan (FU CW III) designed to operate on the $TE_{3,5}$ mode.

Key words: *irregular waveguides, impedance boundary conditions, lossy waveguides, cross-section methods, Neumann's and Dirichlet's problems, terahertz radiation, teragertz gyrotrons, gyrotyron cavities, quality factors, resonant frequency.*

Introduction. THz radiation occupying the range between microwaves and infrared waves presently is a subject of considerable interest. The most promising applications are associated with progress in spectroscopy and monitoring of bio-molecules [18, 6], study and fabrication of new functional micro-and nano-structured materials [7], sophistication of tools for plasma diagnostics and plasma sources [2, 3], remote detection of radioactive materials [15], study of hyperfine structure of positronium [14], THz imaging [5], etc. However, technology for its generating and manipulating is still far from maturity [1]. In this regard, it should be pointed out, that power-handling capabilities of the traditional vacuum sources (BWO's, TWT's, klystrons, orotrons, etc.) and traditional photonic sources (quantum cascade lasers, gas lasers, laser driven THz emitters, etc.) are rather moderate in the THz range (about 1–2 mW). At the same time, recently, gyrotrons, being the most efficient sources of sub-THz radiation in a continuous wave (CW) regime, extended their operation to the THz range [4]. Moreover, gyrotrons seem to have a great potential in this range since they are free from numerous drawbacks inherent to both traditional vacuum and photonic THz sources. The cavities of gyrotrons are rather simple being much more convenient for fabrication and operation in terahertz range compared with other vacuum sources. Nevertheless, the efficiency of THz gyrotrons is still low (about several percents). One of the main reasons is the dissipation of THz radiation inside the gyrotron cavity, which can achieve 65–85 % [4].

It should be pointed out that physics of wave processes in THz gyrotron cavities is yet not clearly understood. So development and application of new methods for their analysis is of considerable interest.

Usually the cavity of the gyrotron is the section of longitudinally irregular waveguide (see, for example, Fig. 1). If it operates in THz range we should consider natural wall losses. In this range the wall losses can be effectively taken into account by imposing impedance boundary conditions (Leontovich conditions) on the cavity walls. So, we come to the problem for analysis of a irregular impedance waveguide.

It should be pointed out that very often in gyrotron theory methods of cross-sections are used which were developed a long time ago [11, 13, 17]. They are rather efficient for irregular waveguides with ideal walls, reducing the problem to the set of ordinary differential equations (SODE). Along with the equations of beam-wave dynamics they still successfully utilized in different numerical codes for modeling a gyrotron operation [16]. However, extreme mathematical and calculational difficulties appear when wall losses should be taken into account [19]. The problem cannot be reduced to a SODE by application of transverse expansions. Even in the case of small losses or lossy waveguide of a constant radius the problem was reduced to the SODE which is coupled with the additional singular integral equation. The numerical solution of the problem have been suggested which is not fully self-consistent. The region of validity of the proposed approximate numerical solution is not clear, and it leads to substantially complicated consideration even without an electron beam.

In the paper we demonstrate capabilities of a recently developed new method for analysis of main dissipative effects (ohmic losses and spurious radiation) in THz gyrotron cavities [20, 21, 23]. It allows an equivalent reduction of the problem to a SODE for an arbitrary longitudinal variation of both radius and impedance.

Capabilities of the method are demonstrated on the specific example. Calculations of the THz gyrotron FU CW III developed in Fukui University [10] is performed. SODE for unknown amplitudes of spurious modes of both polarizations (TE and TM) was solved by the finite difference method. Convergence with respect the number of spurious modes taken into account has been shown. Resonant frequencies, quality factors and field distributions of different modes are calculated with effects of mode conversion and ohmic losses taken into account. The obtained results are compared with those of single mode approximation and obtained by other methods. It is shown that the effect of mode conversion is rather strong leading to a significant contribution of spurious modes to the total output power (~70%). Also it is shown that mode conversion and ohmic losses lead to the notable reduction of quality factors (~50 %).

The rest of the paper is organized as follows. In the second section the idea of the approach is briefly described. The resulting SODE is obtained and some its differences from that obtained by other approaches are addressed. The numerical example of application of the obtained SODE is addressed in the third section. The problem is formulated as an eigenvalue/eigenfunction problem. I.e. SODE is supplemented by boundary conditions on the cavity ends. Usually for gyrotron cavities radiation conditions and evanescent conditions are used for propagating and non-propagating modes respectively. Conclusions resume the obtained results. Also some aspects of basic physics concerning ohmic losses and

© Maksimenko O., Khizhnyak S., Zaginaylov G., 2015

mode conversion in THz gyrotron cavities are formulated. In particular, it is noted that the effect of mode conversion increases with increasing the axial index of modes.

Basic idea of the approach for conversion of Maxwell's equations to the SODE. Consider a longitudinal inhomogeneous lossy waveguide.

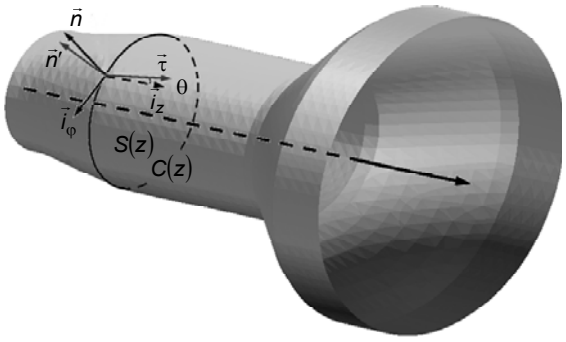

Fig. 1. Geometry of longitudinally inhomogeneous waveguide

In contrast to the methods discussed above, refuse from vector basis functions and from the concept of the reference waveguide. Instead, the electromagnetic field in an arbitrary cross section of irregular waveguide (Fig. 1) express terms of two scalar functions (magnetic and electric Hertz potentials), which satisfy the Helmholtz equation [8]:

$$\begin{matrix}\left(\Delta_\perp + \partial^2/\partial z^2 + k^2\right)\Psi = 0 \\ \left(\Delta_\perp + \partial^2/\partial z^2 + k^2\right)\Phi = 0\end{matrix}, \quad (1)$$

where $k = \omega/c$, c – the speed of light in vacuum, ω – the oscillation frequency, the time factor $e^{-i\omega t}$ is omitted. We represent the unknown functions in the form [19, 20],

$$\begin{matrix}\Psi = \sum_{i=1}^{\infty} A_i(z)\Psi_i(\vec{r}_\perp; z) \\ \Phi = \sum_{i=1}^{\infty} B_i(z)\Phi_i(\vec{r}_\perp; z)\end{matrix}, \quad (2)$$

where $\Psi_i(\vec{r}_\perp; z)$ and $\Phi_i(\vec{r}_\perp; z)$ are eigenfunctions Dirichlet's and Neumann's problems for the Laplace operator, respectively, in the two-dimensional domain $S(z)$:

$$\begin{cases}\left(\Delta_\perp + \alpha_i^2\right)\Psi_i = 0 & \left(\Delta_\perp + \beta_i^2\right)\Phi_i = 0 \\ \partial\Psi_i/\partial n\big|_{C(z)} = 0 & \Phi_i\big|_{C(z)} = 0\end{cases} \quad \vec{r}_\perp \in S(z) \quad (3)$$

Note that the representation for Ψ converges uniformly to Ψ throughout the cross-section $S(z)$, including the contour $C(z)$, which is the boundary of the cross-section. At the same time the representation for Φ converges uniformly to Φ only inside $S(z)$, but it is zero at $C(z)$. The basis functions satisfy the following orthogonality conditions:

$$\begin{matrix}\int_{S(z)} \nabla_\perp \Psi_i^* \nabla_\perp \Psi_k ds = \delta_{ik} \\ \int_{S(z)} \nabla_\perp \Phi_i^* \nabla_\perp \Phi_k ds = \delta_{ik}\end{matrix}, \quad (4)$$

The set of equations (1) is replaced by two infinite sets of projection equalities

$$\begin{matrix}\int_{S(z)} \Phi_i^*\left(\Delta_\perp + \partial^2/\partial z^2 + k^2\right)\Phi ds = 0 \\ \int_{S(z)} \Psi_i^*\left(\Delta_\perp + \partial^2/\partial z^2 + k^2\right)\Psi ds = 0\end{matrix}, \quad (5)$$

Using the second Green's formula in the two-dimensional case, for functions Ψ_i^*, and Ψ

$$\int_{S(z)} \left(\Psi_i^* \Delta_\perp \Psi - \Psi \Delta_\perp \Psi_i^*\right) ds = \oint_{C(z)} \left(\Psi_i^* \frac{\partial}{\partial n}\Psi - \Psi \frac{\partial}{\partial n}\Psi_i^*\right) dl \quad (6)$$

and the same formula for Φ_i^* and Φ, as well as the representations (2) and orthogonality conditions (4), we arrive at the two infinite SODE

$$\begin{matrix}(\hat{L}_1^2 A)_i + p_i^2 A_i + I_i^A = 0 \\ (\hat{L}_2^2 B)_i + q_i^2 B_i - I_i^B = 0\end{matrix}, \quad (7)$$

where $p_i^2 = k^2 - \alpha_i^2$, $q_i^2 = k^2 - \beta_i^2$, $\hat{L}_{1,2} = \delta_{ik}(d/dz) + T_{ik}^{(1,2)}$,

$T_{ik}^{(1)} = \alpha_i^2 \int_{S(z)} \Psi_i^*(\partial/\partial z)\Psi_k ds$, $T_{ik}^{(2)} = \beta_i^2 \int_{S(z)} \Phi_i^*(\partial/\partial z)\Phi_k ds$,

$I_i^A = \alpha_i^2 \oint_{C(z)} \Psi_i^*(\partial/\partial n)\Psi dl$, $I_i^B = \beta_i^2 \oint_{C(z)} \Phi(\partial/\partial n)\Phi_i^* dl$,

$i = 1, ..., \infty$.

The system of equations contains contour integrals $I_i^{A,B}$ with the unknown functions $\Phi\big|_{C(z)}$ and $(\partial/\partial n)\Psi\big|_{C(z)}$ (we cannot use the expansions (2) them), which have to be expressed in terms of the expansion coefficients A_i and B_i in order to get a closed SODE. Since for the waveguide with an arbitrary cross-section the further consideration is cumbersome, we consider specific, but the most widespread and illustrative case of waveguide with the circular cross-section. In this case, the basis functions are Bessel's functions, and the series (2) are Dini's and Fourier-Bessel's series. Expressions for the basis functions can be found in [11]. The contour integrals can be taken elementary resulting in

$$I_i^A = 2\pi R(z)\alpha_i^2 \Psi_i^*(\partial/\partial n)\Psi\big|_{C(z)}$$

$$I_i^B = 2\pi R(z)\beta_i^2 \Phi(\partial/\partial n)\Phi_i^*\big|_{C(z)}$$

Dissipation in the walls can be considered using the popular impedance boundary conditions

$$\vec{n}' \times \vec{E} = -Z_s \vec{n}' \times (\vec{n}' \times \vec{H})\big|_{C(z)}, \quad (8)$$

where $\vec{n}'$ is normal to the surface of the waveguide at the cross-sectional contour $C(z)$ (Fig. 1), $Z_s = k\delta(1-i)/2$ is the impedance of the walls, $\delta = c/(2\pi\sigma\omega)^{1/2}$ is the skin depth of the wall material, σ is the wall conductivity, and $k = \omega/c$ is the vacuum wave number. Rewriting (8) in terms of the Hertz potentials, we obtain

$$\hat{D}_1(z)\frac{\partial}{\partial r}\begin{pmatrix}\Psi \\ \Phi\end{pmatrix} = \hat{D}_2(z)\begin{pmatrix}\Psi \\ \Phi\end{pmatrix}\Big|_{C(z)}, \quad (9)$$

where

$$\hat{D}_1(z) = \begin{pmatrix}1 - \frac{iZ_s \sin\theta}{k}\frac{\partial}{\partial z} & 0 \\ 0 & \frac{iZ_s k}{\cos\theta} + tg\theta\frac{\partial}{\partial z}\end{pmatrix},$$

$$\hat{D}_2(z) = \begin{pmatrix}iZ_s\cos\theta\left(k + \frac{1}{k}\frac{\partial^2}{\partial z^2}\right) & \frac{m}{R}\left(iZ_s\sin\theta + \frac{1}{k}\frac{\partial}{\partial z}\right) \\ \frac{m}{R}\left(ktg\theta - \frac{iZ_s}{\cos\theta}\frac{\partial}{\partial z}\right) & -\left(k^2 + \frac{\partial^2}{\partial z^2}\right)\end{pmatrix}$$

$tg\theta = R'(z)$, m is the azimuthal index, the prime means differentiation with respect to argument, and the azimuthal dependence $\exp(im\phi)$ is omitted.

Relations (9) link Hertz potentials and their normal derivatives on $C(z)$. Thus, to get the closed SODE we can

introduce two new unknown functions, while the other two must be expressed through them and already entered unknown coefficients of the expansions (2). It is also necessary to express the partial derivatives of the unknown functions in (9) in terms of full derivatives. Introducing two new unknown functions $\frac{1}{k}\frac{\partial}{\partial n}\Psi\Big|_{C(z)} \equiv A_0(z)$ and $\Phi|_{C(z)} \equiv B_0(z)$ and using for $\Psi|_{C(z)}$ and its z-derivatives the representation (2), the only unknown function remains in excess, namely $\frac{\partial}{\partial n}\Phi$, which in this partial case coincides with $\frac{\partial}{\partial r}\Phi$. From (1) one is possible to get

$$(\partial/\partial r)\Phi|_{C(z)} = (1/R)\int_0^R \left(-\partial^2/\partial z^2 - k^2 + m^2/r^2\right)\Phi r dr \ . \quad (10)$$

Under the integral sing for Φ one is possible to use the decomposition (2), thereby expressing $(\partial/\partial r)\Phi|_{C(z)}$ through B_i. To express partial derivations in (9) in terms of the introduced unknown functions and their derivations we should use the differentiation rules for the functions of two arguments. For example,

$$\frac{d}{dz}\Phi(R(z);z) \equiv B_0'(z) = R'(z)(\partial/\partial r)\Phi|_{C(z)} + (\partial/\partial z)\Phi|_{C(z)} \quad (11)$$

Further substituting (10) to (11) we can express $(\partial/\partial z)\Phi|_{C(z)}$ in terms of B_0, B_i and their derivations. Other partial z-derivations entering to (9) can be also expressed in terms of A_0, A, B_0, B and their derivations in the same manner.

Thus, we derive two additional ordinary differential equations

$$\begin{aligned} &a_0A_0' + b_0A_0 + c_0B_0' + d_0B_0 = \\ &\sum_{i=1}^{\infty}\left(a_i\left(\hat{F}_1A\right)_i + d_1\left(b_i\left(\hat{L}_2^2B\right)_i + c_iB_i\right)\right) \end{aligned} \quad (12)$$

$$B_0'' + d_2B_0 = \sum_{i=1}^{\infty}\left(a_i\left(\hat{F}_2A\right)_i + b_i\left(\hat{G}\hat{L}_2^2B\right)_i + c_i\left(\hat{G}B\right)_i\right),$$

where $a_0 = -iZ_s\sin\theta$, $b_0 = k(1 - iZ_s tg\theta\sin\theta/kR)$,

$c_0 = -m/R$, $d_0 = -iZ_skm\sin\theta/R$, $d_1 = mtg\theta/R^2$,

$\hat{F}_1 = f_0 + f_1\hat{L}_1^2$, $\hat{F}_2 = f_2\left(k\sin\theta - iZ_s\hat{L}_1\right)$, $\hat{G} = g_0 - g_1\hat{L}_2$,

$f_0 = iZ_s\cos\theta\left(k^2\left(1+tg^2\theta\right) - tg^2\theta m^2/R^2\right)$,

$f_1 = iZ_s\cos\theta(1+tg^2\theta)$, $J_m(\mu_i) = 0$, $J_m'(\mu_i') = 0$,

$f_2 = \left(m/R\cos\theta\right)(1-tg^2\theta)$, $a_i = \left(\pi\left(\mu_i'^2 - m^2\right)\right)^{-1/2}$,

$b_i = \int_0^R \Phi_i r dr$, $c_i = \left(k^2 - \mu_i^2/R^2\right)b_i - \pi^{-1/2}$,

$g_0 = \left(tg^2\theta - (tg\theta)'R + iZ_skR\cos^{-1}\theta(1-tg^2\theta)\right)R^{-2}$,

$g_1 = \left(1+\tan^2\theta\right)\tan\theta/R$,

$d_2 = tg^2\theta\left(k^2 - m^2/R^2\right) + k^2(1-tg^2\theta)$.

Equations (7) and (12) form the closed SODE for unknown coefficients $\{A_i\}_{i=0}^{\infty}$ and $\{B_i\}_{i=0}^{\infty}$. The obtained SODE is fully equivalent to the original system of Maxwell's equations and is suitable for the analysis of waveguides with arbitrary longitudinal irregularities and arbitrary impedances of walls. This approach can be easily generalized to the case of impedance boundary conditions of more general types. Finally, we should note the simplicity, compactness and comparatively small number of unknown functions in the resulting system of equations. For comparison, in the conventional versions of the cross-sectional method four [17] or six [13] infinite sets of unknown expansion coefficients should be introduced even in the lossless case. Also note that the unknown coefficients $\{A_i\}_{i=0}^{\infty}$ and $\{B_i\}_{i=0}^{\infty}$ corresponding to modes of TE and TM polarizations respectively are coupled only through the boundary conditions (eq. (12)). At the same time in conventional variants of cross-sectional methods also TE-TM coupling coefficients are present which are spurious and have no physical sense.

Numerical example. As an example illustrating the results of our approach, consider a gyrotron operating in sub-millimeter (terahertz) range. The gyrotron cavity usually represents a section of a circular waveguide with varying radius (Fig. 1). The central part of the cavity has a constant radius. It is connected with an input section, which is a supercritical down tapper and the outlet part in the form of a smoothly expanding waveguide (see, also [10]).

To analyze the gyrotron cavity SODE (7), (12) must be supplemented by boundary conditions at the ends of the resonator. Usually it is the radiation or evanescent conditions for propagating and non-propagating mode respectively. Also for simplicity, we assume that the resonator with both ends connected with the semi-infinite regular waveguides with perfect walls. This allows us to put $A_0 = B_0 = 0$ on both ends of the resonator.

Specific calculations were performed for the THz gyrotron designed to operate at the $TE_{3,5}$ mode [10]. SODE (7), (12) was solved by a finite difference method. It was shown the numerical results converge with respect to the number of terms considered in (2). The accuracy of calculations was controlled by the energy conservation law. The results obtained for the eigenfrequencies and quality factors of the two first axial resonances of the operational mode are presented in the Table 1. For comparison the results of the single mode approximation (SMA) are also presented.

***Table* 1**

Eigenfrequencies and quality factors of the two first axial resonanses. SMA results without losses are presented in brackets

Mode	Presented Method		SMA	
	frequency, GHz	*Q*	frequency, GHz	*Q*
$TE_{3,5,1}$	424.59	8438	424.58	8982 (16000)
$TE_{3,5,2}$	425.24	3229	425.23	3473 (4240)

Note that the calculated gyrotron operating frequency agrees well with the experimental value [10] as well as with SMA. As for the quality factor, the experimental measurement errors of this magnitude in this frequency range are much smaller than the demonstrated computational errors, so their comparison is not reasonable. Comparing the calculated quality factors with those in SMA approximation with and without ohmic losses, one can assess the impact of ohmic and mode conversion losses on quality factors. In particular, for the first axial resonance which is usually used for the operational regime in gyrotrons the main and significant contribution ($\sim 45\%$) to the reduction of the quality factor is made by the ohmic losses, although the contribution of mode conversion is also notable ($\sim 5\%$).

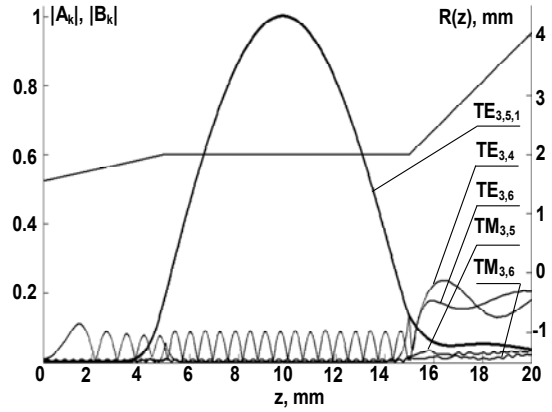

Fig. 2. Field distributions of the operational and the largest spurious modes at the first axial resonance

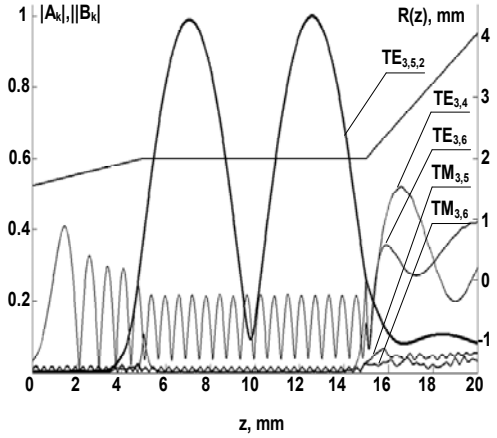

Fig. 3. Field distributions of the operational and the largest spurious modes at the second axial resonance

Fig. 2, 3 show the field distributions of different modes in the case of the main (working) and the second axial resonances respectively (for better visuality the amplitudes of spurious modes are increased fivefold). For the operational $TE_{3,5}$ mode it is basically the same as in the SMA without ohmic losses. However, it should be noted that the contribution of spurious modes is large in the output cross-section and their fraction in the output power is about 70 % or more for both resonances.

Also note some general features of mode conversion for THz gyrotron resonators:

1. Spurious modes appear mainly in the output section of the cavity.

2. The contribution of spurious mode to the total field depends on their radial index and polarization. Spurious modes with radial indexes closer to the radial index of the operational mode have larger amplitudes.

3. The amplitudes of spurious higher radial modes are lower that the amplitudes of spurious lower radial modes with the same polarization and with the same difference in the radial index from the operational mode.

4. The amplitudes of spurious TM modes are substantially lower than the amplitudes of spurious TE modes with the same radial index.

Analysis of the accuracy and convergence of numerical results. The accuracy of calculations was analyzed using two functions $\xi_1(N)=\left|\frac{\omega_{N+1}-\omega_N}{\omega_N}\right|$ and $\zeta_1(N)=\left|\frac{Q_{N+1}-Q_N}{Q_N}\right|$, where ω_N and Q_N are the resonant frequency and the quality factor respectively, calculated taking into account N terms of the expansions (2) for 1100 discretization points along z. Fig. 4, 6 illustrate the convergence of the resonant frequency and the quality factor with respect to N on a logarithmic scale. Also the convergence of numerical results with respect to the number of discretization points was investigated. Fig. 5, 7 show functions $\xi_2(n)=\left|\frac{\omega^{(n+1)}-\omega^{(n)}}{\omega^{(n)}}\right|$ and $\zeta_2(n)=\left|\frac{Q^{(n+1)}-Q^{(n)}}{Q^{(n)}}\right|$, where $\omega^{(n)}$ and $Q^{(n)}$ are the resonant frequency and the quality factor respectively calculated at the number of discretization points $n=100M$ and $N=5$ on a logarithmic scale.

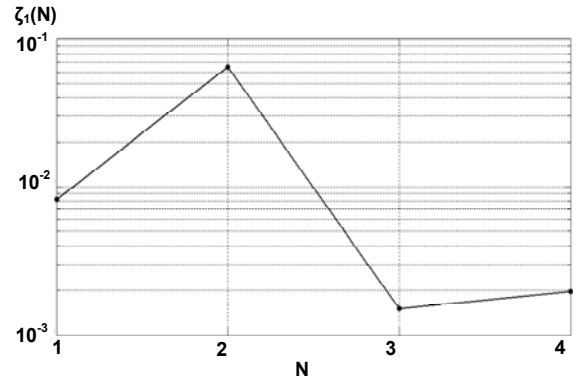

Fig. 4. Convergence of the quality factor at the first axial resonance with respect to the number of modes considered

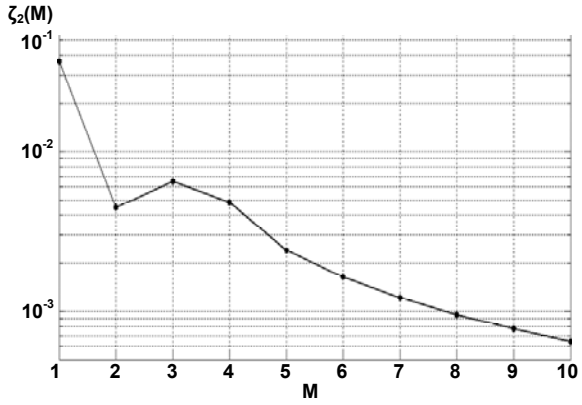

Fig. 5. Convergence of the quality factor at the first axial resonance with respect to the number of discretization points

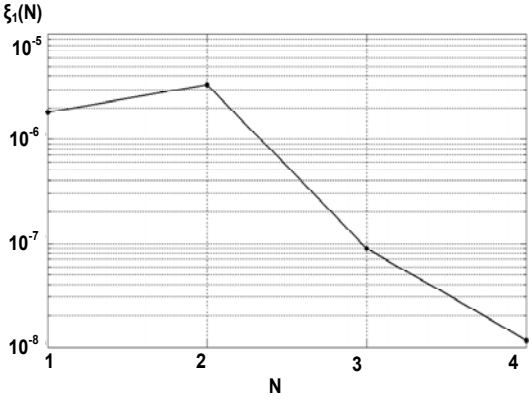

Fig. 6. Convergence of the natural frequency at the first axial resonance with respect to the number of modes considered

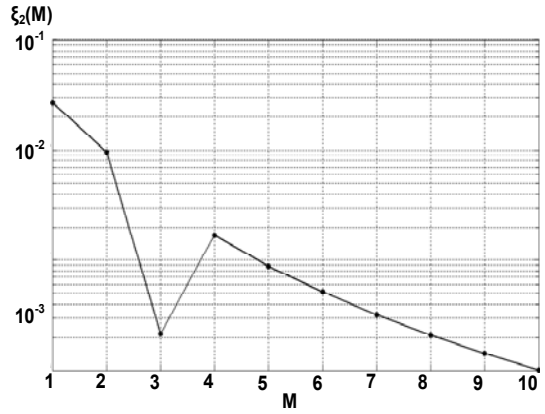

Fig. 7. Convergence of the natural frequency at the first axial resonance with respect to the number of discretization points

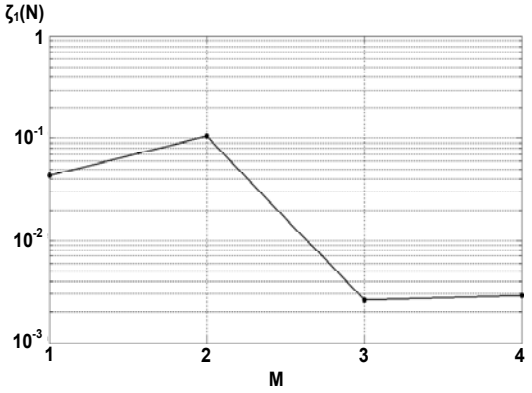

Fig. 8. Convergence of the quality factor at the second axial resonance with respect to the number of modes considered

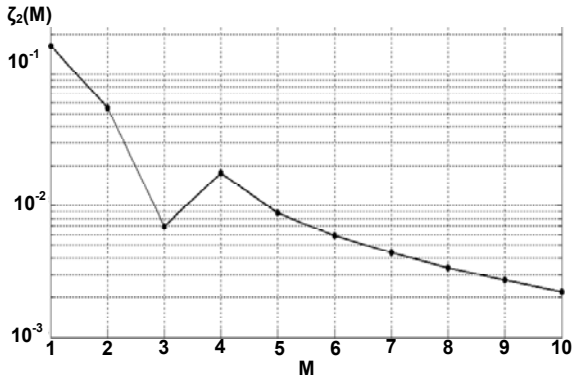

Fig. 9. Convergence of the quality factor at the second axial resonance with respect to the number of discretization points

Numbering of modes were as follows: $N=1$ corresponds to the operating mode $TE_{3,5}$, $N=2$ – $TE_{3,4}$, $N=3$ – $TE_{3,6}$, $N=4$ – $TM_{3,5}$, $N=5$ – $TM_{3,6}$ and so on.

Conclusions. The proposed approach is the further generalization of the cross-section methods which allows us to rigorously analyze different electromagnetic and acoustic problems including inhomogeneous impedance waveguides. It shows advantages and new capabilities of scalar transverse expansions based on the pure abstract solutions of Neumann's and Dirichlet's problems over the less flexible vector expansions based on the vector fields of the reference waveguide.

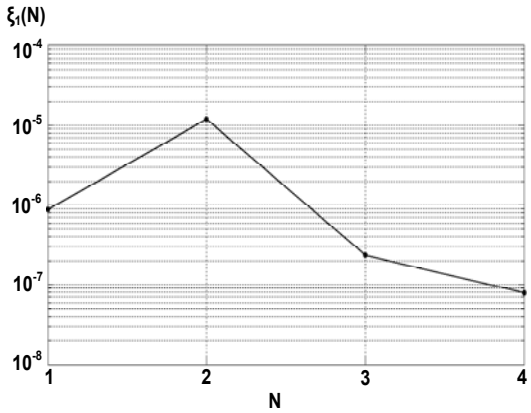

Fig. 10. Convergence of the natural frequency at the second axial resonance with respect to the number of modes considered

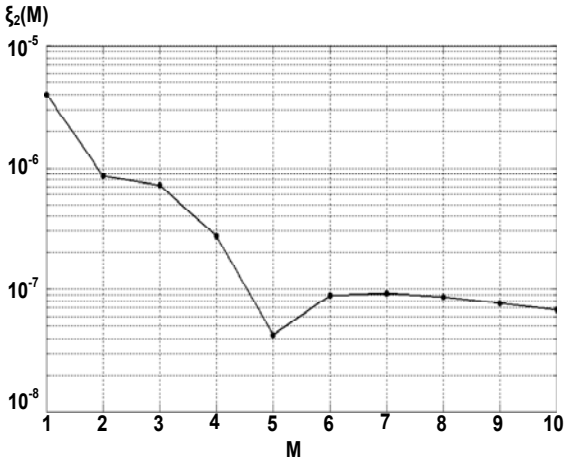

Fig. 11. Convergence of the natural frequency at the second axial resonance with respect to the number of discretization points

Note also the advantages of this approach over the approaches based on the use of curvilinear coordinate systems [9, 12]. Such approaches simplify boundary conditions which are transformed into the boundary conditions corresponding to a regular waveguide. However, much more complex equations for the fields have to be obtained analytically. Also they are associated with much more complicated problems at the stage of numerical implementation.

All these advantages are demonstrated on the basis of "cold" calculations of the gyrotron cavity operating in the THz range. In particular, it is shown that the ohmic losses in the walls of the cavity are the main reason for the substantial reduction of the cavity Q-factor. The contribution of the mode conversion to this effect is not so significant, although it is notable and also should be taken into account in basic considerations and conceptual design of THz gyrotron cavities. The fraction of spurious modes in the total output power is extremely and unexpectedly large (about 70%). Quite probably that such a large level of spurious radiation causes extra energy losses in the output circuits located after the gyrotron cavity (mode converters, output launchers and so on).

Evidently the effects considered are the main reasons of the low efficiency of the present THz gyrotrons. Therefore the development of methods for reducing ohmic and mode conversion losses are of considerable interest. One of them can be based on the use of the corrugated wall of the cavity [22–24].

Finally, note about nearest generalizations of the approach developed. They may be associated with the consideration of irregular impedance waveguides of non-circular cross sections, dielectric waveguides and theories of excitation of such waveguides.

REFERENCE

1. *Booske J. H.*, Vacuum Electronic High Power Terahertz Sources / J. H. Booske et al. // IEEE Trans., Terahertz Science and Technology. - 2011. – Vol. 1. – No. 1. – 54–75 p.;

2. *Bykov Yu. V.*, The development of gyrotrons and their applications for plasma science and material processing / Yu. V. Bykov et al. // Terahertz Science and Technology. – 2014. – Vol. 7. – No. 2. – 70–79 p.;

3. *Glyavin M. Yu.*, The Discharge Maintained by High-Power Terahertz Radiation in a Nonuniform Gas Flow / M. Yu. Glyavin et al. // Radiophys. And Quantum Electronics. – 2014.– Vol. 56.– No. 89. – 561–565 p.;

4. *Glyavin M. Yu.*, Generation of 1.5-kW, 1-THz coherent radiation from a gyrotron with a pulsed magnetic field / M.Yu. Glyavin, A.G. Luchinin, G.Yu. Golubiatnikov // Phys. Rev. Lett. –2008. — Vol. 100. – No. 1. – 015101 p.;

5. *Han S. T.* Compact sub-THz gyrotrons for real-time T-ray imaging / S. T. Han // IVEC. – 2013. – 1–2 p.;

6. *Idehara T.*, The Potential of the Gyrotrons for Development of the Sub-Terahertz and the Terahertz Frequency Range – a Review of Novel and Prospective Applications / T. Idehara et al. // Thin Solid Films. – 2008. – Vol. 517. – No. 4. – 1503–1506 p.;

7. *Idehara T.,* THz Gyrotrons – FU CW Series for high power THz technologies / T. Idehara et al. // Proceedings by 33th IRMMW-THz. – 2008.;

8. *Il'insky A. S*, Propagation, Difraction and Dissipation of Electromagnetic Waves / Ed. by A. S. Il'insky, A. Ja Slepjan, and G. Ja Slepjan // 1993. – London: The IEE and Peter Peregrinous Ltd. Electromagnetic Waves, Series 36. – 277 p.;

9. *Il'insky A. S.*, Methods of studying irregular waveguides / A. S. Il'insky, A. G. Sveshnikov // USSR Comput. Maths., Math. Phys. – 1968. – Vol. 8. – No. 2. – 363–373 p.;

10. *Kao S. H.*, A study of sub-terahertz and terahertz gyrotron oscillators / S. H. Kao, C. C. Chiu, K. R. Chu // Physics of Plasmas. – 2012. – Vol. 19. – No. 2. – 023112 p.;

11. *Katsenelenbaum B. Z.*, Theory of Non-uniform Waveguides. The Cross-Section Method / Ed. by B. Z. Katsenelenbaum // 1998. – London: IEE. – 249 p;

12. *Kravchenko V. F.*, Nonlinear theory of relativistic Cherenkov generators based on irregular waveguides with allowance for finite wall conductance / V. F. Kravchenko et al. // Doklady Physics. – 2007. – Vol. 52. – No. 2. – 96–100 p.;

13. *Mashkovtsev B. M.*, Theory of Waveguides / Ed. by B. M. Mashkovtsev, K. N. Tsibizov, B. F. Emelin // 1966. – Moscow: Nauka. – 354 p.;

14. *Miyazaki A.* The sub-THz direct spectroscopy of positronium hyperfine splitting / A. Miyazaki et al. // Journal of Physics: Conference Series. – 2013. – Vol. 443. –- No. 1. – 012002 p.;

15. *Nusinovich G. S.*, The concept of remote detection of concealed radioactive materials by using high-power THz radiation / G. S. Nusinovich, M. Yu. Glyavin, A. G. Luchinin // Proceedings by 38th IRMMW-THz.- 2013.;

16. *Pagonakis I .Gr.*, Desing of the EU-1MW gyrotron for ITER / I. Gr. Pagonakis, G. Gantenbein, J. Jelonek et al. // Proceedings by 14th IVEC, Paris. – 2013. – 1–2 p.;

17. *Solymar L.* Spurious mode generation in nonuniform waveguide / L. Solymar // IRE Trans. Microwave Theory Tech. –1959. – Vol. 7. – No.7. – 379–383 p.;

18. *Temkin R. J.* Development of terahertz gyrotrons for spectroscopy at MIT / R. J. Temkin // Terahertz Science and Technology. – 2014. – Vol. 7. – No. 1. – 1–9 p.;

19. *Vlasov A. N.*, Numerical solution of fields in lossy structures using MAGY / A. N. Vlasov, T. M. Antonsen // IEEE Trans. ED. – 2001. – Vol. 48. – No. 1. – 45–55 p.;

20. *Zaginaylov G. I.*, New Approach to the Theory of Irregular Lossy Waveguides and its Application to Design of Teraherz Gyrotrons / G. I. Zaginaylov et al. // Proceedings by 43th EuMW, Nuremberg. – 2013. 971–974 p.;

21. *Zaginaylov G. I.*, Novel Approach to the Theory of Longitudinally Inhomogeneous Lossy Waveguides / G. I. Zaginaylov et al. // Proceedings by MSMW'13, Kharkov. – 2013. – 523–525 p.;

22. *Zaginaylov G. I.*, Rigorous calculation of energy losses in cavity of ITER relevant coaxial gyrotron / G. I. Zaginaylov et al. // Proceedings by 35th EuMW, Paris. – 2005. – 1107–1110 p.;

23. *Zaginaylov G. I.,* Theory of irregular impedance waveguides: generalized method of separation of variables / G. I. Zaginaylov, A. V. Maksimenko, V. I. Shcherbinin and K. Schuenemann // Proceedings by MMET – 2014, Dnipropetrovsk, invited paper. – c. 31–35 p.;

24. *Zaginaylov G.I.,* Electromagnetic analysis of coaxial gyrotron cavity with the inner conductor having corrugations of an arbitrary shape / G. I. Zaginaylov, I. V. Mitina // Progress in electromagnetic research B. - 2011. – Vol. 31. – 339-356 p;

Submitted on 30.06.15

Максименко О., мол. наук. спів роб., Хижняк С., ст. наук. співроб.,
ННЦ "Харківський фізико-технічний інститут",
Загинайлов Г., д-р фізико-математичних наук, проф.
ННЦ "Харківський фізико-технічний інститут",
Харківський національний університет імені В. Н. Каразіна

ЕФЕКТИВНИЙ ЧИСЛОВИЙ МЕТОД АНАЛІЗУ КОНВЕРСІЇ МОД ТА ОМІЧНИХ ВТРАТ В ТЕРАГЕРЦОВИХ ГІРОТРОНАХ

В даний час гіротрони є перспективними джерелами терагерцового (ТГц) випромінювання. Однак, вони мають надзвичайно високі омічні втрати на стінках резонатора і випромінювання, яке з'являється в резонаторі гіротрона. Пропонується ефективний метод для розгляду цих ефектів. Він дозволяє без будь-яких спрощень звести крайову задачу для поздовжньо неоднорідного (нерегулярного) відкритого хвилеводу з імпедансними стінками (резонатор гіротрона) до системи звичайних диференціальних рівнянь (СЗДУ). Детально досліджено вплив омічних втрат і конверсії мод на резонансні частоти і добротності резонатора ТГц гіротрона. Показано, що амплітуди паразитних мод можуть бути порівнянні з робочою модою у вихідному перерізі резонатора ТГц гіротрона. Також показана швидка збіжність запропонованого методу з урахуванням числа розглянутих мод. Конкретні розрахунки були виконані для резонатора ТГц гіротрона розробленого в університеті Фукуї, Японія, який працює на моді $TE_{3,5}$.

Ключові слова: *нерегулярні хвилеводи, імпедансні граничні умови, хвилеводи з втратами, методи поперечних перерізів, задачі Неймана і Дирихле, терагерцове випромінювання, терагерцові гіротрони, резонатори гіротронів, добротності, резонансна частота.*

Максименко А., мл. научн. сотр., Хижняк С., ст. научн. сотр.,
ННЦ "Харьковский физико-технический институт",
Загинайлов Г., д-р физико-математических наук, проф.
ННЦ "Харьковский физико-технический институт",
Харьковский национальный университет имени В. Н. Каразина

ЭФФЕКТИВНЫЙ ЧИСЛЕННЫЙ МЕТОД АНАЛИЗА КОНВЕРСИИ МОД И ОМИЧЕСКИХ ПОТЕРЬ В ТЕРАГЕРЦОВЫХ ГИРОТРОНАХ

В настоящее время гиротроны являются перспективными источниками терагерцового (ТГц) излучения. Однако, работа ТГц гиротронов существенно осложняется действием чрезвычайно высоких омических нагрузок на стенки резонатора и появлением побочного излучения. Предлагается эффективный метод рассмотрения этих эффектов. Он позволяет без каких-либо упрощений свести краевую задачу для продольно неоднородного (нерегулярного) открытого волновода с импедансными стенками (которым моделируется резонатор ТГц гиротрона) к системе обыкновенных дифференциальных уравнений (СОДУ). Детально исследовано влияние омических потерь и конверсии мод на резонансные частоты и добротности резонатора ТГц гиротрона. Показано, что амплитуды паразитных мод могут быть сравнимы с рабочей модой в выходном сечении резонатора ТГц гиротрона. Также показана быстрая сходимость предложенного метода относительно числа рассматриваемых мод. Конкретные расчеты были выполнены для резонатора ТГц гиротрона разработанного в университете Фукуи, Япония, который работает на моде $TE_{3,5}$.

Ключевые слова: *нерегулярные волноводы, импедансные граничные условия, волноводы с потерями, методы поперечных сечений, задачи Неймана и Дирихле, терагерцовое излучение, терагерцовые гиротроны, резонаторы гиротронов, добротности, резонансная частота.*

UDC 621.318.3.01

A. Machulansky, Ph.D., B. Babych, stud.
Microelectronics department, Faculty of Electronics,
National Technical University of Ukraine "KPI", Kyiv

DIELECTRIC-METAL COMPOSITES WITH DISPERSED INCLUSIONS OF COPPER FOR MICROWAVE RANGE DEVICES

The comparative analysis of dispersive dependences of the coefficients of passing and absorption received on the basis of calculated according to the theory of the effective environment of Bruggeman and experimental values of complex effective dielectric permeability of dielectric-metal composites on the basis of disperse inclusions of copper in a dielectric matrix in the range of frequencies from 10^{-2} to 10^{10} Hz is carried out. It is established the range of frequencies of application of the theory of Bruggeman for the description of electromagnetic characteristics dielectric-metal structures on the basis of not magnetic metals. Possibility of use dielectric-metal structures as the shielding (protective) coverings for devices of microwave range is shown.

Key words: *dielectric-metal structure, effective dielectric permeability, shielding coverings, disperse inclusions.*

Introduction. The most perspective materials from the point of view of application in electronics for protection against microwave electromagnetic radiation, reduction of mutual influence of electromagnetic radiation of components of electronic devices, are composite dielectric-metal materials.

For development of such materials are generally used model (theoretical) and experimental approaches. But in the first case real frequency dependences of complex dielectric and magnetic permeability that is essential in the microwave range aren't considered. In case of experimental approach usually researches are limited to the narrow range of frequencies that is rather difficult and expensive process.

Therefore an important practical task is increase of reliability of forecasting of electromagnetic properties of materials in the wide frequency range which are used for development of the coverings absorbing and reflecting electromagnetic radiation with the set characteristics, for application in electronic devices.

In this work results of researches of dispersive characteristics of complex dielectric permeability with use of model of the effective environment dielectric-metal composites on the basis of inclusions of copper in the wide range of frequencies and an assessment of their response to electromagnetic influence are presented.

Experimental. Dielectric-metal composite materials were produced by the electromechanical mixing of nanodispersed metal filler with the binding matrix material at room temperature. The nanodispersed powder of Al and Cu was used as metal filler and the epoxy resin as a dielectric matrix. Series of epoxy resin-xAl (x=0÷50 vol. % is a content of the Al nanoparticles) and epoxy resin-xCu (x=0÷40 vol. % is a content of the Cu nanoparticles) compositions was prepared.

Dielectric and *ac* conductivity spectra were measured in the high-frequency range from 1 MHz to 2 GHz by the impedance method described in [4, 3]. The Novocontrol BDS 2100 coaxial sample cell and Agilent 4291B impedance analyzer were used. Cylindrical samples with a diameter of 2÷3 mm and length of 5÷7 mm were prepared. The pasted silver or evaporated gold electrodes were deposited on the flat surfaces of samples [5]. The results of experimental studies of the frequency dependence of the complex dielectric permittivity are presented in Figure 1.

For all studied compositions, dielectric/conductivity dispersion was observed. For the compositions with high metal content, above the percolation threshold, the conductivity plateau screens the power-law dispersion at lower frequencies (Fig. 1). Increase of the metal content results in the increase of the composite dielectric permittivity, loss and conductivity.

For the description and the analysis of complex dielectric permeability composite dielectric-metal structures are widely used model of the effective environment, in particular Bruggeman's theory [7]. According to this theory, effective complex dielectric permeability of a composite ε is connected with dielectric permeability ε_1 and volume concentration of the metal inclusions distributed in isotropic matrixes with dielectric permeability ε_0.

Calculation of dispersive characteristics of complex effective dielectric permeability for Bruggeman's theory composite dielectric-metal materials was carried out for structures in which as a dielectric matrix is epoxy, and as disperse inclusions copper was applied.

As input values of dielectric permeability of a connecting matrix ε_0 are used the experimental dispersive dependences received by us for epoxy which are brought in [1].

For calculation of dielectric permeability of metal inclusions are used ratios of model of Drude-Lorentz [5] taking into account values of plasma frequency ($1.64 \cdot 10^{16}$ Hz) and time of free run of electrons ($2.7 \cdot 10^{-14}$ s) for copper.

Examples of results of calculations of frequency dependences of complex effective dielectric permeability of the studied composites on the basis of Bruggeman's theory are given in Figure 2. For comparison in the same drawings are presented results of experimental studies of frequency dependences similar dielectric-metal structures that executed by us by method of dielectric spectroscopy and given in [6].

From Figure 2 shows that for composites on the basis of copper in the frequency range up to 100 MHz experimental and settlement dispersive characteristics have similar character, but in the range of frequencies higher than 100 MHz are observed considerable mismatches.

These distinctions can be caused by that for calculation of theoretical dispersive characteristics dielectric-metal structures value of dielectric permeability of ideal metal according to model of Drude-Lorentz which doesn't consider feature of electromagnetic characteristics of real nanodispersed metal inclusions and a microstructure of a composite.

For a response assessment of dielectric-metal composites on electromagnetic influence is executed calculation of coefficients of a transmission, reflection and absorption by method of matrixes of transfer [2].

The transfer matrix for a uniform layer is defined by its thickness d_i, index of refraction $n = \sqrt{\mu \cdot \varepsilon}$ and a corner of distribution of light θ_i.

$$T_i = \begin{pmatrix} \cos\varphi_i & \frac{-in_i}{\cos\theta_i}\sin\varphi_i \\ -i\frac{\cos\theta_i}{n_i}\sin\varphi_i & \cos\varphi_i \end{pmatrix} \quad (1)$$

The transfer matrix through all layered structure M is the multiplication of the transfer matrices through the individual layers M_i.

$$\hat{M} = \prod \hat{T}_i \quad (2)$$

© Machulansky A., Babych B., 2015

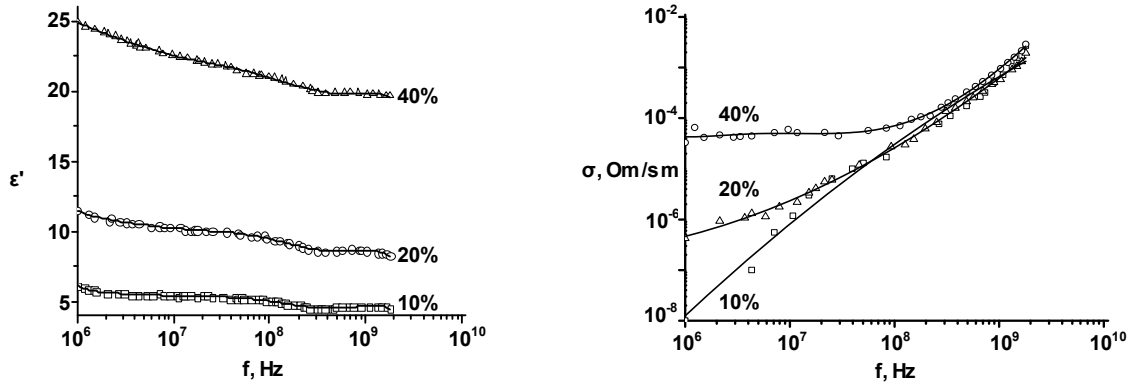

Fig. 1. Frequency dependence of the real part of dielectric permeability and conductivity of dielectric-metal composites at various concentrations of metal inclusions of copper

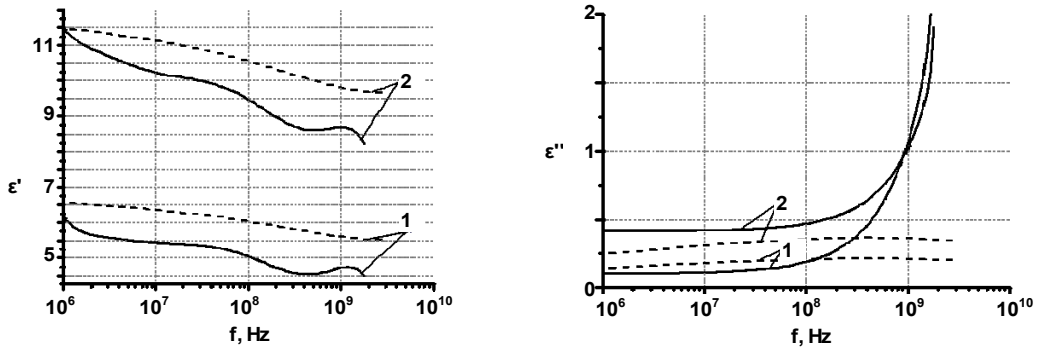

Fig. 2. Results of experimental studies (the continuous line) and numerical calculations for Bruggeman's theory (dashed line) of frequency dependences real and imaginary parts of complex dielectric permeability of dielectric-metal composites at various concentration of metal inclusions of copper: 1 – 10%, 2 – 20%

Amplitude coefficients of reflection and transmission are connected with transfer matrix elements through all structure by expressions:

$$r = \frac{(M_{11} + M_{12}p_1)p_0 - (M_{21} + M_{22}p_1)}{(M_{11} + M_{12}p_1)p_0 + (M_{21} + M_{22}p_1)} \quad (3)$$

$$t = \frac{2p_0}{(M_{11} + M_{12}p_1)p_0 + (M_{21} + M_{22}p_1)} \quad (4)$$

where

$$p_0 = n_0 \cos\theta_0 \quad (5)$$

$$p_1 = n_1 \cos\theta_1 \quad (6)$$

Here n_0 is the refractive index of semi-infinite environment which limits the structure from which the light falls, θ_0 is the angle of incidence, n_1 and θ_1 are appropriate parameters for the last layer.

Energy coefficient of reflection:

$$R = |r|^2 \quad (7)$$

Energy coefficient of a transmission:

$$E = \frac{p_1}{p_0}|t|^2 \quad (8)$$

Energy coefficient of absorption:

$$A = 1 - R - T \quad (9)$$

Examples of dispersive dependences of the coefficients of passing and absorption received on the basis of calculated according to the theory of the effective environment of Bruggeman and experimental values of complex effective dielectric permeability of dielectric-metal composites with dispersive inclusions of copper, presented in figure 3.

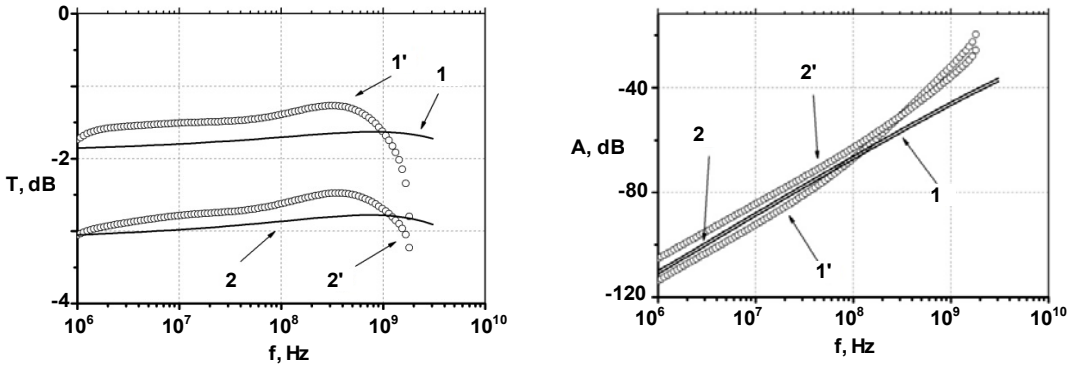

Fig. 3. Dispersive dependences of transmission coefficient (a) and absorption coefficient (b) of dielectric-metal covering 3 mm thick at various concentration of metal inclusions of copper: 1, 1' – 10%; 2, 2' – 20%; model coverings – a solid line, real covering – a dots

From figure 3 it is visible that in the range of frequencies up to 100 MHz high-quality coincidence of characteristics model and real dielectric-metal covering on the basis of disperse inclusions of copper is observed, but at frequencies over 100 MHz we have considerable distinctions.

Conclusions. Thus, the comparative analysis of dispersive characteristics of complex dielectric permeability and the response to electromagnetic influence received on the basis of model of the effective environment and experimental studies showed that at frequencies up to 100 MHz high-quality coordination of characteristics of model and real structures is reached, and in the range of frequencies from 100 MHz to 10 GHz Bruggeman's theory doesn't allow to describe authentically electromagnetic characteristics composite dielectric-metal structures in which metal inclusions are ideal metal of Drude.

Results represent considerable interest for forecasting of electromagnetic characteristics dielectric-metal structures and can be used for creation of devices of microwave appendices.

REFERENCE

1. *Borisova A., Machulyansky A., Yakimenko Y., et al.* "Microwave dielectric, magnetic and shielding properties of composites of metal nanoparticles and epoxy resin" // IEEE PIERS 2013 Stockholm – Progress In Electromagnetics Research Symposium (August 12–15, 2013) – p. 1246.
2. *Born M., Vol'f D.* Osnovy optiki. [Principles of Optics] – M.: Nauka, 1973 – 719 s.
3. *Bovtun V., Kempa M., Nuzhnyy D., et al.* "High-frequency dielectric spectroscopy of $BaTiO_3$ core – silica shell nanocomposites: problem of interdiffusion" – Journal of Advanced Dielectrics 1, No. 3, 309–317 (2011).
4. *Bovtun V., Kempa M., Nuzhnyy D., et al.* "Properties of $BaTiO_3$ confined in nanoporous Vycor and artificial opal silica" – Processing and Application of Ceramics 4 [3], 215–223 (2010).
5. *Machulyansky A., Rodionov M., Yakimenko Y., et al.* "Conductivity of metal (Al, Cu) – dielectric composites and modeling of the single- and multi-layer composite coatings for microwave applications" – IEEE XXXIV International Scientific Conference "Electronics and Nanotechnology" (April, 16–19th, 2014) – p. 164–167.
6. *Sokolov A. V.* Opticheskie svoystva metallov. – M.: FIZ-MAT-LIT., 1961. – 462 s.
7. *Vinogradov A. P.* Elektrodinamika kompozitnyih materialov / Pod red. B. Z. *Katsenelenbauma*. M.: Editorial URSS, 2001. – 208 s.

Submitted on 27.11.15

Мачулянський О., доц., канд. техн. наук, Бабич Б., студ.,
каф. мікроелектроніки, факультет електроніки,
Національний технічний університет України "Київський політехнічний інститут"

МЕТАЛ-ДІЕЛЕКТРИЧНІ КОМПОЗИТИ З ДИСПЕРСНИМИ ВКЛЮЧЕННЯМИ МІДІ ДЛЯ ПРИСТРОЇВ НВЧ ДІАПАЗОНУ

Проведено порівняльний аналіз дисперсійних залежностей коефіцієнтів проходження і поглинання, отриманих на основі розрахованих за теорією ефективного середовища Бруггемана та експериментальних значень комплексної ефективної діелектричної проникності метало-діелектричних композитів на основі дисперсних включень міді в діелектричній матриці в діапазоні частот від 10^{-2} до10^{10} Гц. Встановлено діапазон частот застосування теорії Бруггемана для опису електромагнітних характеристик метал-діелектричних структур на основі немагнітних металів. Показана можливість використання метал-діелектричних структур в якості екрануючих (захисних) покриттів для приладів і пристроїв НВЧ діапазону.

Ключові слова: *метал-діелектричні структури, ефективна діелектрична проникність, захисні покриття, дисперсійні включення.*

Мачулянский А., доц., канд. техн. наук, Бабич Б., студ.,
каф. микроэлектроники, факультет электроники,
Национальный технический университет Украины "Киевский политехнический институт"

МЕТАЛЛ-ДИЭЛЕКТРИЧЕСКИЕ КОМПОЗИТЫ С ДИСПЕРСНЫМИ ВКЛЮЧЕНИЯМИ МЕДИ ДЛЯ УСТРОЙСТВ СВЧ ДИАПАЗОНА

Проведен сравнительный анализ дисперсионных зависимостей коэффициентов прохождения и поглощения, полученных на основе рассчитанных по теории эффективной среды Бруггемана и экспериментальных значений комплексной эффективной диэлектрической проницаемости металлодиэлектрических композитов на основе дисперсных включений меди в диэлектрической матрице в диапазоне частот от 10^{-2} до 10^{10} Гц. Установлено диапазон частот применения теории Бруггемана для описания электромагнитных характеристик металлодиэлектрических структур на основе немагнитных металлов. Показана возможность использования металлодиэлектрических структур в качестве экранирующих (защитных) покрытий для приборов и устройств СВЧ диапазона.

Ключевые слова: *металлодиэлектрические структуры, эффективная диэлектрическая проницаемость, защитные покрытия, дисперсионные включения.*

UDC 621.3.032.266

I. Melnyk, Dr. of Tech. Sc.
Electronic Devices Department, Electronic Faculty,
National Technical University of Ukraine "KPI", Kyiv

METHODIC OF SIMULATION OF GUIDING OF SHORT-FOCUS ELECTRON BEAM IN THE EQUIPOTENTIAL TRANSPORTING CHANNEL OF HIGH VOLTAGE GLOW DISCHARGE ELECTRON GUNS

Methodic of simulation of guiding systems for short-focus electron beams, formed by High Voltage Glow Discharge Electron Guns (HVGDEG), is described in this article. The simulated guiding system consists of the parts of cylindrical or conical parts of tubes and included some focusing magnetic lenses. For providing of calculation the pressure distribution along the way of moving of beam electrons was taking into account. For simulation of electron beam parameters such important physical effects, as dissipation of electrons on the ions of residual gas, ion focusing and pinch-effect are considered. Special algorithm was realized for defining the losses of beam current, caused by settling of beam electrons on the channel's wall. The aim of simulation was minimization of losses of beam current with providing of necessary pressure difference between the discharge chamber of electron gun and the technological chamber.

Key words: *electron beam guiding system, electron beam evaporation equipment, magnetic focusing lenses, ion focusing, pinch-effect, beam current losses*

Introduction. HVGDEG are widely used in the different branches of industry for realizing such complex technological processes, as high-rate electron beam welding in the medium of soft vacuum, deposition of chemically-complex ceramic coatings in the medium of active gases, annealing of different materials and parts of mechanisms, as well as for refining of refractory materials [1, 2]. Among these operations special place occupied the

© Melnyk I., 2015

deposition of ceramic coatings in the medium of active gases. High-rate electron-beam deposition of dielectric, heat-resistant and hardness ceramic coatings in the medium of active gases allows obtaining the high-quality coatings with improved physical parameters [2].

One of the main problems of realizing this technological process is the difference of pressure, necessary for stable operation of HVGDEG and for realizing of coatings deposition. The pressure in gun's chamber is usually greater. In such conditions elaboration of beam guiding systems for providing the required difference of pressure is necessary [4]. In such guiding systems existed the losses of beam current, caused by settling of beam electrons on the channel's wall, and by this reason the beam power in some cases may be significantly reduced. Therefore, during elaboration of beam guiding systems, minimization of energy losses must be provided. For solving this complex optimization task the tools of computer simulation can be successfully used.

In the installations based on traditional electron guns with the heated cathode usually long-focus electron beams guided from region of high vacuum to the region of softer vacuum. Therefore electron beam guiding systems in the equipment, based on HVGDEG, have some important singularities. Firstly it is clear, that the formed beam must be transporting from the level of soft vacuum to the level of higher vacuum and this important fact cause the conditions of beam focusing in the plasma of ionized gas. The second important singularity is that electron beams, formed in HVGDEG, have a large convergence angle and usually can be considered as short-focus beams [1, 2]. Structure scheme of electron-beam installation for deposition of ceramic coatings with HVGDEG is presented at Fig. 1. Here arc discharge is used for maintaining the chemical reaction between the vapor and residual gas [1, 2].

Therefore, the aim of this article is describing of methodic of simulation of corresponded beam guiding systems with taking into account pointed out singularities of beam transporting in the installations for deposition of ceramic coatings, based on HVGDEG. Elaborated mathematical model and its computer realization allows to estimate the losses of beam current and to reduce it's by variation the geometry of guiding channel.

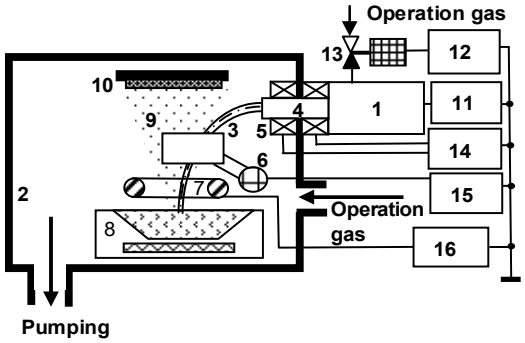

Fig. 1. Scheme of technological installation for deposition of ceramic coatings with HVGDEG:
1 – HVGDEG, 2 – technological chamber, 3 – electron beam, 4 – guiding system, 5 – focusing magnetic lenses, 6 – magnetic system of beam deflection, 7 – ring-like electrode for lighting arcdischarge, 8 – water-cooled crucible with evaporated material, 9 – vapor, 10 – substrate, 11 – high voltage power source, 12 – control system of beam current, 13 – electromagnetic valve, 14 – system for supplying of focusing lenses, 15 – system for supplying of deflection coil, 16 – systemfor supplying of arc discharge

Determination of problems and its' discussion. In papers [3, 4] was pointed out, that for obtaining necessary pressure difference between the discharge chamber of electron gun and the technological chamber solving of the problem of beam guiding from the soft to the higher vacuum in the equipotential channel in the magnetic field of focusing lenses is necessary. This task was considered and solved analytically in these works for the channel with non-linear geometry, described by simple power function:

$$r_{gc}(z) = A(z + z_0)^{\alpha}, \qquad (1)$$

where z – longitudinal coordinate, r_{gc} – radius of channel, z_0, α, A – coefficients, which are defined by input and output radiuses of the channel. But in the work [3] was pointed out and proved, that using of non-linear channel geometry in many cases is not profitable, usually cylindrical or conical geometry of channel is suitable for minimizing of the losses of beam current to the suitable value.

In general, for analyzing the process of electron beam guiding in the equipotential channel considered such interconnected tasks.

1. Calculation of pressure distribution along the length of channel with using the equations of vacuum technique [3].
2. Defined the magnetic fields of focusing lenses [4].
3. Calculation of boundary trajectory of the electron beam with taking into accounts self space charge of beam electrons, dissipation of electrons on the atoms of residual gas, ion focusing of beam in the guiding channel, as well as pinch-effect [4].
4. Considering of dissipation of electrons' initial velocity.

Optimization of guiding channel geometry was realised by the senescence solving of complex task of beam guiding for the different geometry parameters of the channel. The criterion of optimization was the minimizing of losses of beam power in the channel with obtaining the required difference of pressure between the gun's chamber and technological chamber. Mathematically this condition can be written as following equation:

$$I_{los}^{opt} = \min(I_{ls})\big|_{p_g - p_c = \text{const}}, \qquad (2)$$

or for the current of electron beam:

$$I_b^{opt} = \max(I_b)\big|_{p_g - p_c = \text{const}}, \qquad (3)$$

where I_{los} – losses of beam current, I_b – current of electron beam, p_g – pressure in the electron gun, p_c – pressure in the technological chamber.

It is clear, that the losses of beam current caused by the settling of electrons on the channels wall. Method of defining of the losses of electron beam will be considered in the next sections of the article.

Considering now separately the mathematic relations for solving the tasks 1–4, which were determinate beyond.

Simulation of the vacuum properties of guiding channel. With defined values of pressure in the gun chamber p_g and in the technological chamber p_c the necessary productivity of pumping means S_p defined from the main equation of vacuum technique [4]:

$$S_p = U_{gc}\frac{p_g - p_c}{p_c}, \qquad (4)$$

where U_{gc} – vacuum conductivity of the guiding channel.

As have been pointed out in the pervious section, usually for guiding of electron beam used the channels with the cylindrical or with the conical geometry. The conductivity of cylindrical channel with input diaphragm can be calculated with using following equations [3]:

$$W_{gc} = \frac{r_2^2 - r_1^2}{116\pi r_2^2 r_1^2} + \frac{l_c}{968 r_2^3},$$

$$U_{gc} = \frac{1}{W_{gc}}, \qquad (5)$$

and for the conical channel [3]:

$$U_{gc} = \frac{4vr_1r_2}{3l_c(r_1+r_2)}, \quad (6)$$

where r_1 – input radius of the guiding channel, r_2 – output radius of the guiding channel, l_c – length of the channel, W_{gc} – vacuum resistance of the channel, v – velocity of gases molecules. Corresponded equations for vacuum conductivity of the guiding channel with non-linear geometry were also obtained in paper [3]. It must be pointed out, that equations (5, 6) is correct for molecular regime of gas flowing. For calculation the vacuum conductivity of channel in intermediate regime must be used the following correcting coefficient J [4]:

$$J = \frac{1+202(r_1+r_2)\bar{p}+2653\left((r_1+r_2)\bar{p}\right)^2}{1+236(r_1+r_2)}; \quad U_i = JU_m, \quad (7)$$

where $\bar{p}$ – average pressure in the channel, U_i – conductivity of the channel in the intermediate regime, U_m – conductivity of the channel in the molecular regime. Geometrical parameters of cylindrical channel with input diaphragm and of conical channel are presented in Fig. 2.

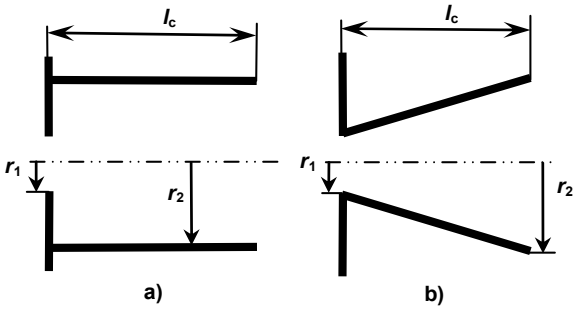

Fig. 2. Geometrical parameters of considered cylindrical (a) and conical (b) guiding channels

During simulation the guiding system value of pressure, obtained from the equations (4–7), was used for defining the ions' concentration along the distance of beam transporting. Corresponded equations for calculation the concentration of ions will be presented in the next section of the paper.

Simulation of interaction of the beam electrons with the ions of residual gas and defining of boundary trajectory of guided electron beam. As have been pointed out beyond, during analyzing propagation of electron beam through the residual gas, such important interconnected physical effects have been considered.

1. Dissipation of electrons on the gas ions corresponding to Rutherford interaction model [4].
2. Influence of self space charge of beam electrons [4].
3. Influence of space charge of ions of residual gas [4].
4. Magnetic focusing of electrons in the residual gas, or pinch-effect [4].

It is known, that for Rutherford model of dissipation the medium angle of deflection of moving particles defined from the equations [4]:

$$\mathrm{tg}\left(\frac{\theta_{\min}}{2}\right) = \frac{10^{-4}Z_a^{4/3}}{2\gamma\beta^2}, \ \mathrm{tg}\left(\frac{\theta_{\max}}{2}\right) = \frac{Z_a^{3/2}}{2\gamma\beta^2}, \quad (8)$$

$$\bar{\theta}^2 = \frac{8\pi r_b^2 n Z_a^2 z}{\beta^4\gamma^2}\ln\left(\frac{\theta_{\max}}{\theta_{\min}}\right), \ \beta = v_e/c, \ \gamma = \sqrt{1-\frac{v_e^2}{c^2}},$$

where $\theta_{\min}$ and $\theta_{\max}$ – correspondently maximal and minimal angles of dissipation, $\bar{\theta}$ – average angle of dissipation, Z_a – charge of nuclear of the residual gas, β – relation of velocity of electrons to the light velocity, v_e – velocity of electrons, r_b – radius of electron beam, n – concentration of the gas atoms, γ – relativistic factor.

Influence of ion focusing to the propagation of electron beam depended from the pressure of residual gas. Ions concentration on the axis of guiding channel n_{i0} defined by the following equation [3–5]:

$$n_{i0} = \sqrt{\pi}r_b^2 B_i p n_e \sqrt{\frac{M\varepsilon_0 n_e}{m_e U_c}}\exp\left(-\frac{U_c}{\varepsilon_0 n_e r_b^2}\right), \quad (9)$$

where B_i – level of the gas ionization, p – pressure in the considered part of the channel, U_c – voltage on the cathode of electron gun, n_e – concentration of electrons in the beam, m_e – mass of electron, ε_0 – dielectric constant, M – molecular mass of the gas atoms. Taking into account relations (8, 9), equations for defining the boundary trajectory of guided electron beam can be written in the following form [3, 4]:

$$f = \frac{n_e}{n_i - n_e}; \quad C = \frac{I_b\left(1-f-\beta^2\right)}{4\pi\varepsilon_0\sqrt{\frac{2e}{m_e}}U_c^{3/2}};$$

$$\frac{d^2r_b}{dz^2} = \frac{C}{r_b} - \frac{er_bB_{z0}^2}{8m_eU_0} + \frac{d\bar{\theta}}{dz}, \quad (10)$$

where U_0 – potential of gas ionization, B_{z0} – induction of the magnetic field on the axis of guiding system. Method of calculation of magnetic field for symmetric focusing lenses will be described in the next section of the article.

Calculation of induction of magnetic field and describing the construction of considered transporting system. For calculation of inductivity of magnetic field on the axis of guiding system with using of symmetric focused magnetic lenses was used well-known approximate relation [3, 5]:

$$B_{z0} = \frac{1{,}257\cdot10^{-4}I_lN_l}{2S_l} \times$$

$$\times\left(\frac{z_l+\frac{S_l}{2}}{\sqrt{\left(\frac{D_l}{3}\right)^2+\left(z_l+\frac{S_l}{2}\right)^2}} - \frac{z_l-\frac{S_l}{2}}{\sqrt{\left(\frac{D_l}{3}\right)^2+\left(z_l-\frac{S_l}{2}\right)^2}}\right), \quad (11)$$

where S_l – the length of non-magnetic gap, D_l –diameter of lens, I_l – current of lens, N_l – number of coils, z_l – lens position relatively to the input aperture of the guiding channel. Scheme of construction of symmetric magnetic lens with defined geometry parameters presented at the Fig. 3. During providing the calculations obtained value of B_{z0} substituted in the equation (10).

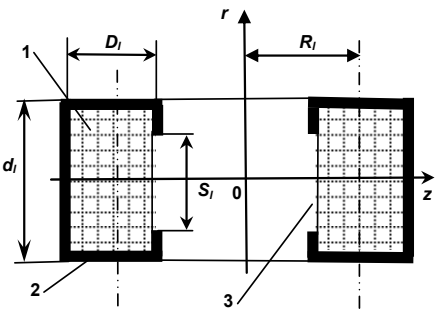

Fig. 3. Construction of symmetric magnetic lens. 1 – lens' coils, 2 – magnetic screen, 3 – non-magnetic gap

The guiding system with 2 magnetic lenses was considered as a suitable construction for experimental electron-beam installation. One of these lenses is located closely to the input aperture, and the second on the distance z_{l2} from it. Scheme of construction of simulated guiding system with defined positions of magnetic lenses presented at Fig. 4.

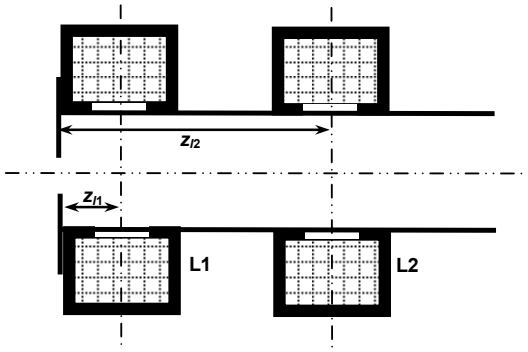

Fig. 4. Construction of simulated guiding system

Using of more focusing lenses usually is not practically profitable. It is caused by the complicity of correct tuning of multi-lenses guiding systems [5]. But in any case in elaborated software analysing of systems with 3, 4 and 5 lenses is also possible. Position of second lens is defined by solving the optimization task, described by relations (2, 3). Algorithm of solving of this task will be described below. Proposed method of calculation of the losses of beam current, caused by the settling of beam electrons on the channel wall, will be described in the next section of this paper.

Simulation of losses of the beam current. In the papers [1, 2] was pointed out, that for realising of technological processes of obtaining the ceramic coatings the minimal pressure of active gas in technological chamber is usually grater, than 10^{-2} Pa. In such physical conditions among the processes of beam interaction with the residual gas, described beyond, the process of dispersion of electrons on the ions of residual gas is most essential. The average angle of electrons' dissipation is defined from the equation (8). In such conditions of beam propagation influence of random collisions is the main factor that defined the radial distribution of beam current density. Therefore, corresponding to the probability theory, such distribution of current density can be accurately described by the Gauss law [4]:

$$j(r) = j_0 \exp\left(-\frac{r_b^2}{\beta_b^2}\right), \qquad (12)$$

where $j(r)$ – function of distribution of beam current density, j_0 – beam current density on the symmetry axis, β_b – parameter of Gauss distribution function.

For using of equation (12) in calculations of losses of beam current parameters of Gauss function j_0 and β_b must be conformed with the beam radius r_b, defined by the boundary beam trajectory, calculated from equation system (4–11). In paper [4] was proposed the numerical method for solving this mathematical task. With known beam radius r_b parameters j_0 and β_b can be calculated by solving such system of non-linear equations [4]:

$$\beta_b = \sqrt{\frac{I_b}{2\pi j_0}}\ ;\ \ \frac{I_b}{\pi r_b^2} = j_0 \exp\left(\frac{r_b^2}{\beta_b^2}\right). \qquad (13)$$

In the paper [4] also have been pointed out, that equation system (13) usually can be solved numerically in few steps with applying the Stephenson method and using such initial estimate [4]:

$$j_0 = \frac{I_b}{\pi r_b^2}. \qquad (14)$$

Therefore, for Gauss distribution of beam current density the losses of current can be defined as [4]:

$$dI_b = \pi\beta_b^2 j_0 \left\{\exp\left[-\left(\frac{r_b - \beta_b}{2}\right)^2\right] - \exp\left[-\left(\frac{r_b}{2}\right)^2\right]\right\}. \qquad (15)$$

Reducing of beam current in the corresponded iteration by coordinate z is defined as [4]:

$$I_b^n = I_b^{n-1} - dI_b^n, \qquad (16)$$

where n – number of iteration.

In the paper [3] also was proposed the method of calculation of beam current losses with taking into account the dispersion of velocity of beam electrons. In this case such equation must be used [3]:

$$\Delta t_e = \frac{r_b}{r_s}\int_{t_s}^{t}\left(\frac{r_s}{r_b}\right)^2 dt,\ \ \beta_b = \Delta t_e\sqrt{\frac{2kT_e}{m_e}}, \qquad (17)$$

where r_s – radial coordinate of boundary beam trajectory in the region of input diaphragm of guiding channel, T_e – the temperature of electron gas in this region. For the technological installations with HVGDEG, which scheme presented at Fig. 1, usually the value of kT_e is in range $kT_e \approx 4\ eV$ [3].

Algorithm of simulation. Calculation of beam losses in the guiding channel was realised in computer software with using following algorithm.

1. Input and verification of required model parameters, namely: pressure in HVGDEG p_g, pressure in technological chamber p_c, productivity of pumping S_p, number of coils of magnetic focusing lenses N_{l1} and N_{l2}, current of magnetic focusing lenses I_{l1} and I_{l2}, voltage on the cathode of electron gun U_c, starting angle of moving of beam electrons in the region of input diaphragm θ_s, starting radius of beam r_s, input and output radiuses of guiding channel r_1 and r_2 (Fig. 2), position of second magnetic lens z_{l2} (Fig. 4). Input parameters r_1, r_2 and z_{l2} are usually changed during the optimization of guiding system.
2. The losses of beam current at the pervious iteration calculated from the equations (13–17).
3. The gas pressure the corresponded iteration calculated from the equations (4–7).
4. The induction of magnetic field of focused lenses calculated from the equation (11).
5. Defining of ions space charge at the corresponded iteration with using equation (9). For providing this calculations substituted the value of gas pressure, obtained in the step 3.
6. Defining of average angle of dissipation of beam electrons with using equations (8).
7. Numerical integration of equation system (10) with using Runge-Kutt method of four order. In this step used the values of induction of magnetic field, obtained at the step 4, of ions' concentration, obtained at the step 5, and of the dissipation angle, obtained at the step 6.
8. Defining the beam losses on the corresponded iteration with using equations (13–17).
9. In the case $p < p_c$ – jumping to the step 3, in contrary – jumping to the step 10.
10. Defining the length of the channel l_c as l_c = z.
11. End of solving the task for the specified values of r_1, r_2 and z_{l2}.
12. Changing the values r_1, r_2 and z_{l2} and solving of optimization task (2, 3) with using the method of golden section.

13. End of solving of optimization task and output of simulation results.

Obtained simulation results will be presented and analyzed in the next section of the paper.

Obtained simulation results and its discussion. Testing of proposed simulation and optimization algorithm was provided for guiding system with two focused magnetic lenses, presented at the Fig. 4. Parameters of simulated system presented in Table 1, and the results of simulation in Fig. 5. Simulation and optimization of guiding system was realized with using the algorithm, described in the pervious section. This algorithm is based on equations (4–7).

***Table* 1**

Input parameters of considered guiding system

Parameter	Value
Acceleration voltage, U_c	10 kV
Starting angle of moving of electrons, θ_s	Changed
Starting current of electron beam, I_s	1 A
Starting radius of electron beam, r_s	1 mm
Diameter of input aperture of channel, r_1	9 mm
Diameter of output aperture of channel, r_2	25 мм
Pressure in the chamber of HVGDEG, p_g	5 Pa
Pressure in the technological chamber, p_c	0.1 Pa
Productivity of pumping, S_p	0.1 m^3/s
Wideness of lenses, d_l	5 sm
Wideness of non-magnetic gap, S_l	1 sm
Parameters of first lens	
Number of coils, N_{l1}	2000
Lens current, I_{l1}	2.5 A
Parameters of second lens	
Number of coils, N_{l2}	2000
Lens current, I_{l2}	Optimized
Position of second lens, z_{l2}	Optimized

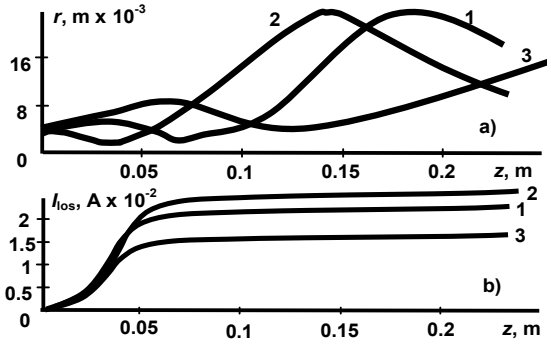

Fig. 5. Boundary trajectory (a) and dependences of losses of beam current from the distance of transporting (b) for different input angels θ_s. 1 – $\theta_s = 15^0$, 2 – $\theta_s = 20^0$, 3 – $\theta_s = 25^0$

On the Fig. 5, a, presented the boundary trajectories of electron beam, and on the Fig. 5, b – corresponded losses of beam current. Optimizing of location of second magnetic lens is realized by analyzing the position of maximum of radius of electron beam in the guiding channel. The current of second magnetic lens was 1.8 A.

Provided investigations shown, that in the case of optimal position of second lens the losses of beam current is not very great, not more than few percents of full current. The dependence of beam current losses from the distance of beam transporting giving important information about the optimal choosing of channel geometry and second lens position. Such cases are possible.

1. The dependence is dome-shaped with maximum, which located in the region of significant reducing the value of beam current. In this case reducing of losses is possible by the reducing the radius of input aperture. Another way of reducing the losses is optimizing the location of second lens.

2. The dependence is exponential, and the maximal losses are near the input aperture. In this case reducing of beam losses is possible by increasing the radius of input aperture.

3. The dependence is exponential, and the maximal losses are near the output aperture. In this case reducing of beam losses is possible by increasing the radius of output aperture.

4. The dependence is similar to linear, but it has some spikes, and in the region of spikes located the focusing lenses. Namely this case is presented at Fig. 5. Parameters of such system are close to optimal, and it can be successfully used in the industrial electron beam installations for deposition of ceramic coatings.

Conclusion. For providing optimization of guiding system in electron beam equipment with HVGDEG second magnetic lens must be located in the region of insignificant increasing of beam losses. In such conditions the current of second lens is choosing by necessary value of beam convergence angle and beam radius on the surface of evaporated material. The results of this work can be successfully used for elaboration the real guiding system for industrial evaporation equipment with HVGDEG.

REFERENCE

1. *Denbnovetskiy S. V.* "High voltage glow discharge electron sources and possibilities of its application in industry for realising of different technological operations". / S. V. Denbnovetskiy, V. G. Melnyk, I. V .Melnyk // IEEE Transactions on plasma science. – Vol. 31, №5, October, 2003. – P. 987–993.

2. *Denbnovetskiy S. V.* Technological Possibilities of High Voltage Glow Discharge Electron Guns. / S. V. Denbnovetskiy, V. I. Melnyk, I. V. Melnyk, B. A. Tugay // Electrotechnics and Electronics. № 5–6, 2009. – P. 189–192.

3. *Denbnovetskiy S. V.* "Modelirovanie transportirovki elektronnykh puchkov iz nizkogo v vysokiy vacuum s uchetom razbrosa teplovyh skorostey elektronov". / S.V. Denbnovetskiy, V. I. Melnyk, I. V. Melnyk // "Prikladnaya Fizika", №3, 2010. – P. 84–90.

4. *Melnyk I. V.* "Modelirovanie transportirovki elektronnykh puchkov iz oblasti nizkogo v oblast' vysokogo vakuuma v ekvipotentsialnom kanale". / I. V. Melnyk // "Elektronnoe Modelirovanie". – Vol. 23 (2001), №4. – P. 82–92.

5. *Molokovskiy S. I.* "Inensivnye elektronnye pushki i puchki" / S. I. Molokovskiy, A. D. Sushkov // Moskva, Energoatomizdat, 1991. – 304 p.

Submitted on 24.10.15

Мельник І., д-р техн. наук,
каф. електронних приладів та пристроїв, факультет електроніки,
Національній технічний університет України "КПІ", Київ

МЕТОДИКА МОДЕЛЮВАННЯ ТРАНСПОТРУВАННЯ КОРОТКОФОКУСНИХ ЕЛЕКТРОННИХ ПУЧКІВ, ЯКІ ФОРМУЮТЬСЯ ЕЛЕКТРОННИМИ ГАРМАТАМИ ВИСОКОВОЛЬТНОГО ТЛІЮЧОГО РОЗРЯДУ, В ЕКВІПОТЕНЦІАЛЬНОМУ КАНАЛІ

У статі описується методика моделювання систем транспортування короткофокусних електронних пучків, які формуються електронними гарматами на основі високовольтного тліючого розряду. Системам транспортування, яка моделюється, складається з відрізків циліндричних та конічних труб, що з'єднуються між собою, і містить декілька фокусувальних магнітних лінз. Під час проведення розрахунків враховувався розподіл тиску вздовж довжини каналу транспортування пучка. Під час розрахунку параметрів електронного пучка, який транспортується, враховувались такі важливі фізичні ефекти, як розсіювання електронів на іонах залишкового газу, іонне фокусування пучка та пінч-ефект. Для обчислення втрат струму пучка, які обумовлені осіданням електронів на стінках каналу, був розроблений спеціальний алгоритм. Ціллю моделювання була мінімізація врат струму пучка за умови забезпечення необхідного перепаду тиску між розрядною камерою гармати та технологічною камерою установки.

Ключові слова: *система транспортування електронного пучка, електронно-променеве устаткування для випаровування, магнітна фокусувальна лінза, іонне фокусування, пінч-ефект, втрати струму пучка.*

Мельник И., д-р технич. наук
каф. электронных приборов и устройств, факультет электроники,
Национальный технический университет Украины "КПИ", Киев

МЕТОДИКА МОДЕЛИРОВАНИЯ ТРАНСПОРТИРОВКИ КОРОТКОФОКУСНЫХ ЭЛЕКТРОННЫХ ПУЧКОВ, ФОРМИРУЕМЫХ ЭЛЕКТРОННЫМИ ПУШКАМИ ВЫСОКОВОЛЬТНОГО ТЛЕЮЩЕГО РАЗРЯДА, В ЭКВИПОТЕНЦИАЛЬНОМ КАНАЛЕ

В статье описывается методика моделирования систем транспортировки короткофокусных электронных пучков, формируемых электронными пушками на основе высоковольтного тлеющего разряда. Моделируемая система транспортировки состоит из соединённых отрезков конических или цилиндрических труб и включает несколько фокусирующих магнитных линз. При проведении расчетов учитывалось распределение давления вдоль длины канала транспортировки пучка. При расчете параметров транспортируемого электронного пучка учитывались такие важные физические эффекты, как рассеяние электронов на ионах остаточного газа, ионная фокусировка и пинч-эффект. Для вычисления потерь тока пучка, обусловленных оседанием электронов на стенках канала, был разработан специальный алгоритм. Целью моделирования являлась минимизация потерь тока пучка при обеспечении требуемого перепада давлений между разрядной камерой пушки и технологической камерой установки.

Ключевые слова: *система транспортировки электронного пучка, электронно-лучевое испарительное оборудование, магнитная фокусирующая линза, ионная фокусировка, пинч-эффект, потери тока пучка.*

UDC 615.849

N. Miroshnichenko, Ph.D., N. Melenevska, Ph.D., E. Kulich, Ph.D.,
L. Aslamova, Ph.D., S. Miroshnichenko, D.Sci., Prof., Yu. Hobta, engineer,
Training-research center of radiation safety, Faculty of Physics,
Taras Shevchenko National University of Kyiv,
Production Research Association "Teleoptic"

RESEARCH OF THE TRANSMISSION COEFFICIENTS DURING OF THE CONE-BEAM TOMOGRAPHY

This article investigates the transmission coefficients of the different environments on the example of aluminum and water. It was found that transmission coefficients calculated by the image brightness and by the doses are differed. It is shown that the correction of the transmission coefficients can be implemented by using corrective coefficients and hardware. It is experimentally found that the addition in the X-tract of the aluminum filter by corresponding size the mismatch of the transmission coefficients, calculated by the image brightness and the doses measured equipment, is negligible.

Key words: *tomography, transmission coefficient, water phantom, radiography, image color-coding.*

Introduction. The X-ray computer tomography (CT) is one of the most effective methods of the modern diagnostics, because it has a high degree of informativeness of the results [4, 8]. However, this information content has also high price as the cost of equipment, and as dose loads experienced by the patient. As in other investigation radiological methods, the CT use the X-rays.

As in other radiological methods of investigations in the CT uses X-rays (X-rays). Tomography is based on the principle of the X-ray sequential scanning of the human body at different angles [5]. CT allows the certain cross-layer image (slice) obtaining of the human body. Thus, the organism is investigated the layers with step in 0.5-10 mm, and each such slice requires to exposure of the patient to the imaging layer. With the help of proper software, the computer processes the received the X-ray absorption data of the human body slices and builds an image of the body at the scanning level. However, we can see by CT the structures that are not visible in conventional radiographs [1].

In the modern CT is carried out the image reconstruction. It allows to provide a 3D model of the investigated objects. For three-dimensional image obtaining the patient is gradually shifted along the rotation axis or rotation is carried out only the radiation sources. It allows to done a sequence of sections. From thus sections are reconstructed three-dimensional image [4]. In addition, for informativeness improving the of obtained image is made their coloring in anatomical colors based on appropriate software [2], figure 1.

X-ray beams pass through the patient's body and leave a mark on the film or CCD [3]. This trail forms a "flat" image of the internal organs of the patient superimposed on each other. Unlike CT, obtained by X-ray picture is a projection image that is not visible to human organs and tissues, but only their shadows. This kind of investigation has a lower informativeness, but it has a low cost of the equipment and a low patient's dose. Unfortunately, coloring such image in anatomic colors does not increase its informativeness due laths images of each other tissues.

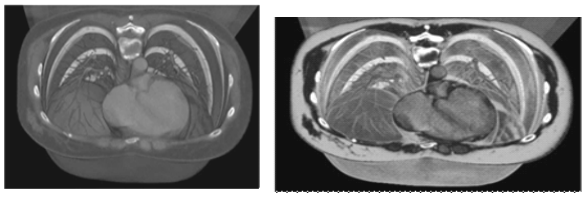

a) b)

Fig. 1. Visualization of a cross section of the chest cavity (the kind of top-down) in: a) gray scale coloring; b) coloring by using anatomical colors

So, the using of CT and X-ray technique advantages for diagnostic quality improving and patient`s radiation dose reducing in comparison with traditional CT is the great interest for medicine.

Problem formulation. X-ray tube emits a thin collimated, fan-shaped X-ray beam perpendicular to the long axis. This beam may be broad enough to cover the entire diameter of the body. Passed through a patient's x-ray beam is fixed system of special detectors. X-ray photons generate electrical signals in the detectors. The greater the intensity of the primary beam reaches the detector, the greater the electrical signal. If we fix the intensity of the transmitted radiation, it is possible to calculate the transmission coefficients of primary beam. During passing through the tissue, X-rays are attenuated, partly due to the absorption of energy, partly due to scattering. Attenuation can be described by the following formula [7]:

$$I = I_0 * e^{-md},$$

where I – the intensity of the transmitted radiation (i.e. radiation at the output of tissue); I_0 – the intensity of the incoming radiation (at the inlet of tissue); m – total linear attenuation coefficient of the tissue; d – the distance is passed by the radiation through the tissue (the thickness of tissue).

© Miroshnichenko N., Melenevska N., Kulich E., Aslamova L., Miroshnichenko S., Hobta Yu., 2015

The attenuation coefficient caused by the atomic number and electron density of tissue. So, atomic number and electron density, they are two parameters that define the properties of tissue to weaken the X-ray radiation. Please note that the transmission coefficient also depends on the energy of X-rays. The transmission coefficient described as follows:

$$K_{tr} = \frac{I}{I_0} * 100\% = e^{-md},$$

where K_{tr} – transmission coefficient of a tissue or a phantom simulating tissue [6].

Therefore, the tissue`s transmission coefficients measuring has the great importance for the diagnosis. For example, the presence of the fatty infiltration hepatic can be diagnosed by identifying portion abnormally low transmittance in the hepatic parenchyma.

X-ray slice informativeness increasing is possible by coloring in anatomical colors of the two-dimensional images. Such color-coding can be performed based on color matching of the tissue or organ its transmittance coefficient for slice. This generated two-dimensional image will be having the usual for the doctor coloring of the anatomical organs and tissues. Therefore, the informativeness increasing of the X-ray slices is possible by obtaining of the two-dimensional images colored in anatomical colors.

Methods. At present, in the first time in Ukraine Scientific and Production Association "Teleoptic" is developed a new generation of tomography – cone-beam computer tomography, figure 2. This complex can operate in three modes: radiography, fluoroscopy and tomography.

Fig. 2. Photo of the experimental complex

For correct coloring of tissues in the anatomical colors necessary to define the matching conditions of the transmission coefficients, recalculated by the image brightness and based on measurements dosimeter. To solve this problem we have been investigated transmission coefficients of in different environments for example aluminum and water.

The experiments were performed in a stationary tomography mode on the receiver Iona-RF-4335 with cesium-iodine screen manufactured by company Pingseng. For current and voltage generating was used generator Indico 200 ("CPI", Canada) and X-rays reproduced X-ray tube manufactured by company "Toshiba".

For checking of the correct transmission coefficients calculated on the basis of measured doses were carried out the experiments repeating similar measurements performed for the apparatus RUM-20M [6]. The measurements were taken at a voltage of 75 kV and a current of 50 mA and time 20...200 ms. As a test object for the study of the absorption coefficients was used the aluminum panels with size of 12*12 cm and thickness of 0...31 mm. In addition to these collimator plates on the X-ray tube has been installed filter with thickness of 2.7 mm. The dose beyond test object is measured by the dosimeter "Redcal", located at the input to the receiver, i.e. after the test object.

The transmission coefficients based on the image brightness calculated by the formula:

$$K_{tr}(B) = \frac{\frac{B}{H}}{\frac{B(2,7)}{H(1)}} * K_n,$$

where B – the measured image brightness, B(2,7) – the measured image brightness with thickness of the aluminum filter 2,7 mm, H – exposure, H(1) = 1 mAs – exposure with thickness of the aluminum filter 2,7 mm, K_n = 34 – normalization coefficient. It allows comparing the experimental data to tabulated values with [6].

The transmission coefficients based on the dosimeter measurements were calculated using the formula:

$$K_{tr}(D) = \frac{\frac{D}{H}}{\frac{D(2,7)}{H(1)}} * K_n,$$

where D – dose, measured after the test object, D(2,7) – dose, measured after the test object with thickness of the aluminum filter 2,7 mm.

The measurement results (Table 1) of the transmission coefficients K_{tr} (D) and K_{tr} (B) compared with similar measurements $K_{tr\ tabl}$, carried out for apparatus RUM-20M [6].

***Table* 1**

Parameters and results of the experiments

U, kV	I, mA	t, ms	H, mAs	Al, mm	Ktr tabl, %	Ktr(D), %	Ktr(B), %	D, mP	B
75	50	20	1	2,7	34,0	34,0	34,0	13,4	4395
75	50	20	1	4,7	20,0	19,3	24,8	7,6	3201
75	50	20	1	7,7	12,5	11,2	17,2	4,4	2224
75	50	20	1	12,7	6,0	3,6	7,2	1,4	935
75	50	40	2	20,7	1,9	1,6	3,6	1,24	935
75	50	80	4	28,7	0,8	0,8	1,9	1,22	983
75	50	200	10	33,7	0,5	0,6	1,6	2,45	2050

As seen from table 1, the transmission coefficients calculated by the measured doses and given in [6], are the same in view of measurement errors. Therefore, hereinafter are compared transmission coefficients, shown in [6] and the calculated by image brightness. In this series of experiments, the transmission coefficients calculated by

the image brightness, are significantly different from transmission coefficients recalculated by the measured doses. However, all three transmission coefficients are the same at the aluminum thickness of 2.7 mm, i.e. only the aluminum filter thickness on the collimator. So, transmission coefficients calculated by doses and image brightness are distinguished. It should be considered the relevant correction coefficients when calculating tomographic images.

In the next series of experiments as the test-objects were used water phantoms with different thicknesses. We check equality of the transmission coefficients, calculated based on the image brightness и shown in [6]. The measurements were carried out at a voltage of 75 kV and a current of 50...250 mA and time 4...20 ms. As a test object for studying the absorption coefficients were used water phantoms with a thickness of 0...14 cm. X-ray tube collimator was setting aluminum filter with thickness of 2.7 mm.The measurement results (Table 4) of the transmission coefficients K_{tr} (B), recalculated on the image brightness, compared with the same measurements $K_{tr\ tabl}$, shown in [8].

***Table* 2**

The experiment parameters and the results of the transmission coefficient calculation

U, kV	I, mA	t, ms	H, mAs	Water, sm	$K_{tr\ tabl}$, %	K_{tr}(B), %	B
75	50	10	0,5	0	100,0	100,0	1870
75	50	10	0,5	2	63,5	64,2	1200
75	50	20	1	5	32,2	36,9	1380
75	100	20	2	5	32,2	37,2	2781
75	100	20	2	7	20,4	23,9	1790
75	160	20	3,2	7	20,4	23,7	2842
75	100	20	2	10	10,3	12,7	950
75	160	20	3,2	10	10,3	13,0	1552
75	160	20	3,2	14	4,2	5,6	669
75	250	20	5	14	4,2	5,7	1060

As seen from Table 2, transmission coefficients calculated by the image brightness are differed from the literary in 20...30%.

For the identification of the transmission coefficients, counted on the image brightness, to the transmission coefficients, taken from [8], you must enter a correction factor K_c. This coefficient can be calculated by the formula:

$$K_c = \frac{K_{tr\,tabl}}{K_{tr\,tabl}(B)}.$$

The results of calculations are presented in Table 3.

***Table* 3**

Table of correction coefficients

$K_{tr\ tabl}$, %	K_{tr}(B), %	K_c
100,0	100,0	1
63,5	64,2	0,989
32,2	36,9	0,873
32,2	37,2	0,866
20,4	23,9	0,854
20,4	23,7	0,861
10,3	12,7	0,811
10,3	13,0	0,792
4,2	5,6	0,750
4,2	5,7	0,737

Therefore, the "right" transmission coefficients must be calculated according to the formula:

$$K_{trc}(B) = K_{tr}(B) * K_c .$$

In the next of experiment's series for correction by hardware of the transmission coefficients calculated based on the image brightness, to water phantom experimentally picked up an additional aluminum filter with different thicknesses. After obtained transmission coefficients based on the image brightness were compared to the similar transmission coefficients given in [6].

Measurements were carried out at a voltage of 99 kV and a current of 50...160 mA, and time of 20 ms. As a test object for the study of the absorption coefficients was used water phantom having a thickness of 0...14 cm. X-ray tube collimator had aluminum filter thickness was 2.7 mm. The front of the water phantom was located aluminum filter thickness 4.0 mm.

The measurement results the transmission coefficients of K_{tr}(B), based on the image brightness, table 4, compared to similar measurements $K_{tr\ tabl}$ given in [6].

***Table* 4**

The experiment parameters and the transmission coefficients

U, kV	I, mA	t, мс	H, mAs	Water, cm	$K_{tr\ tabl}$, %	K_{tr}(B), %	B
99	50	20	1	0	100,0	100,0	6070
99	50	20	1	2	69,3	68,4	4150
99	50	20	1	5	39,9	39,2	2378
99	50	20	1	7	27,6	27,3	1658
99	100	20	2	7	27,6	27,1	3296
99	125	20	2,5	7	27,6	27,0	4100
99	100	20	2	10	15,9	15,5	1885
99	125	20	2,5	10	15,9	15,6	2365
99	100	20	2	14	7,6	7,2	869
99	125	20	2,5	14	7,6	7,6	1146
99	160	20	3,2	14	7,6	7,5	1460

In these experiments, difference the transmission coefficients counted on image brightness to the transmission coefficients of obtained from the literature is 5%. Thus, the introduction of an additional aluminum filter thickness of 4 mm makes it possible to estimate the transmission coefficients based on image brightness without any additional recalculations using the correction coefficient.

Conclusions. The article presents the results of research the transmission coefficients of different environments on the example of aluminum and water. It was found that the transmission coefficient based on the image brightness significantly differ from the transmission coefficients converted at doses measured by the apparatus. It can lead to incorrect image color-coding and, respectively, distortion of the patient's diagnosis. Accuracy is 20...30%. It is unacceptable for use in medical practice.

Correction of the transmission coefficients may be implemented as using correction coefficients and hardware. Experimentally found that by adding an aluminum filter thickness of 4 mm in the X-ray path, the difference does not exceed 5%. This corresponds to a measurement error, and acceptable to the medical practice. Adding extra filter leads to lower absorbed dose to the patient, which also confirms the rationale use of additional filters.

REFERENCE

1. *Akimov P. N.* Comp'uternyj tomograph. – SPb.: Nevskij prospect, 2006.
2. *Jonathan C. Silverstein, Nigel M. Parsad, and Victor Tsirline*. Automatic Perceptual Color Map Generation for Realistic Volume Visualization. – J Biomed Inform., Dec; 41(6):2008. – P. 927–935.
3. *Miroshnichenko S. I.* Tcifrovye priyomniki rentgenovskikh izobrazhenij. – K.: Medicina Ukrainy, 2014. – 100 s.
4. *Paul Suetens* Fundamentals of medical imaging. – Cambridge: United Kingdom at the University Press, 2011, ISBN 978-0-521-51915-1 hardback. – 200 p.
5. *Pavlov I. V.*, Berdinskikh V. G. Tomographiya. – Rostov-n/D.: Feniks, 2005.
6. "Rentgenovskie diagnosticheskie apparaty" v 2 t., Tom 1. Pod red. N. N. Blinova, B. I. Leonova. M.: VNIIIMT, NPO "Jekran", 2001., S. 220.
7. Saratnikov A.M., Butusov P.N. Jadernaja fizika v medicine. – M.: Nauka, 2004.
8. *Volodin A. S.* Comp'uternaya tomographiya. – M.: Medihcina, 2002.

Submitted on 02.10.15

**Мірошниченко Н., канд. техн. наук, Меленевська Н., канд. техн. наук,
Куліч Е., канд. техн. наук, Асламова Л., канд. техн. наук,
Мірошниченко С., д-р техн. наук, проф., Хобта Ю., інж.,
Навчально-науковий центр радіаційної безпеки, фізичний факультет,
Київський національний університет імені Тараса Шевченка
Науково-виробниче об'єднання "Телеоптик"**

ДОСЛІДЖЕННЯ КОЕФІЦІЄНТІВ ПЕРЕДАЧІ ПРИ КОНУСНО-ПРОМЕНЕВІЙ ТОМОГРАФІЇ

У роботі досліджено коефіцієнти пропускання різних середовищ на прикладі алюмінію і води. З'ясовано, що коефіцієнти пропускання, розраховані за яскравістю зображення та за дозами, відрізняються. Показано, що корекція коефіцієнтів пропускання може бути здійснена за допомогою коригувальних коефіцієнтів і апаратними засобами. Експериментально знайдено, що при додаванні до складу рентгенівського тракту алюмінієвого фільтра відповідної величини розбіжність коефіцієнтів пропускання, розрахованих за яскравості зображення і по дозам, виміряних апаратурою, незначна.

Ключові слова: *томографія, коефіцієнт пропускання, водний фантом, рентгенографія, колірне кодування зображень.*

**Мирошниченко Н., канд. технич. наук, Меленевская Н., канд. технич. наук,
Кулич Е., канд. технич. наук, Асламова Л., канд. технич. наук,
Мирошниченко С., д-р технич. наук, проф., Хобта Ю., инж.,
Учебно-научный центр радиационной безопасности, физический факультет,
Киевский национальный университет имени Тараса Шевченко
Научно-производственное объединение "Телеоптик"**

ИССЛЕДОВАНИЕ КОЭФФИЦИЕНТОВ ПЕРЕДАЧИ ПРИ КОНУСНО-ЛУЧЕВОЙ ТОМОГРАФИИ

В работе исследованы коэффициенты пропускания различных сред на примере алюминия и воды. Установлено, что коэффициенты пропускания, рассчитанные по яркости изображения и по дозам, отличаются. Показано, что коррекция коэффициентов пропускания может быть осуществлена с помощью корректирующих коэффициентов и аппаратными средствами. Экспериментально обнаружено, что при добавлении в состав рентгеновского тракта алюминиевого фильтра соответствующей величины расхождение коэффициентов пропускания, рассчитанных по яркости изображения и по дозам, измеренных аппаратурой, незначительна.

Ключевые слова: *томография, коэффициент пропускания, водный фантом, рентгенография, цветовое кодирование изображений.*

UDC 615.47; 616-7

**S. Miroshnichenko, Ph.D., E. Volkov, post-graduate
Aeronavigation Institute, Electronics department,
National Aviation University
Teleoptic PRA, Ltd**

EXPERIMENTAL 3D OBJECTS STEREO X-RAY MEASUREMENT

3D X-Ray images were formed with the help of stereo effect. Object geomtrical size measurement realised with the help of stereo cursor formed on stereo image. For geometrical measurement stereo cursor must match the looked point of object in imagine volume between operator and monitor's screen. The formulas for cursor coordinates in imagened volume was devided. Cursor coordinates calculations based on known information about positions of X-ray tube and digital receptor. For error and effectiveness estimation experimental recearch. It was chosen for experimental measurement we used tomosynthesis scheme when only X-Ray tube moves. For X-ray imaging rectangular parallelepiped and anatomical was taking as test objects. Depth values and it's ratio errors was calculated.

Key words: *3D, X-Ray, stereo effect, anaglyph, geometrical measuring.*

Introduction. Characteristic feature of modern X-Ray is the transition from two-dimensional to three-dimensional images. Such transition conditioned by higher diagnostic value of three-dimensional images. In the USA for 12 years [6] from 1994 the number of computed tomography examinations increased by 3 times. But on the other hand this improvement leads to the growth of patient's effective dose, because three-dimensional images are obtained with computed tomography. For example effective dose for one chest computed tomography is approximately 8 mSv. At the same time chest X-Ray is only 0,1 mSv [3], 80 times less than similar computed tomography.

Modern new directions in a three-dimensional picture generation are allowed to decrease X-Ray doses on a patient, both in computed tomography and in tomosynthesis. But all of them are based on obtained

© Miroshnichenko S., Volkov E., 2015

large series of X-Ray projections. And three-dimensional models of investigated objects are reconstructed from these projections.

Alternative method for X-Ray three-dimensional images is the stereo X-Ray imaging. For such stereo images only two roentgenograms are needed. Three-dimensional image is based on stereo effect and the image is formed in operators mind [9]. That mean that for stereo three-dimensional image 0,1 mSv effective dose is needed. 80 times less then similar computed tomography. But in such stereo systems, there is no realized geometrical measuring of investigated object.

All process consists of directly stereo imaging, when separate images of the object under investigation are taking with some parallax (Fig. 1) Such two images forming result stereo pair [8]. Stereo mate is viewed by operator with special eyeglasses. With the help of stereo eyeglasses each of stereo pair's images is viewed only by a corresponding eye. So they combined in the brain to give the perception of 3D depth.

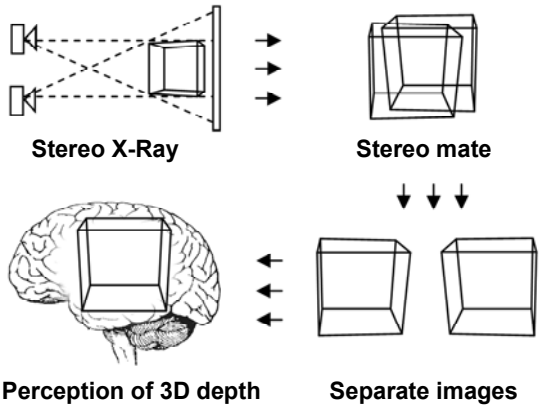

Fig. 1. Stereo X-Ray image reception

Stereo X-Ray does not conflict with the computed tomography systems and tomosynthesis, and can be an additional operating mode of modern complexes. Separate roentgenograms from such units (Fig. 2) are formed in stereo mates [5] and their amount depends on a solvable task.

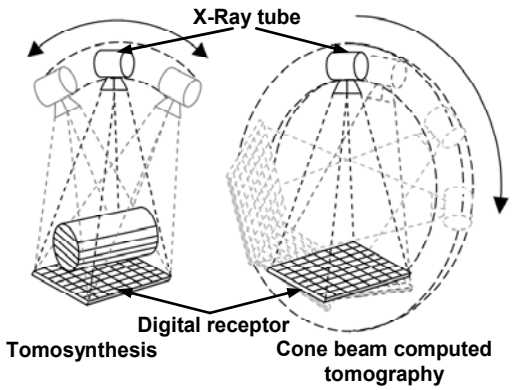

Fig. 2. Cone beam computed tomography and tomosynthesis units rotation geometry

There are some differences in tube and detector's motion geometry. For cone beam computed tomography or C-arm systems tube and detector rotates around the patient. The difference between cone beam and multi-planar tomography is the replacement of few detector rows by a full size receptor in the form of a flat panel [1]. Stereo radiography or tomosynthesis procedures can be also realized due to full sized X-ray detector and cone beam applying. In another word because there is no need to move patient through the gantry and only one rotation of the gantry is needed for image stack receiving. Another geometry type – position of the object under investigation and digital detector is fixed. Offset images of the stereo mates obtained only by X-ray tube moving. Such geometry is used in chest screening or mammography tomosynthesis [6].

Stereo X-ray allows extending possibilities of these systems and minimizing effective patient's dose. Stereo X-ray images can be obtained with smaller number of initial images than required for cross section synthesizing. For chest check stereo X-Ray effective dose is 0,1 mSv and for computed tomography is 8 mSv [8], that is 80 times higher then with stereo X-ray. Such 3D stereo mode allow realization of diagnostic functions on earlier stages with less radiation doses then during tomosynthesis, linear tomography or cone beam computed tomography.

Experimental. To provide diagnostic value in addition to construction of X-ray stereo images the implementation of the geometric measurement of the object is required.

Such measurement can be realized with the help of synthesized stereo cursor [3]. Its position in volume between viewer and monitor`s screen will correspond to certain coordinates of the space between X-ray tube and digital receptor. So when viewer will combine stereo cursor on the 3D X-ray image with object details the real coordinates of such details will be found. Based on such several obtained coordinates the geometrical measurement of the object is performed.

For experimental measurement we used tomosynthesis scheme when only X-Ray tube moves. We will calculate Z coordinate value of sought object's point. The distance between two positions (A and B) of X-ray sources is named base line of stereo image (Fig. 3). Also distances AA' and BB' are known, because it's the distance between X-ray tube and digital receptor. Line m lies in plane of intensifier screen of digital receptors. Let's take some point C of observable object. Geometrical measuring of an object is provided if coordinates of such few points can be found. Point A'' and B'' are projections of point C at digital receptor from X-ray sources, that are placed in points A and B. That means that distances A'A'' and B'B'' are known. Because coordinates of points A'' and B'' can be found from received offset images. Position of point C can be found. Will build line A'''B. It goes through point B and parallel to the line AA''. Two equal triangles ΔAA'A'' and ΔBB'A''' are obtained. Fro this two equal triangles $A'A'' = B'B''$. Will construct line n through point C, which will be parallel to the line m. That gave two similar triangles ΔBB''A''' and ΔBCC'''. From this two similar triangles $BB'/BC'' = A'''B'/CC'''$ and $BC'' = BB' - C''B'$. Because ABC'''C is a parallelogram it will be correct statement $CC''' = AB$. It will be correct $A'''B'' = A'A'' + B'B''$.

$$\frac{BB'}{BB' - C''B'} = \frac{(A'A'' + B'B'')}{AB}$$

Because $CC' = BC'$ depth coordinate value can be found as

$$CC' = \frac{AB \cdot BB'}{A'A'' + B'B''} - B'C$$

So if over displayed X-ray stereo image the image of stereo cursor will be formed, coordinates of such cursor will correspond to similar point of object and placed between digital receiver and X-ray sources.

Synthesized image of cursor creates with the same technology, which used for X-ray stereo image. In such system with fixed digital receptor and X-ray sources

inaccuracy of geometrical object measurements will defined by spatial resolution of digital receiver and inaccuracy of distance measurement between X-ray sources and receptor.

Three-dimensional cursor synthesis is based on referred above expressions. But method effective estimation without operators calling couldn't be done. For experimental measuring geometrical test object was produced. Test object has the form of rectangular parallelepiped. It was placed at 130 mm from digital receptor. At the same time the depth of geometrical test object is 238 mm. The distance between X-Ray tube and digital receptor was equal to 2 m. All operators viewed stereo image on the screen from distance in 60 cm. For such viewed distance parallax of the object's foreground is equaled to 12 mm.

The depth of this geometrical test object was measured. 15 operators were in experimental group.

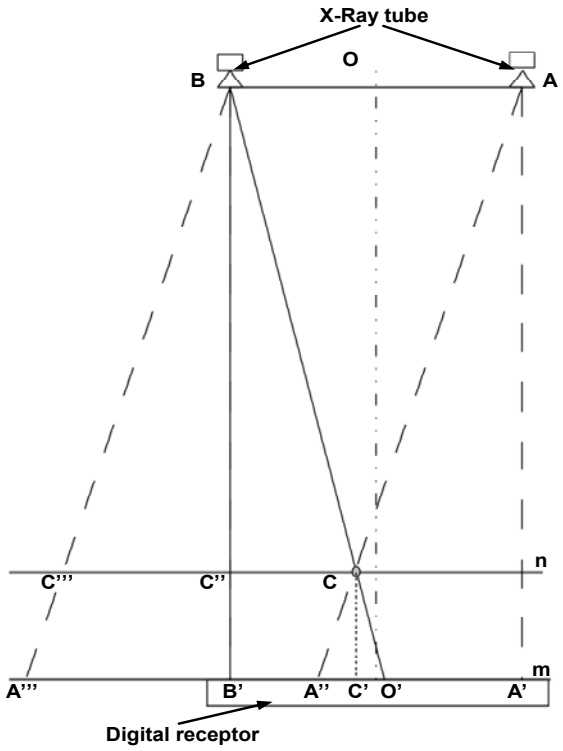

Fig. 3. Geometrical measuring based on X-Ray stereo imaging

Each operator measured object's depth for 3 times in two points of the test object. All operators saw 3D stereo rectangular parallelepiped in front of monitor's screen. For operators the dept of 3D stereo rectangular parallelepiped in front of monitor's screen was from 28 to 36 mm. That means that if operators will watch test object formed with stereoscopic effect from some distance object's size will be approximately the same for them.

For result estimation of measured value of the object's depth will use the value of confidence probability is equal to 95%. Test object's measured depth is

$$z = \bar{z} \pm \Delta z = 237{,}8 \pm 4{,}3\text{мм}, (P = 0{,}95)$$

Ratio error for measured result is

$$\varepsilon = \frac{\Delta z}{z} \cdot 100\% = 1{,}82\%$$

For next experimental measuring we used anatomical test-object. That simulate patient's thorax. Test object consist of ribs, bones and X-Ray test pattern that are based in container with paraffin (Fig. 4). Anatomic test have more details than rectangular parallelepiped and all they are with rounded lines without sharp edges. At the same time there are various values of contrast on image of such test object compared to the image of rectangular parallelepiped.

The distances between test object and digital receptor, digital receptor and X-Ray tube and between operator and monitor's screen are the same as in experiment with rectangular parallelepiped. Number of operators and measuring order the same.

Fig. 4. Anatomical X-Ray test object

Measurement result of depth between two points of anatomic test object is

$$z = \bar{z} \pm \Delta z = 50{,}3 \pm 7{,}3\text{мм}, (P = 0{,}95)$$

Ratio error for measured result is

$$\varepsilon = \frac{\Delta z}{z} \cdot 100\% = 14{,}5\%$$

For anatomic test object ratio error is much higher because it's more complicated to position stereo cursor on plain edge. But at the same time such measurement is much precise than during common radiography.

The next stage of our research is approbation of method jointly doctors and precision increasing of anatomical structures measurement.

Conclusions. Stereo X-Ray imaging allows decreasing patient's X-Ray dose dozen times. But in such 3D systems is no possibility of object's size measurements based on imaginary image. Proposed common stereo cursor forming model allows solving measurement sum in imaginary 3D volume. For 3D stereo image parameters evaluation resolution ratio, X-Ray contrast sensitivity and dynamic range values are proposed.

General approach to the principal tomographic systems constituent element moving permit to found individual cursor forming models for cone beam computed tomography, C-arms units, mammographic and linear tomosynthesis. Despite the well known synthetic 3D stereo effect in operator's mind information about quantitative measurement based on such images is lacking in the literature. This determinates necessity of experimental researches.

As the result of experimental research obtained that realized system don't worsen image quality parameters compared to 2D images; geometrical measurements of rectangular parallelepiped test object is 237,8 ± 4,3 mm, ratio error for measured results – 1,8%; analogous depth

measurement for anatomic test object is 50,31 ± 7,3 mm, ratio error – 14,5 %. We consider that such higher ratio error for anatomic test object is conditioned by smoothness and roundness of anatomical objects, organs and structures.

REFERENCE

1. *Baba R.* Using a flat-panel detector in high resolution cone beam CT for dental imaging. / R. Baba, K. Ueba, M. Okabe // Dentomaxillofacial radiology. – V. 33. – Tokyo. – 2004. – P. 285–290.
2. *Bruevich P. N.* Photogrametrya / P. N. Bruevich. – Moskwa: Nedra, 1990. – 285 p.
3. *Hofer M.* CT teaching manual / M. Hofer. – New York: Thieme, 2007. – 228 p.
4. *Miroshnychenko S. I.* Geometrical measuring at 3D stereoscopoc radiography. / S. I. Miroshnychenko, A. A. Nevhasymyy, E. V. Volkov // 2013 IEEE XXXIII International Scientific Conference Electronics and nanotechnology, April 16–19, 2013, Kyiv, Ukraine: abstracts. – Kiyv. – 2013. – P. 322–324.
5. *Miroshnychenko S. I.* 3D stereo algorithm for X-Ray units. / // / S. I. Miroshnychenko, E. V. Volkov // 2014 IEEE XXXIIIV International Scientific Conference Electronics and nanotechnology, April 15–18, 2014, Kyiv, Ukraine: abstracts. – Kiyv. – 2014. – P. 128–130.
6. NCRP Report No. 160 "Ionizing Radiation Exposure of the Population of the United States". – Mode of access: WWW. URL: www.ncrponline.org/2012/DAS_DDM2_Athens_4-2012.pdf. – Last access: 2015. – Title from the screen.
7. *Prokop M.* Spiral and multi-layer computed tomography / M. Prokop., M. Galansky. – New York: Thieme, 2003. – 1090 p.
8. *Schiffman H. R.* Sensation and perception: An integrated approach / H. R. Schiffman. – New York: John Wiley & sons, 2001. – 608 p.
9. *Valus N. A.* Stereoscopya / N. A. Valus. – Moscwa: Izdatelsttvo akademii nauk SSSR, 1962. – 373 p.

Submitted on 06.10.15

Мірошниченко С., д-р техн. наук, Волков Є. асп.
каф. електроніки, інститут Аеронавігації
Національний Авіаційний Університет
ТОВ "НВО Телеоптик"

ЕКСПЕРИМЕНТАЛЬНЕ СТЕРЕО РЕНТГЕНІВСЬКЕ ВИМІРЮВАННЯ ТРИВИМІРНИХ ОБ'ЄКТІВ

Тривимірні рентгенівські зображення було отримано із використанням стереоефекту. Геометричне вимірювання розмірів об'єкту виконується за допомогою стереокурсору сформованого на зображенні. Для геометричного вимірювання необхідно співставити курсор із шуканою точкою об'єкту в просторі між оператором і екраном монітору. Виконано розрахунок для знаходження координат курсору, що базується на відомих положеннях рентгенівської трубки і детектора. Для оцінки якості і ефективності виконаного розрахунку було проведено експериментальне дослідження. Для проведення експерименту було обрано схему апарату томосинтезу при якій переміщенню підлягає тільки рентгенівська трубка. В якості тестових об'єктів використано прямокутний паралелепіпед і анатомічні тестові об'єкти. Розраховані значення глибини між обраними точками і значення відносних похибок.

Ключові слова: *тривимірний, рентген, стереоефект, анагліф, геометричне вимірювання.*

Мирошниченко С., д-р технич. наук, Волков Е. асп.
каф. электроники, институт Аэронавигации
Национальный Авиационный Университет
ООО "НВО Телеоптик"

ЭКСПЕРИМЕНТАЛЬНОЕ СТЕРЕО РЕНТГЕНОВСКОЕ ИЗМЕРЕНИЕ ТРЕХМЕРНЫХ ОБЪЕКТОВ

Трехмерные рентгеновские изображения получено с применением стереоэффекта. Геометрические измерения размеров объекта выполняется при помощи стереокурсора, сформированного на изображении. Для геометрического измерения необходимо сопоставить курсор с искомой точкой объекта в пространстве между оператором и экраном монитора. Выполнено расчет для нахождения координат курсора, базирующийся на известных положениях рентгеновской трубки и детектора. Для оценки качества и эффективности выполненного расчета проведено экспериментальное исследование. Для проведения эксперимента выбрана схема аппарата томосинтеза, в котором перемещению подлежит только трубка. В качестве тестовых объектов. используем прямоугольный параллелепипед и анатомические тестовые объекты. Рассчитаны значения глубины между выбранными точками и значения относительных погрешностей.

Ключевые слова: *трехмерный, рентген, стереоэффект, анаглиф, геометрические измерения.*

UDC 004.716;52-87;004.735

S. Pidenko, stud., V. Kurashov, Ph.D
partment of Nanophysics and Nanoelectronics, Faculty of Radiophysics
Taras Shevchenko National University of Kyiv

ORGANIZATION OF SPACE AND GROUND SEGMENTS OF THE TRANSMISSION SYSTEM INMARSAT BGAN

In this article we would like to summarize the available data on the organization of interaction of satellites with satellite administration stations, location of arrangement of satellite administration stations and also coverage areas of the global bond. All conclusions in the article are made on the basis of data that are freely available nowadays.

Key words: *inmarsat bgan, space, ground, transmission system, global beam, wide beam.*

Introduction. INMARSAT BGAN system is one of the most perspective system of satellite transmission of information, for example, according to its certain parameters, it is better than the well-known Thuraya [2] satellite communication system. Therefore, it seems appropriate to analyze its basic characteristics in order to obtain reliable information about the quality and reliability of communications.

INMARSAT BGAN [1], [3] (Broadband Global Area Network) is a global coverage broadband communications network. It is Developed and maintained by the international satellite company INMARSAT (International Maritime Satellite Organization) (1979), provides for a broad range of communications services such as telephony, data transfer through TCP/IP traffic, general alert and hazards signals. Area network coverage covers almost all surface of the Earth, except for the Polar Regions, and according to the announcement of the company covers 85% of the globe area.

Main market for BGAN is corporate users who require remote connection with their fixed offices. However, at this time, the market offers devices for personal use.

Space segment communications. BGAN network is based on using the 3 satellites of the fourth generation, designed specifically for the provision of such networks. The satellites had been developed in the light of experience and advanced technologies. Duration life cycle of each of them is 10–15 years. **BGAN** Satellites provide transmission of analogue and digital information in (L) and (C) bands and are compatible with the satellites of the previous generation.

© Pidenko S., Kurashov V., 2015

Launch of the satellites to the orbit took place in 2005–2008. The satellites were put into positions close to the positions of the previous generation **INMARSAT** satellites. In 2008–2009, the orbits of the satellites have been adjusted to new positions where they are now. At the end of 2009, the company **INMARSAT** announced about putting into operation the BGAN network and the discontinuance of the previous generation R-BGAN network.

Power of each of the fourth generation satellites is 60 times the power of any of the predecessors; sensitivity of the receivers is 25 times higher. Number of channels exceeds the total number of channels of all five third-generation satellites. 12 times higher efficiency of frequency resource and in 16 times the number of channels.

The INMARSAT I–4 satellite set provides the following spatial characteristics of coverage:

- GLOBAL BEAM (GB) – which radiates in full disclosure and covers one-third of the Earth's surface (except for the polar regions, the maximum latitude of 76°);
- 19 wide beams – WIDE BEAM (WB) – that provide compatibility with the satellites of the previous generation to continue providing services Fleet F77 128 Kbps, Fleet F55 & F33, Maritime Mini-M and others.;
- 228 NARROW BEAM (NB), has been designed exclusively for high speed data network BGAN.

It should be noted that general use information published by the INMARSAT Company about fourth generation satellites is insufficient. At this time we did not find open detailed information associated with definitions of coverage areas. Do not know how switching between areas and the implementation of procedures for the transfer of control and maintenance (handover) is carried out. Do not know the final purpose of the GLOBAL BEAMs and WIDE BEAMs, organization of interaction between NARROW BEAMs. In addition unknown signal coverage area of these satellites in C-band.

General technical and spatial characteristics of satellites obtained from publicly available sources are given in Table 1.

***Table* 1**

General technical and spatial characteristics of satellites

Characteristics	INMARSAT I4-F1	INMARSAT I4-F2	INMARSAT I4-F3
Abbreviation	APAC	EMEA	AMER
Orbital position	143.5° E	25° E	98° W
Launch Date	March 2005	October 2005	February 2007
Term of exploitation		15 years	
Satellite weight		3000 Kg	
Battery size		45 m	
Emission power		67 dbw	
Width of the frequency band		126 MHz	
Number of channel frequency (200 KHz)		630	

The fact that these characteristics are not sufficient to study the technical parameters of the network, it was necessary to simulate some BGAN parameters and their clarification.

It should be noted that the relatively high technical characteristics of satellites allow to minimize the size of Earth stations (terminals) and reduce power load of path. These conditions, as well as the relatively low price of the terminal are one of the reasons to create the competition for systems developed earlier by other manufacturers and expansion to the end user market.

To date, it is known that INMARSAT Company is preparing to launch the fifth-generation satellites. Three satellites Inmarsat-5, designed and manufactured by Boeing. Launch to the orbit is planned for 2013–2014 from Baikonur (Kazakhstan) by "PROTON" missile carrier. Fifth-generation Satellites are designed to deploy a new global Global Xpress communications network.

***Table* 2**

Mathematically modeled and specified options

Characteristics	INMARSAT I4-F1	INMARSAT I4-F2	INMARSAT I4-F3
Position in orbit	142.7° E	25.5° E	98.2° W
Instability in orbit on a latitude	5° (2.5° ÷ -2.5)	4.5° (2.2° ÷ -2.3)	6° c (3°- -3°)
Angle aperture global beam (settlement)		17,4°	
Aperture wide angle beam (settlement)		≈1,4°	
Angle aperture narrow beam		≈0,6°	
Minimum area cover a narrow beam		≈2900 km	
Minimum diameter cover a narrow beam		≈850 km	
The estimated diameter of the cover in C band		≈4000 km	

In view of the announced information it is hard to foresee the future plans regarding the use of the fourth-generation satellites. There are several assumptions: the most probable, constellation of the fourth generation satellites will be the reconfigured and they will remain to ensure support of the long-standing Inmarsat services and the latest services such as BGAN and Global Xpress will be shifted to the fifth-generation satellites.

Ground segment organization. BGAN network ground segment consists of user and service components.

Service component is the ground control stations and coordination center.

Table 3

Service component

Object type	The location of the	Coordinates	Purpose
Coordination Center	London (United Kingdom)	51.51° N 0.12° W	Coordination of work of the entire BGAN network, ground control stations and coordination center as well as control of the satellites that are in orbit. Organization of maintenance, authentication and authorization.
station management and control (SAS)	Burum Square (Holland)	53.28° N 6.21° E	Main station management and monitoring in the European region. Manages network which is organized in zone I-4F1 of the satellite coverage
station management and control (SAS)	Fucino (Italy)	41, 99N 13, 54	Secondary control station and monitoring in the European region. Provides operation in I-4F1 satellite and I-4F2 coverage zone
Station management and control (SAS)	Paumalu (Hawaii)	21, 66N 158, 05W	Station management and monitoring in the Pacific region. Manages network which organized in I-4F3 satellite coverage zone

These positioning service components, ground segment of BGAN network, provide full overlay of the zones serviced by satellites and provide the ability to transfer information via satellites between regions.

According to advertising by INMARSAT Company, transmission of the signal between the zones covered by the satellites occurs through the management and control station. Transmission of the signal between management and control stations in the European zone is carried out through high-speed fiber-optic communication lines. For example, when transferring information between two correspondents, one of which is located in the Eastern Europe and another in America, the sequence is as follows: **User Terminal (Europe) → I4 F2 satellite → SAS Burum → fiber optic → SAS Fucino → I4 F3 satellite → user terminal (America).**

Analyzing data on the position of fourth-generation satellites in orbit and location of the ground control stations (table 3) identified an asymmetry in the transfer of information between ground stations (table 4), namely the absence of feeder lines between European and other regions. (Table 4)

Table 4

Control stations

Station	I4-F1		I4-F2		I4-F3	
	Az	El	Az	El	Az	El
Burum (Holland)	50,0	-34,2	157,5	25,4	283,4	-14,59
Fucino (Italy)	61,9	-36,2	163,7	38,7	387,2	-21,9
Paumalu (Hawaiian ost)	256,2	20,2	351,7	-72,2	90,9	20,9

I4-F2 satellite has two control stations – Burum and Fucino (Grey color- visible satellite -table 4). At the same time, the ground station Paumalu operates two satellites I4-F1 and I4 F3. This configuration of satellites and ground control stations is not reported or commented by INMARSAT Company.

Conclusions.

- Each satellite is connected through feeder lines with ground control and monitoring center;
- Absence of feeder lines between Euro-Asian and Asia -Pacific regions as well as Euro-Asian and American regions makes it impossible for a common, global, coordinated network of BGAN with center point in London;
- Absence of these lines can be explained by the additional earth station monitoring and control in the Atlantic or in the Asian region (most probably on the Indostan peninsula);
- Absence of explicit feeder lines, also may be due to the use by INMARSAT, additional, Transcontinental satellite links between SAS Paumalu and Burum and/or Fucino. Probably data line does not belong to the company and therefore INMARSAT don't announce it;
- Absence of explicit feeder lines could indicate use of INMARSAT Earth stations that were deployed under a legacy network (INMARSAT C, INMARSAT M, R-BGAN, etc.)

Lack of feeder lines may indicate a transfer Center coordination from London in the region of the Hawaiian Islands (low-probability hypothesis).

Thus, we can conclude that the company Inmarsat BGAN provides high-quality and stable connection almost in any part of the world, except the polar regions corresponding to the data, which the company introduced regarding coverage system.

REFERENCE

1. Inmarsat plc reports Preliminary Full Year Results 2014 [Електронний ресурс]: (London, UK: 5 March 2015. Inmarsat plc (LSE: ISAT.L), the leading provider of global mobile satellite communications services, presented following information for the twelve months ended 31 December 2014.) – Режим доступу до ресурсу: http://www.inmarsat.com/wp-content/uploads/2015/03/Inmarsat_plc_Preliminary_Results_2014.pdf

2. Thuraya [Електронний ресурс]: https://ru.wikipedia.org/wiki/Thuraya#cite_ref-1

3. INMARSAT (загальні відомості) [Електронний ресурс]: http://www.zora.ru/?a=show&id=32

4. Satellite Services Inmarsat [Електронний ресурс]: (Communications for Disaster and Emergency Response UIT – Forum Role of Telecommunmications in Disaster Management Bogotá, Colombia, 24-26 July 2012.) – режим доступу http://www.itu.int/en/ITU-D/Emergency-Telecommunications/Documents/Bogota_2012/presentation/PresentationAlejandraOrnesEn.pdf

Submitted on 19.06.15

Піденко С., студ., Курашов В., канд. фіз-мат. наук,
каф. нанофізики та наноелектроніки, факультет радіофізики, електроніки та комп'ютерних систем
Київский національний університет імені Тараса Шевченка

ОРГАНІЗАЦІЯ КОСМІЧНОГО ТА НАЗЕМНОГО СЕГМЕНТІВ ПЕРЕДАЧІ ІНФОРМАЦІЇ INMARSAT BGAN

В цій роботі ми спробували підсумувати доступні дані щодо організації взаємодії супутників із станціями управління і контролю, місця розташування станцій управління і контролю, і також зони покриття системи глобального зв'язку. Усі висновки у статті зроблені на основі даних, які на цей час знаходяться у вільному доступі.

Ключові слова: *inmarsat bgan, космічний сегмент, наземний сегмент, система передачі, глобальний луч, широкий луч.*

Пиденко С., студ., Курашов В., канд. физ.-мат. наук,
каф. нанофизики и наноелектроники, факультет радиофизики, електроники и компьютерних систем
Киевский национальный университет имени Тараса Шевченко

ОРГАНИЗАЦИЯ КОСМИЧЕСКОГО И НАЗЕМНОГО СЕГМЕНТОВ ПЕРЕДАЧИ ИНФОРМАЦИИ INMARSAT BGAN

В этой работе мы попытались суммировать, доступны данные по организации взаимодействия спутников со станциями управления и контроля, места расположения станций управления и контроля, и также зоны покрытия системы глобальной связи. Все выводы в статье сделаны на основе данных, которые в настоящее время находятся в свободном доступе.

Ключевые слова: *inmarsat bgan, космический сегмент, наземный сегмент, системы передачи, глобальный луч, широкий луч.*

UDC 621.3.088.7

S. Reschikoff, post grad. stud.,
Radio engineering faculty,
Ulyanovsk State Technical University

BASIC RELATIONS FOR CONSTRUCTION OF ADAPTIVE SYSTEM FOR LOW-FREQUENCY NOISE MEASUREMENT OF SEMICONDUCTOR DEVICES

Accuracy of flicker noise measurement is very important for reliability evaluation of semiconductor devices. To reduce measurement time and improve accuracy investigators must take into account the properties of low-frequency noise. To achieve this aim, it is appropriate to create an adaptive noise measurement system. Creating such measurement setup will contribute to the widespread use of noise spectroscopy in manufacturing.

Key words: *low-frequency noise, flicker noise, noise measurements, power spectral density, spectral exponent, corner frequency.*

Introduction. Low-frequency (LF) noise (also: 1/f noise, flicker noise, excess noise) of semiconductor devices is important subject of investigations. It exists in all types of semiconductor devices. Noise measurements are needed not only in research but also in manufacture. In the electronics LF noise is often used for reliability estimation of semiconductor devices [12]. LF noise measurements are also needed for creating low noise devices. For example in [3] are given noise spectra of solar cells and they contain flicker noise. LF noise can also be used as a test signal for research. In this case, it becomes necessary to precise meter built into the laboratory generator. Therefore noise measurement accuracy is very important.

It should be noted, in practice the researcher has to deal with a mixture of white noise (thermal and shot) and LF noise. Its power spectral density (PSD) is

$$G_{\text{nm}}(f) = \frac{A}{f^{\gamma}} + G_0 , \qquad (1)$$

where A is some constant, f is the frequency, γ is the spectral exponent, G_0 is white noise level.

Spectral exponent is often used as an informative parameter [2]. We reviewed publications in this field and found that researchers usually use home-made measurement setups. This shows that industrial measuring systems satisfying the interests of the researchers are not created. In [1] it is noted, that "...in the very low frequency range of the spectrum commercially available instrumentation does not allow to reach sufficient sensitivity for many application". In article [1] block diagram of an automated LF noise measurement system is provided. But the article [1] is devoted to the fact that the instrumentation itself contributes its own internal noise.

Although currently discrete Fourier transform (DFT) is widely used for measure of PSD, some researchers prefer to use the filter bank [2]. Others are engaged in research the problem of optimum bandwidth of analyzing filter [11]. Researchers usually leave the question of error estimation of LF noise parameters measurement without attention in their papers. There may be mentioned paper [5]. But it relates mainly to spectral analysis by DFT.

Method of noise exponent evaluation by three points. There is method of exponent evaluation by three points of spectrum. For calculate exponent we must measure PSD on some frequencies [9]:

$$\gamma_m = \log_k \frac{G_1 - G_{add}}{G_{add} - G_2} , \qquad (2)$$

where G_1, G_2 and G_{add} are PSDs of LF noise on first, second and additional points respectively; $k = \sqrt{f_2/f_1}$.

These measurements of PSD are accompanied by some random errors. In [9] expression for spectral exponent inaccuracy estimation is derived. We transform it to

$$\delta_{\gamma} = \frac{\sqrt{a^2 + b^2 + c^2}}{\left(k^{\gamma} - 1\right)\ln\left(k^{\gamma}\right)} , \qquad (3)$$

$$a = \left(k^{\gamma} + \frac{\left(f_{add}/f_0\right)^{\gamma}}{(1+\delta_{\text{BS}})} \right) \cdot \delta_{G1} ;$$

$$b = \left(1 + \frac{\left(f_{add}/f_0\right)^{\gamma}}{(1+\delta_{\text{BS}})} \right) \cdot \left(1 + k^{\gamma}\right) \cdot \delta_{Gadd} ;$$

$$c = \left(1 + \frac{\left(f_{add}/f_0\right)^{\gamma} k^{\gamma}}{(1+\delta_{\text{BS}})} \right) \cdot \delta_{G2}$$

and where $\delta_{G1}, \delta_{Gadd}$ and δ_{G2} are corresponding mean squared errors of PSD measurement, δ_{BS} is bias error, f_0 is corner frequency of LF noise, f_{add} is frequency of additional measurement point and index $k = f_{add}/f_1 = f_2/f_{add}$.

The relative root mean square random errors of PSD can be estimated by the expression [9]:

$$\delta_G \approx \sqrt{\frac{1}{T \cdot \Delta f_{eff}}} , \qquad (4)$$

where T is the duration of the integration, Δf_{eff} is effective filter bandwidth.

The relative systematic error (or bias error) of PSD can be estimated by the expression:

$$\delta_{\text{BS}} \approx \frac{\gamma(\gamma+1)}{24} \cdot \left(\frac{\Delta f_{eff}}{f} \right)^2 , \qquad (5)$$

where f is the frequency of the measurement point.

From (5) it is evident that δ_{BS} can be influenced by the choice of analysis filter bandwidth value. In the worst case ($\gamma = 3$) it is sufficient f < 0.4, that the bias error was less than 0.1. And in the case of $\delta_{\text{BS}} \ll 1$:

© Reschikoff S., 2015

$$a \approx \left(k^{\gamma} + (f_{add}/f_0)^{\gamma}\right) \cdot \delta_{G1};$$

$$b \approx \left(1 + (f_{add}/f_0)^{\gamma}\right) \cdot \left(1 + k^{\gamma}\right) \cdot \delta_{Gadd};$$

$$c \approx \left(1 + (f_{add}/f_0)^{\gamma} k^{\gamma}\right) \cdot \delta_{G2}.$$

But it is necessary to consider that the formula (5) obtained by expanding in a Taylor series and may give not trustworthiness estimation, when filter bandwidth is quite wide [10].

The principles of adaptive noise measurements. It is assumed that the averaging time is set. Influence of systematic errors of PSD measurement is compensated when relative analysis bandwidths are equal. A priori values of spectral exponent and corner frequency are needed to set the parameters of measurement. For example in case of the junction gate field-effect transistor the frequency exponent has the range $1 < \gamma < 1.5$. The corner frequency can range from below 10 Hz to above 1 kHz [6]. We can take the arithmetic mean as a priori. Let us build a graph for the expression (3) with $\gamma = 1; \delta_{BS} = 0.1;$ and $\delta_{G1}, \delta_{G_{add}}, \delta_{G_2}$ calculated on base: corner frequency is 1000 Hz, relative analysis bandwidth is 0.25, averaging time is 1 s. We can see that there is optimum value of k (Fig. 1).

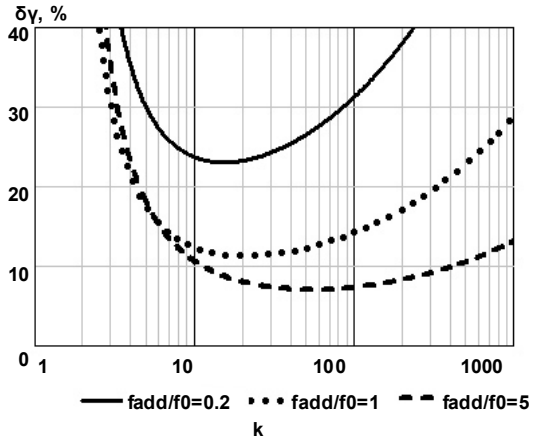

Fig. 1. Dependence of relative error on value of index k

Obviously, there is optimum ratio of additional and corner frequencies (Fig.2).

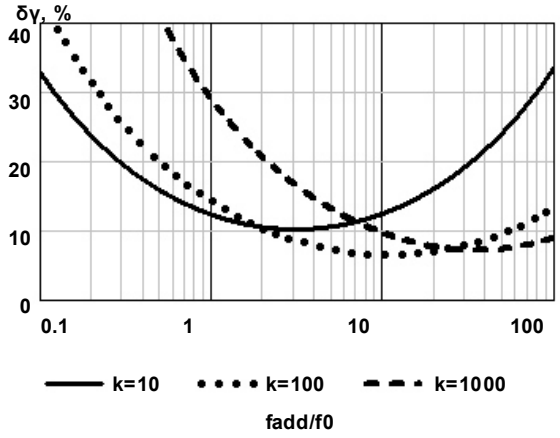

Fig. 2. Dependence of relative error on ratio of additional and corner frequencies

Increasing the error with decreasing ratio of the frequencies is associated with an increase in measurement errors PSD (with the same averaging time). If the measurement error of PSD remained constant, the error in the determination of γ with a decrease in ratio of the frequencies would only decrease.

To determine the optimum values of k and f_{add}/f_0 it is necessary to differentiate (3). From Fig. 1 and Fig. 2 it is obvious that the minimum points of functions $\delta_{\gamma}(k)$ and $\delta_{\gamma}(f_{add}/f_0)$ will have the same abscissa as the minimum points of functions $\delta^2_{\gamma}(k)$ and $\delta^2_{\gamma}(f_{add}/f_0)$ respectively. A preliminary squaring the expression (3) can simplify differentiation. Differentiating (3), one can form a system of two equations. And then we may determine the optimal values of f_{add}/f_0 and k. Graphical solution of the problem of determining the optimum parameters can be seen in Fig.3. It is surface plot for values of function of two variables $\delta_{\gamma}(f_{add}/f_0, k)$. The optimum parameters are the coordinates of the vertex of the surface. The surface of the function is built for the case: $\gamma = 1.5; \delta_{BS} = 0.1;$ and $\delta_{G1}, \delta_{G_{add}}, \delta_{G_2}$ calculated on base: corner frequency is 100 Hz, relative analysis bandwidth is 0.25, averaging time is 2 s.

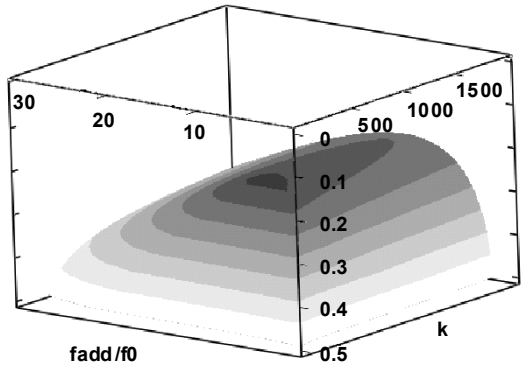

Fig.3. Surface plot of spectral exponent inaccuracy

From (3) it is clear, that the optimum values of k and f_{add}/f_0 may depend on the δ_{BS} and γ. Thus, it can be assumed that the table of optimal values k and f_{add}/f_0 for any γ can be made in advance.

Conclusion. The system can evaluate the difference between the real and a priori parameters of LF noise during measurement and make a decision on retuning filters. Although numerical simulation shows that the retuning of filters for adapting to a different value of γ is usually impractical. This is due to the fact that when retuning the filters (in the middle of the measurement time) is lost time that could be spent on the average at nonoptimal points (without retuning).

But it is known that DFT could be represented as result of processing by filters with different bandwidths by means of frequency averaging [7]. So, this algorithm is especially useful when using spectral analysis by DFT, because we may change k and f_{add}/f_0 for the same measurement. Moreover, the application of DFT gives other possibilities [8].

The paper [4] confirmed that the creation of an automated noise measurement system is an actual problem. But described in [4] measurement system is not adaptive.

Relations considered in the article allow us to estimate the measurement error of the LF noise parameters, and to find the optimum measurement conditions. Creating a measurement setup based on these principles, will greatly improve the accuracy of noise measurements.

REFERENCE

1. *Ciofi C.* Dedicated instrumentation for high sensitive, low frequency noise measurement systems / C. Ciofi, G. Giusi, G. Scandurra, B. Neri // Fluctuation and Noise Letters. – 2004. – V.4, №2. – P. 385–402.

2. *Gorlov M. I.* Measurement of the noise parameters of semiconductor devices / M. I. Gorlov, D. Yu. Smirnov, D. L. Anufriev // Measurement Techniques. – 2006. – V.49, № 12. – P. 1241–1245.

3. *Giusi G.* Applications of integrated solar cells in low noise instrumentation / G. Scandurra, G. Cannata, G. Giusi, C. Ciofi // Noise and Fluctuations (ICNF), 2013 22nd International Conference on. – P. 1–4.

4. *Giusi G.* Automatic measurement system for the DC and low-f noise characterization of FETs at wafer level / G. Giusi, O. Giordano, G. Scandurra et al // IEEE International Instrumentation and Measurement Technology Conference (I2MTC) 2015, 11–14 May 2015. – P. 2095–2100.

5. *Giusi G.* Estimation errors in $1/f^{\gamma}$ noise spectra when employing DFT spectrum analyzers / G. Giusi, G. Scandurra, C. Ciofi // Fluctuation and Noise Letters. – 2013. – V.12, №1.

6. *Northrop R. B.* Analysis and Application of Analog Electronic Circuits to Biomedical Instrumentation / R. B. Northrop. – Boca Raton, FL: CRC Press, 2012.

7. *Reschikoff S. E.* Adaptive Algorithm for interpretation of Low-frequency Noise DFT / S. E. Reschikoff // Informatyka, matematyka, avtomatyka, Sumy, 20–25 April 2015. – P. 171.

8. *Reschikoff S. E.* Advanced Noise Generator Method of Flicker Noise Measurement / S. E. Reschikoff // Fizyka, elektronika, elektrotehnika, Sumy, 20–25 April 2015. – P. 143.

9. *Reschikoff S. E.* Otsenka pogreshnosti opredeleniya pokazatelya spektra NCh-shuma / S. E. Reschikoff // 19-i Mezhdunarodnyi molodezhnyi forum "Radioelektronika i molodezh' v XXI veke", Kharkiv, 20–22 April 2015). Vol.2. – P. 164–165. (in Russian)

10. *Reschikoff S.* On reliability of optimum analysis bandwidth formula for flicker noise / S. Reschikoff // 1st International School and Conference on Optoelectronics, Photonics, Engineering and Nanostructures St. Petersburg, Russia, March 25–27, 2014. – P. 105–106.

11. *Sergeev V. A.* The systematic errors of the measurement of the parameters of low-frequency noise with a $1/f^{\gamma}$ spectrum / V. A. Sergeev, O. A. Dulov // Measurement Techniques. – 2008. – V.51, № 10. – P. 1122–1127.

12. *Vandamme L. K. J.* Noise as a diagnostic tool for quality and reliability of electronic devices / L. K. J. Vandamme // IEEE Trans. Electron Devices. – 1994. – V.41, № 11. – P. 2176–2187.

Submitted on 18.09.15

Резчиков С., асп.,
Радіотехнічний факультет,
Ульяновський державний технічний університет

ОСНОВНІ СПІВВІДНОШЕННЯ ДЛЯ СТВОРЕННЯ АДАПТИВНОЇ СИСТЕМИ ДЛЯ ВИМІРЮВАННЯ НИЗЬКОЧАСТОТНОГО ШУМУ НАПІВПРОВІДНИКОВИХ ПРИЛАДІВ

Точність вимірювання флікер-шуму дуже важлива для оцінки надійності напівпровідникових приладів. Щоб зменшити час вимірювання та підвищити точність дослідники повинні враховувати властивості низькочастотного шуму. Для досягнення цієї мети доцільно створити адаптивну систему вимірювання шуму. Створення такої вимірювальної установки буде сприяти широкому використанню шумової спектроскопії у виробництві.

Ключові слова: *низькочастотний шум, флікер-шум, шумові вимірювання, спектральна щільність потужності, показник спектра, частота перегину.*

Резчиков С., асп.,
Радиотехнический факультет,
Ульяновский государственный технический университет

ОСНОВНЫЕ СООТНОШЕНИЯ ДЛЯ СОЗДАНИЯ АДАПТИВНОЙ СИСТЕМЫ ДЛЯ ИЗМЕРЕНИЯ НИЗКОЧАСТОТНОГО ШУМА ПОЛУПРОВОДНИКОВЫХ ПРИБОРОВ

Точность измерения фликкер-шума очень важна для оценки надежности полупроводниковых приборов. Чтобы уменьшить время измерения и повысить точность исследователи должны учитывать свойства низкочастотного шума. Для достижения этой цели целесообразно создать адаптивную систему измерения шума. Создание такой измерительной установки будет способствовать широкому использованию шумовой спектроскопии в производстве.

Ключевые слова: *низкочастотный шум, фликкер-шум, шумовые измерения, спектральная плотность мощности, показатель спектра, частота перегиба.*

UDC 621.272.832.01

V. Sidorenko, Ph. D., Yu. Semenets, eng.,
S. Skripka, Ph. D., M. Gorovenko, stud., P. Kravchuk, stud.
Department of Quantum Radio Physics, Faculty of Radio Physics, Electronics and Computer Systems,
Taras Shevchenko National University of Kyiv

THE DEEPER INVESTIGATION OF SUBSURFACE INHOMOGENEITIES OF DIELECTRIC OBJECTS BY CONTROLLING THE LOCAL FIELD DIAGRAM OF THE PROBE OF A NEAR-FIELD MICROWAVE MICROSCOPE

In this paper we propose a new method for controlling the local field diagram of the probe of near-field microwave microscope during the scanning. This can be achieved by implementing the mechanism for changing the length of the probe needle during the scanning. We have shown experimentally that this method can be effective for obtaining images of a sample at different depths. The method allows recognizing the images of at least two delimited layers of a dielectric sample. We have shown the possibility of the investigation of internal inhomogeneities of dielectric medium without using complex algorithms to solve the incorrect inverse problems.

Key words: *near-field microwave microscopy, local field, near-field microwave introscopy.*

Introduction. At the present, the study of radio-physical methods for the remotely sensing of subsurface medium is a relevant and promising direction. A special place is occupied by the scanning near-field microscopy in optical and microwave ranges [7]. In the microwave range, the fundamental studies of local fields of electrodynamic systems awaken the keen interest. A local field, in contrast to a reactive near field, depends on the radius of the curve of the probe needle tip, on the geometry of the probe, and has a gradient character of the field distribution. The quasi-static approximation is applicable to this field in numerical calculations. Scanning near-field microwave microscopy has future trends of the application not only for the investigation of the surface distribution of inhomogeneities in dielectric and semiconductor samples, but also for the volume distribution of these inhomogeneities [6, 5, 8, 4, 3]. In other words, the matter concerns the near-field microwave introscopy or tomography.

To implement the method of near-field microwave introscopy, it is necessary to carry out a series of scans for a single sample, using different types of probes at different distances from a sample [3, 1]. Then, you need

© Sidorenko V., Semenets Yu., Skripka S., Gorovenko M., Kravchuk P., 2015

to solve the incorrect inverse problem which has not always a satisfactory solution and requires a lot of computer time for calculations.

The aim is to find the simple and effective methods for subsurface investigations of medium without having recourse to complex mathematical calculations. These methods should be of practical value for a wide range of tasks.

It is supposed that by controlling the diagram of probe element local field of the near-field microwave microscope we obtain the effective methods to investigate subsurface layer of a dielectric sample. The first and most logical solution was the use of different types of probe needles [3, 1, 2]. These needles have different local field diagrams. As a result, it is possible to obtain a set of different images. This allows us to get more information about the object: the slope of the crack, the shape and the depth of the defect, etc.

Experimental. In this paper, we have proposed the method for controlling the local field diagram of the probe which allows changing the effective depth of scanning a dielectric layer.

The idea is to control the local field diagram without changing the type of a probe needle. This can be achieved by implementing the mechanism for changing the length of the needle during scanning. In that case, the change of the length of the needle must be performed before the return of the probe needle to the starting point of scanning, that is, before the rescan of the surface area of a sample.

Shortening of the probe needle reduces the effective thickness of the dielectric layer, where the main part of the energy of the local field is concentrated. Thus, we can focus on the upper dielectric layer which has a thickness less than the effective depth of the scanning. Focusing on the lower layer can be implemented in software, after separating the image of the upper dielectric layer.

As shown in Fig. 1, with shortening the probe needle the microscope sensitivity decreases. Consequently, the noise will be visible in the picture. This is due to the parallel capacitance between the probe needle and the resonator body. Fig. 2. shows the dependence of the resonator frequency on the time. The frequency measurement was performed at rest. The experimental curve shows that the level of the wanted signal must be above 10 kHz. This is the first disadvantage of this approach which puts a restriction on the minimum length of the needle. To increase the sensitivity, and hence to remove this restriction, it is necessary to reduce the parallel capacitance. When increasing the length of the needle, starting from a certain value, the sensitivity is not increased. This is due to the losses of field energy by radiation.

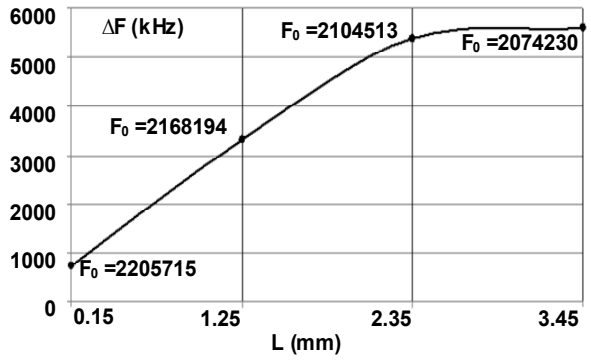

Fig. 1. The sensitivity (ΔF) of the microscope vs. The length L of the probe needle. The dielectric permittivity of a homogeneous sample ε ≈2.3. F_0 (kHz) – the frequency of the resonator without contact of the probe with the sample surface

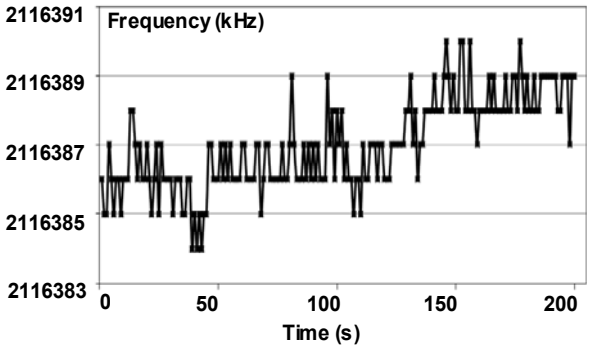

Fig. 2. The drift of resonator frequency was measured at rest. The readout of the frequency has 1s interval

For this experiment, two test samples of polymeric materials, with a dielectric permittivity in the range of 2–2.6, were taken. When scanning, the probe needle length was varied from 0.15 to 3.5 mm. Signal levels of resulting images were aligned on the perturbations of the upper layer. The comparison was made in relative units.

Fig. 3 shows the profile of images for the first sample. A strip in the layer A, 65 μm thick with ε≈1, is located at the depth of 30 μm. A strip in the layer B is located at the depth of 190 μm. We can see how the intensity of the layer B image is increasing in comparison with the intensity of the layer A image when the needle is lengthened. The ratio of the width of strips is ≈5.

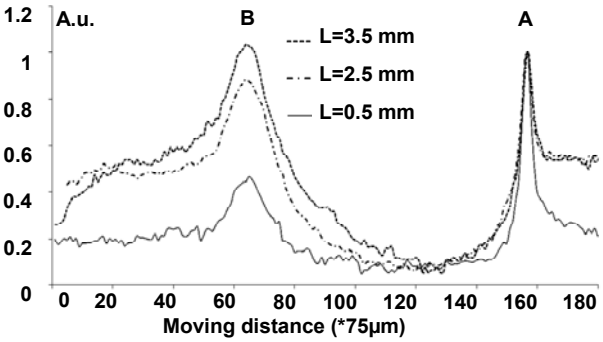

Fig. 3. The image profile of the distribution of dielectric inhomogeneity of a sample, composed of two layers. The dielectric permittivity ε of the sample is ≈2.3, of strips – ≈1. The distance between the layers is 95μm. The thickness of the layers – 65μm. L – the length of probe needle

In Fig. 4 the result of the investigation of the second sample is shown. The layer B is located at the depth of 220μm. The layer A – 30μm. The ratio of the width of the strips is ≈3. It is seen that for L> 2.3mm, the change of the ratio between the intensities of the layers is minor.

For comparison, we present profiles of previously obtained images of the sample in Fig. 4. This sample consists of two layers of polymeric material (ε ≈ 2.3). In each layer a notch in the form of strips of equal width is made. The scanning was performed at different heights above the sample surface. The length of the needle was not changed.

The diameter of the hole in the resonator is constant and is equal to 1 mm. The diameter of the probe needle is 0.7–0.8mm. The radius of the curve of the needle tip ≈15 mm.

As can be seen from Fig. 3 and Fig. 4, a diagram of the local field varies strongly enough to enable focusing on the upper dielectric layer. The scanning at different heights

above the sample surface does not offer visible advantage because the ratio of the intensities of the two layers does not change in fact.

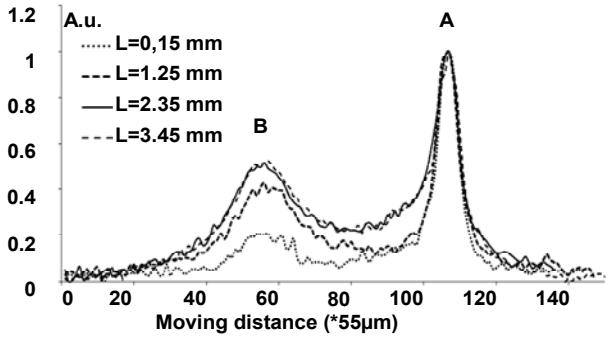

Fig. 4. The image profile of the distribution of dielectric inhomogeneity of a sample composed of two layers. The dielectric permittivity ε of the sample is ≈2.3, of strips – ≈1. The distance between the layers is 125μm. The thickness of the layers – 65μm. L – the length of probe needle

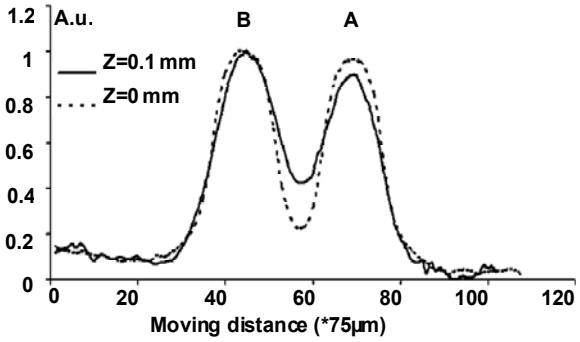

Fig. 5. The image profile of the distribution of dielectric inhomogeneity of a sample, composed of two layers. The dielectric permittivity ε of the sample is ≈2.3, of strips – ≈1. Z is a distance between the probe needle tip and the sample surface. The length of the needle is constant

For visual proof, we performed the scanning of the third sample made from the same material. For the first and the second scanning the minimum and maximum length of the probe needle were chosen. The strip of the layer A is 75 μm thick and is located at a depth of 40 μm. The strip of the layer B is 250 μm thick, and is located at a depth of 190 μm.

As shown in Fig. 6 the effective depth of the scanning significantly increases when the needle has a maximum length. The image of the upper layer is unchanged. The noise level becomes noticeable for the image Fig. 6. a), when the length of the needle is minimal. The image of the lower layer is easily visible only in the case of a maximum length of the needle.

Conclusions. Thus, by implementing the mechanism of changes in the length of the probe needle, we can get a set of several images of the sample surface during a single scan, which will be useful for the investigation of subsurface in homogeneities at different depths.

It was experimentally demonstrated, on several samples, the advantage of the proposed method in comparison with those known before, such as: the scanning at different heights above the surface of a sample, the use of different types of probe needles. Based upon these experimental results, we can conclude that this method of the scanning is quite effective to obtain images of the distribution of in homogeneities in at least two layers of a sample. We have an opportunity to get a sufficiently simple and effective way to investigate the internal in homogeneities of a sample. These results will be valid for all scales where the classical electrodynamics is applicable. The principal possibility to investigate the internal in homogeneities by the methods of near-field microscopy without complex mathematical calculations has been shown.

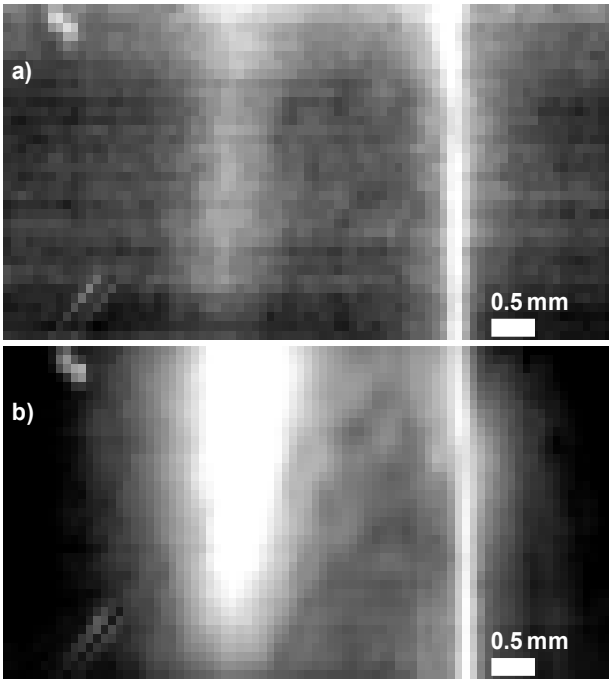

Fig. 6. The images of a dielectric sample with ε≈2 were obtained after the scanning of the surface area of the sample by near-field microwave microscope with an active probe. Dielectric permittivity ε of the inhomogeneity ≈1. The length of the needle: a) L = 0.15 mm; b) L = 3,45mm.

As would be expected, the task of near-field tomography or introscopy is achieved only through the control of the diagram of local field. Another approach, such as the change of the position of a probe needle tip above the sample surface, is very doubtful from a practical point of view.

REFERENCE

1. *Gaidai Yu. A.*, *Sidorenko V. S.*, *Semenets Yu. G.*, *Yaremkevych D. D.*, Features of ellipsoidal type probes with anizotropic field diagram in near-field microwave microscopy // IX international conference "electronics and applied physics" Taras Shevchenko National University of Kyiv, Faculty of Radiophysics. – 23–26 October 2013. Kyiv, Ukraine. – P. 68–69.

2. *Gaidai Yu. O.* Form preserving regularization in near-field microwave microscopy inverse problems / Yu. Gaidai, V. Sidorenko, O. Sinkevich, Yu. Semenets // Visnyk KU, Ser. Radio Physics & Electronics. – 2011. – Iss. 16. – P. 17–19.

3. *Gayday Yu. A.* Near-Field Microwave Tomography of Subsurface Dielectric Layers/ Yu. A. Gayday. V. S. Sidorenko and O. V. Sinkevych // Radioelectronics and Communications Systems. – 2012. – Vol.55. – No. 4. – P. 131–135.

4. *Gayday Yu. O.*, *Sidorenko V. S.*, *Semenets Yu. G.*, *Gorovenko M. V.*, Interface system near-field microwave microscope with a computer via a USB interface and control experiment // XIVth international young scientists' conference on applied physics Taras Shevchenko National University of Kyiv, Faculty of Radio Physics, Electronics and Computer System. – 11–14 June 2014. Kyiv, Ukraine. – P. 223–224.

5. *Gayday Yu. O.*, *Sidorenko V. S.*, *Sinkevich O. V.* Near-field microscope for investigation of dispersion of dielectric permittivity // Bulletin of Taras Shevchenko National Univ. Ser. Radio Physics & Electronics. – 2008. – Iss. 11. – P. 16–18.

6. *Gaykovich K.* Scanning near-field electromagnetic tomography // Journal of "NANO and MICROSYSTEM TECHNIQUE". – 2007. – Iss 8. – P. 50–65.

7. *Mironov V. L.* Fundamentals of the scanning probe microscopy – M.: Tekhnosfera, 2004. – 144 p.

8. *Sinkevich O. V.*, *Sidorenko V. S.*, *Gaidai Yu. A.* Near-field microwave microscope with the active probe // Scientific works Fourth International Young Scientists Conference "Problems of Optics & High Technology Material Science SPO 2003". – Kyiv (Ukraine). – 2003. – P.45–46.

Submitted on 15.04.15

Сидоренко В., Семенець Ю., Скрипка С., Горовенко М., Кравчук П.
каф. квантової радіофізики, факультет радіофізики, електроніки та комп'ютерних систем
Київський національний університет імені Тараса Шевченка

ЗБІЛЬШЕННЯ ГЛИБИНИ СКАНУВАННЯ ПІДПОВЕРХНЕВИХ НЕОДНОРІДНОСТЕЙ ДІЕЛЕКТРИЧНИХ ОБ'ЄКТІВ ШЛЯХОМ КЕРУВАННЯ ДІАГРАМОЮ ЛОКАЛЬНОГО ПОЛЯ ЗОНДА БЛИЖНЬОПОЛЬОВОГО МІКРОХВИЛЬОВОГО МІКРОСКОПА

У статті запропоновано новий метод, який дозволяє керувати діаграмою локального поля зонда ближньопольового мікрохвильового мікроскопу в процесі сканування. Цього можна досягти, реалізувавши механізм зміни довжини голки зонда під час сканування. Експериментально показано, що даний метод може бути ефективним для отримання зображень розподілу діелектричної неоднорідності зразка на різних глибинах. Він дозволяє розпізнати зображення принаймні двох розмежованих шарів діелектрика. Ми показали можливість дослідження внутрішніх неоднорідностей діелектричного середовища, не вдаючись до складних алгоритмів розв'язання обернених некоректних задач.

Ключові слова: *ближньопольова мікрохвильова мікроскопія, локальне поле, ближньопольова мікрохвильова інтроскопія.*

Сидоренко В., Семенець Ю., Скрипка С., Горовенко М., Кравчук П.
каф. квантовой радиофизики, факультет радиофизики, электроники и компьютерных систем
Киевский национальный университет имени Тараса Шевченко

УВЕЛИЧЕНИЕ ГЛУБИНЫ ИССЛЕДОВАНИЯ ПОДПОВЕРХНОСТНЫХ НЕОДНОРОДНОСТЕЙ ДИЭЛЕКТРИЧЕСКИХ ОБЪЕКТОВ ПУТЁМ УПРАВЛЕНИЯ ДИАГРАММОЙ ЛОКАЛЬНОГО ПОЛЯ ЗОНДА БЛИЖНЕПОЛЕВОГО МИКРОВОЛНОВОГО МИКРОСКОПА

В статье предложен новый метод, позволяющий управлять диаграммой локального поля зонда ближнеполевого микроволнового микроскопа в процессе сканирования. Этого можно достичь, реализовав механизм изменения длины иголки зонда во время сканирования. Экспериментально показано, что данный метод может быть эффективным для получения изображений распределения диэлектрической неоднородности образца на различных глубинах. Он позволяет распознать изображения по крайней мере двух разграниченных слоёв диэлектрика. Мы показали возможность исследования внутренних неоднородностей диэлектрической среды, не прибегая к сложным алгоритмам решения обратных некорректных задач.

Ключевые слова: *ближнеполевая микроволновая микроскопия, локальное поле, ближнеполевая микроволновая интроскопия.*

UDC 538.945

V. Shaternik, Dr.Sc., A. Shapovalov, Ph.D., O. Suvorov, Ph.D Stud., M. Belogolovskii, Dr.Sc.
Department of Superconductive Electronics,
G. V. Kurdyumov Institute for Metal Physics of NAS Ukraine,
O. Prokopenko, Ph.D., M. Pustovoit, Stud.
Faculty of Radiophysics, Electronics and Computer Systems,
National Taras Shevchenko University of Kyiv

NOVEL FUNCTIONALITY OF JOSEPHSON JUNCTIONS WITH RESONANCE-PERCOLATING CHARGE TRANSPORT

The new type of Josephson junctions with a resonance-percolation charge transport have been fabricated and investigated. Measured I–V curves of these junctions demonstrate that the well-known characteristic parameter of these junctions (named the I_CR_N product) has record values. By using an atomic force microscope we have investigated a relief of the every layer of the fabricated Josephson junction, as a result it has been demonstrated a possibility to observe a formation of the cluster structure of tungsten in silicon layer in the Josephson junction barrier on nanosized level.

Key words: *Josephson junction, Andreev reflection, resonance-percolation charge transport, atomic force microscope, semiconductor, metal clusters*

Introduction. The direct tunneling process through an S-I-S junction (here S is a superconductor, I is a tunnel barrier, as a result Andreev reflections are negligibly small in the S-I interfaces) depends on electron spectrum and on distribution of electron excitations in the electrodes, while charge transport through the Andreev bound state (BS) resonance levels carry Josephson superconducting current across an S-N-S junction [2]. The case of novel type Josephson heterostrucrure [1] like as superconductor – doped semiconductor – superconductor is perspective taking in account a possibility of realization in it of the both cases of tunneling (the resonant and well known direct) in dependence on the dopant (for example, W) concentration value. It means there is here a possibility of realization of the resonant tunneling process through multiple electron (hole) states localized in the dopant clusters inserted in the barrier (for example, in a doped semiconductor). And on the other hand it is interesting to do experimental investigation (by atomic force microscope (AFM) and other techniques) of these semiconductor barriers with the dopant clusters inserted in its.

Experiment. Among different low-temperature superconductors MoRe compounds are known to have relatively high critical temperatures T_c up to 12 K, high hardness and mechanical strength. Due to these factors, this material is very opportune for hybrid superconducting heterostructures. 100 nm thick MoRe films with 45 % Re (their T_c was about 10 K) were deposited onto dielectric substrates at ambient temperatures by using dc magnetron sputtering technique in a vacuum chamber with argon at 1 Pa. W:Si barrier interlayers as well as Nb:Si films offer two degrees of freedom to adjust the junction parameters: the barrier thickness d and the tungsten content C_W. To form Si tunnel barriers with nanoscale W dopants, we used a target which consists of a pure Si wafer and a number of tungsten wires. The tungsten concentration C_W in the mixture was changed from 0 to 10 at %. A schematic view of the fabricated junctions is given in fig. 1.

Current-voltage characteristics (I–V curves) of the fabricated tunnel junctions and Josephson junctions have been measured at various temperatures. The deposited multilayers such as Si(W) layer on the substrate (a polycrystalline Al_2O_3) and MoRe layer on the Si(W) one have been investigated experimentally by AFM.

© Shaternik V., Shapovalov A., Suvorov O., Belogolovskii M., Prokopenko O., Pustovoit M., 2015

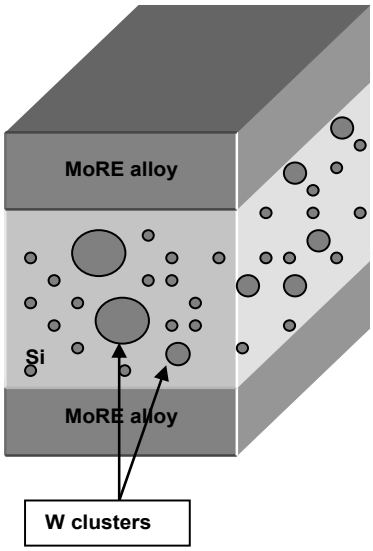

Fig. 1. Schematic view of the fabricated MoRe-Si(W)-MoRe junction

Results. MoRe-Si(W)-MoRe junctions (at small tungsten concentration C_w~4at%.) demonstrate existence in them the tunneling effect [5] (see curves 1, 2 in the fig. 2 a) at bias voltages close to en energy of the impurity level [3] formed by the tungsten cluster in a silicon barrier.

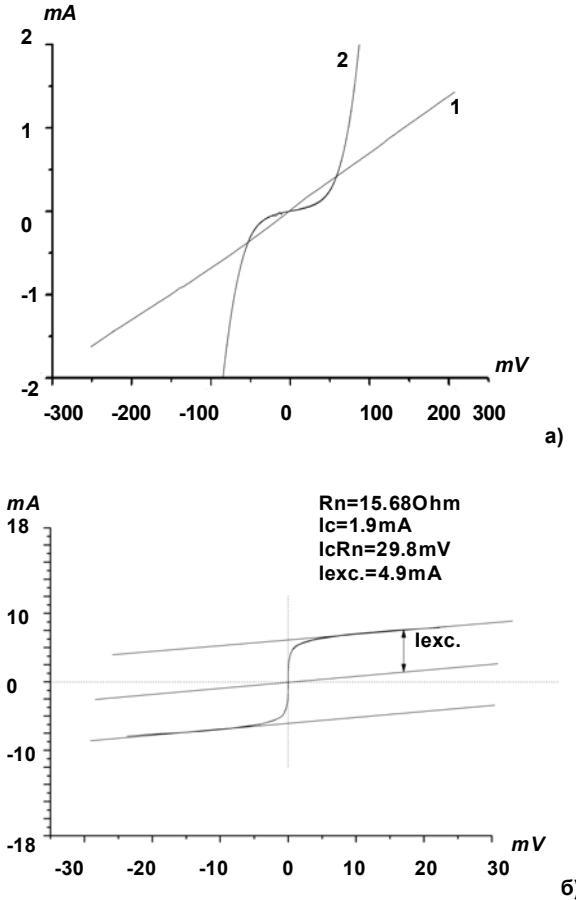

Fig. 2. a) I–V curves of the tunnel junctions : 1 – silicon barrier without tungsten, 2 – silicon barrier with the small tungsten concentration c_w ~4at% and barrier thicknesses d =12 nm. b) Typical non-hysteretic I–V curve of MoRe – Si :W (c_w= 8.0 at.%) – MoRe Josephson junction with Si :W barrier thicknesses d = 12 nm, T = 4.2 K

But at the high relatively concentration values (c_W ~6–9 at%) MoRe-Si(W)-MoRe junctions demonstrate a Josephson superconducting current appearance [4] (see fig. 2, b). Usually, the differential resistance values (in linear region of their quasiparticle I–V curves) of these junctions are higher enough (10–100 times) in comparison with the differential resistance values of the Josephson tunnel junctions with the well-known direct tunneling and having the same values of the Josephson critical current. So, it means (see fig. 2, b) the fabricated junctions have large enough values (up to 10–30 mV) of the well-known parameter named I_CR_N product (Josephson critical current I_C multiplied by R_N – resistance of the junction in normal state). Now it's not so clear a reason of this phenomena but it seems very attractive and perspective. It's important and interesting that the high voltage asymptotes of the quasiparticle I–V curves of the fabricated junctions do not cross the origin of coordinates (see fig. 2, b), it means they are not described by Ohm low in the high voltage region, and it means that through these junctions the sufficient excess quasiparticle currents $I_{exc.}$ flow (the asymptotes of the quasiparticle I–V are parallel to the Ohm low curves for the junctions in the normal state and here are shifted (up or down) by the excess current I_{exc}), one can see in fig. 2, b the I_{exc} = 4.9 mA.

To investigate experimentally the silicon layers Si(W) with tungsten clusters in them (c_W= 4.0 at.%) we have measured (by using Atomic Force Microscope) a relief of the deposited multilayers (AFM is in non contact mode of it operation): i) Si(W) layer deposited on the substrate (a polycrystalline Al_2O_3) and ii) (for a comparison) the MoRe layer deposited on the Si(W) layer (see fig. 3).

There are two basic modes of dynamic operation of AFM: amplitude modulation (AM) mode and frequency modulation (FM) mode. Depending on the mode of operation, the AFM uses F_{ts} or some entity derived from F_{ts} as the imaging signal (if V_{ts} is a potential energy between the tip and sample, usually, a z component of the tip-sample force:

$$F_{ts} = -\frac{\partial V_{ts}}{\partial Z} \qquad (1)$$

F_{ts} has long-and short-range contributions. In vacuum, there are short range chemical forces (fractions of nm) and van der Waals, electrostatic and magnetic forces with a long range up to 100 nm ($F_{ts} \sim 1/z^6$ (Baym 1969)). Assuming additivity and disregarding the discrete nature of matter by replacing the sum over individual atoms by an integration over a volume with a fixed number density of atoms, the van der Waals interaction between macroscopic bodies can be calculated ("Hamaker (1937) approach"). This approach does not account for retardation effects due to the finite speed of light and is therefore only appropriate for distances up to several hundred angstroms. For a spherical tip with radius R next to a flat surface (z is the distance between the plane connecting the centers of the surface atoms and the center of the closest tip atom) the van der Waals potential is given by Israelachvili (1991):

$$V_{VdV} = -A_H R / 6_Z \qquad (2)$$

The van der Waals force for spherical tips is thus proportional to $1/z^2$, while for pyramidal and conical tips, a 1/z-force law holds (Giessibl, 1997). The "Hamaker constant" A_H depends on the type of materials (atomic polarizability and density) of the tip and sample. For the most solids and interactions across vacuum, A_H is of the order of 1 eV. For a list of A_H for various materials, see French (2000); Krupp (1967). The van der Waals interaction can be quite large – the typical radius of an etched metal tip is 100 nm and with z = 0.5 nm, the

van der Waals energy is ≈ −30 eV, and the corresponding force is ≈ −10 nN. Because of their magnitude, van der Waals forces are a major disturbance in force microscopy.

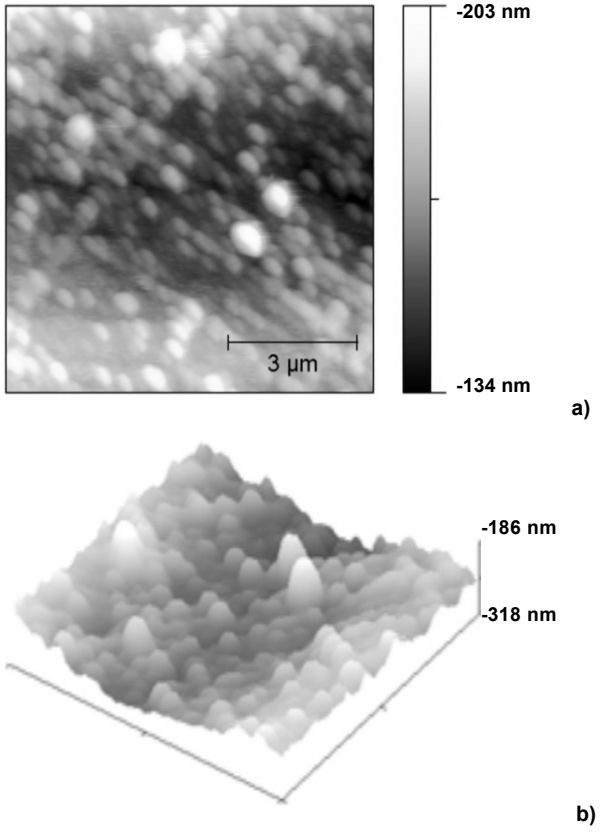

Fig. 3. The measured images of reliefs of the deposited multilayers (for their surface van der Waals forces): a), b)- the Si(W) layer (c_W= 4.0 at.%) deposited on the substrate (a polycrystalline Al_2O_3). a) a surface view, b) 3-D image

One can see (the most clear in the fig. 3 a),b)) a large number of the uniformly distributed "balls" (with diameters close to 100 nm) which are inserted in the silicon layer surface, these "balls" have height close 20–40 nm and formed a number of separate channels. So, it seems we see some spatial images of the mentioned above tungsten clusters inserted in the silicon layer and these images like balls. As it's mentioned above the AFM feels Van der Waals forces of the atomic clusters, so as a result we see (by AFM) enlarged images of the real tungsten clusters (inserted in the silicon), and we think the real cluster diameter is close 3–10 nm.

Discussion. To interpret the obtained current-voltage characteristics (at various tungsten concentrations) we propose a model of a resonant percolation charge transport in the investigated junctions. According to [3] impurity atom (cluster) insertion in the barriers results in an appearance of a localization of the charges in them, and the calculated in [3] I–V curves for this case are very similar to our curve 2 in the fig. 2 a). If concentration of the impurities in the barrier is increasing a quantum percolation resonant transport mode becomes possible (such idea has been proposed in [5] firstly). So, in our work experimentally there is realized the effect of the electron resonant tunneling through a number of their states which are localized in the tungsten clusters inserted in the silicon layers in the junctions. If the tungsten concentration become higher some threshold value and as a results after achieving a some percolation threshold the superconducting Josephson currents appear in the fabricated junctions (see fig. 2 b)).

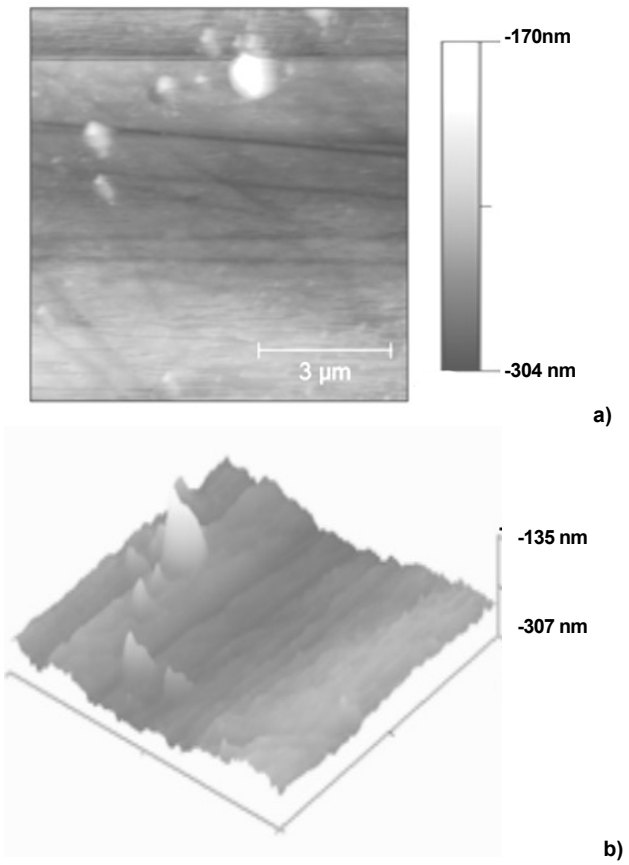

Fig. 4. a), b) MoRe layer deposited on the mentioned above (Fig. 3 a), b)) Si(W) layer. a) a surface view, b) 3D image

Metallic dopants in Si represent the ultimate limit of a quantum dot where the space confinement is given by its three-dimensional Coulomb potential with the charging energy ΔE which leads to the Coulomb blockade effect. The observed a strong suppression around zero voltage bias and the sharp rise in current above certain voltages V_{th} (note that it is almost vertical in the curve 2) can be ascribed to the fact that in these cases V_{th} exceeds the charging value of $e/2C$. We can check this assumption by estimating the charging energy of a nanoscale W cluster with a radius R~1 nm. Its capacitance $C \approx \varepsilon R$ with $\varepsilon = 12$ for Si, determines the threshold voltage value $V_{th} \sim e^2 / (2\,\varepsilon R) \approx 60$ meV which agrees well with the measured data (fig. 2 b, curve 2). Other version of the possible (in our case) Coulomb blockade behavior does appear on the base of analysis of the observed cluster image pictures (see fig. 3 a), b)). If we see here a number of the regular cluster series we can propose the existence of the blockade in a some number of the clusters in series, for example, not one but three clusters with $V_{th} = 20$ meV have joint threshold voltage $V_{th3} = 3{*}V_{th} = 60$ meV. One can see this estimation of the cluster diameter (~3–10 nm) is in agreement with the results of AFM measurements given above.

If the dopant concentration increases further, we can expect the emergence of metallic nanoclusters with energy spacing one to two orders of magnitude smaller than those of single-atom dopants and, as a result, the formation of a strongly inhomogeneous set of charge traps within the dielectric material with localized energies E_0.

Transparency D(E) of the chain of localized states [2,3] is

$$D(E) = \frac{1}{1 + (E - E_0)^2 / \Gamma^2} \qquad (3)$$

Γ is the half-width of the localized level.

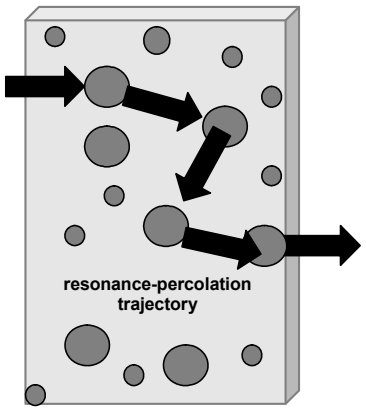

Fig. 5. Schematic view of a resonance-percolation trajectory

At relatively high concentrations (c_W ~ 6–9 at. %) of tungsten in the silicon barriers an existence of a resonant tunneling effect is observed (if percolation limit is overcome) through localized levels of scattering centers (W atoms) (see fig. 5). Simultaneously, at some conditions in these junctions a superconducting Josephson current appears on the base of the percolation resonant tunneling (see fig. 2 b)).

The aim of the work is to use the effect of resonance-percolation trajectories in order to find a barrier composition which would allow a relatively simple fabrication process, performances comparable to currently used state-of-the-art junctions, and the possibility to adjust superconducting characteristics over a wide range of critical current densities and characteristic voltages without any principal technological changes at the same time.

Conclusions. AFM (in FM mode) experimental investigation of the surface of the silicon layers with tungsten clusters inserted in them gives the possibility to obtain a quality express information about the space distribution of these clusters in the layer with high enough space resolution up to 1 nm. To do a quantity description of the obtained data it's necessary: 1) to know the parameter named "Hamaker constant" A_H for the investigated materials; 2) to calculate a dependence of the polarization rate of the two-phases material on the cluster size (inserted in them). Simultaneously, we experimentally confirmed that a radius of action of the van der Waals forces equals approximately ~ 100 nm. In our case this method demonstrates high sensitivity and space resolution for the silicon-tungsten system. To measure experimentally the tungsten cluster size in silicon it's necessary to do further special investigations.

We have measured by using atomic force microscope (AFM) a relief of the silicon layers Si(W) with tungsten clusters inserted in them, in which some enlarged images of these tungsten clusters have been observed. We use these Si(W) layers to fabricate Josephson junction with resonance-percolation charge transport in them. We have presented a simple theoretical formalism for a set of resonance-percolating trajectories inside a thin dielectric film. We believe that these results can form a base for novel type Josephson junctions with enhanced superconducting properties and, at the same time, well-separated metallic electrodes.

Publication is partially based on the research provided by the grant support of the State Fund For Fundamental Research of Ukraine (project F64/008).

REFERENCE

1. Gudkov. A. L., Properties of planar Nb/α-Si/Nb Josephson junctions with various degrees of doping of the α-Si layer / A. L. Gudkov, M. Yu. Kupriyanov, A. N. Samus // Journal of Experimental and Theoretical Physics. – 2012, – Vol. 114, № 5, – P. 818–829.

2. Lifshits I. M., O tunnelnoy prozrachnosti neuporyadochennyih sistem / I. M. Lifshits, V. Ya Kirpichenkov. // ZhETF. – 1979. – T. 77. – P. 989–990.

3. Matveev K. A., Interaction-induced threshold singularities in tunneling via localized levels / K. A. Matveev, A. I. Larkin // Phys. Rev. B 46, – 1992. – P. 15337–15339.

4. Shaternik V. E., Niobium nitride Josephson junctions: Experiment and computer simulations / V. E. Shaternik, S. Yu. Larkin, T. A. Khachaturova // Physica C, – 2006. № 435, – P. 96–98.

5. Transition from Coulomb blockade to resonant transmission regime in superconducting tunnel junctions with W-doped Si barriers. / V. E. Shaternik, A. Shapovalov, M. Belogolovskii et al // Materials Research Express, – 2014. – Vol 1, – P. 35–38.

6. Charge transport under microwave irradiation in Josephson heterostrucrures superconductor-doped semiconductor-superconductor / V. E. Shaternik, A. Shapovalov, O. Suvorov et al // Physics and Engineering of Microwaves, Millimeter and Submillimeter Waves (MSMW), International Kharkov Symposium on. – 2013. – P. 655–657.

Submitted on 24.12.15

Шатернік В., д-р фіз.-мат. наук, Шаповалов А., канд. фіз.-мат. наук,
Суворов О., асп., Білоголовский М., д-р фіз.-мат. наук
від. надпровідної електроніки Інститут металофізики ім. Г. В. Курдюмова НАН України
Прокопенко О., канд. фіз.-мат. наук, Пустовойт М., студ.
каф. нанофізики та наноелектроніки, факультет радіофізики, електроніки та комп'ютерних систем
Київський національний університет імені Тараса Шевченка

ПЕРЕХОДИ ДЖОЗЕФСОНА ПОКРАЩЕНОЇ ФУНКЦІОНАЛЬНОСТІ ІЗ РЕЗОНАНСНО-ПЕРКОЛЯЦІЙНИМ ТИПОМ ТРАНСПОРТУ ЗАРЯДУ В НИХ

Одержано та досліджено новий тип джозефсонівських структур із резонансно-перколяційним типом транспорту заряду. На основі аналізу ВАХ цих структур показано, що для цього типу структур є характерними рекордні значення характеристичної напруги – добутку IcRn. За допомогою атомно-силового мікроскопу досліджена топографія окремих шарів цієї джозефсонівської структури. Показана можливість спостерігати на наноструктурному рівні формування кластерної структури вольфраму в кремнієвій матриці бар'єру джозефсонівського переходу.

Ключові слова: *перехід Джозефсона, Андріївське відбиття, резонансно-перколяційний транспорт заряду, атомно-силовий мікроскоп, надпровідник, металеві кластери.*

Шатерник В., д-р физ.-мат. наук, Шаповалов А., канд. физ.-мат. наук,
Суворов А., асп., Белоголовский М., д-р физ.-мат. наук
отд. сверхпроводниковой электроники
Института металлофизики им. Г. В. Курдюмова НАН Украины,
Прокопенко А., канд. физ.-мат. наук, Пустовойт М., студ.
каф. нанофизики и наноэлектроники, факультет радиофизики, электроники и компьютерных систем
Киевского Национального университета имени Тараса Шевченко

ПЕРЕХОДЫ ДЖОЗЕФСОНА УЛУЧШЕННОЙ ФУНКЦИОНАЛЬНОСТИ С РЕЗОНАНСНО-ПЕРКОЛЯЦИОНЫМ ТИПОМ ТРАНСПОРТА ЗАРЯДА В НИХ

Получены и исследованы новый тип джозефсоновских структур с резонансно перкаляционным типом транспорта заряда. На основание анализа данных ВАХ этих структур показано что для этого типа структур характерны рекордные значения характеристического напряжения – произведения IcRn. С помощью атомно-силовой микроскопии исследованы топография поверхности отдельных слоев этой джозефсоновской структуры. Показана возможность наблюдать на наноструктурном уровне формирование кластерной структуры вольфрама в кремниевой матрице барьера джозефсоновского перехода.

Ключевые слова: *переход Джозефсона, Андреевское отражение, резонансно-перколяционный транспорт заряда, атомно-силовой микроскоп, сверхпроводник, металлические кластеры.*

UDC 53; 533.9.082.5

A. Skarbuta, stud., S. Olszewski, Ph.D.
Department of Computer engineering, Department of Radio Engineering and electronic systems,
Faculty of Radiophisics, Electronics and Computer Systems,
Taras Shevchenko National University of Kyiv

ABELIZATION PROCEDURE FOR RECOVERING OF EMISSION INTENSITYS' 3D DISTRIBUTIONS FOR DIRECT FLOW PLASMATRON TORCH FROM 2D IMAGES

Sources of non-equilibrium atmospheric pressure plasma play an increasingly central role in various plasma-chemical technologies. For instance, the destruction of toxic high-molecular compounds in aqueous solutions, the reforming of hydrocarbons in synthesis gas, and the creation of nano-materials with organic liquids. This paper presents the algorithm for recovering optical parameters of 3D spatial distribution for direct flow plasmatron torch using abelization and segmentation methods. The offered results of calculations are based on purposed algorithm.

Key words: *direct flow plasmatron torch, 3-D spatial distribution, abelization, segmentation.*

Introduction. Experimental study of the direct flow plasmatron torch dynamics [3] showed that it can not be considered as optically thin emission source (fig. 1). However, the spatial distribution of emission properties is a source of information on the physical and chemical processes that occur in its' volume.

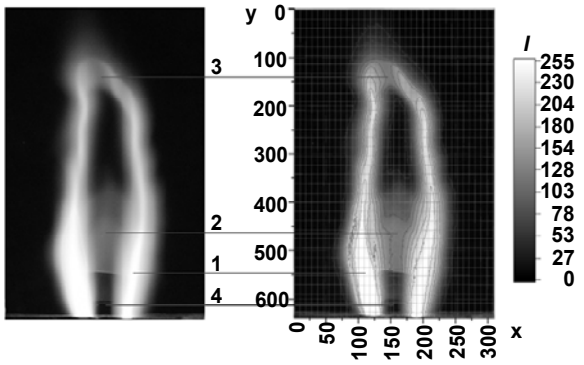

**Fig. 1. Direct-flow plasmatron plasma torch:
1 – area of classical arc; 2 – area of transverse arc;
3 – area of secondary discharge; 4 – "dead zone"**

Among the existing methods for restoring spatial distribution characteristics of the object, abelization procedure occupies a key place. Input data for such a procedure is registered as hardware signal that, in general, is integral emission intensity along the line of sight.

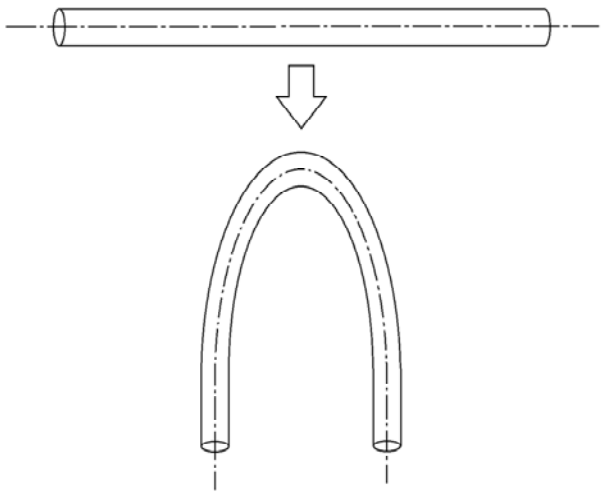

Fig. 2. Formation nature of classical arc

However, the abelization method can be adequately applicable only for objects with a known symmetry, which in practice occurs quite often. However, direct flow plasmatron torch is created by stochastic and deterministic disturbances of objects' initial symmetry, which has previously known cylindrical symmetry (fig. 2).

In this work the algorithm for recovering optical parameters of 3D spatial distribution for direct flow plasmatron torch using abelization and segmentation methods is shown.

Experimental. Overall unbalanced – the object is divided into fragments, which are generated by symmetry conditions flare formation [4]. Recovery process of optical parameters' 3D spatial distribution of the flare was conducted in two stages. At the first stage the fragmentation of the image on items with uniform cylindrical geometry. The second stage is the consistent implementation abelization for each fragment separately from the "stitching" results on the boundary between fragments.

Algorithm of searching the area with uniform parameters for local cylindrical coordinate system is based on finding for each isosurface point the least remote opposite point on image of this isosurface. To select isosurface, the image segmentation algorithm based on analysis of pixels was used [1]. The symmetry axis angle and intersection point of the symmetry axis and highlighted axis coordinate ξ_0 on the image were calculated from obtained points coordinates. The procedure was performed for all isosurface points of image. The neighboring areas for which the deviation between parameters ξ_0 and φ was not exceeded the given pre-specified accuracy, were referred to the same fragment (fig. 3).

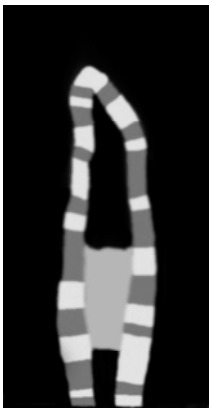

Fig. 3. Direct flow plasmatron torch fragmented image

As the measure of general image asymmetry were considered the value $\eta = \frac{S_0 - \overline{S}}{S_0}$, where – is the full torch image area, – the average area of the uniform geometry fragments (fig. 4).

© Skarbuta A., Olszewski S., 2015

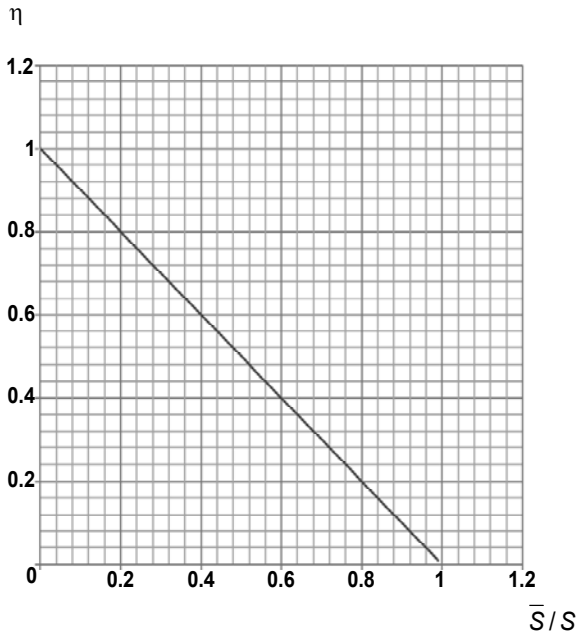

Fig. 4. Image asymmetry value

An abelization was used for each such fragment as for an object with cylindrical symmetry. For this case, the most appropriate abelization method is the Pierce method [2].

The calculations of a_{jk} coefficients for solving linear algebraic equations systems are carried by the formulas:

$$r_k = r_0 k$$

$$\sin(\alpha) = \frac{\sqrt{r_k^{\,2} - r_{k-1}^{\,2}}}{r_k}$$

$$a_{k,k} = \frac{r_k^{\,2}}{2}\left(\arcsin\left(\frac{\sqrt{r_k^{\,2} - r_{k-1}^{\,2}}}{r_k}\right) - \frac{\sqrt{r_k^{\,2} - r_{k-1}^{\,2}}}{r_k}\right)$$

$$a_{k-i,k} = \frac{r_{k+i}^{\,2}}{2}\left(\arcsin\left(\frac{\sqrt{r_{k+i}^{\,2} - r_{k-1}^{\,2}}}{r_{k+i}}\right) - \frac{\sqrt{r_{k+i}^{\,2} - r_{k-1}^{\,2}}}{r_{k+i}}\right) - \sum_{p=0}^{i}\sum_{q=0}^{i-1} a_{k-p,k-q}$$

If the divergence is less than the pre-specified level of accuracy, a "stitching" of the parameters on the border between fragments were made by averaging neighboring elements. Otherwise, to parts that are not "stitched", the additional running algorithm with increase accuracy class was implemented. The convergence of the algorithm is satisfactory when image asymmetry value is $\eta \le 0.95$.

Block diagram of the algorithm is shown on fig. 5.

Parameters ε_1 and ε_2 were used in the process of clustering and stitching information into one.

The parameter ε_1 characterizes the acceptable derivations that allow to determine the identity of single torch element to present or next cluster. The parameter ε_2 adjusts the degree of difference for corresponding elements of two adjacent uniform clusters during the procedure of stitching.

The calculations were carried out for direct flow plasmatron torch image, shown on fig. 1, which is typical for this kind of torches. The result of the calculations is three-dimensional matrix, whose elements are the three-dimensional distribution of the emission intensity.

Calculations were performed for the full image area, but in this paper we present the most informative sections that are substantially differ from each other, and show that the algorithm is indeed possible to apply for areas with completely different geometry [5].

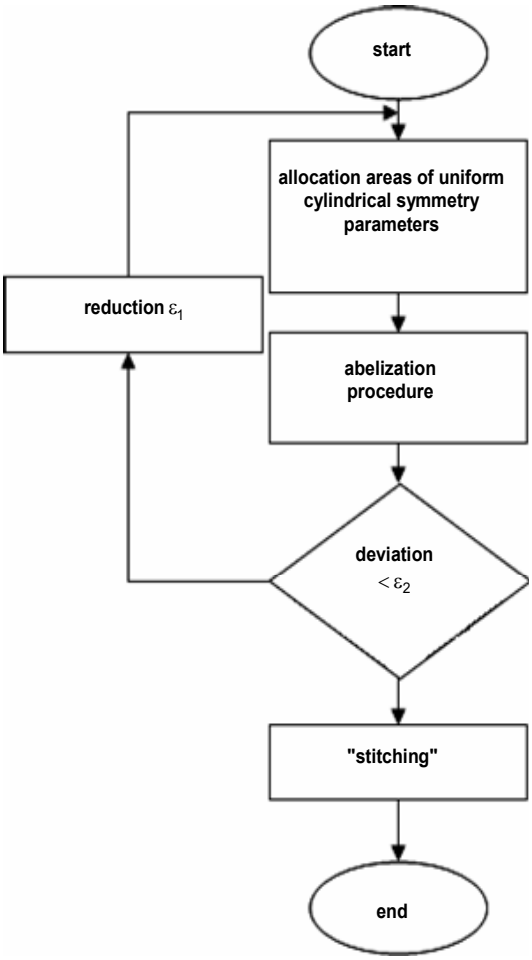

Fig. 5. Block diagram of the algorithm

Let us consider the emission characteristics' spatial distribution for the key sections (fig. 6) of the torch that characterize its different areas (fig. 1).

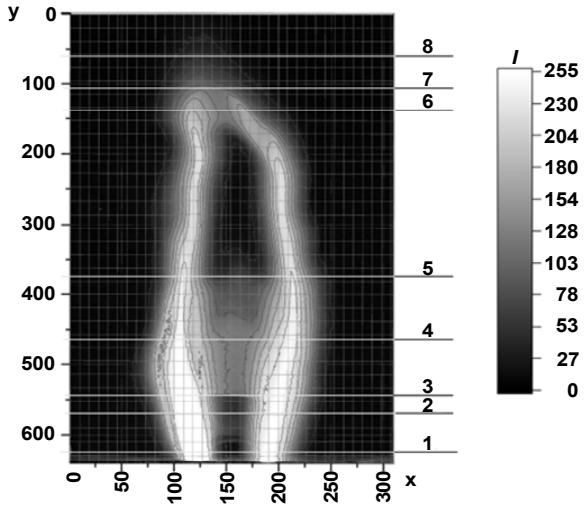

Fig. 6. Direct flow plasmatron torch cuts for which are shown the calculation results of the optical emission intensity distribution

Fig. 7 shows the emission characteristics' spatial distribution for "dead zone" area.

As can be seen from the fig. 7 there are no optical radiation in the surrounding areas of the electrodes (classical arc). "Shelf" in the left side of the graph occurs because the data is lost on the initial images. The similar situation persists on the next graphs, but due to the symmetry of the system it may be neglected. For the restoration of full information one "column" is enough.

As can be seen from the figure 7, there is no other kinds of optical radiation except for the surrounding areas of the electrodes (primary arc). "Shelf" in the left side of the graph occurs due to the data loose on the initial image, caused by the matrix photosensitive off-scale during the registration of emission properties from the source. The following graphs performed the similar situation, but due to the symmetry of the system it may be neglected, since the restoration of full information is enough even for one "column".

Fig. 8 shows the occurance of transverse arc area of direct flow plasmatron torch.

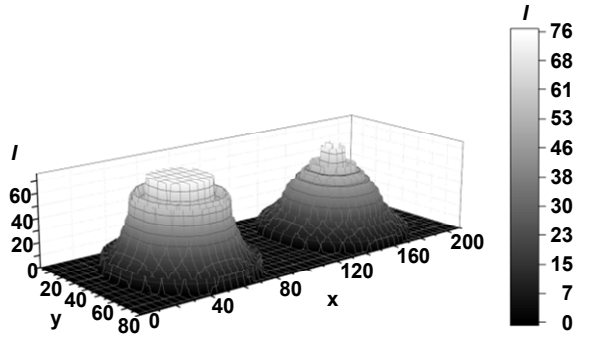

Fig. 7. The intensity distribution of optical emission direct flow plasmatron torch. Cut 1*

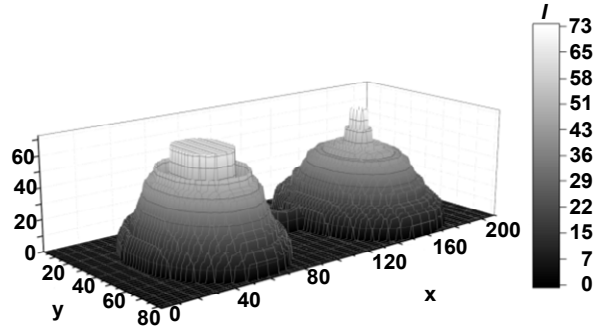

Fig. 8. The intensity distribution of optical emission direct flow plasmatron torch. Cut 2*

Fig. 9 clearly shows a zone of classical arc and transverse arc zone, which has a higher emission intensity and accordingly, higher plasma temperature. A "column" consists of the main narrow channel plasma torch with a higher temperature, which is surrounded by a layer of cold plasma, that uniformly, "bell-shaped" decreases. We can speak about the correctness and accuracy of the proposed algorithm because the similar torch was observed in some another similar experimental studies.

Fig. 10 shows direct flow plasmatron torch cut in the middle of transverse arc area.

Fig. 11 shows a top of transverse arc area, where we can observe that the thickness of a cold plasma decreases and the decrease gradient becomes higher.

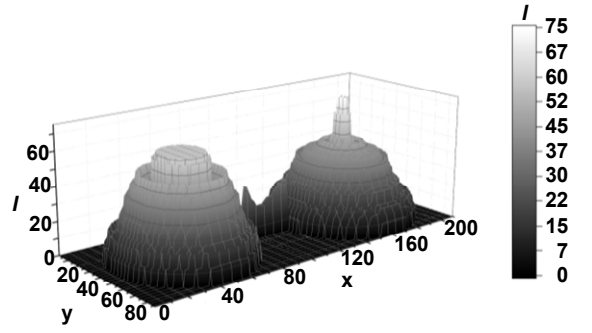

Fig. 9. The intensity distribution of optical emission direct flow plasmatron torch. Cut 3*

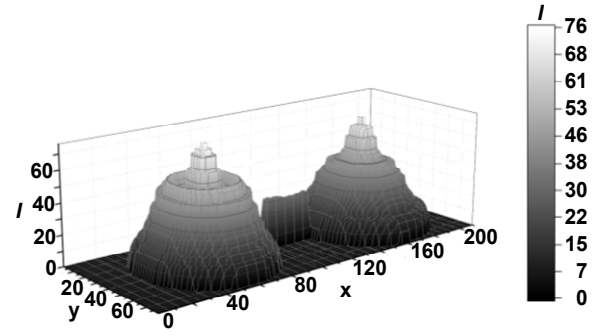

Fig. 10. The intensity distribution of optical emission direct flow plasmatron torch. Cut 4*

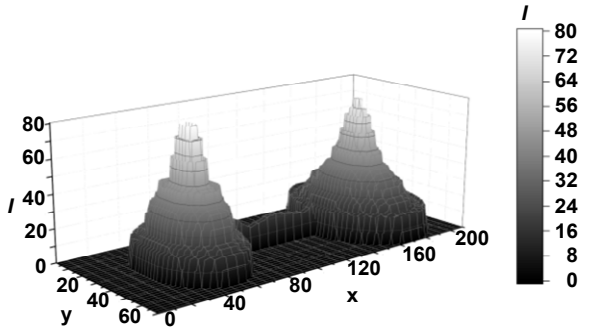

Fig. 11. The intensity distribution of optical emission direct flow plasmatron torch. Cut 5*

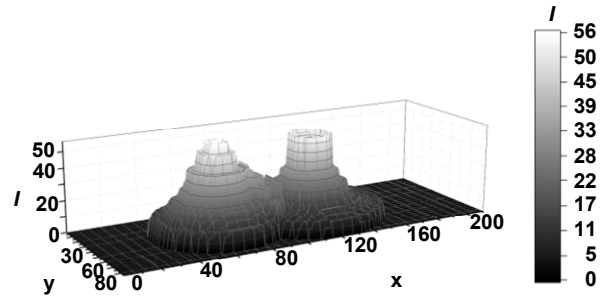

Fig. 12. The intensity distribution of optical emission direct flow plasmatron torch. Cut 6*

Figures 13–15 show secondary discharge area cuts. On the border of the classical arc area and transverse arc area two peaks are still clearly tracked, however they are "blurring" further, and the plasma becomes more uniform.

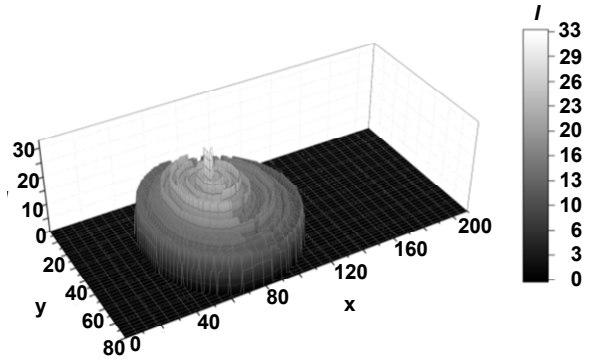

Fig. 13. The intensity distribution of optical emission direct flow plasmatron torch. Cut 7*

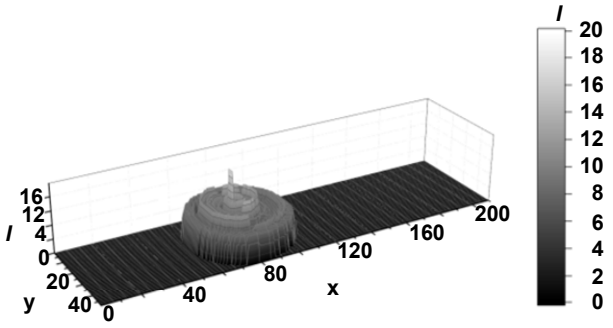

Fig. 14. The intensity distribution of optical emission direct flow plasmatron torch. Cut 8*

Conclusions. In the absence of methods, which meet all restrictions imposed by the object of study, the new algorithm was proposed, which bases on the Pierce abelization and segmentation.

The proposed algorithm is suitable for restoring of optical parameters spatial distribution from 2D images for objects with complex geometry. Geometry of objects must be generated by deterministic and stochastic perturbations of initial symmetry. Regular symmetry areas must be uniform and general image asymmetry value less than 0.95.

Plasma torches largely correspond to these demands, so this algorithm can be used for such objects most adequately.

To clarify the results of calculations, it may be useful to apply the methods of computer tomography and probe plasma diagnostics in further studies.

REFERENCE

1. *Jahne B.* Cifrovaja obrabotka izobrazhenij / B. Jahne // 2007. – Tekhnospera, Moskow. – 584 p.

2. *Kuznecov Je. I.* Metody diagnostiki vysokotemperaturnoj plazmy / Je. I. Kuznecov, D. A. Scheglov // 1980, Atomizdat, Moskow. – 160 p.

3. *Olszewski S. V.* Gidrodinamichna model' plazmi fakelu prjamotochnogo plazmotrona z paralel'nimi cilindrichnimi elektrodami / S. V. Olszewski, D. V. Dmitriev, P. V. Bondarenko, S. O. Kostenko // Intellectual systems of decision-making and problems of computational intelligence ISCDMCI'2013: Mater. mizhnar. nauk. konf., 20–24 May. 2013 y. Evpatoria, Ukraine. – 114–116 p.

4. *Olszewski S. V.* Vidnovlennja trivimirnih rozpodiliv intensivnosti viprominjuvannja fakelu prjamotochnogo plazmotrona za dvovimirnimi zobrazhennjami / S. V. Olszewski, A. M. Shkarbuta // Intellectual systems of decision-making and problems of computational intelligence ISCDMCI'2015: Mater. mizhnar. nauk. konf., 25–28 trav. 2015 r., Zalizny Port, Ukraine. – 153–155 p.

5. *Shkarbuta A. M.* Abelization procedure application for recovering of emission intensity 3d distributions of direct flow plasmatron torch from 2d images / A. M. Shkarbuta, S. V Olszewski // Proceedings by XV Intrnational Young Scientists' Conference on Applied Physics 10–13 June. 2015 y., Kyiv, Ukraine. – 108–109 p.

Submitted on 20.06.15

Шкарбута А., студ., Ольшевський С., канд. фіз.-мат. наук
каф. комп'ютерної інженерії, каф. радіотехніки та радіоелектронних систем,
факультет радіофізики, електроніки та комп'ютерних систем
Київський національний університет імені Тараса Шевченка

ПРОЦЕДУРА АБЕЛІЗАЦІЇ ДЛЯ ВІДНОВЛЕННЯ ТРИВИМІРНИХ РОЗПОДІЛІВ ІНТЕНСИВНОСТІ ВИПРОМІНЮВАННЯ ФАКЕЛУ ПРЯМОТОЧНОГО ПЛАЗМОТРОНА ЗА ДВОВИМІРНИМИ ЗОБРАЖЕННЯМИ

Джерела нерівноважної плазми атмосферного тиску відіграють важливу роль в різних плазмохімічних технологіях. Це руйнування токсичних високомолекулярних сполук у водних розчинах, реформінгу вуглеводнів в штучному газі, і створення нано-матеріалів з органічними рідинами. Ця стаття присвячена алгоритму відновлення просторового розподілу оптичних параметрів факелу прямоточного плазмотрону. Підґрунтям алгоритму є використання методів абелізації та сегментації. Результати обрахунків ґрунтуються на запропонованому алгоритмі.

Ключові слова: *факел прямоточного плазмотрону, просторовий розподіл, кластерізація, абелізація.*

Шкарбута А., студ., Ольшевский С. канд. физ.-мат. наук
каф. компьютерной инженерии, каф. радиотехники и радиоэлектронных систем,
Факультет радиофизики, электроники и компьютерных систем
Киевский национальный университет имени Тараса Шевченко

ПРОЦЕДУРА АБЕЛІЗАЦИИ ДЛЯ ВОССТАНОВЛЕНИЯ ПРОСТРАНСТВЕННЫХ РАСПРЕДЕЛЕНИЙ ИНТЕНСИВНОСТИ ИЗЛУЧЕНИЯ ФАКЕЛА ПРЯМОТОЧНОГО ПЛАЗМОТРОНА ПО ДВУМЕРНЫМ ИЗОБРАЖЕНИЯМ

Источники неравновесной плазмы атмосферного давления играют важную роль в разных плазмохимических технологиях. Таких как разрушение токсичных высокомолекулярных соединений в водных растворах, реформинга углеводородов в искусственном газе и создание наноматериалов с органическими жидкостями. Эта статья посвящена алгоритму восстановления пространственного распределения оптических параметров факела прямоточного плазмотрона. Алгоритм основан на использовании методов абелизаци и сегментации. Приведены результаты работы алгоритма.

Ключевые слова: *факел прямоточного плазмотрона, пространственное распределение, кластеризация, абелизация*

Наукове видання

ВІСНИК

КИЇВСЬКОГО НАЦІОНАЛЬНОГО УНІВЕРСИТЕТУ ІМЕНІ ТАРАСА ШЕВЧЕНКА

РАДІОФІЗИКА ТА ЕЛЕКТРОНІКА

Випуск 1(23)

Друкується за авторською редакцією

Оригінал-макет виготовлено ВПЦ "Київський університет"

Автори опублікованих матеріалів несуть повну відповідальність за підбір, точність наведених фактів, цитат, економіко-статистичних даних, власних імен та інших відомостей. Редколегія залишає за собою право скорочувати та редагувати подані матеріали. Рукописи та дискети не повертаються.

Формат 60x84$^{1/8}$. Ум. друк. арк. 9,8. Наклад 300. Зам. № 216-7721.
Гарнітура Arial. Папір офсетний. Друк офсетний. Вид. № Рф1.
Підписано до друку 31.03.16

Видавець і виготовлювач
ВПЦ "Київський університет"
01601, Київ, б-р Т. Шевченка, 14, кімн. 43
☎ (38044) 239 3222; (38044) 239 3172; тел./факс (38044) 239 3128
e-mail: vpc@univ.kiev.ua
http: vpc.univ.kiev.ua
Свідоцтво суб'єкта видавничої справи ДК № 1103 від 31.10.02